Evaluation of Low-Current Orificed Hollow Cathodes

by

Matthew Thomas Domonkos

A dissertation submitted in partial fulfillment
of the requirements for the degree of
Doctor of Philosophy
(Aerospace Engineering)
in The University of Michigan
1999

Doctoral Committee:

Associate Professor Alec D. Gallimore, Chair
Professor Luis P. Bernal
Professor Ward D. Getty
Professor Yue Ying Lau
Doctor Ira Katz, Maxwell Technologies Federal Division

For my parents

ACKNOWLEDGMENTS

I could not have prevailed in this effort without the support of a number of others. First and foremost, I must thank my God for giving me a life where I would be able to accomplish the things I have. By extension, I am indebted to my parents, my brother, my sister, and their families. They have been my primary support throughout my education. As such, this dissertation is in part theirs as well.

My advisor, Professor Alec Gallimore, has been tremendously supportive of my research by providing an open learning environment, ample funds for my experimentation, and invaluable insight when I missed the obvious and not-so-obvious. I am also grateful to Dr. Ira Katz for his insight and for jump starting my modeling efforts—the computer just doesn't look much like a tool to an experimentalist. I also thank the other members of my committee, Professor Luis P. Bernal, Professor Ward D. Getty, and Professor Yue Ying Lau.

The work presented in this thesis was supported primarily by the NASA John H. Glenn Research Center as part of a NASA Graduate Student Research Program Fellowship, reference Grant No. NGT-3-52311. Michael Patterson of NASA Glenn put up with me and provided additional technical and equipment support. In addition, the entire On-Board Propulsion Branch at NASA Glenn has helped me in some form in my graduate career. I especially acknowledge all of the technical assistance from Mike Pastel, Bob Roman, Ralph Jacko, Fred Jent, Bob Kozlo, Hardy Hartman, Winston Johnson, John Miller, Glen Bowers, Wayne Condo, and Randy Miele. And for helping me get my foot in the door at NASA Glenn in the first place, I thank Jim Parkes and Roger Myers.

The technical and administrative assistance at the University of Michigan's Aerospace Engineering Department was also instrumental in my work. I greatly appreciate the work of Margaret Fillion, Tom Griffin, Gary Gould, Dave Mclean, and, even though he could be a real pain, Terry Larrow.

Of course, I couldn't really manage this work without the company of those who also chose this peculiar form of self-abuse. Colleen, John, James, and Brad helped keep my mind fresh in spite of the expiration date, not to mention what great friends they have been to me. I've also enjoyed a beer or two with Patty, Jose, Farnk, Jon, George, Tim, Mike, and Sang.

PREFACE

The research presented in this dissertation focuses on the development of low-power and low-flow-rate orificed hollow cathodes for low-current applications. For electric propulsion in the 100 to 300-W range, cathode power and flow consumption can become greater than ten percent of the respective totals for the system. For kW-class electric propulsion systems, consumption of power and propellant by the cathode is typically only a few percent of the total for the thruster. This research aims to scale orificed hollow cathodes for low-current electric propulsion, with the ultimate goal of cathodes for 100-300-W electric propulsion which consume significantly less than ten percent of the power and flow-rate.

A number of 3.2-mm outer diameter cathodes were designed based on scaling existing 6.4-mm diameter cathodes to low-current. The orifice aspect-ratio was varied between cathodes to examine the effects of orifice geometry on performance, and a cathode was also built with a removable, enclosed keeper to test the effectiveness of the enclosure for reducing cathode power consumption. Alternate cathode geometries were also investigated. The performance of these cathodes was measured in both diode and triode discharges. A temperature distribution in the cathode was measured using an imaging radiometer in order to evaluate the dominant mechanisms of heat transfer away from the high-temperature thermionic emitter. Langmuir probes were used to measure the electron temperature, number density, plasma potential, and electron energy distribution function of the plasma internal to the hollow cathode, in the cathode-to-keeper gap, and downstream of the keeper.

A computer model, combining elements of other hollow cathode models, was developed to examine the operation of low-current hollow cathodes. Both the insert and orifice regions were modeled, and the insert region predictions agreed with the experimental data. The results also supported several of the conclusions of the experimental investigation regarding cathode optimization. The model failed to predict the elevated internal cathode pressure observed experimentally. A constricted arc in the orifice was hypothesized to be responsible for the elevated pressure due to a combination of arc heating and the pinch effect. Simplified models were constructed to provide theoretical support to the constricted arc hypothesis.

The theoretical and experimental results were used to design a second-generation laboratory model, low-current hollow cathode. The design was modified to limit thermal conduction, facilitate ionization in the insert region, and increase electron transport downstream of the keeper. The cathode consumed 20 percent less power at the same flow-rate as the best of the cathodes tested previous. Additionally, the improved cathode was able to operate in spot-mode at much lower flow-rates than the first-generation cathodes.

TABLE OF CONTENTS

LIST OF FIGURES

LIST OF TABLES

NOMENCLATURE

A	Normalization constant
A_{eff}	Effective emission area on the insert (m^2)
A_o	Orifice area, m^2
A_{pr}	Langmuir probe area
A_R	Richardson coefficient (60 A/cm^2-K^2)
b	Exponential constant for EEDF curve fit or coefficient
c	Speed of light (3×10^8 m/s)
c_i	Ion acoustic speed (m/s)
c_p	Specific heat at constant pressure (J/kg-K)
C	Constant
C_a	Coefficient a of a polynomial curve fit
d_h	Heater diameter including radiation shields (mm)
$d_{i,i}$	Inner diameter of the cathode insert (mm)
$d_{i,o}$	Outer diameter of the cathode insert (mm)
d_m	Hard-sphere molecular diameter (2.1×10^{-10} m for xenon)
d_o	Orifice diameter (m unless otherwise noted)
$d_{t,i}$	Inner diameter of the cathode tube (mm)
$d_{t,o}$	Outer diameter of the cathode tube (mm)
e	Electron charge (1.6×10^{-19} C)
E	Electron energy (eV)
E_{ds}	Electric field in the double sheath adjacent to the insert (V/m)
E_x	Axial electric field (V/m)
f	Escape fraction of emitted electrons
f_{ex}	Fraction of excitations causing ionization
$f(E)$	Normalized electron energy distribution function, EEDF
$f(v_e)$	Normalized electron speed distribution function
h	Planck constant (6.626×10^{-34} J-s)
I_D	Cathode discharge current (A)
I_e	Electron current to the Langmuir probe (A)
$I_{e,ins}$	Electron current from the insert region to the orifice region (A)
$I_{e,ori}$	Electron current emitted from the orifice (A)
I_i	Bohm ion current at sheath boundary (A)
$I_{i,emit}$	Emitted ion current from the orifice (A)
$I_{i,ori}$	Orifice ion current (A)
$I_p(x)$	Pixel intensity at position x (arbitrary units)
$I_{p,max}$	Maximum pixel intensity on a line profile (arbitrary units)
$I_{p,min}$	Minimum pixel intensity on a line profile (arbitrary units)
I_{pr}	Langmuir probe current (A)
j	Current density (A/m^2)
$j_{e,back}$	Plasma electron backstreaming flux ($\#/m^2$)
$j_{e,thm}$	Thermionic electron current density (A/m^2)
j_i	Ion flux, ($\#/m^2$)
J_i	Bohm ion current density at sheath boundary (A/m^2)

k	Boltzmann constant (1.38 x 10^{-23} J/K)
K_L	Coefficient of loss through orifice entrance (0.5)
l_{ch}	Characteristic length scale in plasma region (cm)
l_{c-k}	Length of cathode-to-keeper gap (mm)
l_{htr}	Length of heater on cathode tube (mm)
l_i	Insert length (mm)
l_k	Thickness of keeper orifice (mm)
l_{k-a}	Length of keeper-to-anode gap (mm)
l_o	Orifice length (mm)
l_{tip}	Orifice plate thickness (mm)
$\ln\Lambda$	Coulomb logarithm
L_{eff}	Effective emission length from the insert (m)
m_e	Electron mass (9.11 x 10^{-31} kg)
m_i	Ion mass (2.19 x 10^{-25} kg for xenon)
$\dot{m}$	Mass flow-rate (mg/s or sccm) (1 sccm = 0.097 mg/s)
M_e	Atomic mass of an electron (1/1836)
M_i	Atomic mass of an ion (131 for xenon)
M_o	Atomic mass of a neutral (131 for xenon)
n	index of refraction
n_x	Number density of species x(cm^{-3} or m^{-3})
N_{eo}	Number density-rate of electron impact ionization events (#/m^3-s)
N_{sph}	Number of particles in a Debye sphere
p	Pressure (Pa)
p_c	Critical sonic pressure (Pa)
p_{in}	Pressure in the insert region (Pa)
q_{conv}	Convective power loss (W)
$q_{e,back}$	Convective power loss due to backstreaming electrons (W)
$q_{e,con}$	Convective power loss due to electron current (W)
$q_{e,thm}$	Convective power input by thermionic electrons (W)
q_{ex}	Power loss due to radiation of excited states (W)
$q_{i,loss}$	Convective power loss due to ion loss (W)
$q_{i,ori}$	Convective power input by orifice ions (W)
q_{ion}	Ionization power loss (W)
q_{Ohmic}	Ohmic heat generation (W)
r	Radial coordinate (m)
r_o	Orifice radius (m)
R	Resistance (Ohms)
R_{sp}	Specific gas constant (63.1 J/kg-K for xenon)
t	Time (s)
t_{eq}	Equipartition time (s)
$T(x)$	Cathode temperature at a position x (ºC)
T_{BB}	Blackbody temperature of a body (ºC)
T_x	Temperature of species x (eV or K)
T_{max}	Maximum cathode temperature on a line profile (ºC)
T_{min}	Minimum cathode temperature on a line profile (ºC)
T_{wall}	Temperature of the orifice wall, (K)

T_β	Brightness or emittance corrected temperature of a body (ºC)
$\bar{u}_o$	Average gas velocity (m/s)
U_{ex}	Average excitation energy (eV)
v_d	Drift velocity (m/s)
v_e, $\bar{v}_e$	Electron thermal speed (m/s)
$\bar{v}_i$	Average ion speed (m/s)
V_{ds}	Voltage across a planar double sheath (V)
V_f	Floating potential (V)
V_p	Plasma potential (V)
V_{pr}	Langmuir probe voltage (V)
V_{sph}	Volume of a Debye sphere (cm^3)
x	Distance from an established zero point (mm) or exponent on the electron energy for EEDF curve fit
$\langle x \rangle$	Property x averaged over Maxwellian distribution
Z	Charge state
ε	Emittance of a surface
ε_o	Permittivity of free space (8.85×10^{-12} F/m)
ϕ_{eff}	Effective work function (eV)
ϕ_i	Ionization potential (12.12 eV for xenon)
ϕ_o	Material work function (eV)
γ	Ratio of specific heats (5/3 for xenon)
η	Plasma resistivity (Ω-m)
κ	Thermal conductivity (W/m-K)
λ	Wavelength of pyrometer optics (m)
λ_D	Debye length (cm or m)
λ_{ee}	Electron mean free path for self-collision (m)
λ_{ex}	Electron mean free path for excitation (m)
λ_{ion}	Electron mean free path for ionization (m)
μ	Permeability (H/m) or dynamic viscosity (N-s/m^2)
μ_o	Permeability of free space ($4\pi \times 10^{-7}$ H/m)
$\nu_{a,b}$	Collision frequency of a with b (Hz)
ρ	Mass density (kg/m^3)
ρ_o	Mass density in the orifice (kg/m^3)
σ	Self collision cross section for ions and neutrals (m^2)
$\sigma_{a,b}$	Collision cross section for a colliding with b (m^2)
σ_{ex}	Electron-impact excitation cross-section (m^2)
σ_{ion}	Electron-impact ionization cross-section (m^2)

Subscripts

coll	Collected particle

e	Electron
emit	Emitted particle
ex	Excited neutral
i	Ion
ins	Insert
o	Neutral
ori	Orifice
p	Plasma
pr	Primary

LIST OF APPENDICES

Appendix

CHAPTER 1

INTRODUCTION

Hollow cathodes, in their various forms, are used in a wide variety of applications where high current densities, low cathode-fall voltages, and extended lifetimes are required.[1,2,3,4,5,6] Electric propulsion devices, plasma contactors, lasers, and magnetrons all use hollow cathodes in some form. Hollow cathodes are capable of operation at a fraction of an Ampere up to several hundred Amperes, all in an arc discharge. At high pressure internal to the hollow cathode, discharge voltages can occur below the ionization potential of the propellant due to the formation of a negative anode sheath. Lifetimes up to 28,000 hours have been demonstrated, with even greater lifetimes theoretically possible.[6,7,8] These operating characteristics make hollow cathodes ideal for use with electric propulsion systems and as space plasma contactors.

1.1 Hollow Cathode Applications

1.1.1 Ion Thrusters

Ion thrusters employ two hollow cathodes as shown in Figure 1.1. The discharge hollow cathode creates an internal plasma which enables emission of an electron current in excess of space charge limitations. A magnetic circuit is created within the ion thruster using permanent magnets in a ring-cusp configuration.[9] The electrons emitted by the gas-fed hollow cathode stream toward the anode along the magnetic field lines. Neutral propellant molecules (usually xenon) are also injected directly into the discharge chamber. Collisions between the electrons and neutrals create the ions in the discharge chamber. The magnetic circuit also acts to control the effective anode area and to contain the high-energy electrons for ionization while thermalized low temperature (a few eV) electrons conduct the current to the anode.[9] The ions are focused and accelerated by the grids, while the electrons are contained within the discharge chamber. An external hollow cathode emits an electron current equal to the ion beam current to neutralize the space charge within the beam. The hollow cathode neutralizer uses a keeper electrode to sustain its discharge. Loss of ions to the walls of the discharge chamber and the neutral flux through the grids constitute the major sources of performance degradation. Additionally, the neutralizer flow is also considered a loss since it is used only to bridge the neutralizer to the ion beam electrically. Typical operating conditions of the NSTAR ion thruster used on the Deep Space One spacecraft are reported in Table 1.1.[10] Also listed in Table 1.1 are the target parameters for a 100-300-W ion thruster which could fulfill the primary propulsion role for small spacecraft.[11,12] The discharge hollow cathode is operated at a relatively high current to increase the plasma density within the discharge chamber, while the keeper on the neutralizer is kept at low-current to optimize efficiency. Flow to both cathodes is kept to the minimum necessary for the operating conditions.

The high specific impulse makes ion thrusters ideal for planetary probes where the low thrust density can be tolerated.

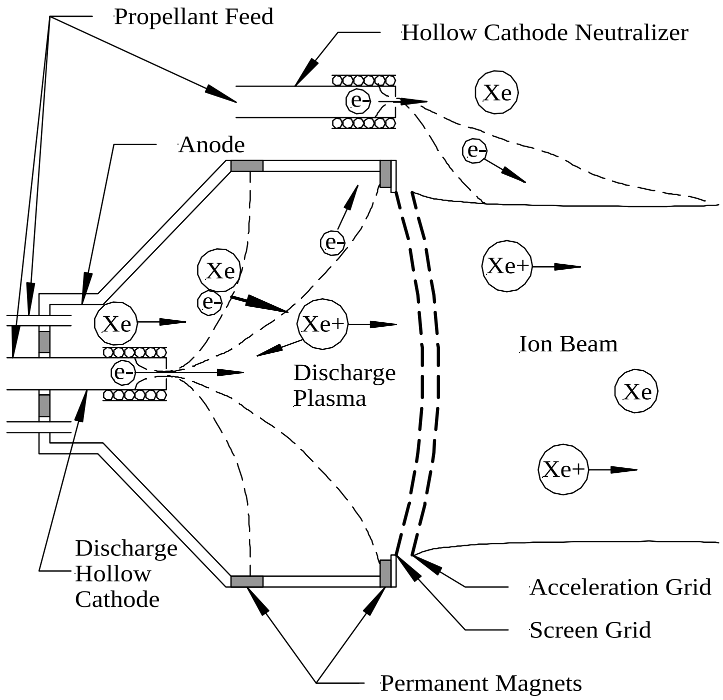

Figure 1.1 - Ion Thruster Schematic

Table 1.1 – NSTAR and 100 to 300-W Class Ion Thruster Operating Characteristics[10,11,12]

Parameter	*NSTAR Nominal Conditions*	*100 to 300 W Thruster Targets*
Discharge Voltage, V	25 to 28	28
Discharge Current, A	4.8 to 12.8	1.05 to 1.90
Beam Voltage, V	634 to 1096	600 to 900
Beam Current, A	0.54 to 1.76	0.09 to 0.2
Neutralizer Keeper Voltage, V	14.2 to 21.2	20
Neutralizer Keeper Current, A	1.5	0.1
Coupling Voltage, V	-13.6 to –14.2	15
Main Flow-rate, mg/s	0.59 to 2.32	0.15 to 0.34
Cathode Flow-rate, mg/s	0.21 to 0.36	Included in main flow.
Neutralizer Flow-rate, mg/s	0.21 to 0.30	0.05
Power, kW	0.51 to 2.32	0.1 to 0.3
Thrust, mN	21.6 to 92.6	4 to 11.3
Specific Impulse, s	2200 to 3300	2000 to 2950
Efficiency	0.45 to 0.66	0.38 to 0.54

1.1.2 Hall Thrusters

Single-stage Hall thrusters typically employ only one hollow cathode, although some are equipped with two for redundancy. In the case of Hall thrusters, the hollow cathode acts as the discharge cathode and the neutralizer, as shown in Figure 1.2. An annular anode is surrounded by inner and outer electromagnets which create a radial magnetic field. Electrons traveling from the cathode to the anode are caught in an $\vec{E}\times\vec{B}$ azimuthal drift. The strength of the magnetic field scales inversely with the anode diameter since higher field strengths become necessary to contain the electrons as the confinement scale decreases. The Hall-effect increases the electron mobility, enabling electron-impact ionization of the neutrals. The ions are accelerated axially by the closed-drift of electrons. The magnetic field strength is insufficient to magnetize the ions. Beyond this electron cloud, the Debye lengths are very short, and the ions are quickly shielded from the influence of the acceleration region. Like its ion thruster counterpart, the hollow cathode also emits an electron current to neutralize the ion beam. While the hollow cathodes are typically equipped with a keeper, the discharge current is usually sufficient to maintain the high temperature needed for cathode operation. The flow of propellant to the cathode again represents a performance degradation since the flow is only weakly ionized and the few ions formed are not accelerated to a significant velocity. Typical operating conditions for the D55 anode layer (Hall) thruster are listed in Table 1.2.[13,14,15,16] The higher thrust density of Hall thrusters makes them more ideal for satellite stationkeeping applications due to trip time and satellite packaging constraints.

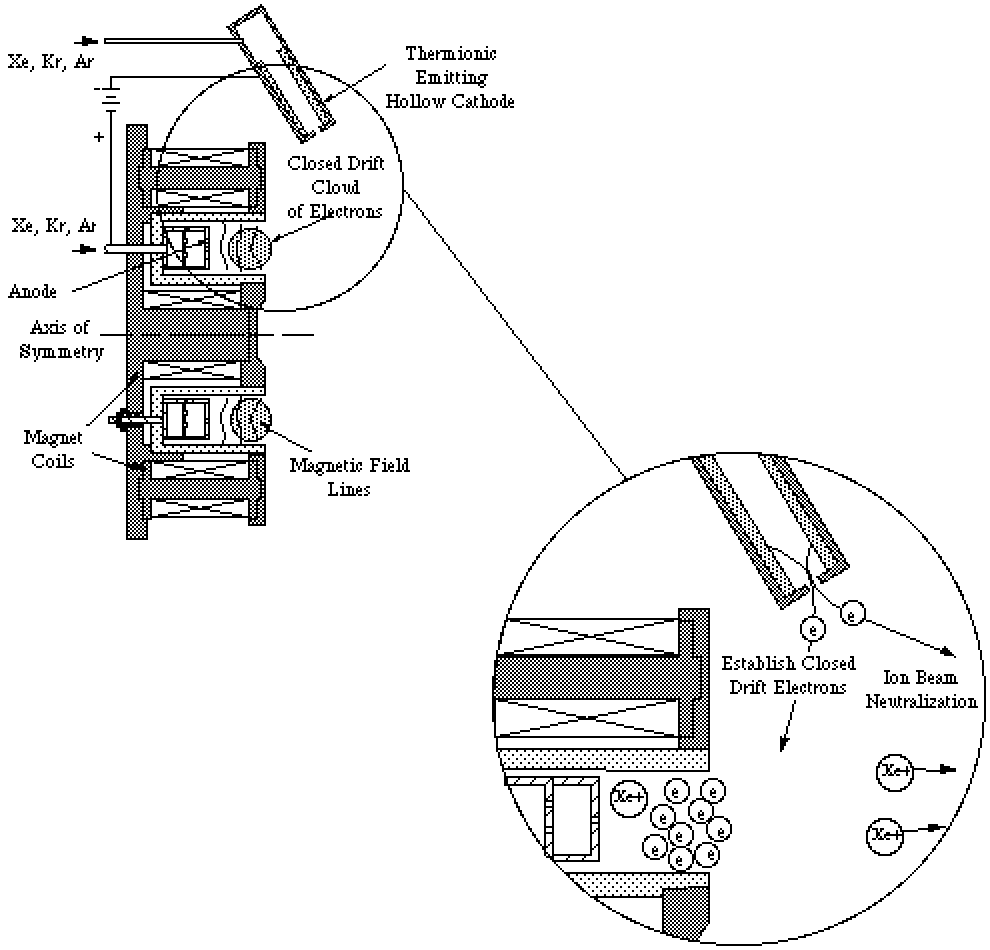

Figure 1.2 - Schematic of Hall thruster Operation

Table 1.2 - D55 Anode Layer Thruster and SPT-30 Stationary Plasma Thruster Operating Characteristics[13,14,15,16]

Parameter	*D55 Nominal Conditions*	*SPT –30 Nominal Conditions*
Discharge Voltage, V	300	150 to 250
Discharge Current, A	4.5	0.6 to 1.0
Discharge Flow-rate, mg/s	4.76	0.6 to 1.0
Cathode Flow-rate, mg/s	0.78	0.1
Cathode Floating Voltage, V	-13 to -15	Not reported.
Power, kW	1.35	0.09 to 0.26
Thrust, mN	39 to 118	4.9 to 13.2
Specific Impulse, s	1250 to 2700	521 to 1230
Efficiency	0.5 to 0.6	0.14 to 0.31

1.1.3 Plasma Contactors

Hollow cathodes have also found application as plasma contactors.[6,17,18,19] Photoemission of electrons from spacecraft surfaces cause charging relative to the ambient space plasma. Spacecraft charging also occurs when high voltage solar arrays are used.[17] This leads to arc discharges which damage instruments, or the spacecraft charge imbalance distorts measurements being made by scientific payloads.[19] The plasma contactor regulates the spacecraft potential relative to the space plasma. Hollow cathode plasma contactors are operated with keeper electrodes, and consequently the keeper power and propellant supplies for the cathode must be onboard the spacecraft. Typical operating conditions for the Space Station Plasma Contactors (SSPC) are listed in Table 1.3.[17] With plasma contactors, the plasma flow facilitates the transfer of charge between the spacecraft and the ambient plasma, and system lifetime may be limited by the onboard propellant supply.

Table 1.3 - Space Station Hollow Cathode Plasma Contactor Operating Parameters[17]

Parameter	*Nominal Conditions*
Keeper Current, A	3.0
Keeper Voltage, V	12.2 to 20
Flow-rate, mg/s	0.44 to 0.88
Coupling Voltage, V	10 to 16

Plasma contactors, and ion and Hall thrusters all use hollow cathodes as electron sources. The orificed hollow cathode, depicted in Figure 1.3, emits electrons thermionically from a low work-function insert, and a plasma is generated by electron-neutral collisions. The plasma mitigates the space charge limitations of an ordinary thermionic emitter. In order to evaluate the effectiveness of hollow cathodes as electron emitters, it is useful to define the operational parameters to be optimized. Several works have documented the conditions necessary for extended-life of hollow cathodes.[8,18,20,21,22] Besides the clear need to reduce the contaminants, spot-mode operation, characterized by small amplitude oscillations of current and voltage, minimizes the discharge voltage and appears to mitigate orifice plate erosion.[6,23] Optimization of cathode operating conditions must satisfy the constraints of system mass and life, and consequently the focus of the work by Mandell and Katz has been to minimize the flow-rate needed to sustain spot-mode operation.[24] Power consumption of the cathode plays a large role in the determination of propulsion system efficiency. In the context of this thesis, the conditions necessary for extended lifetimes are treated as a precondition for any tests or analyses. Consequently, power consumption and flow-rate are the performance parameters of interest here.

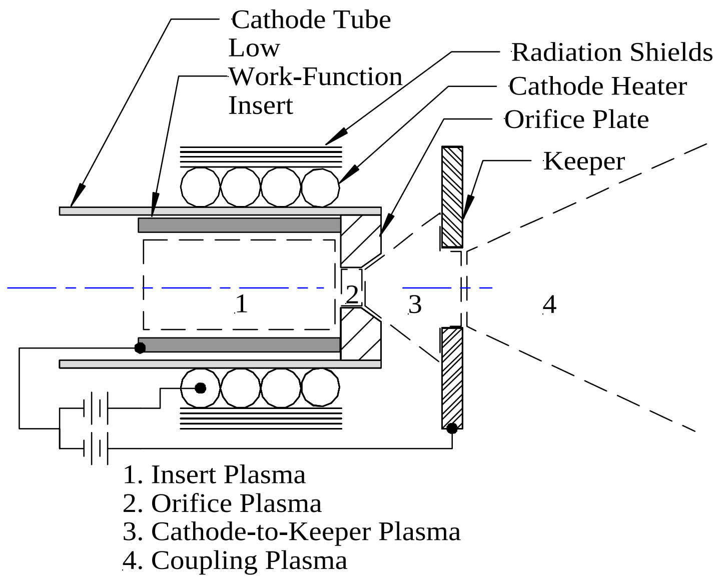

Figure 1.3 - Generalized Orificed Hollow Cathode Schematic

The present state-of-the-art, as employed on Deep Space One and the Electric Propulsion Demonstration Module (EPDM) on the Space Technology Experiment (STEX) spacecraft, appears to be adequate; however, the push toward sub-500-W electric propulsion has prompted efforts to provide similarly efficient thrusters in a smaller and lower thrust package. To achieve reductions in the scale of plasma discharges is non-trivial. As the device size is reduced, the ratio of the ion production volume to the surface area decreases. This increases the fraction of ions lost to the walls of the thruster, degrading the efficiency. In order to mitigate this, ion and Hall thruster designs have modified the magnetic circuit to confine the electrons for ionization while tailoring the ion production to favor regions where the probability of a wall collision is reduced.[11] This technique becomes less pragmatic for thruster cathodes; the additional hardware required to include magnets will reduce the volume to surface area ratio even further. Robson et al[19] developed a hollow cathode plasma contactor which included a magnetic circuit to facilitate low-current and flow-rate operation. By positioning the cathode so that it takes advantage of the magnetic circuit of the thruster, a similar benefit can be realized. The hollow cathode can be further optimized for low-current, low-flow-rate applications, although cathode models to date have neglected processes which become important in the low consumption operating regime.[5,24,25,26,27]

1.2 Overview of Hollow Cathode Physics

Several different types of cathodes are referred to as hollow cathodes. Generally speaking, all hollow cathodes are thermionic devices which rely on electron bombardment ionization of a neutral gas to generate a plasma. The open-channel hollow cathode, depicted in Figure 1.4, is one of the simplest hollow cathode devices. The arc attaches upstream of the cathode exit plane, and these devices typically operate above 1500 ºC due to the high work function of the tube material.[5] A variation on the orificed hollow cathode is shown in Figure 1.5. This design utilizes an orifice to increase the neutral density near the low-work function emitter, facilitating ionization. The work function of lanthanum hexaboride is approximately 2.6-eV, and self-heating of the pellet is insufficient to maintain the necessary emission current density. Consequently, this type of cathode requires continuous operation of the cathode heater. The hollow cathodes being discussed in this work consist of a refractory metal tube with an orifice plate welded to the downstream end as shown in Figure 1.3. A low work function insert emits electrons to create the insert plasma which flows downstream through the various regions illustrated. The cathode heater is used initially to heat the insert to emission, and self-heating sustains the discharge following ignition. The keeper is typically used to initiate the discharge and maintain it when the emission current, the current to beam or space plasma, is insufficient to provide the self-heating for stable operation. The various regions of the discharge are discussed in more detail below.

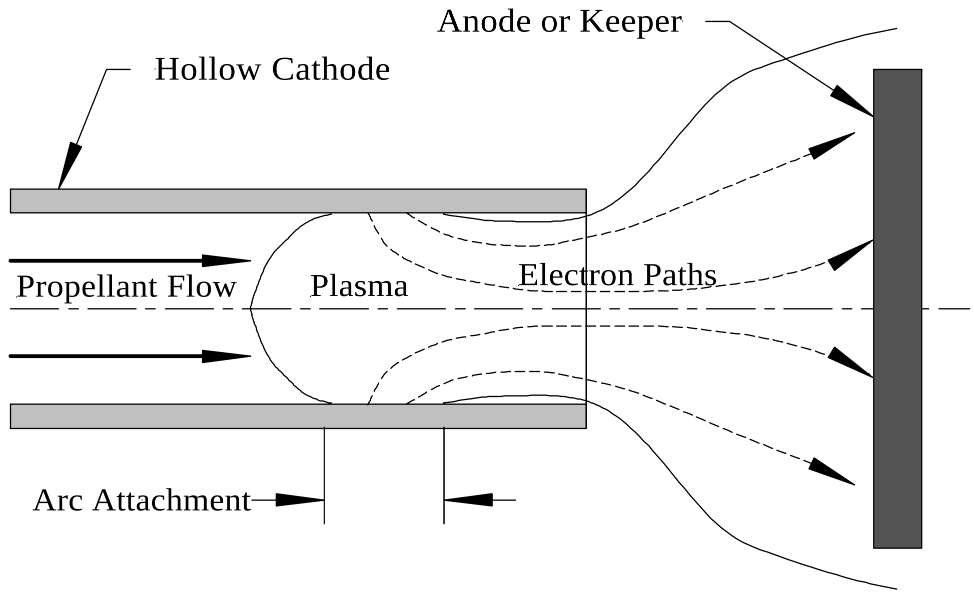

Figure 1.4 - Schematic of an Open-Channel Hollow Cathode.

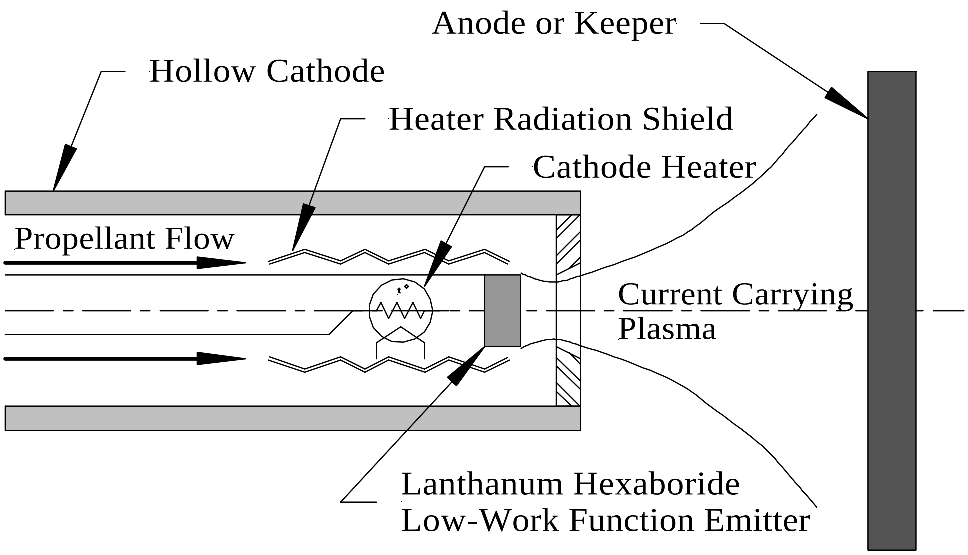

Figure 1.5 - Hollow Cathode with Orifice and Thermionic Emitting Pellet.

1.2.1 Insert Region

The cathode insert is made of porous tungsten impregnated with a 4:1:1 molar mixture of barium oxide (BaO), calcium oxide (CaO), and aluminum oxide (Al_2O_3). This composite has a low work function, and the mechanisms controlling insert properties have been described in detail.[7,8,21,22,28,29] Rittner, Rutledge, and Ahlert[28] first proposed the mechanisms responsible for the low-work function operation of the impregnated cathodes. While the specific mechanisms governing the generation and transport of barium have been argued, the consensus agrees that gaseous barium, liberated from compounds within the insert, is transported to the surface of the cathode.[28,29] A barium and oxygen monolayer on the surface of the cathode reduces the work-function.[28,29] The calcium oxide has been linked to the reduction in the rate of barium evaporation. Suitch[29] states that the insert must operate in the range from 1000-ºC to 1100-ºC; below 1000-ºC, the discharge becomes unstable, and above 1100-ºC, the impregnant evaporates at a rate which curtails the lifetime. This statement of the optimal insert operating temperature range is oversimplified. The results of a recent life test indicate that cathode life can reach 28,000 hours with an orifice plate temperature above 1100-ºC, and the insert still contained constituent elements of the impregnant.[6] For the purposes of the present investigation, it is sufficient to consider the insert as a thermionic electron emitter with established operating procedures and temperature regime which enable demonstrated life to 28,000 hours.[6]

The emission of thermionic electrons from the insert creates a negative charge density immediately adjacent to the cathode surface, as shown in Figure 1.6. Ions from the plasma are accelerated toward the insert by the radial electric field. The presence of a relatively high-electron density near the insert surface results in a change in curvature in the sheath potential profile which several authors have referred to as a double sheath.[25,26,30,31] Figure 1.6 exaggerates the structure of the sheath to emphasize the presence of electrons in the sheath. A double sheath develops at the boundary between quasineutral plasmas of different densities where the sheath is ion-attracting for one plasma and electron-attracting for the other. The thermionic electrons are accelerated by the potential of the sheath and comprise a high-energy component to the electron population within the cathode.[31] The high-energy electrons are referred to here as primary electrons, using Siegfried's terminology.[25] The primary electrons perform the bulk of the ionization within the cathode, by both electron impact ionization and step-wise excitations. Through these collisions and Coulomb collisions, the primary electrons become thermalized. The bulk of the insert volume contains a partially ionized quasineutral gas with a two component electron population. Only the thermal electrons in the tail of the distribution are able to stream back to the insert. The remaining thermal electrons are accelerated toward the axis and the orifice by the electric field. The Debye lengths are on the order of a few hundred nanometers to a few micrometers. Ions in the insert region are accelerated toward the insert double sheath by the radial electric field. Ions enter the sheath at or above the acoustic speed, according to the Bohm sheath criterion.[25,26,31,32] The collisions and recombination of the ions on the insert surface heat it to sustain the discharge. This ion current also accounts for part of the total cathode current. The primary electrons comprise the balance of the discharge current from the insert region.

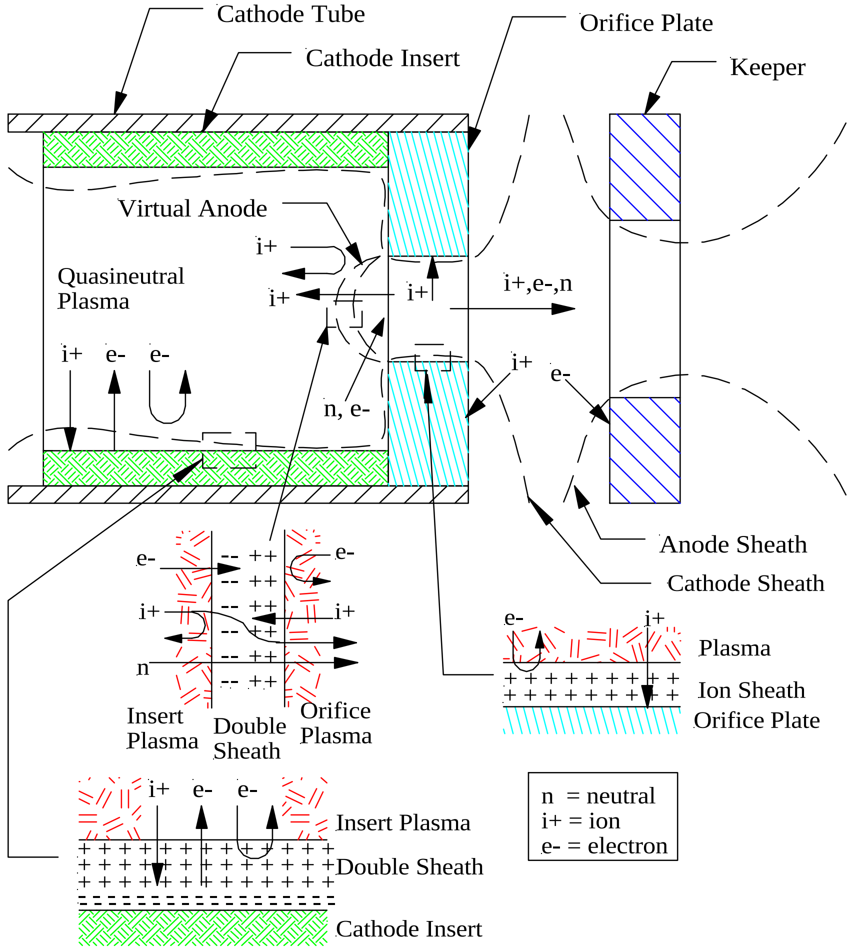

Figure 1.6 - Schematic of Hollow Cathode Physics

1.2.2 Orifice Region

A double sheath forms at the boundary between the insert and orifice regions.[27,33] The electrons are accelerated into the orifice region by this sheath, while orifice region ions entering the sheath are accelerated toward insert region. The density and electric field gradients prevent ions born in the insert region from entering the orifice.

The highest current density in the hollow cathode occurs in the orifice. The Debye length is much smaller than the orifice diameter, and most collision mean free paths are ten to one hundred times smaller than the dimensions of the orifice.[24] Consequently most of the ions created in the orifice recombine on the orifice walls. The electrons in the orifice ionize the neutrals at a rate sufficient to replenish the ions lost to the boundaries.[24] The electron population within the orifice continues to diffuse toward the outlet, carrying the discharge current in the process. Given that the Debye lengths are much smaller than the dimensions of the orifice, the small electric field in the plasma drawing the ions toward the cathode potential surfaces is countered by ambipolar diffusion at the orifice exit. This allows ions to be emitted from the cathode.

1.2.3 Cathode-To-Keeper

Sheath thickness increases rapidly outside the cathode as the density decreases. If the current density of emitted ions is sufficient to maintain quasineutrality, then the electrons readily stream toward the keeper due to the slight axial electric field present outside of the sheaths. This mode of operation, referred to as spot-mode, is typified by relatively high flow-rate, low discharge voltage (8 to 20-V), and small amplitude voltage fluctuations. As the flow-rate, and consequently the ion current density, is decreased, the sheaths must grow in order to draw the electrons to the keeper or anode. Electron temperatures increase due to a decrease in inelastic collisions and the shape of the electric field. The density in the region is sufficiently low that many of the excited atoms and ions decay before successive collisions ionize them. This mode of operation is referred to as plume-mode because it is usually associated with a luminous plasma plume between the cathode and the keeper or anode. Other characteristics which typify plume-mode include relatively high discharge voltages (20 to 30-V) and large amplitude, high-frequency discharge voltage fluctuations (>4-V and >1-MHz). Some researchers have postulated that the creation of ions within the cathode-keeper gap in plume-mode leads to cathode orifice plate erosion;[23] the large voltage fluctuations accelerate the ions past the sputter threshold of the orifice plate material.

1.2.4 Downstream Plasma

Downstream of the keeper, Williams and Wilbur have observed the formation of a potential hill.[34] Williams and Wilbur postulated that immediately downstream of the keeper, the density is still sufficient for ionization to occur.[34] The electrons, having greater thermal velocity than the ions, expand from this region leaving a net positive charge density in this region which accounts for the potential hill. Further downstream, the electrons and ions, being many Debye lengths from the electrodes, expand spherically until they encounter another plasma where a double sheath forms. This expansion region is especially critical for determining the emission current that a plasma contactor can provide. Given the geometries of typical Hall and ion thrusters, the beam plasmas are expected to be closely coupled to the cathode plasma, and the expansion of the cathode plasma cannot be treated without considering the beam.

1.3 Summary of Hollow Cathode Development

Some of the earliest work with orificed-hollow cathodes for electric propulsion devices was conducted by researchers at the NASA Lewis Research Center (LeRC) and Hughes Research Laboratories (HRL) beginning in the 1960's.[1,23,35,36,37] The initial development work focused on the neutralizer hollow cathode for the Space Electric Rocket Test II (SERT II) mercury ion thruster. Rawlin and Pawlik characterized the operation in spot and plume-modes and established that the cathode performance was insensitive to orifice aspect ratio over the range which they tested.[1] By 1969, Rawlin and Kerslake had demonstrated cathode lifetimes to more than 10,000 hours, and began investigating the use of impregnated tungsten inserts.[36] Byers and Snyder determined that cathode power scaled inversely with keeper and collector surface area presented to the cathode.[35] An investigation performed at the Jet Propulsion Laboratory (JPL) in 1971 determined the cathode tube temperature distribution experimentally and analytically.[38] Mirtich reported the findings of an investigation into orifice plate erosion and temperature distributions in hollow cathodes for 30-cm ion thrusters in 1973.[37] An investigation of the operating characteristics of hollow cathodes with barium oxide impregnated porous tungsten inserts found that cathode operation with these inserts was effectively identical to cathode operation with a rolled foil insert with a low work function coating.[39] The impregnated tungsten orifice plates used in this investigation degraded over several hundred hours of operation, suggesting that the barium had evaporated.[39] Rawlin also reported on the results of a 13,000 hour life test of a mercury hollow cathode in 1973.[23] The orifice plate had eroded from the downstream end in accordance with the theory by Rawlin mentioned in the previous section.[23] While experimental investigations of hollow cathodes at NASA LeRC, HRL, and JPL have continued to the present, several efforts to model hollow cathode processes were reported or started in the 1970's.[5,6,20,25,40,41,42]

While Fearn and Philip did not present a predictive model, they were able to quantify several of the parameters necessary for the development of such a model.[40] This work focused primarily on the current emission processes. It was postulated that spot-mode operation occurred when the internal surface area of the orifice was sufficient to carry the discharge at an experimentally determined current density; the current attached to the upstream end of the orifice plate and the insert in plume-mode. A cathode was constructed with a solid tantalum insert to determine the role of the low work function impregnant. While discharges were obtained with the solid tantalum insert, the cathode generally operated at higher power and temperature than the cathode with a low work-function insert. In an attempt to better quantify the role of the orifice geometry, the upstream side of the orifice was chamfered, and the performance was compared with a straight orificed hollow cathode. Qualitatively, the results supported the authors' contention concerning the physics of spot and plume-modes. A discussion concerning electron-impact ionization concluded that this mechanism was feasible at high flow-rates, but the path lengths became too great to account for the ionization at low-flow-rates. The present work assumes that electron impact ionization and excitation are the dominant mechanisms controlling the plasma generation for reasons that will be discussed later.

Rehn and Kaufman performed some of the first investigations into the use of noble gases with hollow cathodes.[41,42] The initial investigation involved a parametric experimental study of the effects of changing the geometry of the hollow cathode assembly. This work provides experimental evidence that the ionization processes determine cathode performance over a wide range of operating paramenters.[41] The collaborative work by Rehn and Kaufman was an attempt to define parameters which govern cathode operation independent of geometry and propellant.[42] While the results showed distinct branches for spot and plume-modes while using a keeper, the data obtained using a cylindrical anode failed to show similar structure.[42] These analyses are attractive because of the ease of use, however, a predictive model requires more detail.

One of the first attempts to comprehensively model the hollow cathode discharge was performed by Ferreira and Delcroix.[5] This model uses theoretical derivations for the mass flow, the ionization rate, and the radial and axial transport of charged particles.

This model is the only instance where an ionization model is used for an inert gas cathode. The use of an ionization rate model mitigates the issues associated with the assumption of an equilibrium plasma. While this model details the physical processes, the thermal analysis for the cathode tube relies upon empirically determined temperature profiles. Consequently, the model lacks the flexibility necessary to predict the behavior of new designs.

Siegfried and Wilbur developed a model for a mercury orificed hollow cathode.[25,43] To provide validation data for the model, the charged particle fluxes to the insert and orifice surfaces were quantified. The internal plasma was also probed to determine the electron temperature, number density, and plasma potential. While this model uses a semi-empirical equation to predict internal pressure as a function of flow-rate and current, it also uses an ionization model to account for the primary electrons and their contribution to the ionization in the insert region. The effective emission length on the insert was determined to be approximately two mean free paths for the primary electrons. Unfortunately, the use of an ionization model complicates the application of the overall set of equations to other propellants. The model also included a simplified heat transfer analysis of the energy transport to the cathode tube.

In the 1980's, interest in inert gas thrusters increased, and the use of the hollow cathode as a plasma contactor emerged.[34,44] These new developments created the need for two new aspects to the modeling of hollow cathodes: 1) examination of the coupling of the hollow cathode plasma with the space or discharge plasma, and 2) an insert region model for inert gases. The first of these necessities was addressed in the work by Williams and Wilbur.[34] They developed a model to describe the formation of the potential hill downstream of the cathode and the expansion of the plasma from the downstream side of the potential hill. In addition, they measured a plasma double layer between the contactor plasma and the ion source plasma.

Salhi and Turchi sought to address the need for an orificed hollow cathode model for inert gas propellants.[26,45,46] Salhi began by developing an insert region model similar to that used by Siegfried.[25,26] However, Salhi used a theoretically derived relation for the cathode pressure and modeled the electron number density using a two-temperature Saha equation. It should be noted that the mass flow-pressure relation in Salhi[26] contains two errors, and the two-temperature Saha equation was developed mathematically, without physical basis. A parametric study of the plasma properties inside the insert region was conducted to provide validation data for the model. The results of the experimental investigation agreed with the trends reported by Siegfried, while adding spectroscopic temperature and insert internal temperature measurements.[25] One of the changes Salhi[26] made to his model as a result of the experimental investigation was to incorporate the radial variation in the heavy particle temperature as a function of the discharge current. The major shortcoming of the model by Salhi[26] in terms of the current work is the assumption of electron cooling being the only heat rejection term for the insert. Conduction and convection to the neutrals are terms which become important at low-power density.

The models of Siegfried[25] and Salhi[26] both focus on the processes in the insert region and neglect the orifice physics. Mandell and Katz have developed a model for hollow cathode operation which is based primarily upon the processes within the orifice.[24] The insert region is treated simply as a plasma source. Ion loss in the orifice is balanced by volume ionization based upon a simplified model which takes only electron-impact ionization into account. By also solving a power balance in the orifice, the electron temperature and number densities are calculated. The model is able to predict the transition from spot to plume-modes based on whether the ion current expelled is sufficient to maintain charge neutrality in the cathode-keeper gap. Given the high current density within the orifice and the relatively large voltage drop predicted across the orifice, the need for modeling the insert physics is clear, particularly for low-power cathodes.

In addition to the efforts in the United States, the United Kingdom, and France mentioned above, similar work for the European RIT 10 ion thruster and space plasma contactors for tethers has been conducted in Germany and Italy.[27,47,48,49] The work by Capacci, et al. presents a model which incorporates all of the plasma regions depicted in Figure 1.3. The insert region model is based primarily on the work of Siegfried and uses the Saha equation to evaluate the electron number density.[25] The Saha equation is only strictly valid for a thermal plasma where the electrons and ions have the same temperature. A planar double sheath approximation is used at the entrance to the orifice. Within the orifice, the Saha equation is again used; the equilibrium assumption necessary for the Saha equation may be violated considering the plasma has typically two or more particle temperatures. A detailed thermal analysis from previous work is also used in the model.

1.4 Contributions of Research

The research to be presented here has focused on the development of hollow cathodes for low-flow-rate and low-power applications. The devices tested were designed based on extrapolation from existing space qualified hollow cathodes, and the limitations of this basic design were examined in the search for an optimal design. The principal goal of this dissertation was to minimize the power and propellant consumed by hollow cathodes for electric thrusters and plasma contactors. The experimental investigation included the following contributions:

- A parametric investigation of the effects of orifice aspect ratio over a larger range than previous studies.
- Thermographic analysis of the cathode temperature distribution to establish the nature of the dominant heat transfer mechanisms in the cathode tube and to enable cathode material selection to minimize cathode power consumption.
- Observation of cathode pressures for small insert and orifice inner diameters.
- Examination of the electron energy distribution function in the plume of the hollow cathode.
- Internal plasma diagnostics for low-current 3.2-mm hollow cathodes.

In addition to the experimental investigation supporting the optimized cathode goal, a conglomeration of several cathode models was developed to facilitate the optimization process. The conglomeration was dictated by the extreme operating conditions and the need to include the contributions of each section of the hollow cathode discharge (Figure 1.3). By modeling the hollow cathode processes from end-to-end, more of the physics are included than in previous models.

CHAPTER 2

EXPERIMENTAL APPARATUS

The purpose of the experiments reported here was to generate cathode performance data at low-current and mass flow-rate to use in the design optimization process. Just as it was initially unclear how to scale hollow cathodes to low-power applications effectively, the operating conditions and plasma parameters in low-current discharges were *a priori* unknown. Consequently many of the experiments performed in this investigation were similar to those reported elsewhere.[25,26,35,38] Quantifying the differences in operating characteristics between 6.4 and 3.2-mm diameter hollow cathodes was one of the principal goals of the experimental investigation. In order to go beyond previous experiments, thermography was used to evaluate external cathode temperature profiles, and the electron energy distribution function was measured in the internal and emitted plasmas. The temperature profiles on the cathode indicate which mechanisms of heat loss are dominant. Ionization rates, both inside and outside the cathode, are strongly dependent upon the electron energy distribution function. By understanding the heat loss and ionization mechanisms, the accuracy of a predictive model is improved, and the apparatus described here were essential to the overall optimization effort.

2.1 The Hollow Cathodes

The design and fabrication of the hollow cathodes used in this investigation were derived from existing hollow cathode and plasma contactor procedures.[6,17] Since the cathodes were laboratory models, a number of the specifications and inspection procedures required for flight hardware were either relaxed or omitted. However, the author attempted to follow the flight hardware procedures when it was reasonable to do so, in order to facilitate the transition from laboratory models to flight units.

2.1.1 Hollow Cathode Design and Fabrication

An engineering schematic of the 3.2-mm diameter hollow cathodes is presented in Figure 2.1. The cathode orifice plates were made from two-percent thoriated tungsten. This material has a low sputter yield and a long history of use for hollow cathode orifice plates. The orifice and chamfer on the downstream end were made using a lathe. Following the machining, the orifice plate was cleaned in a heated, ultrasonic bath of acetone for one half hour, and then a bath of ethyl alcohol for one half hour. This cleaning procedure was used for all metallic components used in the cathode; the insert, heater, and propellant isolator were used as is, without additional cleaning. The cathode tube was a molybdenum-rhenium alloy, which was used because of its strength at high-temperature and its resistance to oxygen adsorption. Materials which adsorb oxygen may release it at high operating temperatures, thereby poisoning the cathode. To reduce the oxygen content of the alloy, the tube is heated in a hydrogen furnace after it has been machined to accept the orifice plate. Next, the orifice plate is electron beam welded to the cathode tube.

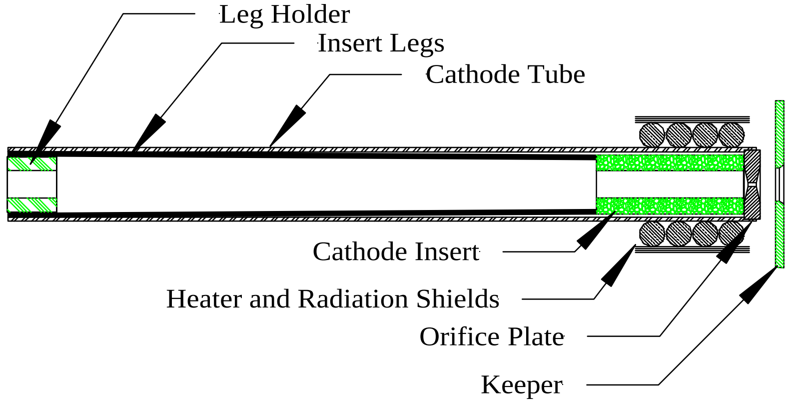

Figure 2.1 - Engineering Schematic of the Orificed Hollow Cathode

Refractory metal electrical leads attached to the upstream end of the emitter were swaged into electrical contact the with cathode tube through the use of a leg holder. This also fixed the position of the emitter within the cathode tube. A sheathed tantalum heater was wound and friction fit to the end of the cathode tube. Twelve wraps of 0.13-mm thick tantalum foil were spot-welded to the heater to serve as a radiation shield. The cathode insert was a cylindrical tube of sintered porous tungsten impregnated with 4BaO-CaO-Al_2O_3 by molar ratio.

The initial set of experiments involved performance evaluations of two mechanically identical cathodes. When attempting to assess experimentally the effects of varying the orifice geometry on the performance of hollow cathodes, the ideal technique is to change only the orifice plate. This was done by Siegfried,[25] using a slide valve with three orifice geometries. Siegfried's[25] experiment was conducted on a mercury hollow cathode, and the aspect-ratios (l_o/d_o in Figure 2.2) of the orifices were negligibly small in comparison with those considered in the current investigation. A similar experiment performed with the aspect-ratios of interest would have been feasible. However, throughout the current investigation, the experiments were designed for hollow cathode assemblies which could easily be integrated with a thruster. Consequently, to test the effects of varying the orifice aspect-ratio on the performance of the cathode, separate assemblies were fabricated and tested. The variance in performance between mechanically identical cathodes was examined in order to validate that the observed performance changes were due to orifice geometry changes. For reference, the convention used in this work for the hollow cathode dimensions is illustrated in Figure 2.2, and the specific cathode geometries tested are listed in Table 2.1. The cathodes AR6 and AR6´ were used to determine the unit-to-unit variance, enabling accurate comparison of test results between cathodes of differing geometries.

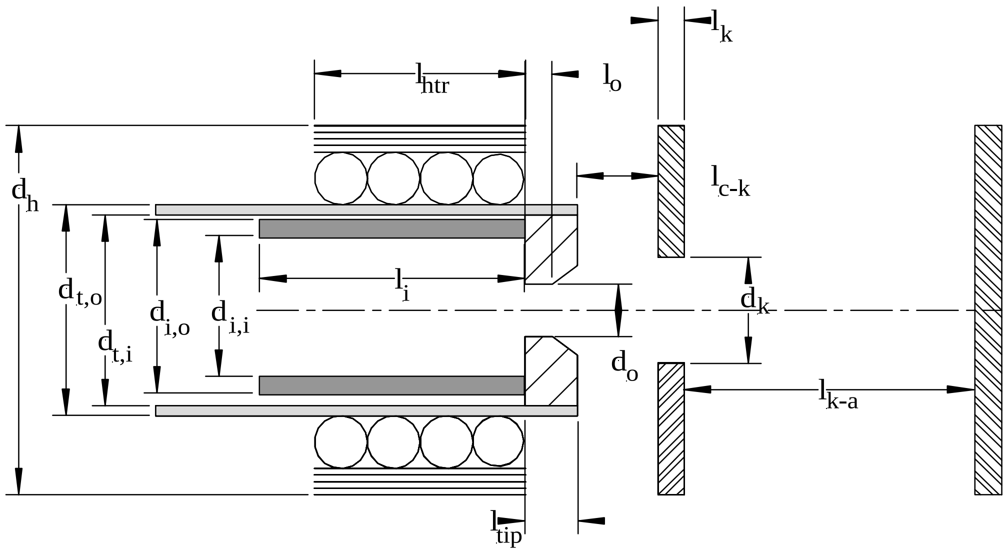

Figure 2.2 - Definition of Hollow Cathode Dimensions

Table 2.1 - Dimensions of the Orificed Hollow Cathodes Tested in this Investigation in mm

Cathode	$d_{t,o}$	$d_{t,i}$	$d_{i,o}$	$d_{i,i}$	l_i	d_o	l_o	l_{tip}	l_{c-k}	d_k	l_k
AR1	3.18	2.67	2.29	1.22	12.7	0.12	0.18	1.22	1.00	2.29	1.52
AR3	3.18	2.67	2.29	1.22	12.7	0.13	0.38	1.22	1.00	2.29	1.52
AR3-a	3.18	2.67	2.29	1.22	12.7	0.08	0.23	1.22	1.00	2.29	1.52
AR6	3.18	2.67	2.29	1.22	12.7	0.13	0.71	1.22	1.00	2.29	1.52
AR6´	3.18	2.67	2.29	1.22	12.7	0.13	0.71	1.22	1.00	2.29	1.52
OK1	3.18	2.67	2.29	1.17	12.7	0.13	0.71	1.22	1.00	2.29	1.52
EK1	3.18	2.67	2.29	1.17	12.7	0.13	0.71	1.22	1.00	2.29	1.52

Three factors motivated the particular orifice geometry chosen for AR6 and AR6´. The orifice diameter was chosen based on the expected maximum emission current of the cathode. The orifice has been found to erode over a few tens of hours until the ratio of the current to the orifice diameter is below 12 A/mm.[50] Consequently, the diameter was chosen to be 0.13 mm which corresponds to a maximum current of 1.56 A. The cathodes were operated at up to 1.50 A for several hours at a time. The orifice length was determined both by the need to facilitate ionization within the orifice and by fabrication considerations. As the physical path length for electrons increases within the orifice, the probability for ionization increases. To first order this effect causes ion flux from the orifice to scale with the orifice length; the ion flux from the cathode is directly tied to the ionization rate. By increasing the ion density in the orifice, the flux of ions emitted is increased, allowing the cathode to remain in spot-mode emission at lower flow-rates compared to cathodes with shorter orifices.[24] The power deposited in the orifice also scales with length, and a trade-off must be made. The third consideration is the ability to fabricate the cathode. The limiting fabrication issues with the techniques used here were the electron beam weld of the orifice plate to the cathode tube and drilling the orifice. For orifice plate thickness less than about 1.2-mm, the electron beam would melt the entire orifice plate, destroying the orifice. Consequently, the overall thickness was set to 1.2-mm. This still allowed the orifice length to be adjusted from 0 to 1.2-mm by varying the depth of the chamfer. The final orifice length of 0.71-mm was set to increase the power deposition to the cathode at low-currents where self-heating is reduced and to reduce the flow-rate necessary to maintain spot-mode emission. The cathode tube outer diameter was set to 3.2-mm due principally to the availability of both tube material smaller than the 6.4-mm standard and appropriately sized inserts. By using 3.2-mm, as opposed to 6.4-mm, diameter tubes, conduction and radiation losses from the cathode were reduced. All of the inserts used in this study, except where noted, were chosen because of their availability, and no attempt was made in the initial studies to optimize this component.

Given that the orifice aspect-ratio of the baseline cathode was nearly 6, considerably higher than is typically used in orificed hollow cathodes, the focus of part of the initial investigation was to examine the effects of orifice aspect-ratio. This was accomplished by varying the orifice length. The resulting cathodes, AR1 and AR3, had orifice aspect-ratios of just over one and approximately 3, as their names suggest. These ratios were selected because AR1 closely approximates the geometry of 6.4-mm diameter cathodes and AR3 provides an intermediate geometry between the extremes. The orifice geometry was expected to play a large role in determining cathode performance since conducting most of the current through the orifice causes the most extreme plasma conditions (temperature and number density) to occur in the constricted channel. Ions backstreaming to the cathode face account for only a small fraction of the total current.[25]

The cathode AR3-a was designed for slightly lower currents than the cathodes mentioned previously. The projected current limit of this cathode was 1-A. The aspect-ratio was chosen in part to reduce the power deposition in the orifice. The fabrication techniques also drove the design toward a shorter orifice.

Initially cathode AR6´ was fabricated with an insert made of rolled tantalum foil dipped in the emissive mixture R500. This cathode is referred to AR6´´ and was further distinguished from all the other cathodes by an insert inner diameter on the same order as the orifice diameter. This insert was later discarded in favor of a standard impregnated porous tungsten insert. The R500 emissive mixture was also used to coat 0.5-mm diameter tungsten wires which were bundled to serve as an electron emitter in two multichannel hollow cathodes. Neither of these cathodes had an orifice plate. They are referred to here as MC7 and MC13 indicating the number of wires bundled in the insert. Figure 2.3 shows an end view of the cathodes. These were intended to operate at reduced voltage when compared with an orificed hollow cathode due to the less constricted path for the current and the increased emitter surface area. Multichannel hollow cathodes have been used successfully in a number of other applications.[51,52]

The keeper design and gap were invariant throughout the testing of the effects of orifice geometry. After the performance of AR3 had been characterized, a molybdenum mesh keeper was installed as shown in Figure 2.4. This configuration, referred to as AR3-A was chosen for ease of alignment and to test the performance of this type of keeper.

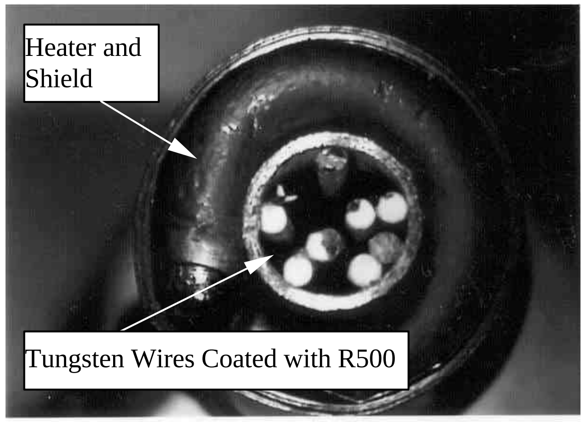

a) MC7 with R500 Visible (White Areas Indicate R500)

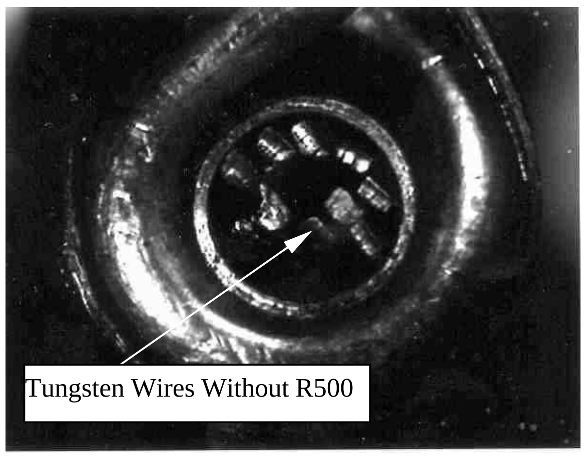

b) MC13 Post-Test (Note the Depletion of R500)

Figure 2.3 - End View Photographs of the Multichannel Hollow Cathodes

One of the most basic means to improve the efficiency of low-current hollow cathodes is to thermally isolate the high temperature elements to the extent possible. The distinction between low-current, less than 2.0-A, and high-current, greater than 2.0-A, hollow cathodes is important; as the total emission current is reduced, the electron cooling of the emitter surface becomes fractionally smaller compared to conductive and radiative losses. When considering the design illustrated in Figure 2.1, modifications were incorporated to reduce the conduction and radiation losses from the cathode. Without changing the tube material, increasing the length of the tube was chosen to reduce the conductive losses; in this case, the low-temperature “reservoir” of components were farther from the high-temperature emitter. This configuration was tested with the open keeper geometry, OK1, shown in Figure 2.5. This design also enabled the use of a removable, enclosed keeper, as depicted in Figure 2.6. The use of an enclosed keeper provides a radiation enclosure for the cathode. Since this cathode was operated with both open and enclosed keepers, the performance benefits of the enclosed keeper system were quantified.

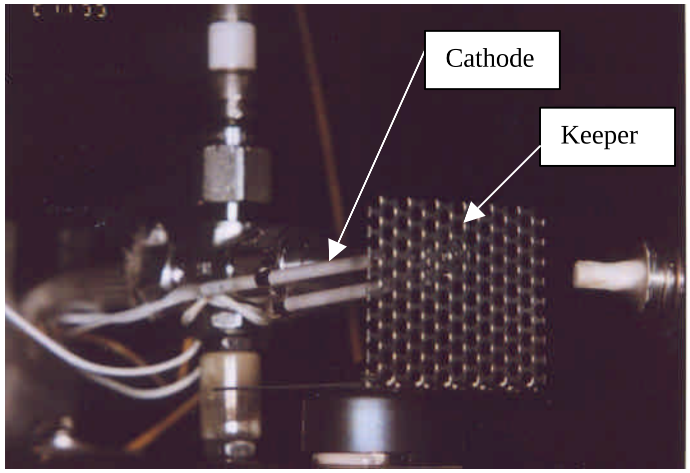

Figure 2.4 - AR3 (AR3-A) with Mesh Keeper, Internal Langmuir Probe, and Thermocouples

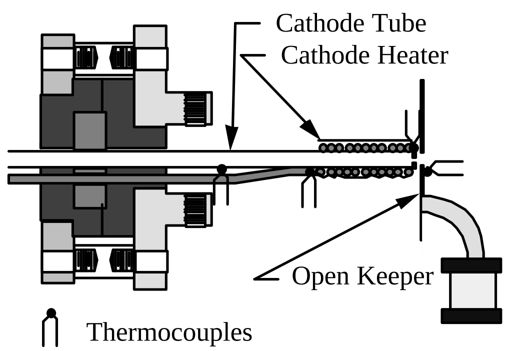

Figure 2.5 - Open Keeper Configuration of the Extended Tube Cathode (OK1)

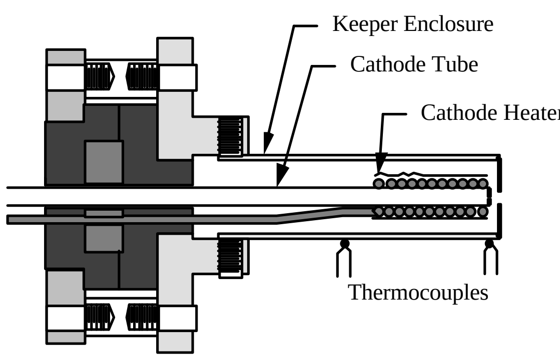

Figure 2.6 - The Enclosed Keeper Cathode

2.1.2 Hollow Cathode Operation

The barium impregnated emitter in the hollow cathode required conditioning after exposure to atmosphere and prior to operation. The procedure was derived from a cathode activation process first reported by DePauw.[53] Initially the cathode and feed system up to the flow controller or metering valve were evacuated to less than 1.3 x 10^{-4} Pa for at least 12 hours. Next, the cathode was heated to approximately 500 ºC on the insert for three hours. The heater was then deactivated for 30 minutes. Finally the cathode was heated to approximately 1000 ºC for one hour and then allowed to cool for 30 minutes. This process removed the adsorbed carbon dioxide and water in the insert while preparing the surface for electron emission. In practice, it was infeasible to directly measure the insert temperature, and the orifice plate temperature was assumed to provide an accurate approximation.

The cathode ignition procedure was directed toward low-voltage (<40 V) ignition of the discharge. Figure 2.7 shows the circuit used in these experiments. Initially the heater was activated to raise the cathode temperature to at least 1000 ºC. After several minutes, a 0.4 to 0.5 mg/s flow of xenon was initiated; steady-state operating flow-rates for these cathodes were below 0.3 mg/s. Once the feed lines had pressurized, the keeper power supply was turned on. In most cases this procedure was sufficient to initiate the discharge. In some instances, it was necessary to use a high-voltage (>500 V) igniter power supply attached in parallel with the keeper supply to start the discharge. Following ignition, the heater coil was de-energized.

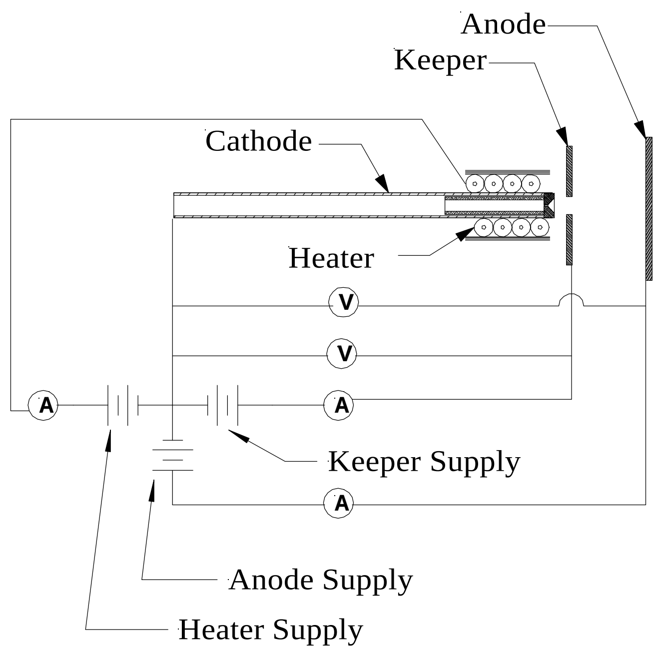

Figure 2.7 - Circuit Diagram for the Hollow Cathode in a Triode Configuration

The performance characterizations were conducted by varying the flow-rate at constant current in a diode discharge between the keeper and cathode. The discharge was held at a constant condition for at least 15 minutes prior to taking data. The cathode was operated initially in spot-mode, and the flow-rate was decreased until the onset of plume-mode. Spot-mode is also characterized by having a small AC component in the current (<<0.1-A) and voltage (<1-V), and a small luminous "spot" at the orifice of the cathode.[1] Plume-mode by contrast has a luminous "plume" that extends downstream to the keeper and beyond, and the AC component of the current and voltage becomes a large fraction of the DC values. The limitations on the regime of discharge currents were determined by cathode temperature at large relative current and by discharge stability at low relative current. Spot-mode emission at orifice plate temperatures below 1300 ºC was chosen as an operational limit for these experiments to be consistent with practices proven to enable lifetimes greater than 10,000 hours.[64] The cathode tip temperature has been considered that which is the most closely related to the insert temperature.[26,64] If the temperature is too high, the barium in the insert evaporates more quickly than it can be replenished through diffusion, and the discharge becomes unstable; low temperatures are insufficient to drive the chemical reactions at a rate that sustains the low work function surface of the emitter.[28] Since the lower limit represents a non-destructive condition, the cathodes were operated at as low of an orifice plate temperature as stable operation permitted.

The goal of the performance characterizations was to obtain the lowest power and flow-rate for spot-mode emission. By focusing on a diode discharge, comparison between the performance of the hollow cathodes was straightforward. This approach assumes that the total emission current, the sum of the keeper and secondary anode emission currents, dominates the conditions at the cathode, regardless of the distribution of the current to the keeper and secondary anode.

2.2 Diagnostics and Experimental Techniques

Since the ultimate goal of this investigation was to determine a means to optimize hollow cathodes for low-current applications, the power and propellant consumption were the primary focus of the experiments. The performance of each of the cathodes was determined by examining the variation in the operating voltage and mode as a function of flow-rate and current. This type of examination yielded the end product, the mass flow and power consumed by the cathode in spot-mode. Detailed experiments focused on processes known to affect cathode performance were conducted in order to determine more precisely the mechanisms governing cathode performance. Heat loss from the emitter constitutes one of the major performance-influencing processes. Consequently a detailed thermal study was conducted to determine the mechanisms governing heat loss. The character of the plasma discharge and electron transport also influences cathode performance, and plasma properties were measured both in the insert region and downstream of the keeper using electrostatic probes. The thermography, plasma, and several other diagnostics are summarized in this section.

2.2.1 Cathode Performance

The cathode performance was considered the relationship between the cathode power and the flow-rate required to maintain spot-mode emission. Consequently the voltage, current, and flow-rate were monitored in all of the experiments. Current and voltage of both the discharge and the heater were monitored using digital multimeters and a computer data acquisition system. Figure 2.7 shows the circuit with the multimeter positions, and Figure 2.8 illustrates the computer data acquisition scheme. A digital oscilloscope with x10 voltage probes was used to observe high frequency fluctuations in the discharge voltage. The computer data acquisition and control system enabled extended duration (> 100 hours) tests which were performed to examine the performance variance in time. Although cathode life times were expected to be two orders of magnitude longer than the extended duration tests, the term of these performance evaluations was deemed sufficient in the context of the present investigation. Figure 2.9 shows some of the data collected during a 160 hour test of AR1. The heater was only activated during cathode conditioning and ignition. About 52 hours into the test, the cathode was shut-down during a performance characterization, and the cathode was restarted the following day. Performance characterizations are shown in Figure 2.9 where the mass flow-rate varied greatly over a relatively short period. The cathode operating temperature varied by less than 100 ºC during the discharge.

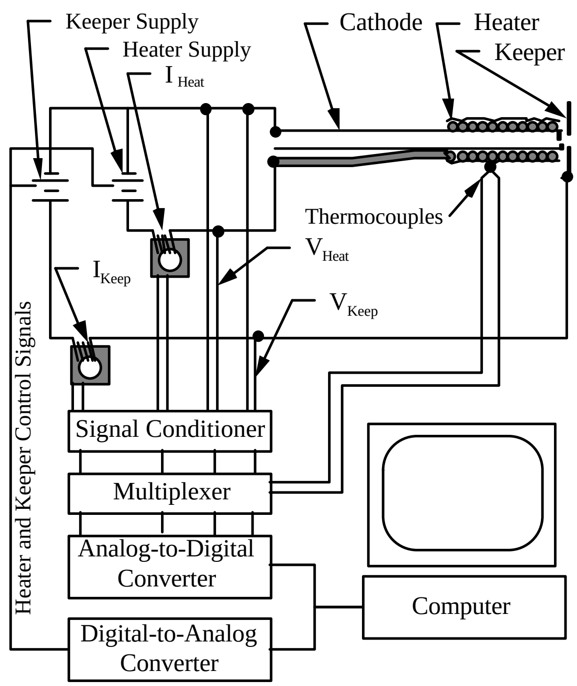

Figure 2.8 - Cathode Control and Diagnostic Scheme

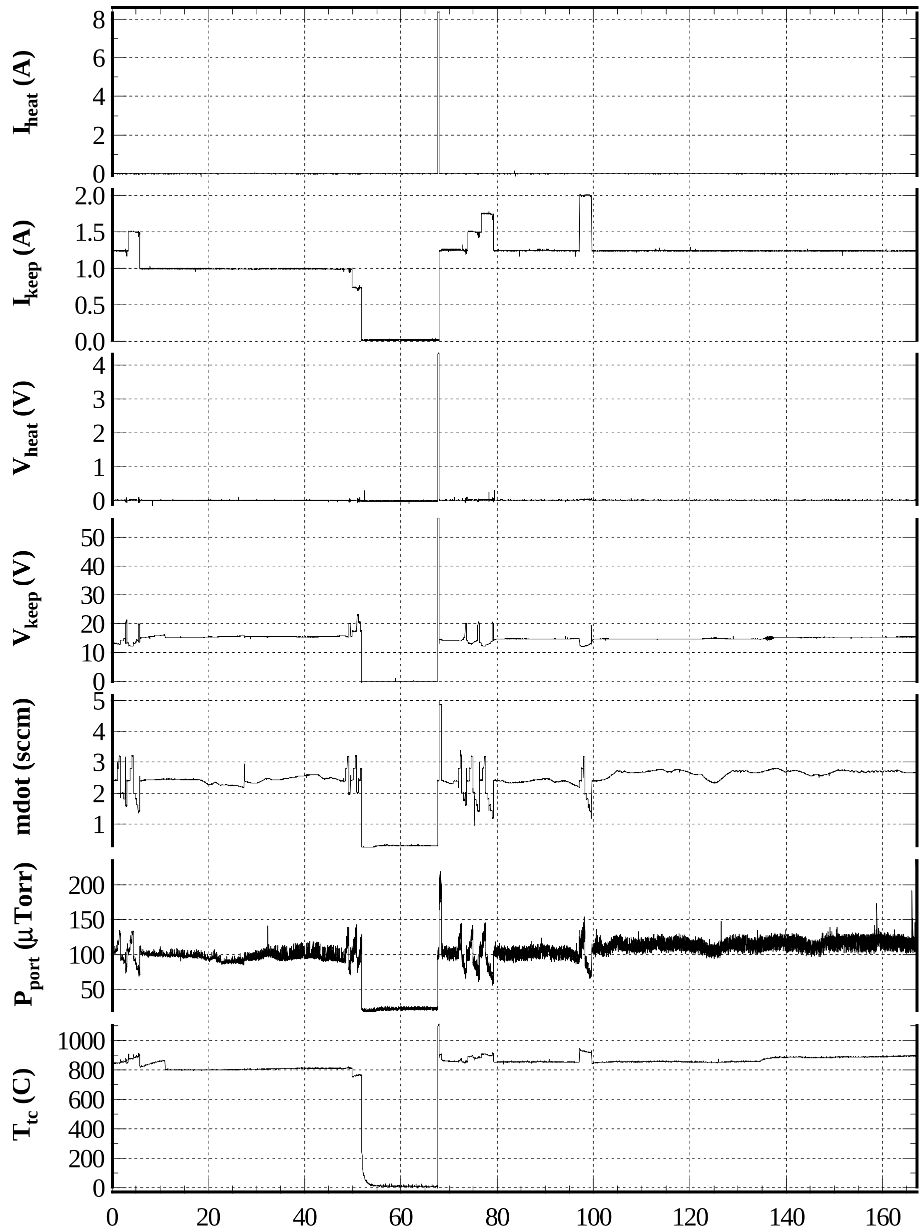

Figure 2.9 - Sample Data Log from AR1.

The xenon flow system is illustrated in Figure 2.10. The flow-rate was measured using either a Unit UTM-1101 mass flow meter or a Unit 1660 mass flow controller both with a full-scale flow of approximately 0.5 mg/s. The flow meters and controller were calibrated using a National Institute of Standards and Technology (NIST) traceable bubble flow meter. The flow-rates reported here are accurate to within $\pm 7\times10^{-3}$ mg/s.

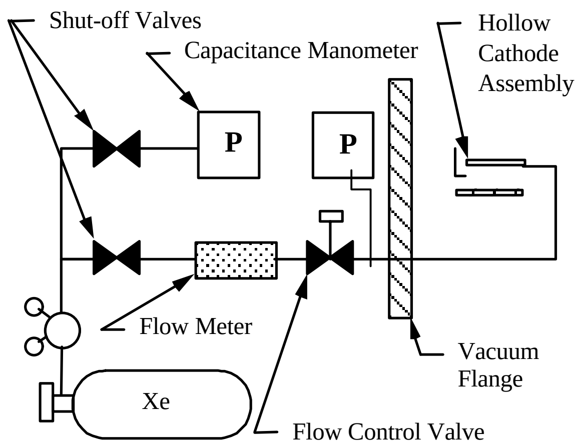

Figure 2.10 - Simplified Flow Schematic

While cathode performance and emission capabilities are the primary concerns for the overall thruster design, the cathode pressure when combined with plasma diagnostics enables a detailed physical picture of the cathode processes to be developed. Salhi[26] found that the pressure in a 6.4-mm diameter cathode with a 1.21-mm diameter orifice was approximately 665 Pa on xenon at operating conditions similar to those reported here. As an approximation, the cathode pressure scales as the ratio of the orifice areas. Given the data from Salhi,[26] the enclosed/open keeper cathode, AR1, AR3, AR6, and AR6´ were expected to operate in the range of 40 kPa. Consequently, a MKS capacitance manometer with a full-scale range to 133 kPa and accuracy over four decades was used to measure the pressure inside the cathode. The capacitance manometer zero agreed well with the other vacuum gages in the vacuum chamber, and the atmospheric pressure reading was accurate to within 1.3 kPa. Although the interrogation point was approximately 0.5-m upstream of the cathode insert, it was concluded that the measured pressure accurately represented the cathode internal pressure; calculation of the Reynolds number and expected pressure drop based on Poiseuille flow yielded results on the order of 10 and 1-Pa, respectively.

2.2.2 Cathode Temperature Distributions

Type R thermocouples were used for accurate, calibrated point measurements of the cathode temperature. Thermocouples operate on the principle that the Fermi energy varies between any two materials, and by joining two dissimilar metals, an electric field is established at the interface between the materials. The resulting Seebeck voltage can be measured and compared with data from thermocouple tables for a specific combination of materials. Type R thermocouples consist of platinum and platinum 90% / rhodium 10% wires welded to each other at the ends. The ANSI tolerances for type R thermocouples are ±1.4 ºC from 0 to 538 ºC and ±0.25% from 538 to 1482 ºC.[54]

The thermocouple readout was calibrated against a NIST traceable standard prior to the tests reported here. Random errors in the thermocouple measurements were negligible since readout values never oscillated more than 0.5 ºC during a sampling.

Systematic errors in the thermocouple measurements were most likely to occur due to poor thermal contact with the cathode material. To minimize the error due to contact thermal resistance, the thermocouples were spot welded to the cathode surfaces. In the worst case for the thermocouple attached to the orifice plate, the power conducted away from the site was on the order of 1000 times smaller than the discharge power and comparable to the radiative component in the absence of the thermocouple.[55] Consequently the temperature measurement had an estimated uncertainty of less than one percent.

The thermocouple data provided discrete measurements of the cathode tube temperatures with a high degree of accuracy. In order to fully evaluate the thermal design of a hollow cathode, a continuous temperature map enables determination of the dominant heat transfer and deposition methods. Optical measurements provide data over the entire visible surface of the cathode while sacrificing some of the accuracy of thermocouples. A combination of these temperature measurements is described below.

2.2.2.1 Thermal Imaging System

Cathode and enclosed-keeper temperature profiles were acquired with the imaging system illustrated in Figure 2.11. The overall scheme was conceptually similar to that reported by Polk and Goodfellow[56] with appropriate modifications based on the expected temperature range. A commercially available imaging radiometer was used because the anticipated temperature range required the capability of scanning beyond visible wavelengths. The radiometer had a spectral bandpass of 8-12 μm. A coated zinc selenide viewport, with a transmittance greater than 95% between 8 and 12 μm, was installed for these experiments. The radiometer incorporated germanium optics which have a high transmittance in the infrared. A 3.0x germanium telescope, with a transmittance of 0.80, was used with close-up optics to enlarge the cathode image. Within the radiometer, incoming light was scanned horizontally and vertically using electromechanical servos and focused onto a mercury-cadmium-telluride detector. The detector was encased in a dewar cooled by liquid nitrogen. The finite size of the detector limited the true spatial resolution of the diagnostic. This limitation was especially apparent at boundaries where emissivity and temperature changed over a small distance. The effect was to attenuate the measurement in the high intensity region and to inflate the values in the low temperature area. The extent to which this occurred in this investigation will be discussed later. The system was rated for temperatures ranging from 0 to 1500 °C with selectable spans from 5 to 500 °C. Each of these temperature spans had a maximum dynamic range of 8 bits using the image averaging software.

The video output of the radiometer was connected to an 8 bit grayscale frame grabber board in a computer. The grayscale acquisition relied only on the luminance portion of the video signal. The resulting image on the computer had an intensity between 0 and 255 dependent upon the input luminance. The radiometer system attached a grayscale bar to the image as seen in Figure 2.12, which was used as a check of the linearity of the transfer function of the frame grabber board; a linearly increasing profile of the pixel intensity in the grayscale bar ensured that the radiometer output was being represented accurately on the computer. Figure 2.13 shows an infrared image of the enclosed-keeper with a reference mark for position calibration. The line profile tool in the image acquisition package was used to evaluate the distribution of pixel intensity along a line drawn on the image. The pixel profile was related to the temperature profile through the transfer functions. For this investigation, only centerline profiles were acquired since the emitted radiation intensity depended only on the normal emittance; this technique minimized apparent temperature variation due to emittance and geometric effects.

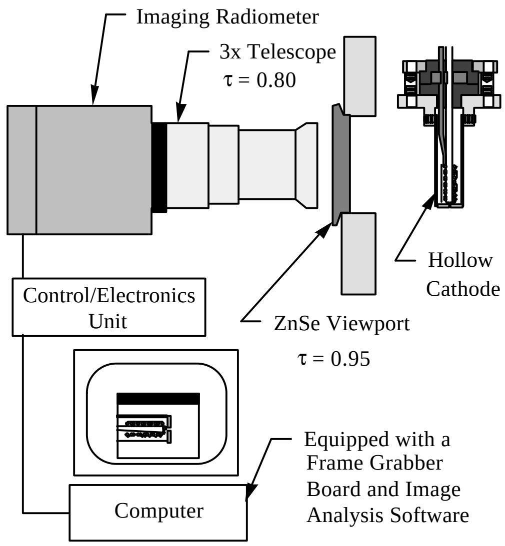

Figure 2.11 - Thermography Experimental Set-Up

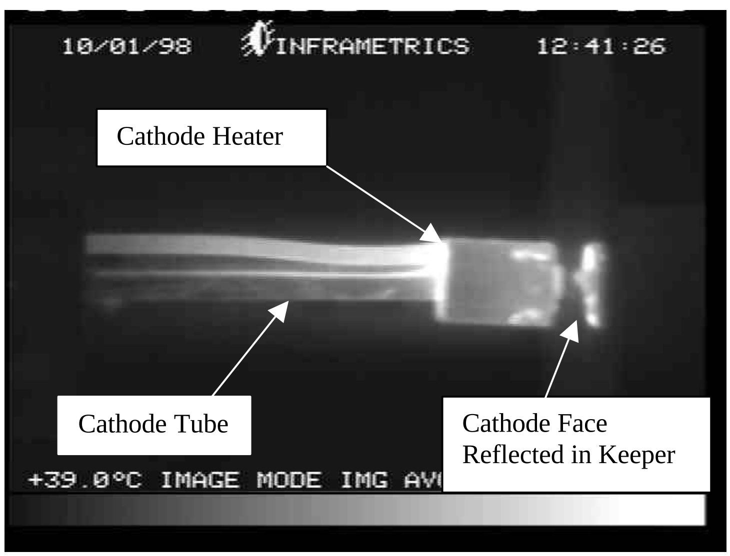

Figure 2.12 - Sample Image Generated by the Imaging Radiometer

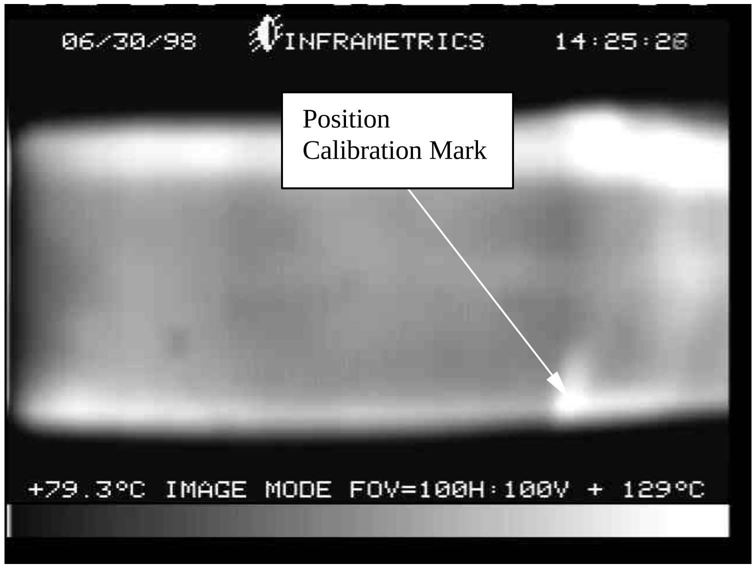

Figure 2.13 - Radiometer Image of the Enclosed Keeper.

2.2.2.2 Calibration of the Radiometer

Although the radiometer was capable of correcting for the estimated emittance of the cathode and the transmittances of the viewport and lenses, the images were left uncorrected for the following reasons: 1) uncertainty in the emittance of the target as a function of wavelength and temperature and 2) uncertainty in the true transmittance of the optics. Instead, the temperature profiles were compared with thermocouple data to provide a calibration. This method assumed that the thermocouples were in equilibrium with the cathode tube at the point of interrogation, that they were a negligible heat sink, and that the temperature distribution was azimuthally symmetric, since the thermocouples were located opposite of the radiometer. Type R thermocouples were spot welded to selected locations on the cathode and keeper. Although the spot weld provided a low thermal resistance contact between the thermocouple and the cathode or keeper, the tendency of the thermocouple to act as a heat sink was mitigated by using 0.25 mm diameter wire. The assumption of azimuthal symmetry was taken for convenience, and the results of the destructive analysis of the 28,000 hour hollow cathode suggest a high degree of azimuthal symmetry for all the cathode properties.[6] The calibration procedure required at least two thermocouple references on each material in the field of view of the radiometer. With two temperature measurements, a slope and an offset were determined using Equation (2.1) for the transfer function between pixel luminance and temperature.

$$T(x) = \left(I_p(x) - I_{p,\min}\right)\frac{\left(T_{\max} - T_{\min}\right)}{\left(I_{p,\max} - I_{p,\min}\right)} + T_{\min} \qquad \textbf{(2.1)}$$

Essential to an accurate temperature calibration, position calibrations were performed using known references within the image. The position calibration was saved to the computer viewport which provided the same scale for all the images collected during a test. In the case of the enclosed keeper, only two thermocouples were required for calibration since the material properties were assumed to be uniform.

2.2.2.3 Profile Acquisition and Processing

Once the camera was sighted on the cathode or keeper and the spatial calibration was configured, data acquisition consisted of grabbing a frame and downloading the line profile. The frame grabber software was configured to average 10 images, which when combined with the four image average performed by the radiometer control package, yielded an overall averaging of 40 frames. Further averaging appeared to have a negligible impact on the smoothness of the line profiles. Images were acquired at all the conditions represented in the performance characterization. Temperatures and operating conditions were recorded for reference and calibration of the image data.

The line profile data were recorded as a spreadsheet column. From the spatial calibration, position in the column was related to a location along the cathode or keeper centerline. Next, the pixel intensity was correlated to the thermocouple measurements. Thus by definition the line profiles matched the thermocouple data reported here. Figure 2.14 shows a line profile prior to temperature calibration.

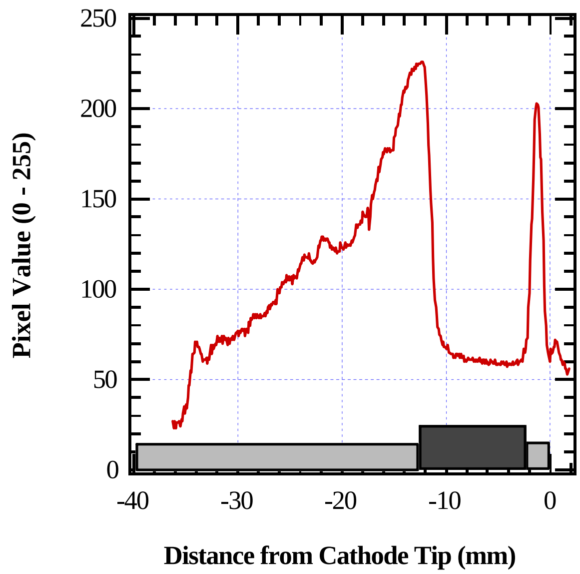

Figure 2.14 - Sample Line Profile Results From the Radiometer

2.2.2.4 Error Analysis of the Temperature Measurements

The accuracy of the thermocouple data was discussed previously, and the image data were averaged to minimize the random errors. Calibrating the image against thermocouple data eliminated the difficulty in obtaining a thorough characterization of the surfaces and optics which would be required to treat the radiometer output as an absolute measurement of the two-dimensional temperature field. The largest source of systematic error was associated with the inability of the radiometer to handle large temperature gradients in the two-dimensional space of the image. This effect can be seen in Figure 2.14. At the boundaries between the cathode tube and the heater radiation shield, the pixel data failed to reflect the same sharp transition in intensity expected with a step change in both temperature and emittance. This data artifact was characteristic of the imaging radiometer. The data from these transition locations were omitted when presenting the temperature profiles.

2.2.2.5 Optical Pyrometer Based Orifice Plate Temperature Measurements

In most of the tests reported here, the orifice plate temperature was measured independently of the thermocouples using an optical pyrometer. Both a disappearing filament pyrometer and an optical thermometer were used. The disappearing filament pyrometer operates by comparing the color of an incandescent filament with that of the target. The pyrometer used in these investigations had a correction for the emittance of the material, and a value of 0.39 was used based on previous work.[57] Ramalingam and Jacobson[58] measured the emissivities of various tungsten alloys, and their data indicate an emissivity as high as 0.525 depending upon temperature and composition. In addition, the effect of the surface geometry of the orifice plate will determine the effective emittance as seen by the pyrometer. Corrected temperatures for an emittance of 0.53 were also obtained using the transfer function for the pyrometer power supply. The pyrometer data reported in Chapter 3 represents the mean value, with the error bars extending to the limits of the estimated emittance. The definition of emissivity was used to calculate a temperature span for the optical thermometer. Wein's Law can be used to derive the following equation relating brightness temperature (T_β) to the blackbody temperature (T_{BB}) with a correction for emittance (e):[54]

$$\frac{1}{T_b} = \frac{1}{T_{BB}} - \frac{l\, nk}{hc} \ln e \qquad \textbf{(2.2)}$$

where λ is the wavelength transmitted by the red filter of the pyrometer, n is the index of refraction, k is Boltzmann's constant, h is Planck's constant, and c is the speed of light. Here the brightness temperature is defined as the temperature necessary for a blackbody to emit the observed radiation intensity, and the blackbody temperature, T_{BB}, is the true body temperature corrected for the emittance. Using Equation (2.2), the mean temperature between the limits of the emittance is reported here. By using the limits of the estimated emissivities (0.39 to 0.53), the accuracy of the optical thermometer temperature measurement was approximately ±1 percent.

2.2.3 Plasma Diagnostics

2.2.3.1 Langmuir Probes

Langmuir probe diagnostics were conducted in the emission plasma downstream of the keeper, in the cathode-to-keeper gap, and in the insert region of AR3 as part of this investigation, as shown in Figure 2.15. The temperature, number density, and character of the distribution of the plasma both internal and external to the hollow cathode influence the power deposition to the cathode and the keeper. The plasma properties also allow for accurate descriptions of the current conduction processes.[24] The insert plasma properties are important for understanding the power deposition to the insert, for providing an accurate description of the particle flux to the orifice entrance, and for determination of the parameters governing the cathode internal pressure. Measurement of the plasma properties in the orifice was considered infeasible with electrostatic probes. The mechanisms governing spot and plume-mode operation can be discerned from the character of the plasma in the cathode-keeper gap. The emission plasma properties determine the ease of the charge transport to a secondary anode, ion beam, or ambient plasma.

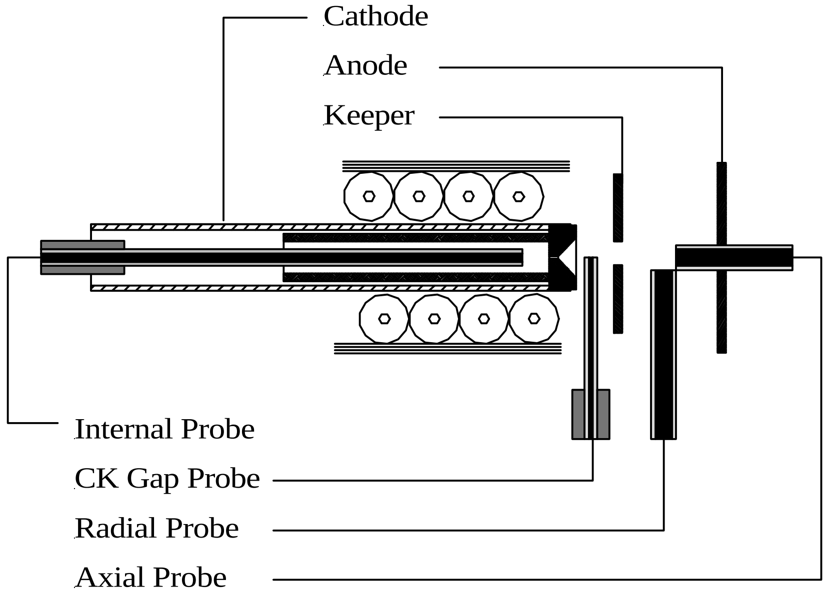

Figure 2.15 - Langmuir Probe Locations and Designations.

Planar Langmuir probes were used for all of the results presented here. The probe diameters were chosen to be 2-mm in the emission plasma, 0.13-mm in the cathode-to-keeper gap, and 0.25-mm in the insert region, much larger than the expected Debye lengths and yet small enough to draw a negligible current in the electron saturation condition (~20 mA). Downstream of the keeper, one probe was placed with its face perpendicular to the flow from the cathode (axial probe), and the other probe was oriented parallel with the flow (radial probe). The cathode assembly, complete with the secondary anode located 60 mm downstream of the keeper, was mounted to a linear translation stage which moved the assembly with respect to the probes. The probes were positioned on axis with the hollow cathode, and data were taken at 5-mm increments between 2 and 52-mm downstream of the keeper. In addition, a 0.5-mm diameter planar Langmuir probe was used to examine the plasma 5-mm downstream of the keeper of both MC7 and MC13. This probe was operated similarly to the axial and radial probes on AR3. The cathode-to-keeper gap of AR3 was increased to 4-mm to enable a planar Langmuir probe to be inserted radially into the gap. Again, the translation stage was used to move the cathode with respect to the probe. The test configuration dictated a fixed probe for the insert region, and axial resolution was only possible by replacement of the probe. The results presented here were from three such tests, and the reader should be aware that the radial location of the probe was confined by the insert and the alumina shield on the probe, but otherwise undetermined. The probes extended to 1.5, 0.7, and within 0.5-mm upstream of the orifice. The discharge appeared to be unaffected by the presence of any of the Langmuir probes.

The axial and radial probes, downstream of the keeper, were biased using a bipolar power supply with a triangular voltage ramp at a few Hz. The axial and radial probes were biased with respect to the secondary anode. The current was measured using a calibrated shunt resistor. A digital oscilloscope was used to record the probe current and voltage, and a computer data acquisition system was used to download the current-voltage (I-V) characteristics. A source meter was used to bias and measure the I-V characteristic of the internal probes and the cathode-to-keeper (CK) gap probe. The insert probes were ramped with respect to cathode potential, and the CK gap probe was biased with respect to the keeper. The source meter sent the current and voltage data of the probe directly to a computer via a GPIB connection.

Simplified Langmuir probe analysis was performed to reduce the data. The assumptions for this analysis are listed below for reference:[59]

- Infinite, quasineutral, and homogeneous plasma.
- Maxwellian electron and ion populations with $T_e >> T_i$. Note that experimental laser induced fluorescence data show that this assumption does not strictly hold.[60]
- Electron and ion mean free paths much greater than probe or sheath dimensions.
- Charged particles collected at the probe surface without reflection or reaction.
- Sheath size is small compared to probe dimensions.

Implicit in the assumption of a homogeneous plasma is the requirement of isotropy in the velocity distribution. The electron temperature was taken as the inverse slope of the natural log of the electron current near the floating potential as shown in Equation (2.3). The plasma potential was taken as the probe voltage at the peak of the first derivative of the current, defined in Equation (2.4). The electron number density was calculated based on the current at plasma potential for the axial, radial, and internal probe data because the measurement of the ion saturation current was insufficiently accurate. Equation (2.5) defines the electron number density calculated from the plasma potential current. The ion saturation current was defined as the probe current at ten electron temperatures below the floating potential and was used to obtain the electron number density for the cathode-to-keeper gap plasma; use of the electrometer permitted a high degree of accuracy in measuring the ion saturation current. The electron number density was calculated in the ion saturation region using Equation (2.6). The details of the Langmuir probe and EEDF analysis are summarized in Appendix A.

$$T_e = \left[\frac{d\left(\ln I_e\right)}{dV_{pr}} \right]^{-1} \quad \textbf{(2.3)}$$

$$V_p = V_{pr}\left(\frac{dI_{pr}}{dV_{pr}} = maximum \right) \quad \textbf{(2.4)}$$

$$n_e = \frac{I_{pr}\left(V_p\right)}{eA_{pr}} \left(\frac{2p\, m_e}{kT_e} \right)^{0.5} \quad \textbf{(2.5)}$$

$$n_e = -\frac{I_{pr}\left(V_f - 10T\right)}{eA_{pr}} \left(\frac{2p\, m_i}{kT_e} \right)^{0.5} \quad \textbf{(2.6)}$$

2.2.3.2 Electron Energy Distribution Function Measurement

In addition to the standard Langmuir probe analysis, the electron energy distribution functions were evaluated by examining the character of the second derivative of the probe current with respect to voltage. For an isotropic electron population, the second derivative of the probe current is approximately proportional to the electron energy distribution function (EEDF)[61,62]

$$f\left(E\right) \simeq A\sqrt{E}\,\frac{d^2 I_{pr}}{dV_{pr}^2} \quad \textbf{(2.7)}$$

where A is a normalization constant and the electron energy, E, is defined as

$$E = V_p - V_{pr}. \quad \textbf{(2.8)}$$

The second derivative of the probe current was obtained by numerical differentiation. Rundle, et al.[63] measured the electron energy distribution function in an O_2 glow discharge, and used the generalized formula

$$f\left(E\right) = A\sqrt{E}\,\exp\left(-bE^x\right) \quad \textbf{(2.9)}$$

where A, b, and x are constants, to curve fit the distribution data. The case where x = 1 is the Maxwellian distribution, and when x = 2, Equation (2.9) yields the Druyvesteyn distribution. The coefficients in Equation (2.9) were determined by fitting the second derivative to an exponential with the argument E^x. The exponent, x, was allowed to vary between 1 and 2, and the correct value of x was determined by the quality of the fit. The coefficient b was determined directly from the fit, while A was determined by normalizing the distribution function.

In practice, it was necessary to fit the probe current and its first derivative to cubic splines so that the numerical differentiation yielded meaningful results; in the absence of the cubic spline fits, small random fluctuations at high values of E were magnified by both the numerical differentiation and the factor of $E^{1/2}$ in Equation (2.9). Additionally, the plasma potential used in Equation (2.8) was the probe voltage at the peak of the second derivative of the probe current. This modification was chosen to yield a distribution function that more closely followed the form of Equation (2.9), and the difference in the value of the potential was typically less than 1-V.

The nature of the Langmuir probe current-voltage characteristics were such that all of the best curve fits indicated a Druyvesteyn distribution, and an example is depicted in Figure 2.16. In each case, the second derivative reached its peak with a diminishing negative slope rather than the sharp peak indicative of a Maxwellian distribution. The derivative of a cubic spline accurately reflects a sharp change in slope only if sufficient points are included in the spline. Consequently, the EEDF data were used to examine the structure of any populations in the tail of the distribution and as a check of the electron temperature calculated using the standard Langmuir probe analysis.

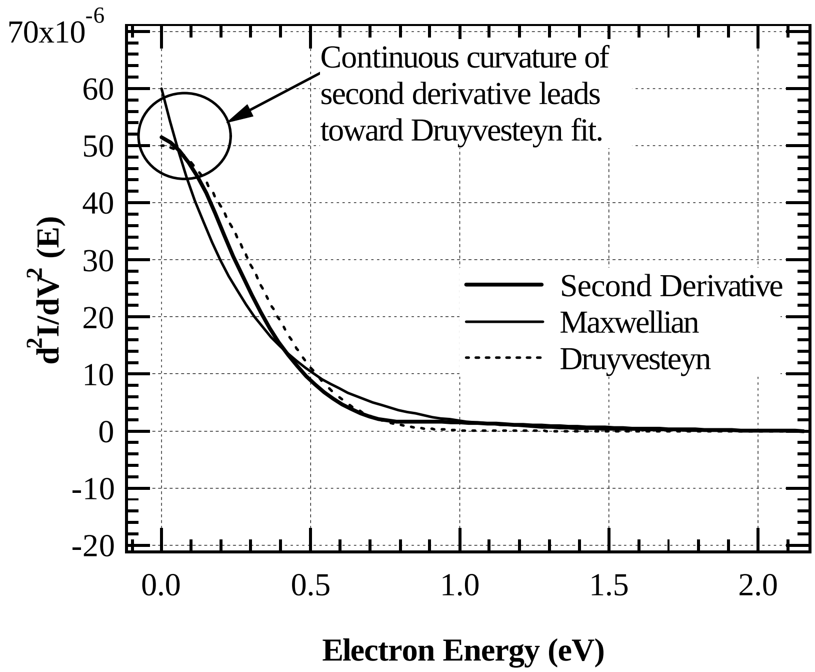

Figure 2.16 - Comparison of Numerically Evaluated Second Derivative of Probe Current with Maxwellian and Druyvesteyn Characteristics.

2.3 Vacuum Facilities

The SSPC and NSTAR ion thruster programs have developed hollow cathodes with demonstrated lifetimes to just under 28,000 hours.[6] In the course of these development efforts, it was discovered that the quality of the vacuum and the cleanliness of the feed system played key roles in determining cathode life. The method adopted was to eliminate all impurities introduced to the cathode to the extent possible. This approach has enabled long-lived cathodes at the expense of facility simplicity and cost. The following section describes the feed system requirements and vacuum facility capabilities, both of which follow the SSPC test-stand protocols.

2.3.1 Feed System Components

The feed systems, all similar to the one illustrated in Figure 2.8 (page 24), consisted of electropolished stainless steel tubing, and all fittings were either orbital-welded or used VCR metal gasket seals. This construction minimized the potential for trapped volumes within the feed system which may contaminate the cathode. The valves were chosen to have metal seals and minimal use of polymers or lubricants in their construction. A capacitance manometer and feed system vent-to-vacuum line were included to determine leak rates. Heater tape was wound about the outside to permit system bake-out.

2.3.2 Feed System Bake-Out

After any modifications to the feed system where internal surfaces were exposed to the atmosphere, such as xenon bottle replacement, the feed system was baked-out at vacuum. The goal of this procedure was to expel most of the contaminants that adhere to the feed system surfaces. First the system was evacuated to high vacuum for at least 12 hours. Heater tape was then activated to maintain tube temperatures in excess of 373-K for a minimum of 24 hours. The feed system was allowed to return to room temperature before continuing.

2.3.3 Feed System Evaluation

After the bake-out, the leak rate of the feed system was determined to verify feed system integrity. This was done by closing the feed system to vacuum and monitoring the pressure and temperature of the system for at least 24 hours. With an estimate of the feed system volume, the leak rate was determined to be less than 1.5×10^{-5} sccm for each of the test stands used in this investigation. The reader should note that for xenon, 1 sccm is equivalent to approximately 0.097 mg/s.

2.3.4 Feed System Purge

Prior to cathode activation the feed system from the flow control valve through the cathode was evacuated to high vacuum for at least 12 hours. Using this procedure, the contaminants from the feed-system interior were removed at ambient temperature when they are less likely to react with the cathode surfaces.

2.3.5 Vacuum Chambers

Three vacuum facilities were used in this investigation: 1) Port 2 of Tank 11 at NASA Glenn Research Center (GRC), 2) Vacuum Facility 52 (VF-52) at GRC, and 3) the Cathode Test Facility (CTF) at the University of Michigan’s Plasmadynamics and Electric Propulsion Laboratory (PEPL). Both VF-52 and the CTF were constructed in the course of this investigation. The CTF measured 0.61-m in diameter by 2.44-m long and is depicted in Figure 2.17. Figure 2.18 shows the VF-52 chamber, which was 0.61-m in diameter by 0.91-m long. Port 2 was 0.3-m in diameter by 0.3-m long. All of these facilities were cryopumped, and Port 2 and CTF have base pressures in the high-10^{-6} Pa range. Cryopumps provide the pumping speed necessary for cathode testing while maintaining a pristine environment for cathode exposure. During cathode operation, the tank pressure in all three facilities varied from 3 to 11 x 10^{-3} Pa. Pressure was measured using a cold cathode gage in the CTF, and Bayard-Alpert ion gages in both Port 2 and VF-52.

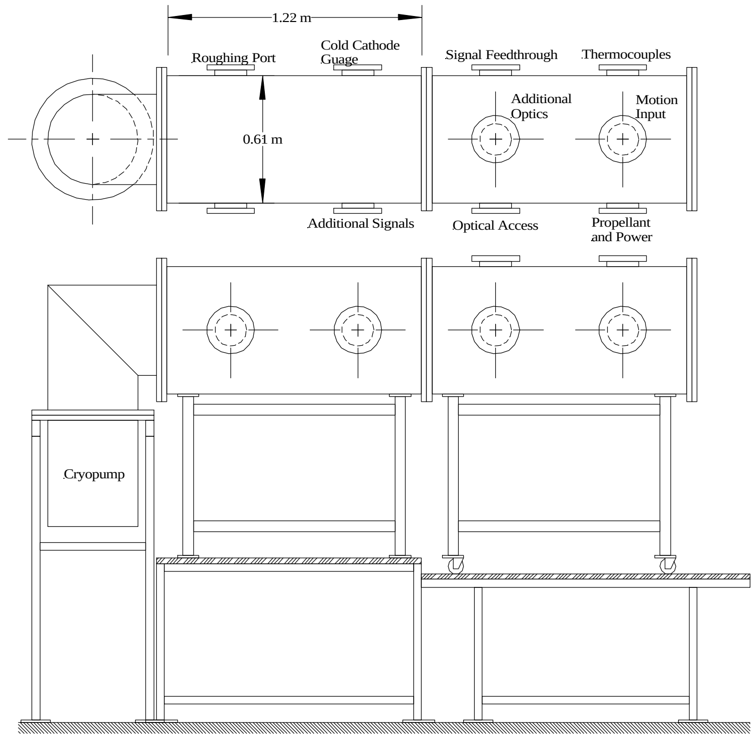

a) Schematic

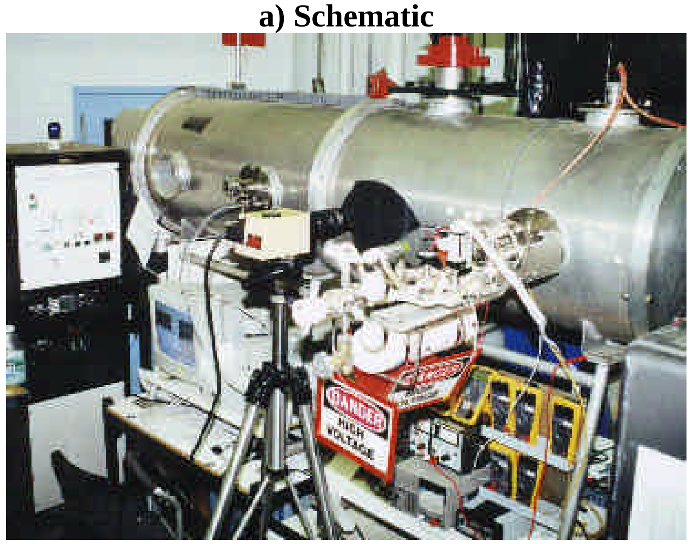

b) Photograph with Thermography Experiment

Figure 2.17 – The Cathode Test Facility at the Plasmadynamics and Electric Propulsion Laboratory

Figure 2.18 - The VF-52 Test Stand at the NASA Lewis Research Center

CHAPTER 3

INITIAL EXPERIMENTAL INVESTIGATION OF 3.2 MM ORIFICED HOLLOW CATHODES

The experiments reported in this chapter form the foundation upon which to design more efficient cathodes and more effective design tools. The first step in the experimental investigation was to benchmark the performance of the first generation laboratory model low-current hollow cathodes. Performance influencing and performance related data were also sought. Since the hollow cathode is a thermionic device, the rate of heat transfer from the high-temperature emitter directly influences the power consumption. Consequently, detailed temperature profiles were made. While others have measured the plasma properties in a variety of hollow cathodes, the character of the plasma was examined to compare with the previous studies and for use in validating the predictive model described in Chapter 4.

3.1 Cathode Performance

Cathode performance has various definitions. The cathode-to-keeper discharge power, minimum flow-rate for spot-mode emission, and the emission current (either beam or thruster discharge current) as a function of flow-rate were the three components which were emphasized in this work. The cathode-to-keeper discharge power and the cathode flow in the Hall thruster or ion thruster neutralizer adversely impact thruster efficiency. The ideal situation is to have an electron emitter that requires zero input power or flow while emitting all the electrons needed by the thruster or for plasma contacting applications. While this goal is beyond the capabilities of hollow cathodes, and any other electron emitter, this section reports on the efficiency of the first generation laboratory model cathodes.

3.1.1 Performance Variance

When attempting to assess experimentally the effects of varying the orifice geometry on the performance of hollow cathodes, the ideal technique is to change only the orifice plate. This was done by Siegfried,[25] using a slide valve with three orifice geometries. The experiment was conducted on a mercury hollow cathode, and the aspect-ratios (L_o/D_o) of the orifices were negligibly small in comparison with those considered in the current investigation. A similar experiment performed with the aspect-ratios of interest would have been feasible. However, throughout the current investigation, the experiments were designed for hollow cathode assemblies which could easily be integrated with a thruster. Consequently, to test the effects of varying the orifice aspect-ratio on the performance of the cathode, separate assemblies were fabricated and tested. In order to validate that the observed changes in performance were due to orifice geometry changes, it was necessary to examine the operating variance between cathodes fabricated to identical specifications.

For reference, the work on the ISS plasma contactor has demonstrated variances of ±0.5-V above 7-sccm of Xe, increasing to approximately ±1.0-V around 5-sccm.[17] The flow-rate where the spot-to-plume-mode transition occurred appeared to be invariant.[17] Sarver-Verhey[64] demonstrated that over the life of a 6.4-mm diameter cathode, the operating voltage for a given flow-rate and current can vary by at least ±1.0-V. It should be noted that the fluctuations referred to here occur over many tens to thousands of hours.

The voltage-flow-rate characteristics of two mechanically identical cathodes, AR6 and AR6´, at 0.75-A and 1.50-A are presented in Figure 3.1 and Figure 3.2, respectively. The characteristics show a variance of approximately ±1.0-V in the spot-mode regime, and the transition flow-rate varied by as much as 0.4-sccm. These variances were typical of those observed throughout the range of operating conditions evaluated. The keeper voltage fluctuations for individual cathodes were examined over the course of tens of hours and were found to be on the order of 0.2-V when operated at constant current and flow-rate. Figure 3.1 and Figure 3.2 show that the variance between subsequent characterizations was on the order of 0.2-V. This effect was attributed to changes in the insert chemistry which occurred at differing rates depending upon cathode operating conditions between the performance characterizations. The transition flow-rate generally increased with time. This effect was attributed to an increase in the orifice diameter, and comparison of microscopic images of the orifice supported this conclusion. Given that similar fabrication and operating procedures were employed with both the 3.2-mm diameter hollow cathodes and the ISS plasma contactors, the variance exhibited in Figure 3.1 and Figure 3.2 was taken to be a reasonable representation of the performance variance expected with these cathodes. Consequently, the overall voltage and transition flow-rate variances were taken to be ±1.4-V and ±0.25 sccm.

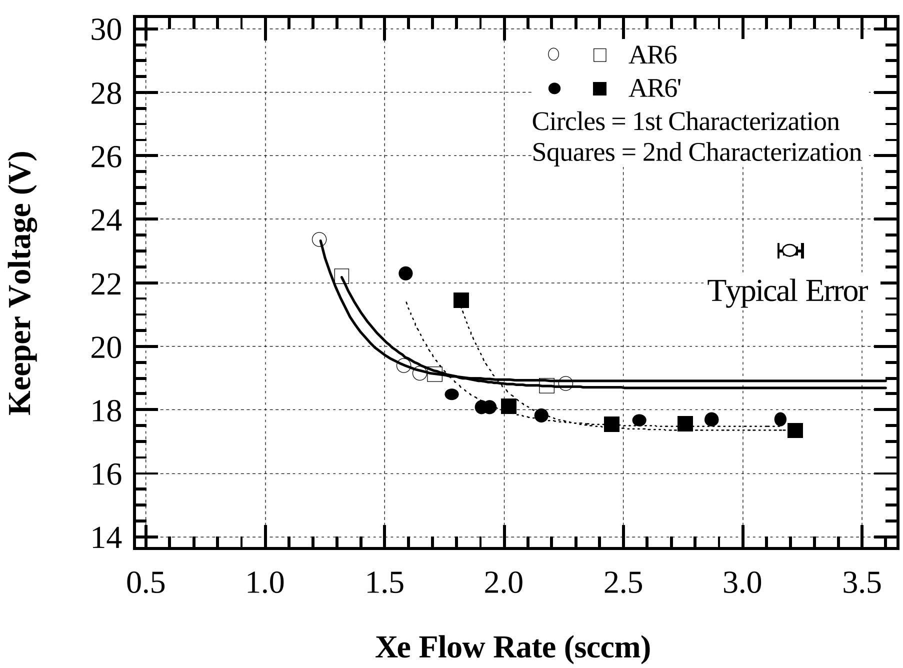

Figure 3.1 - Variance in Performance Characterizations of AR6 and AR6´ at 0.75-A.

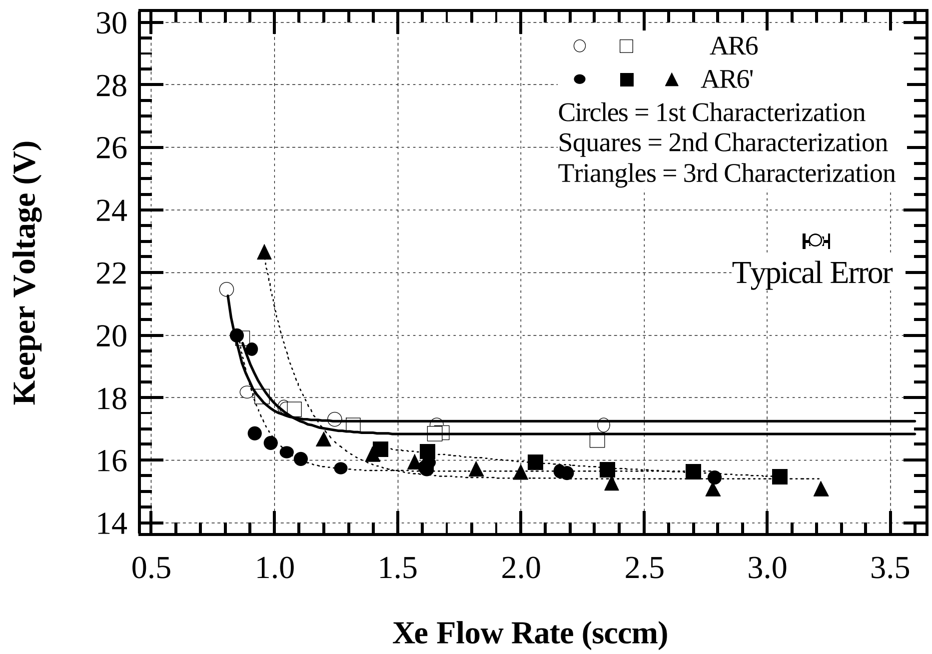

Figure 3.2 - Variance in Performance Characterizations of AR6 and AR6´ at 1.50-A.

The variation noise, differences between cathodes manufactured from the same specifications, could be minimized by rigidly attaching the insert to the cathode tube. As a consequence of the fabrication technique followed for the cathodes tested in this investigation, the axis of the insert may be misaligned with the orifice axis. Figure 3.3 illustrates that the worst case results in a misalignment of the axes by 16 percent of the insert diameter. The relaxed specification on the insert outer diameter introduced an indeterminate mechanical alteration between cathodes and contributed to the variation noise shown in Figure 3.1 and Figure 3.2.

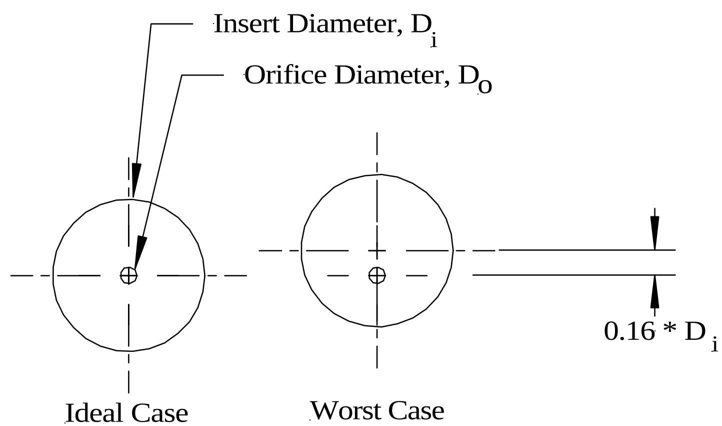

Figure 3.3 - Illustration of the Range of Possible Misalignment of the Orifice and Insert Centerlines.

3.1.2 Spot and Plume-Mode Characterization

Figure 3.1 and Figure 3.2 illustrate typical performance characterizations. The portion of the curves where the voltage is only weakly dependent upon the flow-rate is known as spot-mode. Spot-mode is also characterized by having a small luminous "spot" at the orifice of the cathode.[1] Plume-mode by contrast has a luminous "plume" that extends downstream to the keeper and beyond. The spot and plume-mode current and voltage oscillations for AR3 appear in Figure 3.4. The period of the oscillations in plume-mode was far shorter, 200 ns, than the transient response time of the regulated DC power supply, 50 μs, used to drive the discharge. The magnitude of the voltage oscillations appeared to be limited only by the output capability of the power supply. With the voltage fluctuating between zero and 55-V, ions created in the cathode-keeper gap will be accelerated toward the cathode at up to 55-V, as postulated by Rawlin.[23]

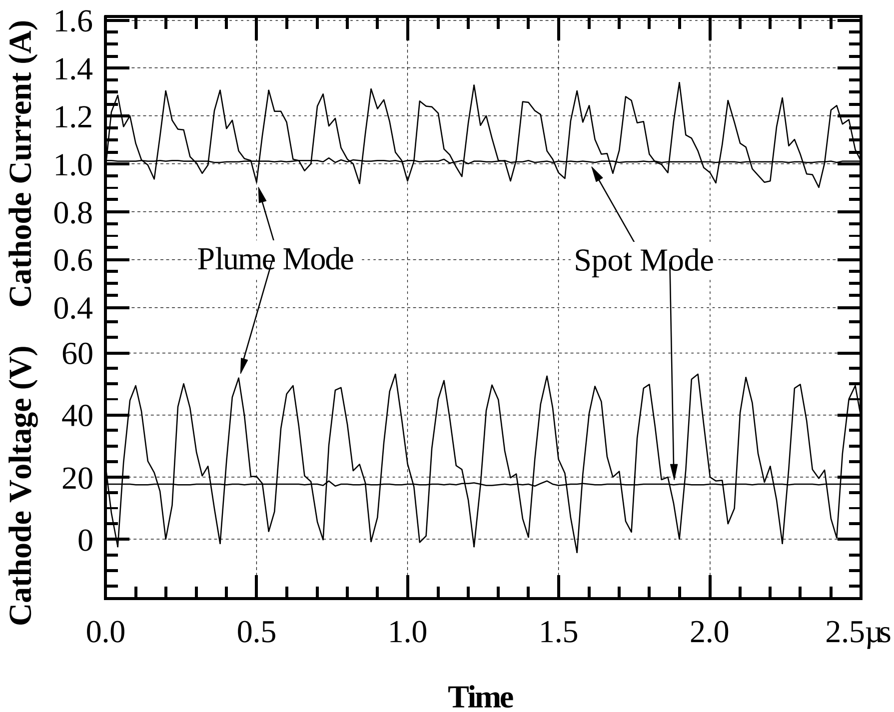

Figure 3.4 - Time Resolved Comparison of Spot and Plume-Mode Current and Voltage Signals

The data presented in Figure 3.4 were analyzed in the frequency domain, and the resulting power spectra are plotted in Figure 3.5. Spot-mode current and voltage consisted of much smaller amplitude components beyond 100 kHz. The dominant peak in plume-mode occurred at 5.91 MHz, and the harmonics were also observed. Several other peaks in the power spectrum of plume-mode voltage and current were also observed. As will be shown later in this chapter, these frequencies were much smaller than the electron plasma frequency, but possibly on the order of the ion plasma frequency at the keeper.

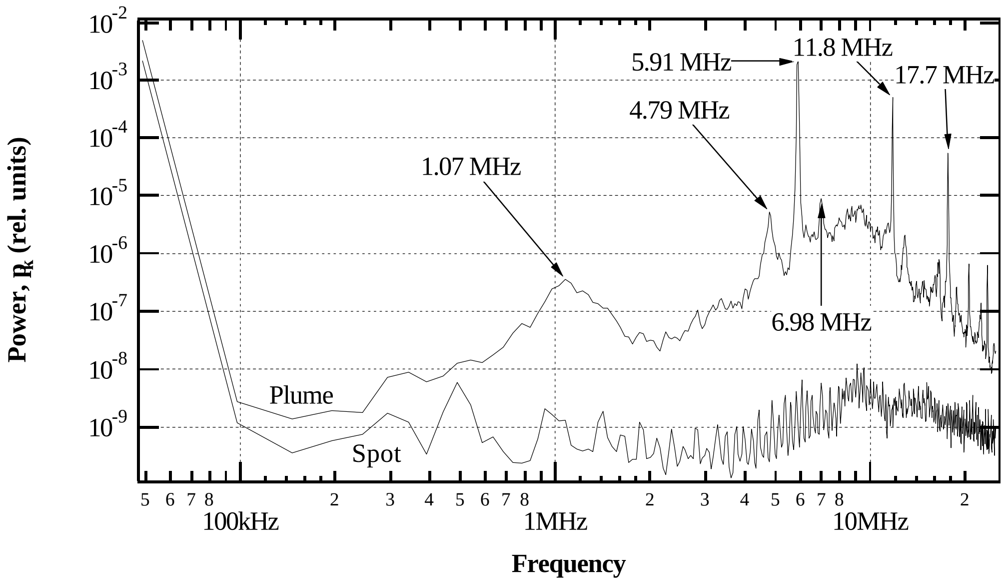

a) Keeper Voltage

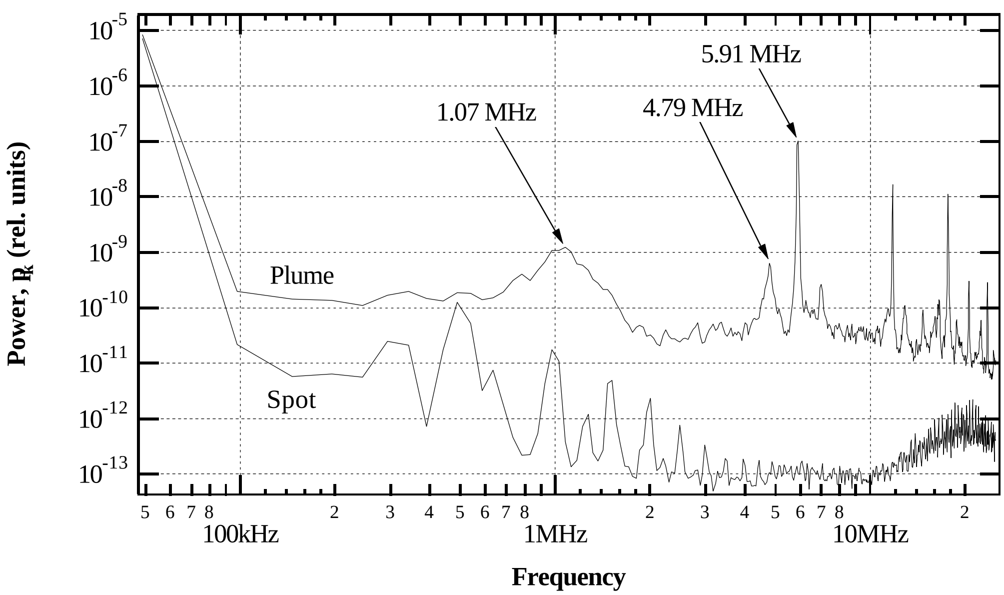

b) Keeper Current

Figure 3.5 - Power Spectra of the Keeper Voltage and Current in Spot and Plume-Modes.

3.1.3 Voltage-Flow-rate Characterizations

The primary means used to compare the performance of the cathodes was the voltage-flow-rate characteristics in a diode discharge between the cathode and the keeper. Figure 3.6 through Figure 3.12 present the results of the performance characterizations of

AR6, AR6´, AR3, AR1, OK, and EK, respectively. The sudden increase in keeper voltage at low-flow-rate indicates the onset of plume-mode. The operating envelope of AR6 was limited to 0.75-A to 1.50-A, as opposed to AR6´ which operated down to 0.50-A. AR6 was unstable at 0.50-A, and the data were omitted from Figure 3.6. The spot-mode voltage of AR6 varied from 17 to 19-V, with a negligible difference between the 1.25-A and 1.50-A conditions. In addition to stable operation at 0.50-A, AR6´ also operated at lower voltage in spot-mode than AR6. AR6´ required slightly more flow to maintain spot-mode emission. The disparity between AR6 and AR6´ was discussed in Section 3.1.1.

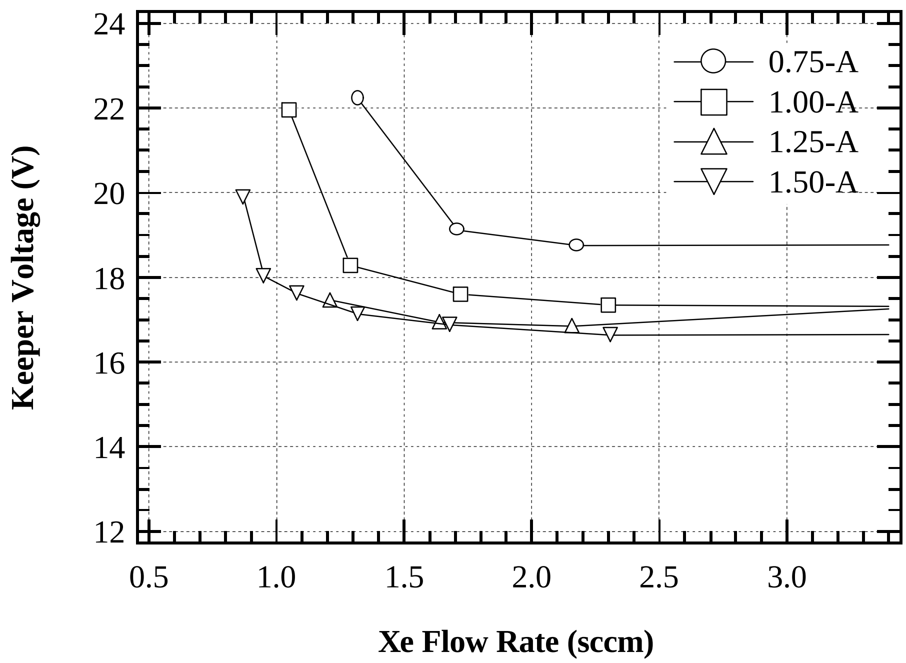

Figure 3.6 - Diode Performance Characterization of AR6.

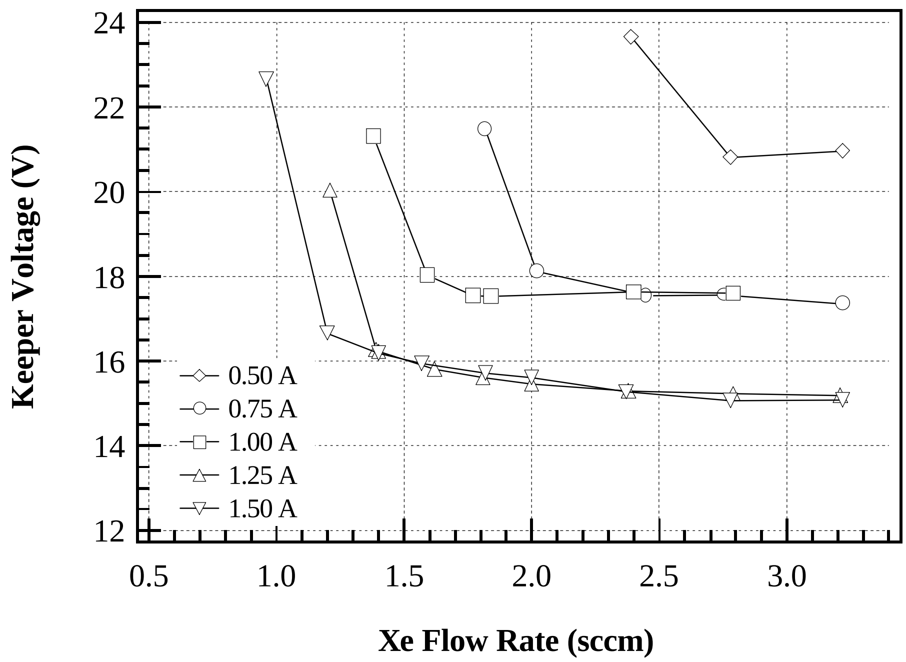

Figure 3.7 - Diode Performance Characterization of AR6´.

Since AR3 and AR1 had shorter orifices than AR6 and AR6´, it was expected that their operating voltage would be lower than AR6 or AR6´. As Figure 3.8 shows, AR3 operated very similarly to AR6´. While the performance characterization of AR3 was only conducted between 0.75 and 1.50-A, AR3 was able in subsequent tests to operate down to 0.50-A continuously. The operating regime of AR1 is depicted in Figure 3.9, and it differs from AR6, AR6´, and AR3 significantly. AR1 was marginally stable at 0.75-A, and while 1.50-A was effectively the Kaufman limit on current for AR1, optical pyrometer measurements of the orifice plate temperature indicated that the cathode was still within the predetermined limit of 1300 ºC. The shorter orifice of AR1 paid dividends with the reduced voltage operation, however, the flow-rate required for spot-mode emission was increased. Reducing the orifice diameter had the expected effects on operating voltage and minimum spot-mode flow-rate as indicated in Figure 3.10, namely an increase in the keeper voltage and a decrease in the minimum spot-mode flow-rate. While AR3-A performed as expected in terms of voltage and flow consumption, the operating regime was more limited than the other cathodes, and it failed to achieve equilibrium below 0.65-A.

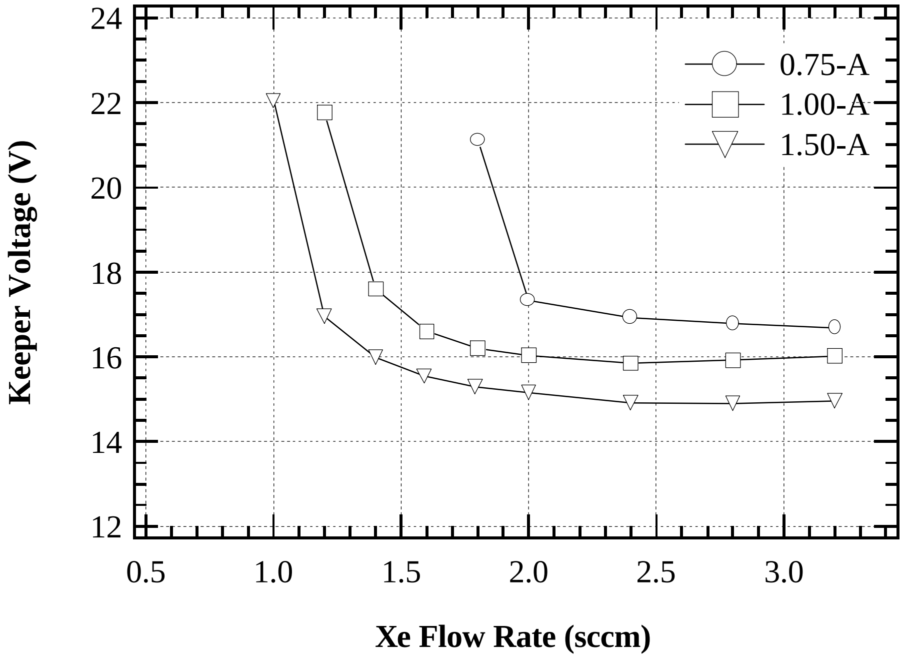

Figure 3.8 - Diode Performance Characterization of AR3.

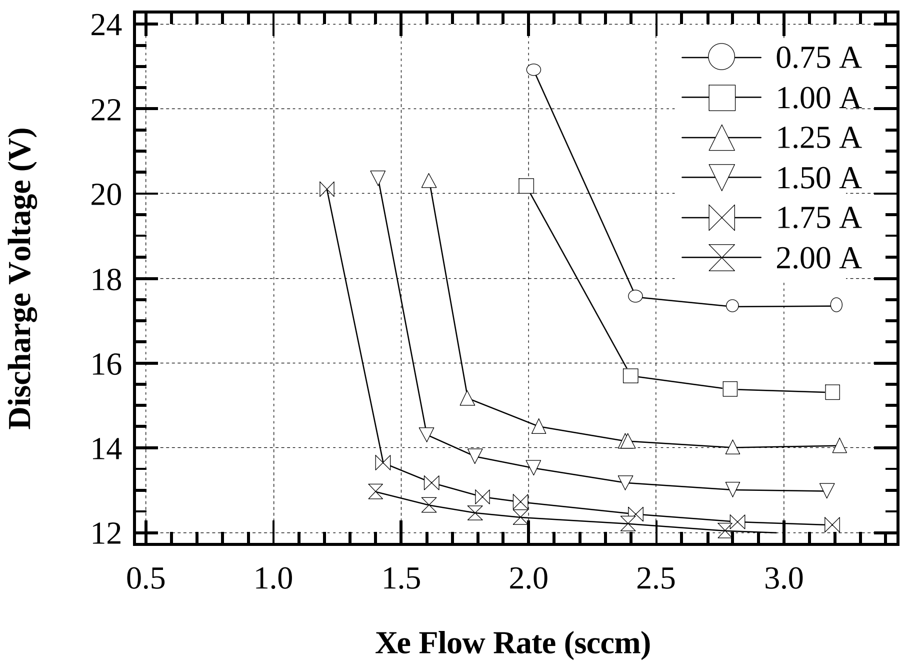

Figure 3.9 - Diode Performance Characterization of AR1.

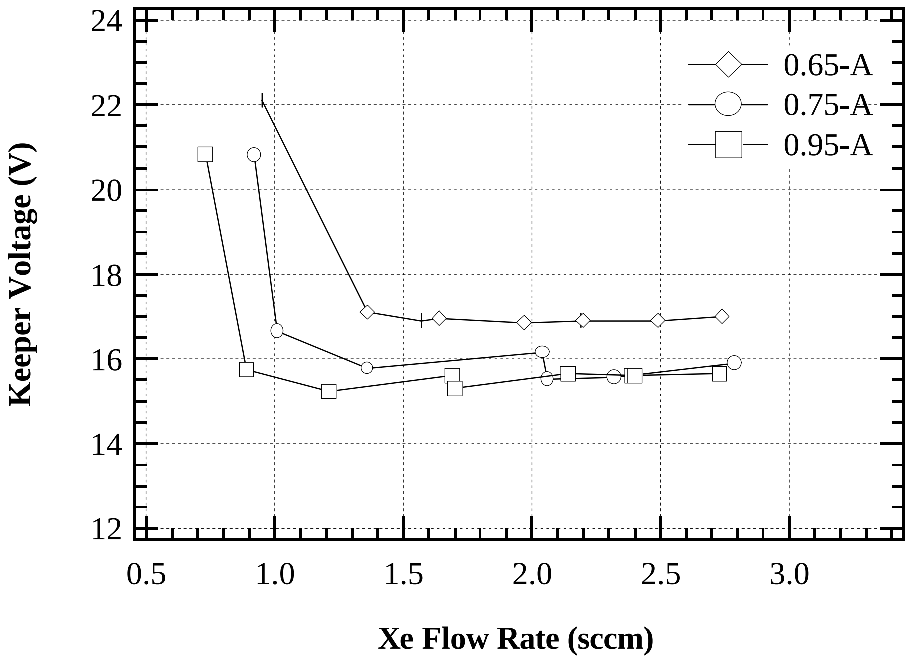

Figure 3.10 - Diode Performance Characterization of AR3-A.

While the cathode with the extended tube used to test the open (OK) versus enclosed keeper (EK) geometries had an orifice plate mechanically identical to AR6 and AR6´, the insert was from a different batch and had a slightly smaller inner diameter. This fact when coupled with the lengthening of the cathode tube invalidated the comparison of OK with AR6 and AR6´ as mechanically identical cathodes. Nevertheless, Figure 3.11 shows that the spot-mode voltage was similar to that of AR6 while the transition flow-rate was somewhat lower for OK. As shown in Figure 3.12, the enclosed keeper led to a reduction in the spot-mode voltage.

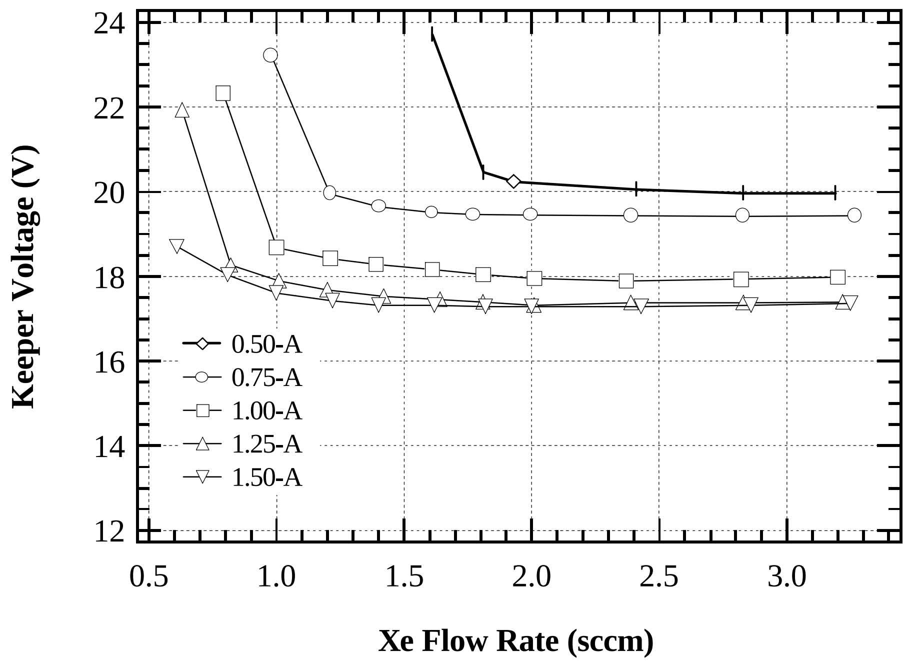

Figure 3.11 - Diode Performance Characterization of OK.

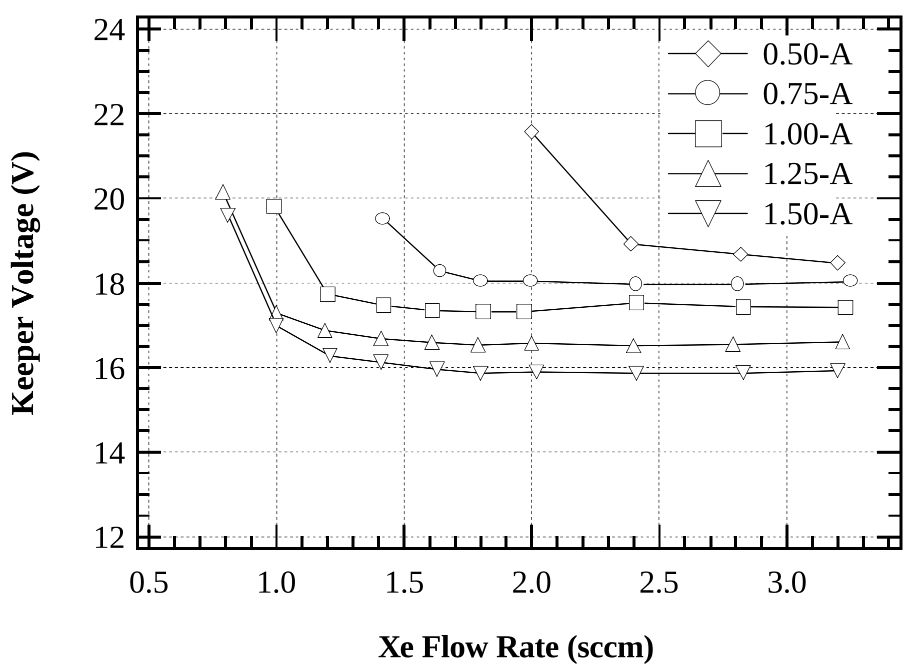

Figure 3.12 - Diode Performance Characterization of EK.

3.1.4 Effects of a Small Insert Inner Diameter

The second cathode with an orifice aspect ratio of approximately six, AR6´, was initially fabricated with an insert whose inner diameter was on the order of the orifice diameter. Salhi and Turchi[45] reported that the insert inner diameter should be much larger than the orifice diameter for optimal performance. The increased physical path length enables the primary electrons, those accelerated through the cathode sheath, to support a higher degree of ionization. By easing the ion production process, performance is enhanced. On this basis, AR6´´ was expected to require much higher flow-rates for spot-mode emission than the cathodes with 1.2-mm inner diameter inserts. Figure 3.13 depicts the performance characterization of AR6´´. The propellant flow-rate required for spot-mode emission was nearly seven times that required by the other orificed cathodes presented in this study. With the short physical path lengths, a high neutral density was necessary to allow ionization; the high neutral density also acts to quench the discharge by lowering the electron temperature. Contrary to the trends observed in the other orificed hollow cathodes, the keeper voltage of AR6´´ scaled with discharge current. This suggests that the plasma conductivity was relatively insensitive to the increased power deposition.

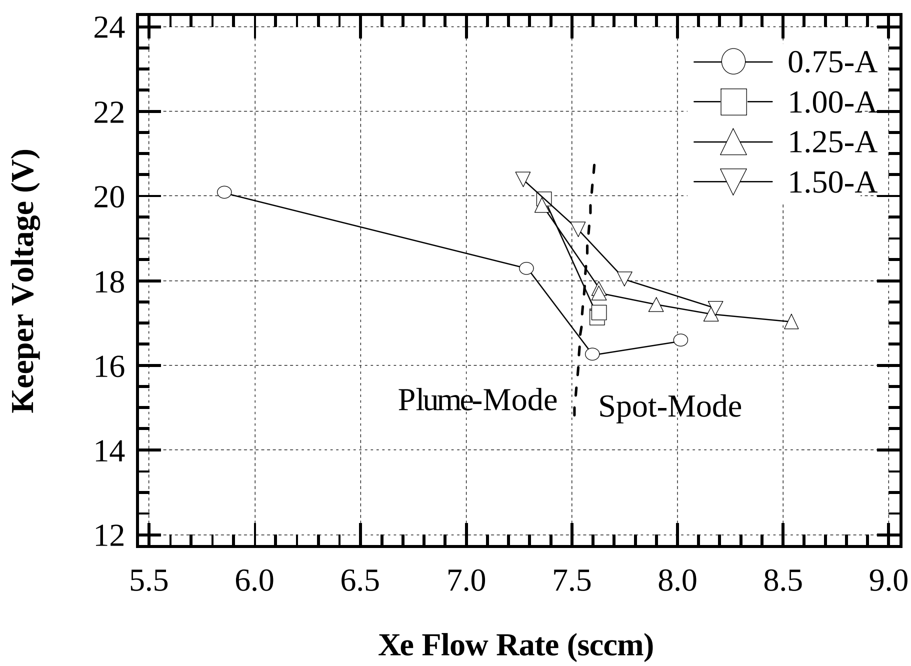

Figure 3.13 - Diode Performance Characterization of AR6´´.

3.1.5 Multichannel Cathode Performance

The multichannel cathodes, MC7 and MC13, operated only in plume-mode by the definition presented earlier. The discharge voltage oscillated at several megahertz with an amplitude on the order of the discharge current. As both Figure 3.14 and Figure 3.15 illustrate, the operating voltages were quite low, especially when compared to the plume-mode voltages of the orificed cathodes. The discharge current envelope was comparatively larger than most of the orificed cathodes. To establish an upper limit to the operating current, the maximum temperature at any point within the cathodes was limited to 1300 ºC. An optical pyrometer was focused on the tungsten wires slightly upstream of the exit plane of the cathodes, because both multichannel and open tube hollow cathodes have a peak temperature just upstream of the cathode tip.[5,52] Despite using similar criteria to limit the operating temperature of the multichannel cathodes, the R500 coating on the wires was nearly depleted after less than 20 hours as Figure 3.14 shows. The initial characterization of MC7 at 1.00-A was nearly 4-V lower than the characterization after only 15 hours of operation. Post test visual inspection of both MC7 and MC13 indicated that most of the R500 had been removed, and Figure 2.3 shows pre- and post-test images for comparison. This type of operation is a show-stopper for the R500 coated wires. However, the use of lanthanum hexaboride in a multichannel hollow cathode may be feasible since it can operate up to about 200 ºC warmer than R500 or 4:1:1 impregnated porous tungsten. The plume-mode operation of the multichannel cathodes and the relatively large amount of propellant required by the cathode make these devices unattractive for use as ion beam neutralizers or plasma contactors. The multichannel cathodes may be acceptable for ion thruster discharge cathodes where the high flow-rate can be better tolerated.

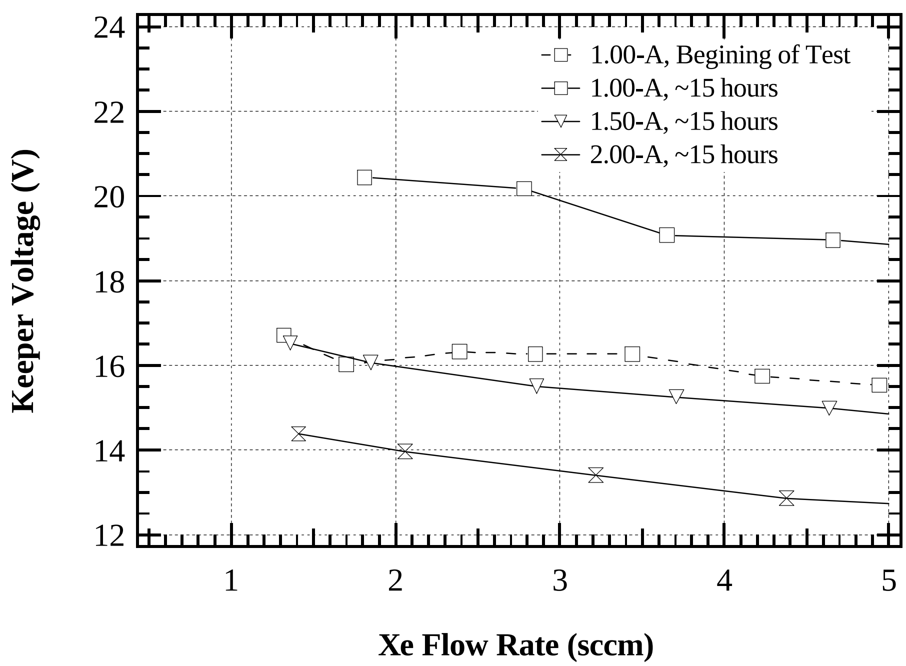

Figure 3.14 - Diode Performance Characterization of MC7.

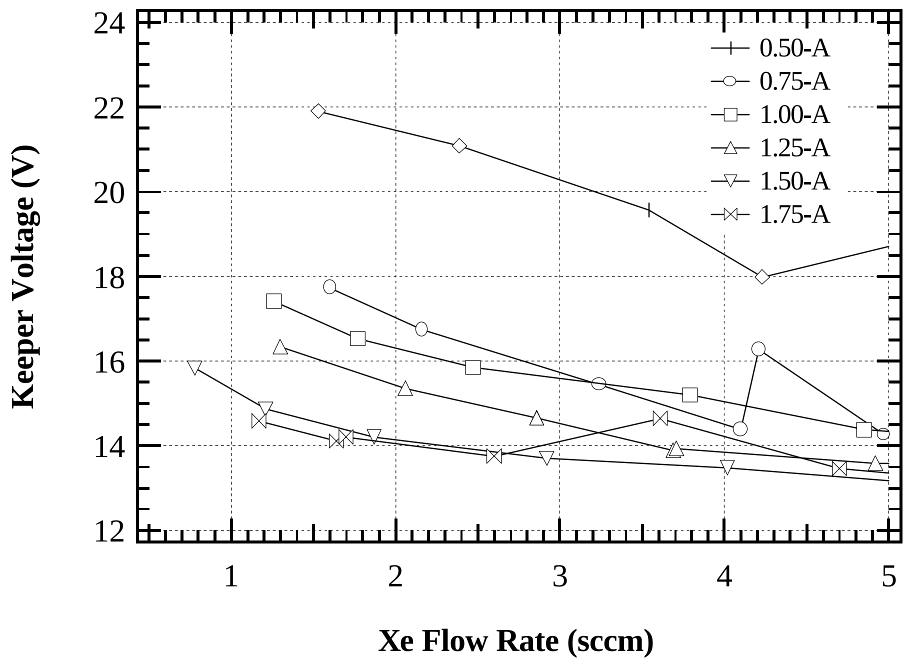

Figure 3.15 - Diode Performance Characterization of MC13.

3.1.6 Minimum Power in a Diode Discharge

Cathode power consumption at the minimum flow-rate condition for spot-mode emission is plotted as a function of the discharge current in Figure 3.16. When comparing AR1, AR3, and AR6´, the smallest aspect-ratio cathode consumed the least amount of power at a given current. While this result was expected since power scales with orifice length according to Ohm’s law, AR3 and AR6´ operated at roughly equal power levels throughout the range of currents. This result suggests that the change in power consumption with orifice length occurs more rapidly at low aspect-ratios. The power consumption for AR1 was the lowest of all the cathodes tested. Changing the orifice diameter resulted in a negligible change in the power consumption as evidenced by Figure 3.16b. The use of an enclosed keeper reduced the power requirement on the order of five to ten percent over the open keeper configuration. Since the enclosed keeper provides a superior radiation environment, the small improvement in power consumption by using the enclosed keeper suggests that conduction was the dominant heat transfer mechanism for the cathode tube; if the open keeper were radiating strongly, the enclosed keeper would improve the performance more significantly than observed. The operating temperature must also be taken into account in making this statement, and the results of a thermographic analysis are presented later.

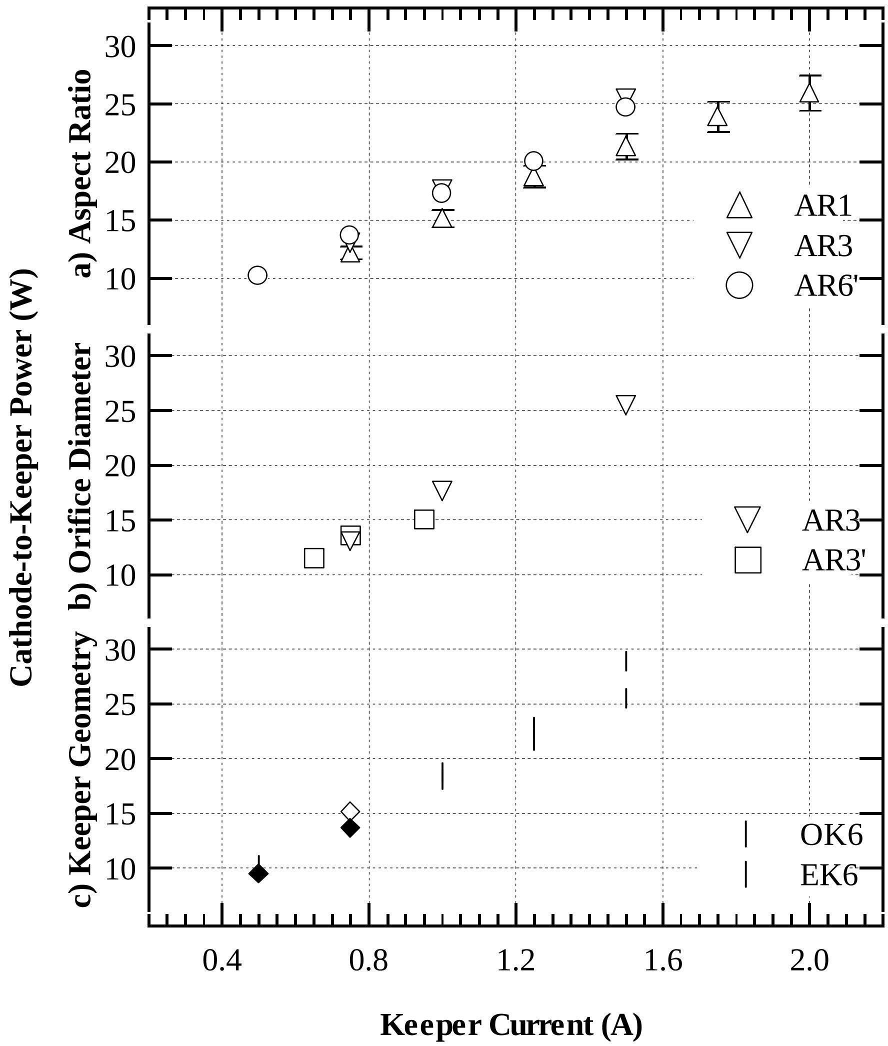

Figure 3.16 - Cathode-to-Keeper Power at the Spot-Mode Minimum Flow-rate.

3.1.7 Minimum Spot-Mode Flow-rate in a Diode Discharge

The flow-rate required for spot-mode emission, plotted in Figure 3.17, also strongly influences efficiency in low-power thrusters. The model by Mandell and Katz[24] predicts that ion production within the orifice, and consequently ion flux out of the orifice, increase with orifice length for a given current, diameter, and flow-rate. As the orifice length is increased, the electron temperature in the orifice also increases due to Ohmic heating. The elevated electron temperature and increased channel length facilitate ionization. Figure 3.17a shows that the model predictions were consistent with the trends observed for aspect-ratios between 1 and 6. The AR6´ and AR3 cathodes appeared to transition at approximately the same flow-rates, suggesting diminishing returns in optimizing the transition flow-rate by increasing the orifice length. Indeed, one must also consider the ion losses as the orifice aspect-ratio is increased. The results in Figure 3.17b demonstrated the expected trend that as orifice diameter decreases, the flow-rate required for spot-mode operation also decreases. The increased current density within the orifice facilitates ion production and emission; ion emission occurs by ambipolar diffusion outside of the cathode sheath and may constitute several mA of current. The transition flow-rate was less for the open keeper configuration than for the enclosed keeper. This result was unexpected because the pressure in the cathode-keeper gap is expected to be greater with the enclosed keeper, thereby facilitating ion transport by reducing the cathode sheath size. An increase in the neutral density in the cathode-to-keeper gap also impedes the flow of ions through collisions with neutrals. This adverse effect appeared to dominate the operation of the enclosed keeper.

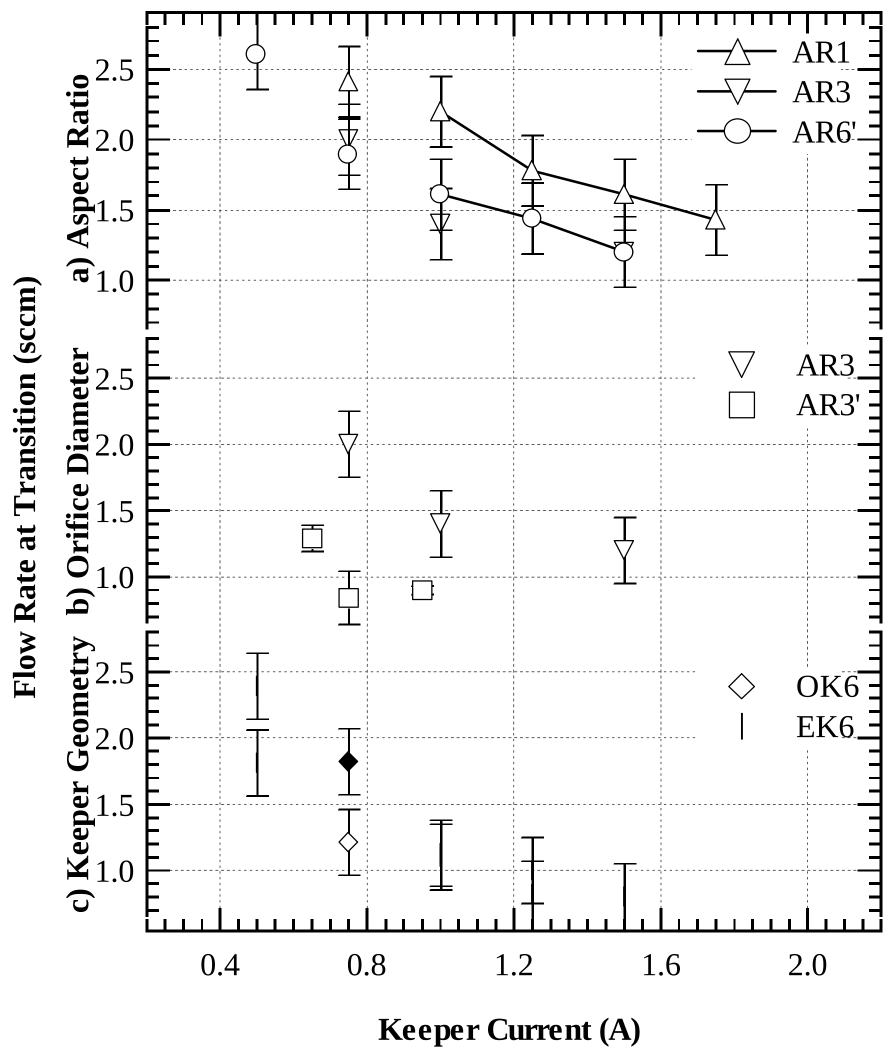

Figure 3.17 - Minimum Spot-Mode Flow-rates.

3.1.8 Electron Emission Characteristics in a Triode Discharge

A secondary, planar anode 48 mm in diameter was placed 60-mm downstream to assess the electron emission capability of the 3.2-mm diameter hollow cathodes. The flow was set to the minimum for spot-mode operation in a diode discharge, and the secondary anode was biased with respect to the cathode. The resulting characteristics are shown in Figure 3.18. Despite decreasing flow-rates, the emission current scaled with the keeper current. Additionally, current saturation occurred at a bias of approximately 20-V. The AR3 cathode with a mesh keeper yielded emission currents of 0.17-A at 20-V and 0.30-A at 24-V with a 0.75-A keeper current at 2.4 sccm. Since the mesh keeper and orifice geometry were expected to contribute weakly to the change in emission current, the effect of increasing the flow at 0.75-A to the keeper was established; an increase of 0.6 sccm led to a 100 percent increase in the emission current.

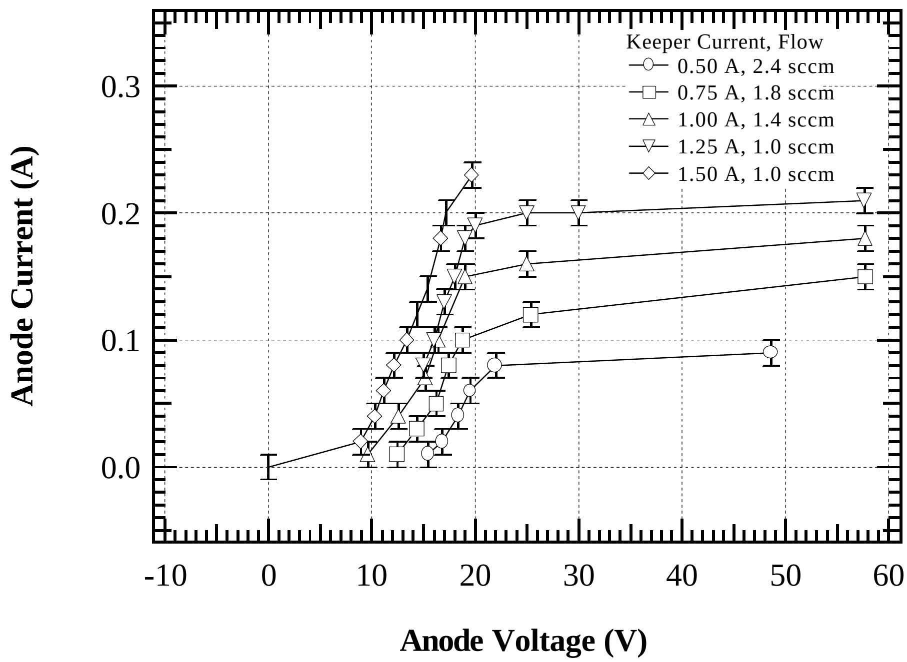

Figure 3.18 - Current-Voltage Characteristics of EK6 for the Second Anode in a Triode Configuration.

The floating potential of the cathode with respect to the tank, shown in Figure 3.19, also provided information on the ability of the cathode to emit an electron current. Increasing the keeper current and decreasing the flow-rate both led to floating potentials closer to facility ground. Plume-mode data indicate the lower limit of emission at a given keeper current. In spot-mode, the maximum emission current occurred at the floating potential closest to ground for a given flow-rate.

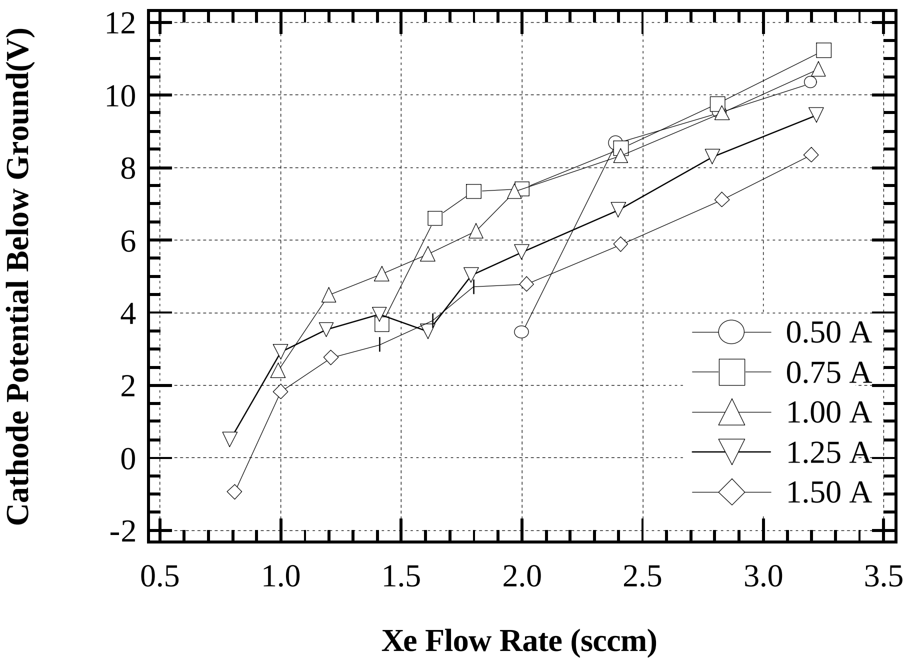

Figure 3.19 - Cathode Potential of EK6 as an Indicator of Emission Capability.

3.1.9 Cathode Operating Pressure

While cathode performance and emission capabilities are the primary concerns for the overall thruster design, the cathode pressure when combined with plasma diagnostics enables a detailed physical picture of the cathode processes to be developed. Salhi[26] found that the pressure in a 6.4-mm diameter cathode with a 1.21-mm diameter orifice was approximately 665 Pa on xenon at operating conditions similar to those reported here. As an approximation, the cathode pressure scales with the ratio of the orifice areas. Given the data from Salhi,[26] the enclosed/open keeper cathode, AR1, AR3, AR6, and AR6´ were expected to operate in the range of 40 kPa. The cathode operating pressures for EK6 and AR3 are plotted in Figure 3.20. Both cathodes were operated in diode mode for these data, and the pressure scaled strongly with the flow-rate at all of the discharge currents. Between 1.00-A and 1.50-A, the pressure appeared to be more weakly dependent upon current than below 1.00-A. For the enclosed keeper cathode, the transition to plume-mode occurred at approximately 39.2 kPa regardless of the current and flow-rate. The argument that the pressure scales principally with orifice area fails to account for the reduced pressure operation of AR3 compared with EK6, which has an identical orifice diameter; cathode pressure is also proportional to orifice length. Conceptually this is reasonable when one considers that the orifice geometry approaches a Poiseuille flow condition.

To assess the cathode pressure as a function of neutral flow, the cathode pressure was monitored while flowing xenon in the absence of a discharge at room temperature and with an orifice plate temperature of 1228-K, maintained by the cathode heater. Figure 3.20 also shows the pressure variation with neutral flows for EK6 at room temperature (298-K) and at 1228-K. The xenon was assumed to be in equilibrium with the cathode orifice temperature. The discharge processes account for the increase in pressure of approximately 200 percent over a neutral flow at 1228-K.

The start-up transients are depicted in Figure 3.21 to illustrate the effect of the discharge on cathode pressure. Initially, the cathode was starved for propellant and operated in plume-mode, while the propellant feed line between the metering valve and the cathode pressurized. The facility pressure was also observed to decrease upon ignition, indicating that a significant fraction of the flow was involved in raising the cathode internal pressure. Approximately three minutes after ignition, the cathode pressure was sufficient (~39.2 kPa) to transition to spot-mode. The cathode took more than 7 minutes to reach a steady state pressure. In this particular case, the cathode tip temperature dropped 170 K transitioning from the preheat condition to a steady discharge. Despite an orifice plate temperature of 1033-K, the presence of the discharge drove the cathode pressure to more than twice that observed with a purely neutral flow at 1228-K.

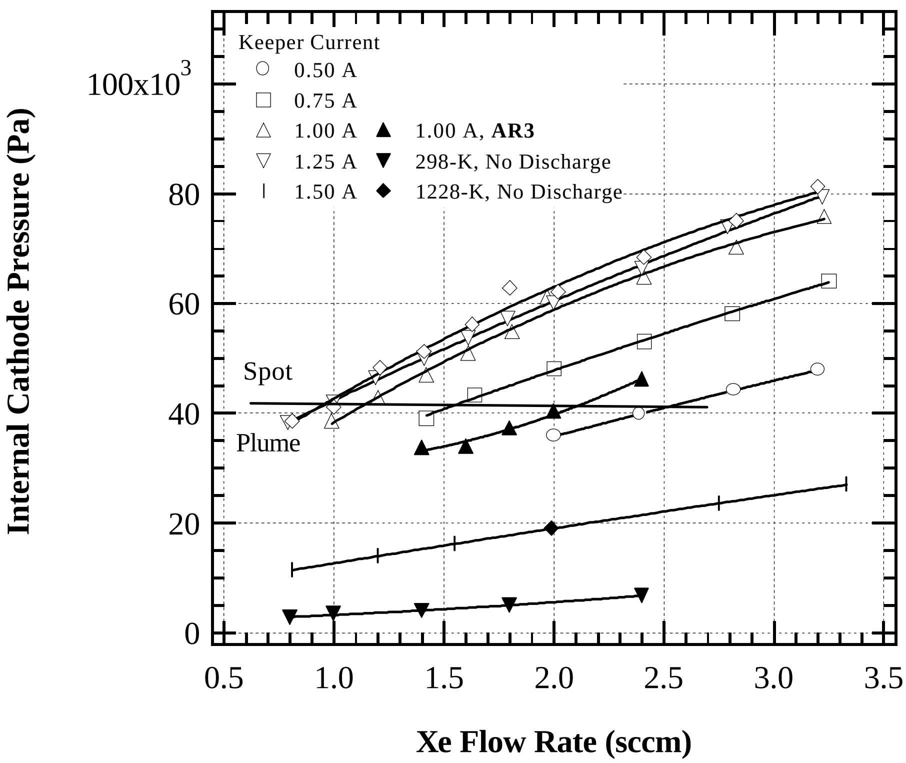

Figure 3.20 - Cathode Internal Pressure Under Various Operating Conditions. Results for EK6, Except Where Noted.

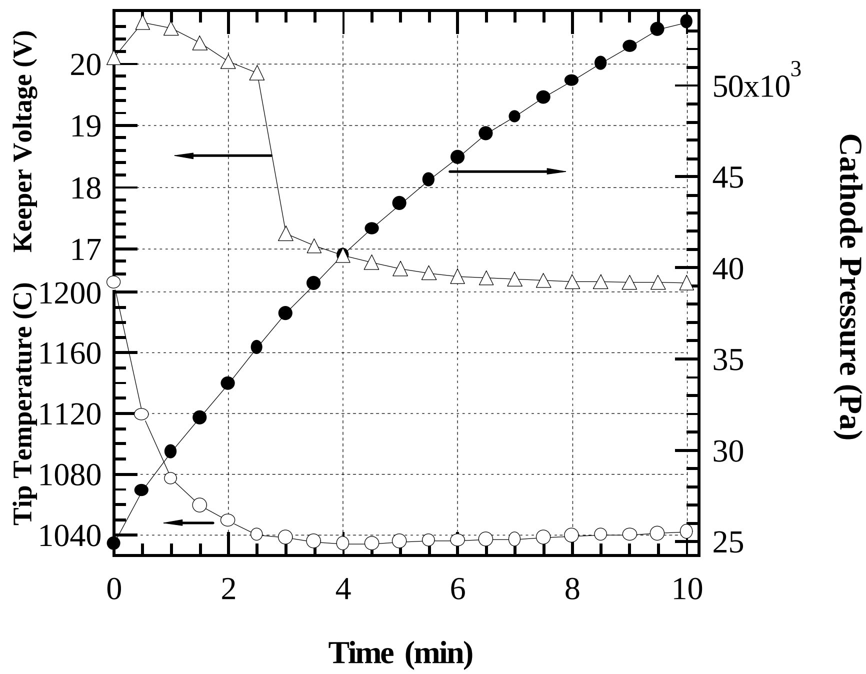

Figure 3.21 - Start-Up Transient Response of Cathode Pressure for EK6.

3.2 Cathode Temperature Distribution

3.2.1 Axial Temperature Distribution

The degree to which an axial temperature profile deviates from linearity indicates the relative importance of radiation heat transfer with respect to conduction. Several of the temperature profiles acquired in this investigation are plotted in Figure 3.22 through Figure 3.25. The thermocouple data and radiometer generated profiles are separated in Figure 3.22 to illustrate the calibration technique. The data markers represent the calibration locations for the thermocouples. All of these data were taken in a diode discharge with the keeper. At 0.50-A, the shape of the profiles appeared similar upstream of the radiation shields. The enclosed keeper cathode operated approximately 100 ºC higher at the tip. The slopes and slope changes in the profiles for both configurations are approximately equal beyond –12 mm upstream. Estimates limited the radiative transfer to about 0.4 W/cm of axial length at –12 mm, while the conduction was 2 to 4 Watts. Consequently, thermal conduction was found to be the dominant heat transfer mechanism in the upstream section of the tube at low-current. The resolution of the camera was insufficient to accurately determine the profile at the cathode tip. At 1.25-A and 1.50-A, the enclosed keeper upstream profiles were noticeably more linear than the open keeper distributions. By limiting the radiative transfer, the use of an enclosed keeper simplifies the problem of cathode optimization; minimizing the heat losses is accomplished by limiting thermal conduction. The profiles on the heater shield and the cathode tip temperatures followed the same trends throughout the current range tested. As is shown in the next section, the temperatures were weakly dependent upon on the flow-rate, and the data presented in Figure 3.22 through Figure 3.25 were representative of the distributions at all of the flow-rates tested.

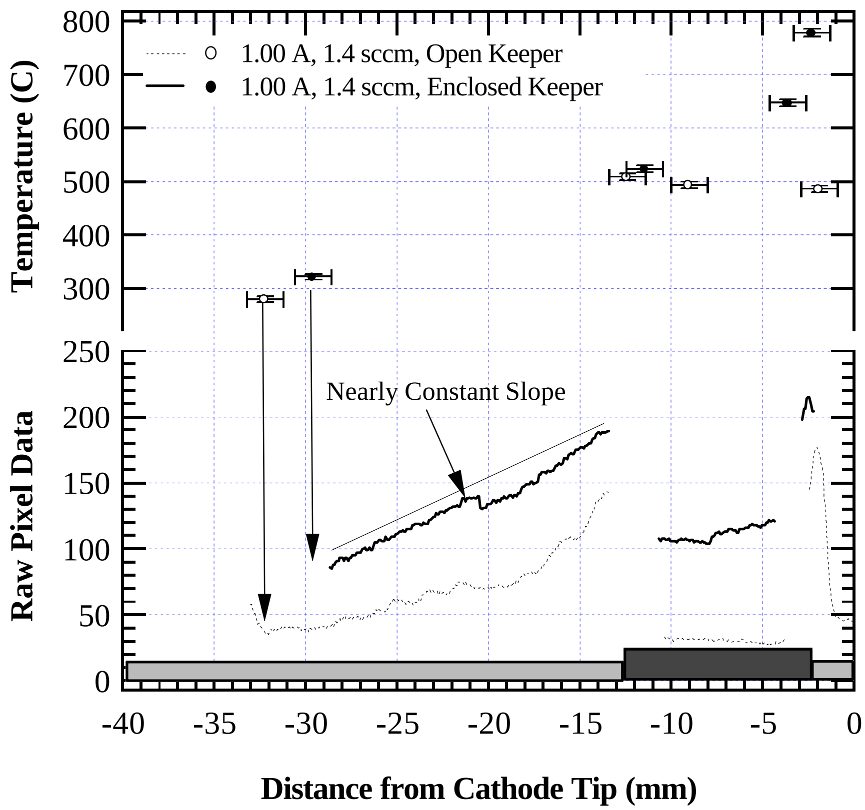

Figure 3.22 - Illustration of the Raw Thermocouple and Radiometer Data. Both EK and OK Were Operated at 1.00-A.

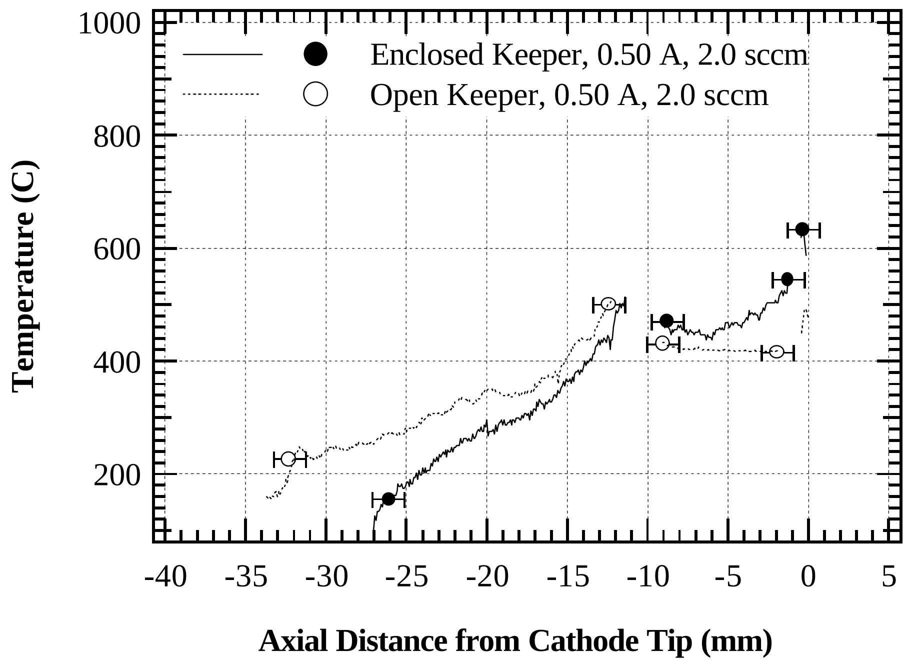

Figure 3.23 - Axial Temperature Profiles of EK and OK at 0.50-A.

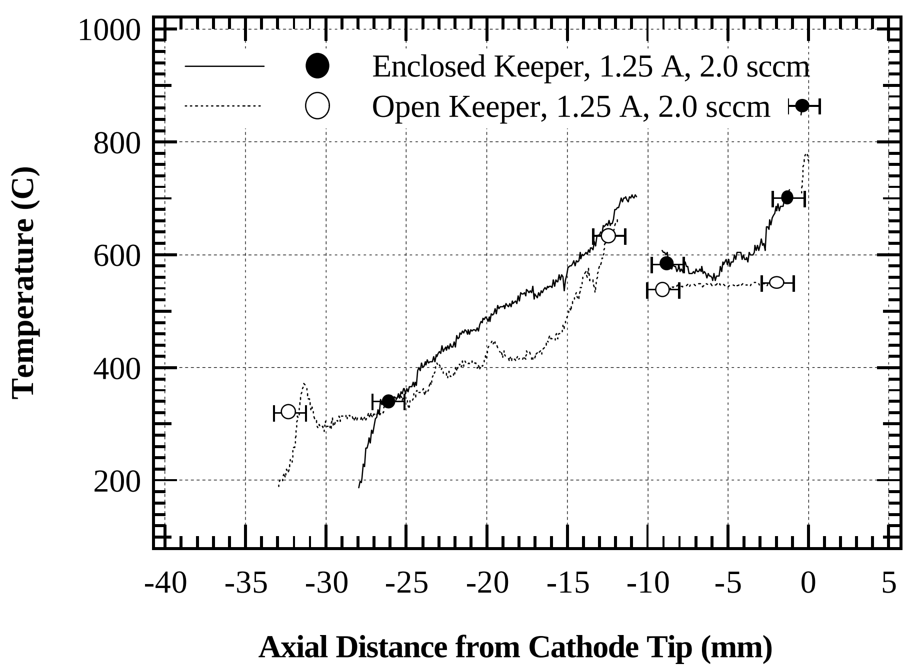

Figure 3.24 - Axial Temperature Profiles of EK and OK at 1.25-A.

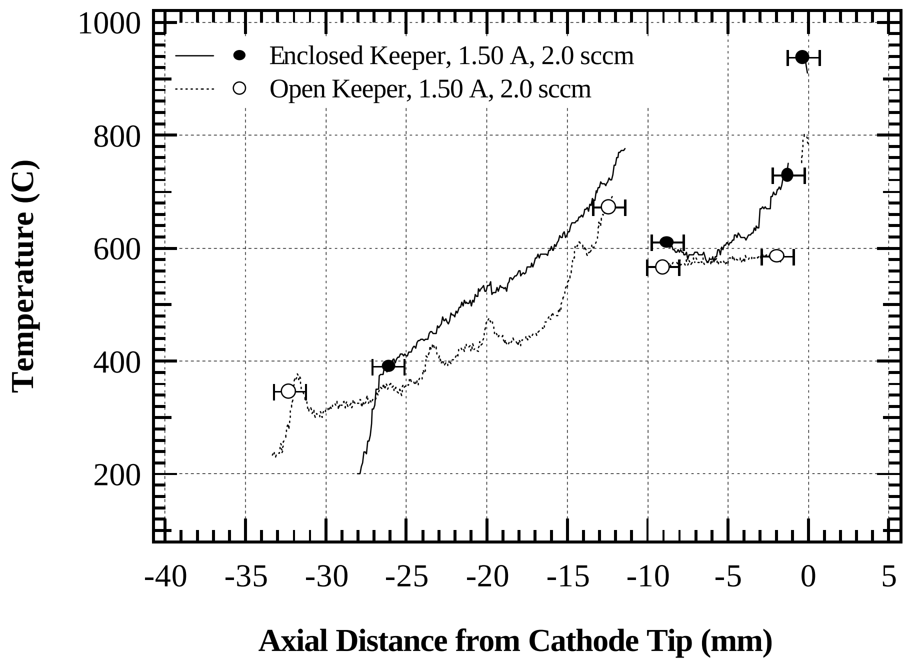

Figure 3.25 - Axial Temperature Profiles of EK and OK at 1.50-A.

Keeper temperature was most sensitive to the flow-rate as shown in Figure 3.26, and the minimum operating temperature was reached at 2.0-sccm. The onset of plume-mode created a large increase in the mean temperature along the profile. The shape between -7 and -27 mm appears to reflect radiative heat transfer from the cathode tube; the drop around 12 to 16 mm roughly corresponds to the location of the cathode heater shields which radiate considerably less than the cathode tube. The increase in keeper temperature beyond -27 mm was also seen in the raw data, and is believed to be an effect of the inability of the radiometer to measure accurately near sharp gradients in emittance or temperature.

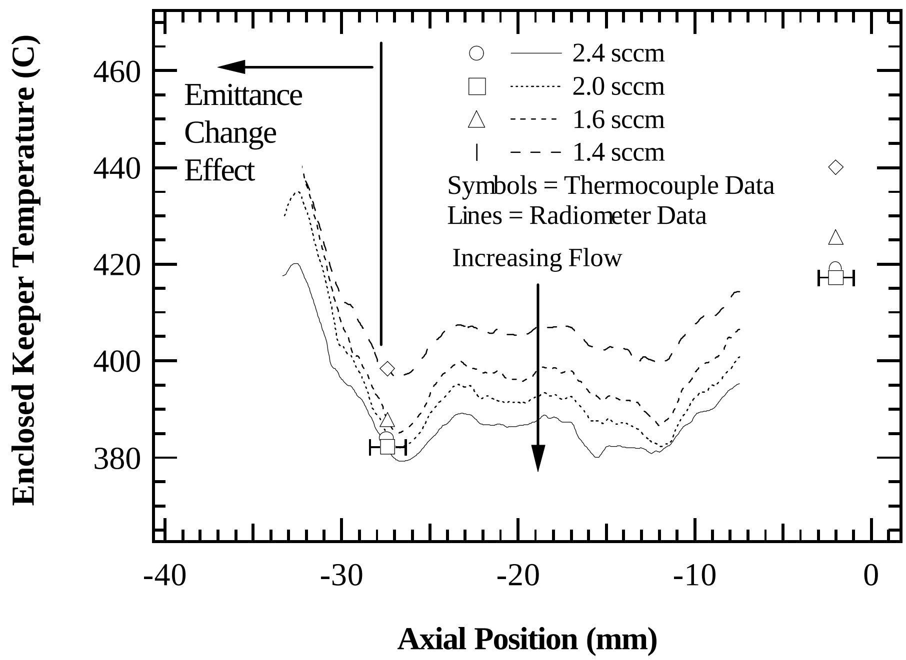

Figure 3.26 - Axial Temperature Profiles of the Enclosed Keeper at 1.00-A.

3.2.2 Tip Temperature Variation with Geometry

A disappearing filament optical pyrometer with emissivity correction was used to determine the orifice plate temperatures. The variation of the orifice plate temperatures with geometry, current, and flow-rate is presented in Figure 3.27 through Figure 3.29. The temperature was observed to scale in proportion with the aspect ratio. As the aspect ratio increases, the power loss in conducting current through the orifice also increases, leading to the observed temperature differences. Figure 3.29 shows the orifice plate temperatures for EK6 and OK6 as a function of flow-rate for three currents. In all cases the enclosed keeper operated at higher temperatures than the open keeper. Most of the orifice plate temperature data exhibited a slight increase in temperature at the onset of plume-mode, the lowest flow-rate for each curve. The contributing factors are the bombardment of the orifice plate by ions created in the cathode-keeper gap, and increased power deposition to the anode, thereby altering the thermal radiation environment.

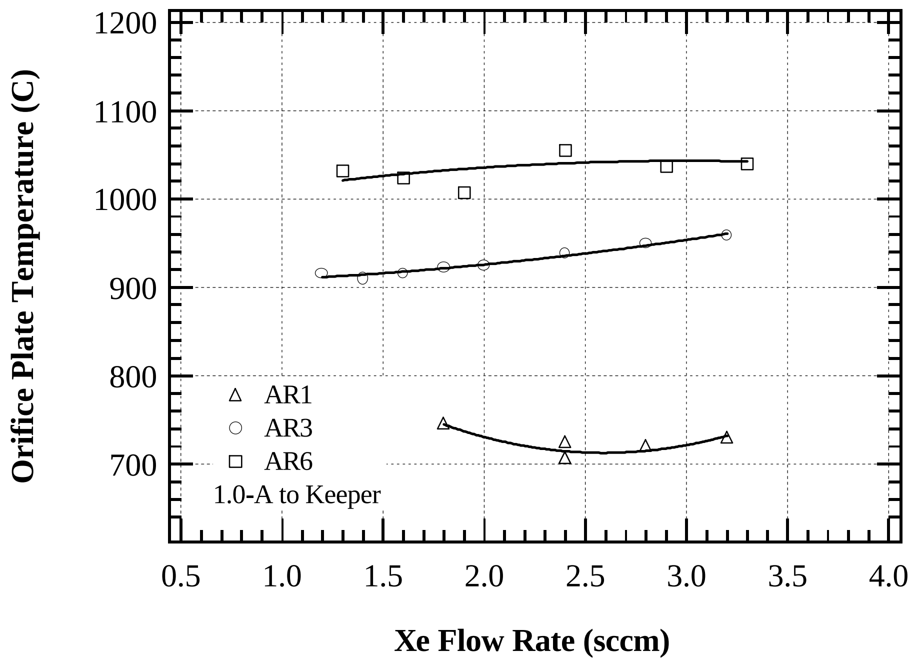

Figure 3.27 - Orifice Plate Temperature Dependence On Aspect-Ratio in a 1.00-A Discharge to the Keeper.

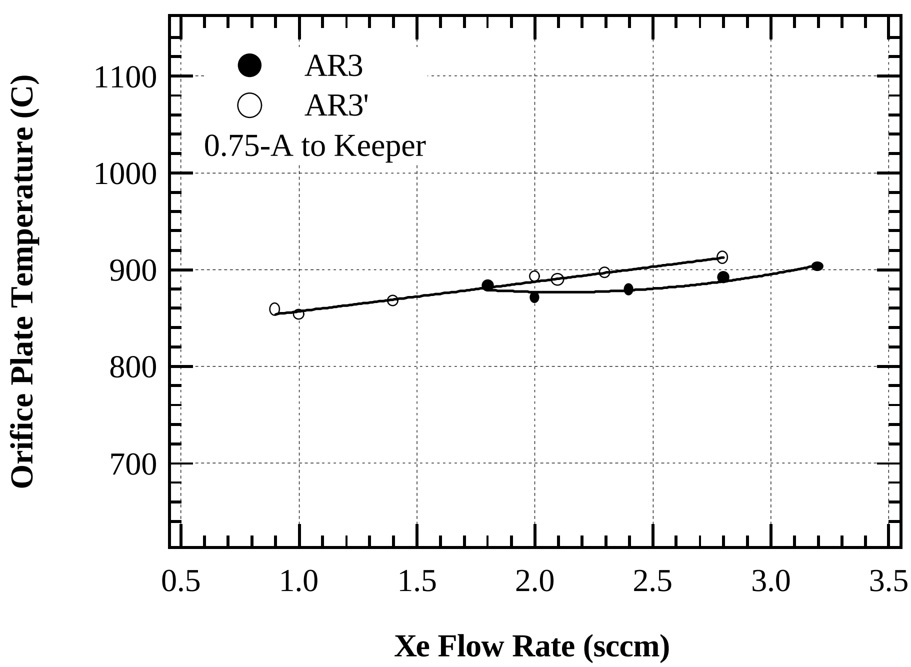

Figure 3.28 - Orifice Plate Temperature Dependence On Orifice Diameter in a 0.75-A Discharge to the Keeper.

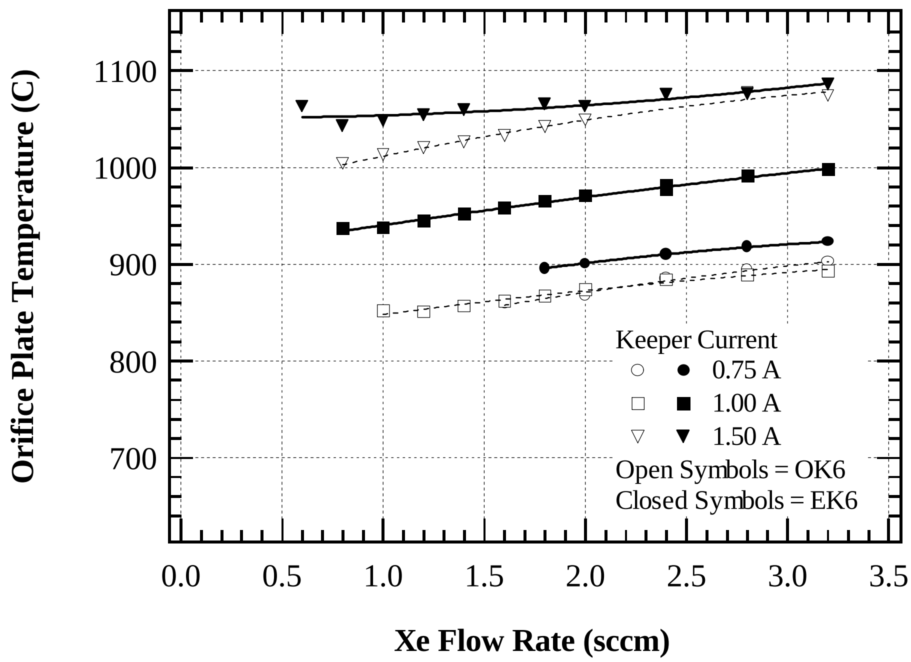

Figure 3.29 - Orifice Plate Temperature Dependence On Keeper Type in a Diode Discharge.

3.3 Cathode Plasma Characteristics

The focus of the measurement of the plasma properties was to obtain information approaching the extremes of the operating envelope of the cathodes. Consequently, the cathodes were operated throughout the range of currents and in spot and plume-modes. Table 3.1 summarizes the operating conditions during the probe diagnostics.

Table 3.1 - Cathode Operating Conditions for the Emission Plasma Parameters.

Figures	*Keeper Current (A)*	*Keeper Voltage (V)*	*Anode Current (A)*	*Anode Voltage (V)*	*Flow-rate (sccm)*	*Mode*
Figure 3.37, Figure 3.40	0.50	18.60	0.00		2.4	Plume
Figure 3.37, Figure 3.42	0.75	24.42	0.00	1.31	1.3	Plume
Figure 3.36, Figure 3.37, Figure 3.38, Figure 3.40, Figure 3.41, Figure 3.42	0.75	17.20	0.00	2.30	2.4	Spot
Figure 3.42	0.75	17.05	0.00		3.3	Spot
Figure 3.38,	0.75	17.28	0.17	20.00	2.4	Spot

Figure 3.41, Figure 3.42						
Figure 3.36, Figure 3.38, Figure 3.41, Figure 3.42	0.75	16.52	0.30	24.22	2.4	Spot
Figure 3.37, Figure 3.40, Figure 3.42	1.50	15.75	0.00	5.78	2.4	Spot

3.3.1 Insert Plasma

Both Siegfried[25] and Salhi[26] have measured the plasma properties in the insert region of 6.4 mm outer diameter hollow cathodes, and despite the different propellants, both measured similar temperatures, potentials, and number densities. The goal in the present investigation was to verify that the plasma properties in 3.2-mm diameter hollow cathodes were of the same order as those measured by Siegfried[25] and Salhi.[26]

The axial variation of the insert plasma properties with flow-rate is plotted in Figure 3.30. The plasma potential rose slightly with decreasing flow-rate and more strongly as the orifice was approached. The potential values and the trends were similar to those observed by Salhi.[26] The plasma property variation with current 0.7 mm upstream of the orifice is depicted in Figure 3.31. Here the plasma potential was observed to decrease with increasing current, again comparable to the data taken by Salhi.[26] As will be shown later for the external plasmas, the electron temperature in spot-mode generally remained below 1 eV in the insert region as well. The electron temperature was observed to increase as the current was increased. The axial variation in the plasma number density shown in Figure 3.30 exhibited a much sharper gradient than that observed by either Siegfried[25] or Salhi.[26] Otherwise, the number density data followed the same trends and were approximately equal in peak magnitude to the data by Siegfried.[25] Salhi[26] measured the plasma number density to be a factor of five higher in magnitude than those reported here. The tendency of the high neutral density within the insert region will be to quench the discharge, and the sharp gradients in number density reported here reflect that intuition.

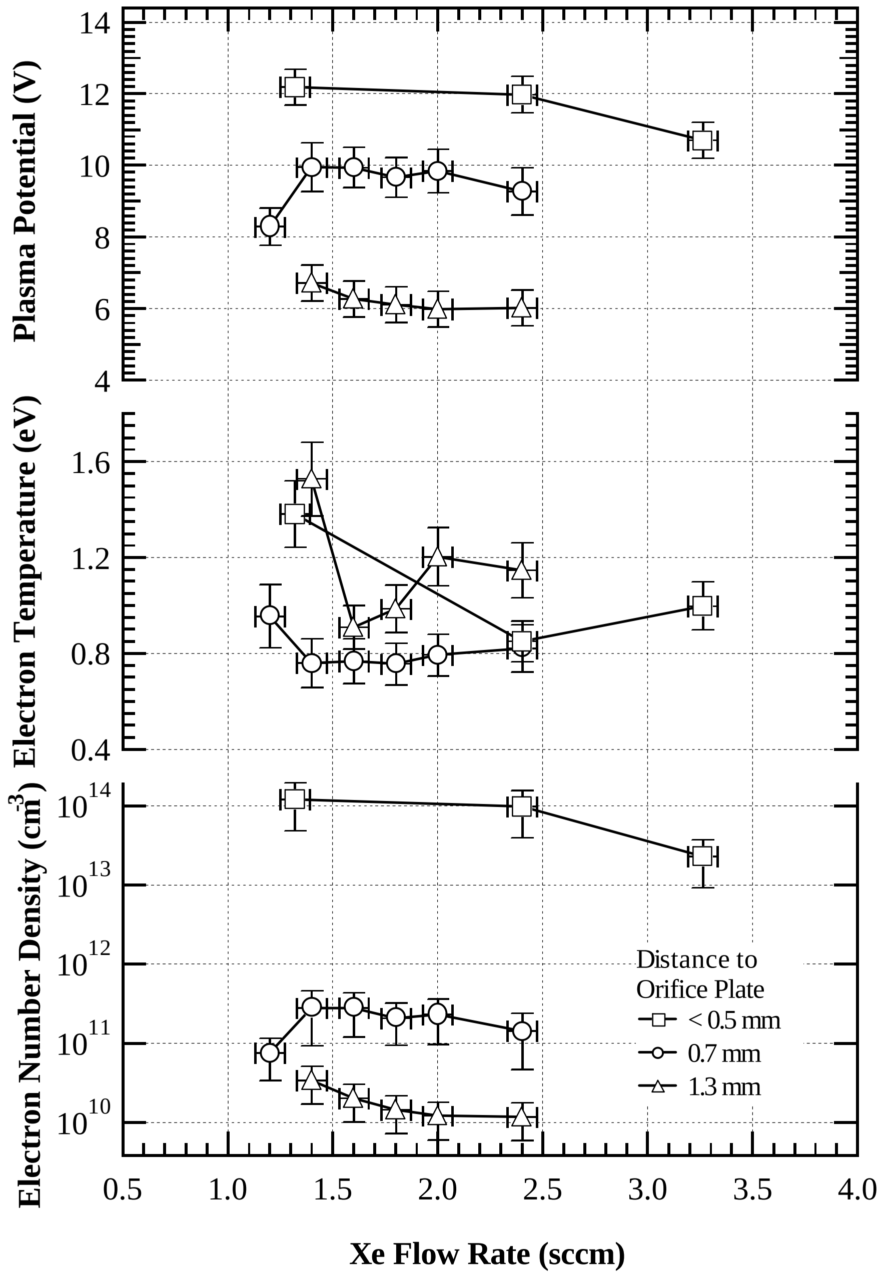

Figure 3.30 - Variation of Internal Plasma Characteristics with Flow-rate.

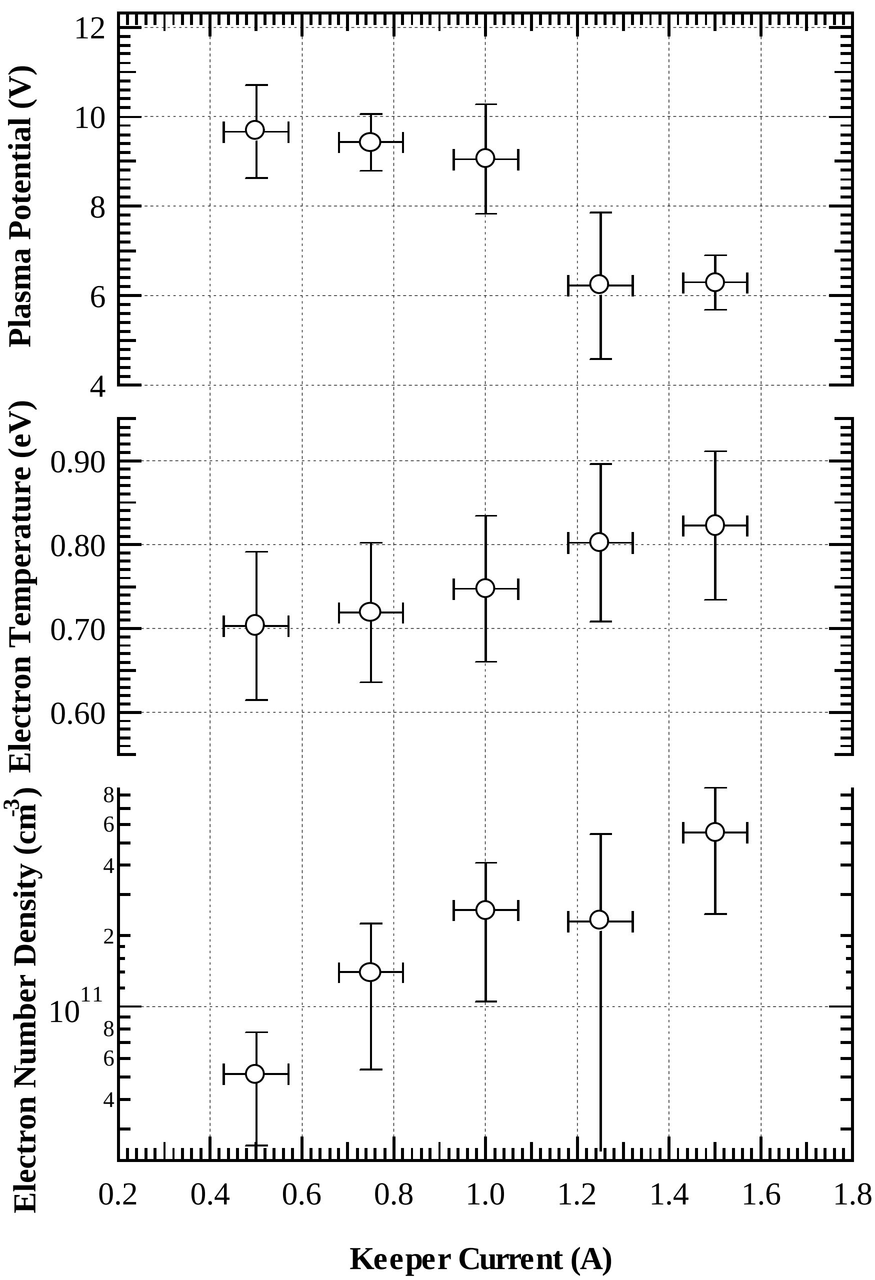

Figure 3.31 - Variation of Internal Plasma Characteristic with Current Approximately 0.7-mm Upstream of the Orifice Plate.

The variation of the internal plasma electron energy distribution function with flow-rate and keeper current is plotted in Figure 3.32 and Figure 3.33, respectively. While the character of the EEDF data most closely resemble the Druyvesteyn distribution, the traces plotted here exhibit a higher degree of structure. As mentioned in Chapter 2 and Appendix B, the EEDF methodology precluded the measurement of the low-energy spread electron beam indicative of the primary electrons emitted from the insert and accelerated through the cathode sheath. The EEDF data were taken primarily to assess whether the plasma was in equilibrium and to characterize the degree of error introduced by using the Maxwellian assumption to calculate the electron temperature. For a Maxwellian distribution, the electron temperature is two-thirds of the average electron energy.

$$T_e = \frac{2}{3}\langle E \rangle = \frac{2}{3}\int Ef\left(E\right)dE \tag{3.1}$$

The average electron energy was calculated using the results of the EEDF analysis, and Table 3.2 shows the comparison of the calculated average electron energy with the electron temperature deduced from the standard Langmuir probe analysis. At each current, the two calculations for the electron temperature agree to within a few percent, and the level of disparity between the methods was considered acceptable for the present investigation.

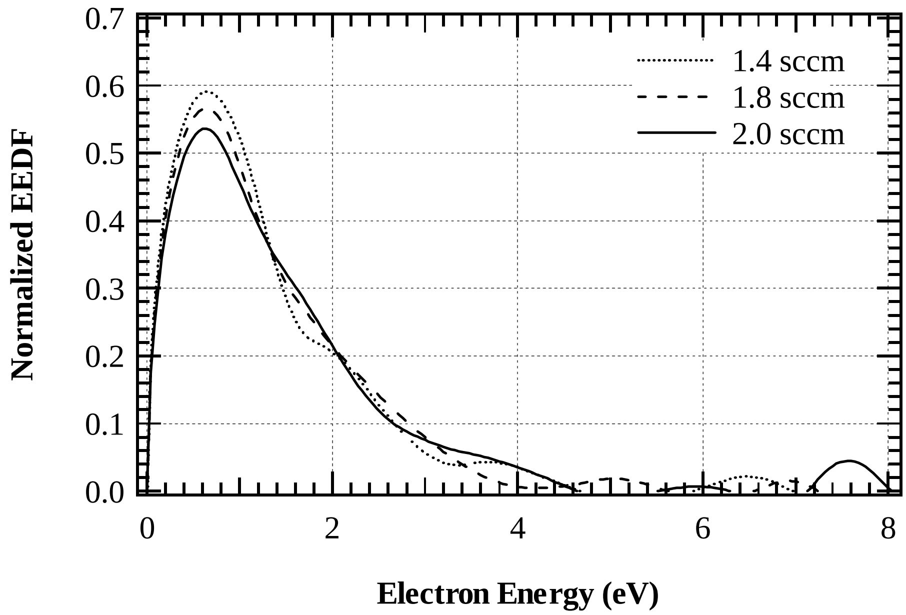

Figure 3.32 - Internal Plasma Electron Energy Distribution Function Variation with Flow-rate at 0.75-A, 0.7-mm Upstream of the Orifice Plate.

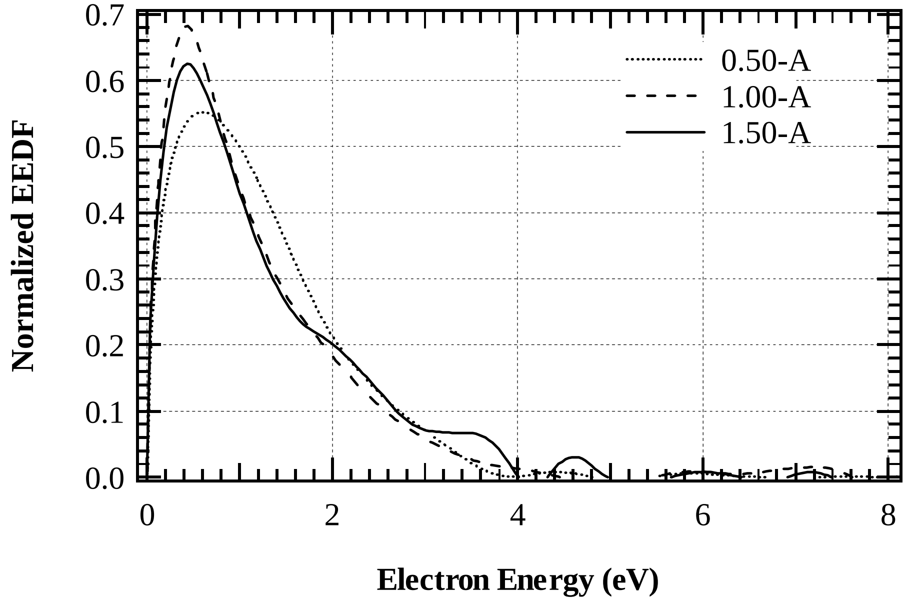

Figure 3.33 - Internal Plasma Electron Energy Distribution Function Variation With Current at 2.0-sccm, 0.7-mm Upstream of the Orifice Plate.

Table 3.2 - Comparison of the Langmuir Probe and EEDF Derived Internal Electron Temperatures for AR3 at 2.0-sccm.

Current (A)	T_e *(eV)*	$2/3 \langle E \rangle$ *(eV)*
0.50	0.61	0.68
0.75	0.73	0.80
1.00	0.77	0.76
1.25	0.80	0.79
1.50	0.80	0.84

3.3.2 Cathode-To-Keeper Plasma

Although the current density is greatest in the orifice and the plasma in the cathode-to-keeper gap greatly influences the onset of plume-mode, little experimental data have been taken in these regions using electrostatic probes, due to the small scales of the orifice and CK gap. To the authors' knowledge, the electron number density in the orifice has yet to be measured experimentally. Siegfried and Wilbur[43] measured the fraction of the current collected by the orifice plate as a whole. To gain insight into the physical conditions within the orifice, the model developed by Mandell and Katz[24] was used. The electron density was calculated to vary from 5 x 10^{14} to 1 x 10^{16} cm^{-3} for the geometries and test conditions in this investigation. At this density, with electron temperatures of up to 2.5 eV, the electrons, ions, and neutrals undergo several thousand collisions along the length of the orifice. The collisional heating of the ions by electrons significantly increases the heavy particle temperature.[26] This is believed to be the mechanism responsible for the elevated pressures observed in Figure 3.20 during cathode operation. A more detailed presentation of this phenomenon appears in Chapter 4.

Plasma potential data were sought by Williams et al.[60] in order to explain ion velocities observed by laser induced fluorescence (LIF) measurements. The plasma parameters in the CK gap are presented in Figure 3.34. Both cases at 1 sccm were plume-mode, while the condition at 3 sccm was spot-mode. Only the potentials for two of the conditions are reported in Figure 3.34 because the noise associated with plume-mode operation made it difficult to determine the plasma potential accurately. The potential variation in spot-mode supports the notion that charge neutralization in the gap was maintained, while in plume-mode, the plasma was more highly negative with respect to the keeper, thereby creating a more favorable condition for ions to maintain quasineutrality. The electron temperature distributions also corroborated this explanation; the increased electron temperature in plume-mode was a manifestation of the onset of space-charge limitations to the electron flow. The electron number density varied from 3×10^{12} to 2×10^{13} cm^{-3}. The error on the number density was calculated to be approximately ±60 percent. The density decreased with diminishing flow-rate, dwindling current, and axial distance from the cathode.

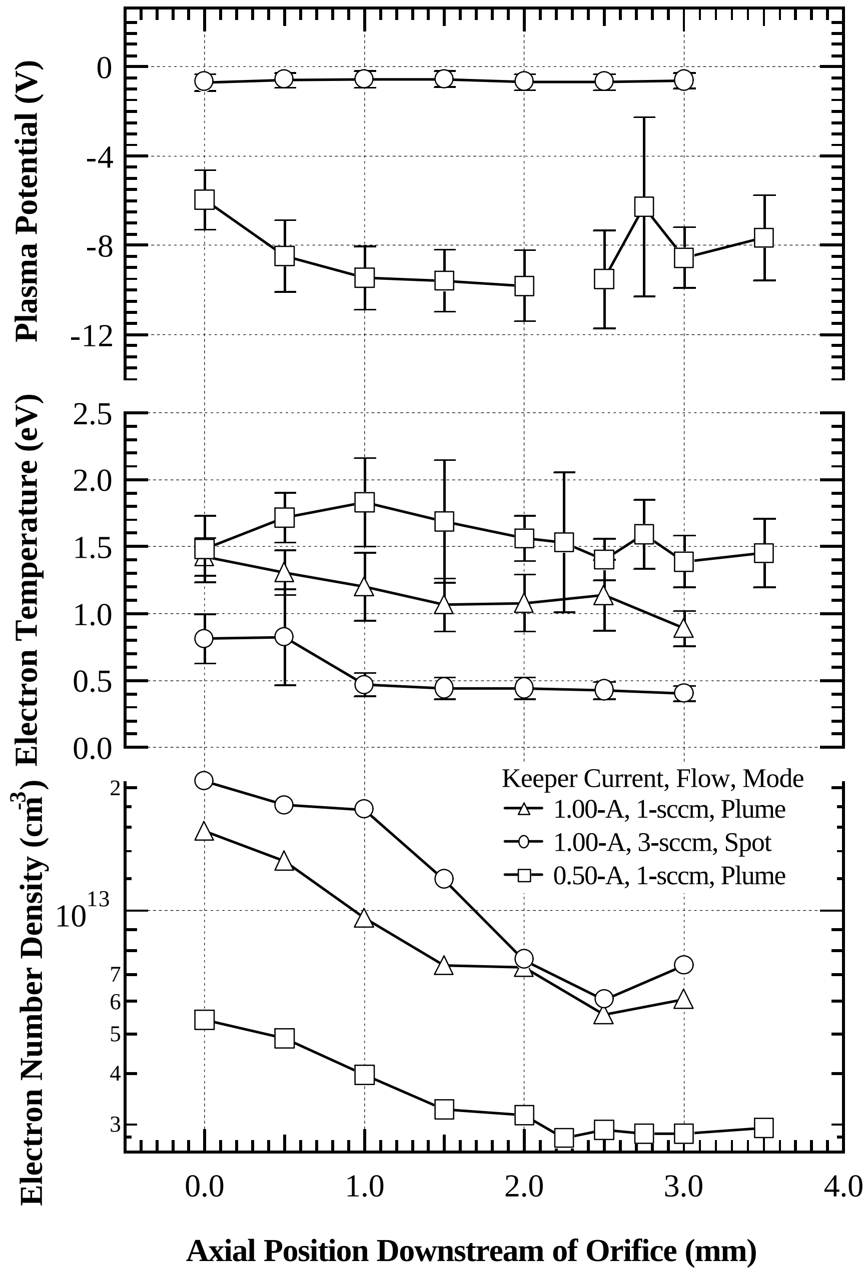

Figure 3.34 - Variation of Plasma Properties in the Extended Cathode-to-Keeper Gap of AR3. Plasma Potential Was Measured With Respect to the Keeper.

Figure 3.35 depicts the spot-mode electron energy distribution functions in the cathode-to-keeper gap. The bulk of the electrons formed a distribution that approximated a Druyvesteyn distribution to 1.5 eV. Between 1.5 and 4 eV, the tail of the distribution appeared inflated. The tail decayed with axial distance from the orifice, indicating that collisional events were driving the distribution toward equilibrium. The decrease in electron energy with axial distance from the orifice was also apparent in Figure 3.35. Although the EEDFs were Druyvesteyn, the average electron energy was approximately 1.5 times the calculated electron temperatures, again showing agreement between the two measurements.

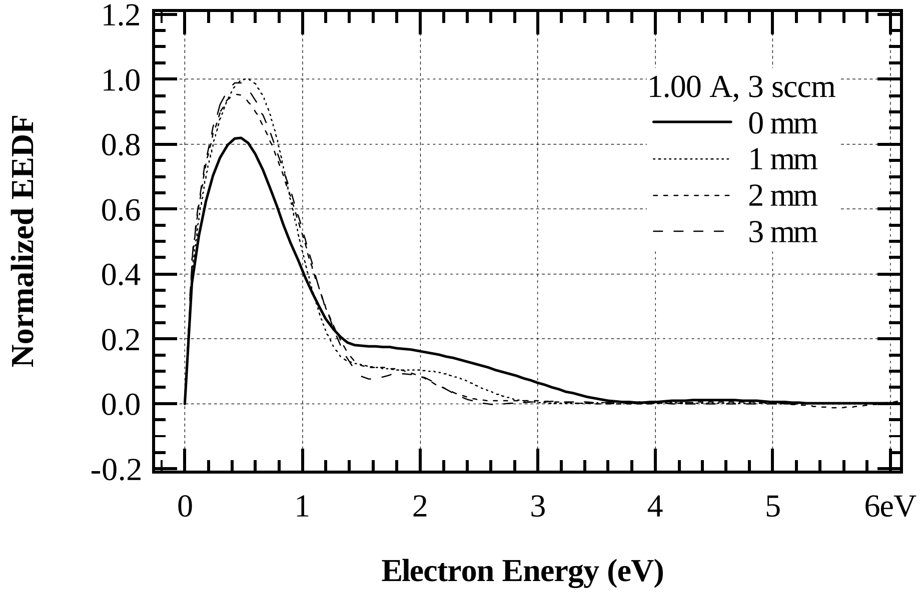

Figure 3.35 - Spot-Mode Electron Energy Distribution Functions in the Cathode-to-Keeper Gap of AR3.

3.3.3 Plasma Downstream of the Keeper

Since axial and radial Langmuir probes were used downstream of the keeper, it was possible to assess the relative anisotropy of the emitted plasma; an isotropic plasma is also assumed in the classical Langmuir probe analysis. When no current is being extracted to the secondary anode, the ability of an electron to stream past the keeper is determined by its energy, and the temperature of the plasma increases with distance from the keeper. By extracting a current to the secondary anode, the net charge density in the gap is decreased, allowing lower-temperature electrons to populate the space. However, by extracting a current, the axial electron energy is increased, and the degree of isotropy in the plasma is decreased. These effects can be seen in Figure 3.36. When the assembly was operated as a diode, the axial and radial temperatures differed by approximately 0.2 eV. As expected, the difference between the temperatures increased when electron current was extracted axially, indicating a higher degree of anisotropy. As a result of this analysis, the radial Langmuir probe data were considered to be more representative of the true plasma temperature, and only the results obtained with the radial probe are presented below.

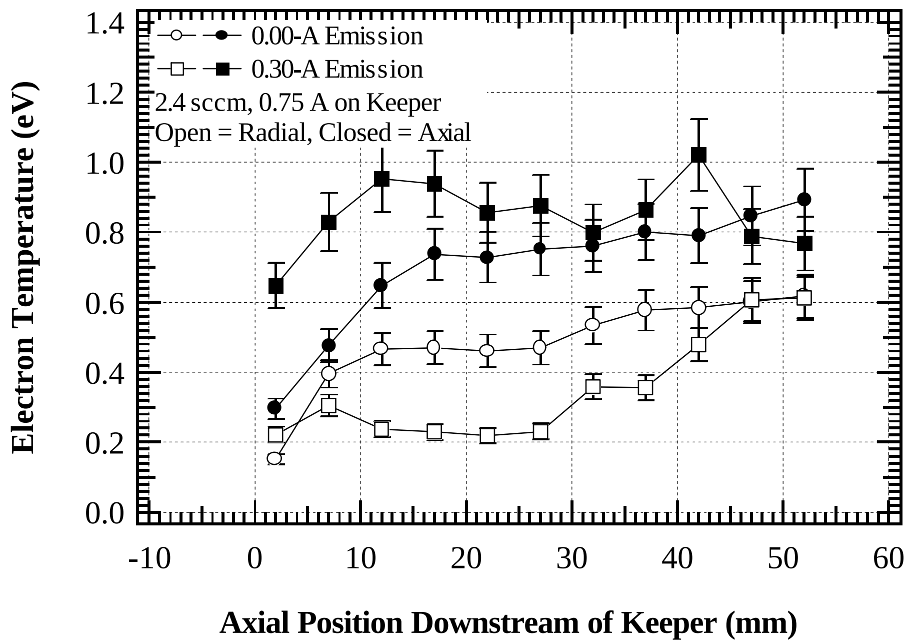

Figure 3.36 - Variation in Observed Electron Temperatures in the Radial and Axial Directions.

A comparison of the electron temperatures in spot and plume-modes is depicted in Figure 3.37. The spot-mode electron temperatures were consistently less than 1 eV, while in plume-mode, the electron temperature varied from approximately 1.5 to 2.5 eV. These results are consistent with the theory for spot and plume-modes described in Reference 23. In spot-mode, the ion flux to the keeper and beyond was sufficient to neutralize the space charge, and a low-energy population of electrons is emitted. When the ion flux becomes too small in plume-mode, space charge limitations allow only a high-energy electron population to escape. The high-energy electron population excites and ionizes the xenon at an increased rate, giving rise to the greatly increased light emission from the plasma. Figure 3.38 illustrates that as the secondary anode extracts a current, lower-energy electron populations were obtained, although the change was only a few tenths of an electron volt. The electron temperatures immediately downstream of the keeper and immediately upstream of the secondary anode were invariant in these tests. The discharge with the secondary anode deposited energy into the emission plasma, raising the electron temperature near the anode. While the EEDFs appeared Druyvesteyn as shown in Figure 3.39, calculation of the average electron energy yielded results in agreement with the electron temperatures in Figure 3.37 and Figure 3.38.

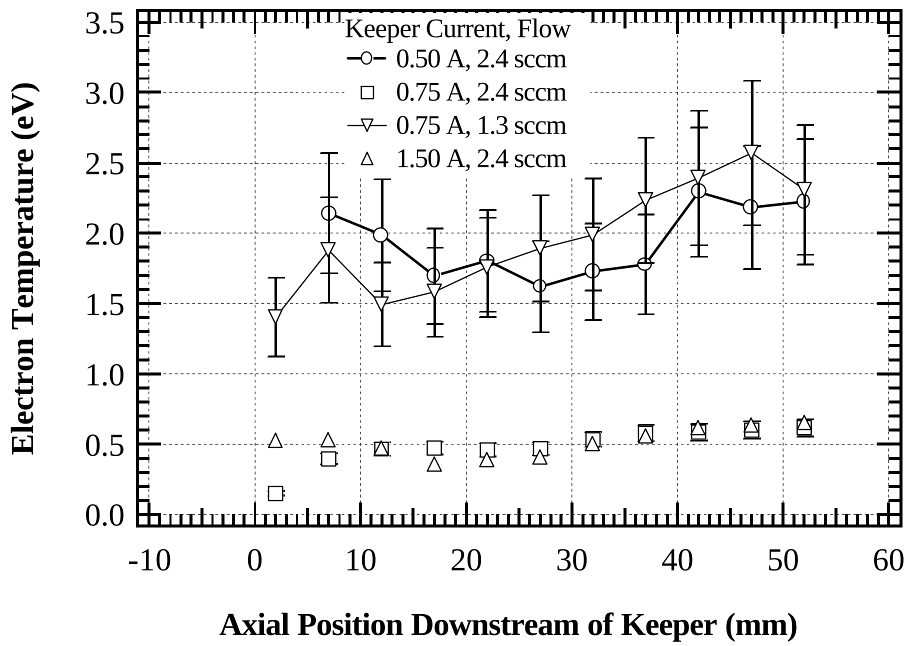

Figure 3.37 - Emission Plasma Electron Temperature In Spot and Plume-Mode

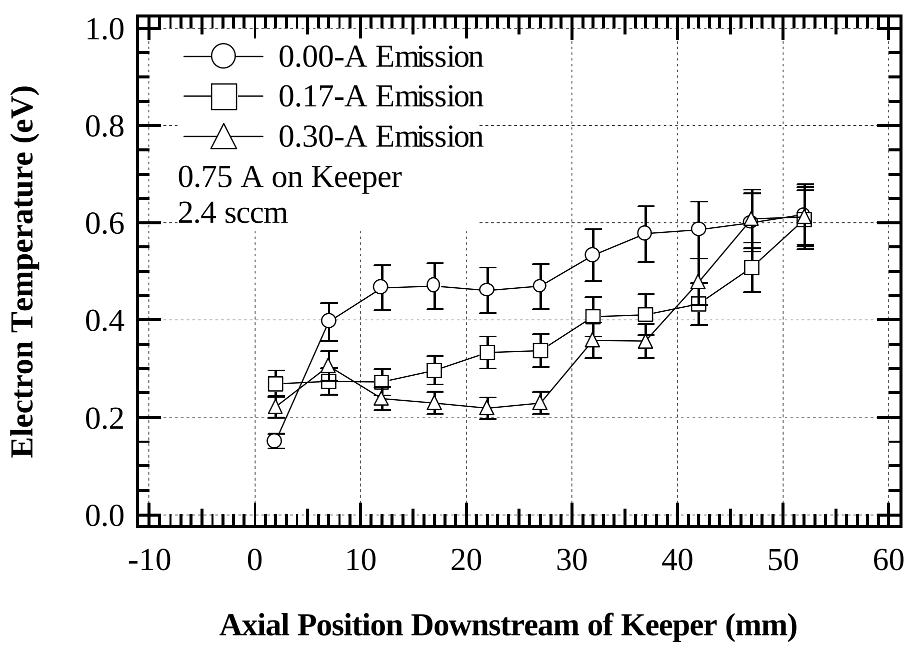

Figure 3.38 - Emission Plasma Electron Temperature with Electron Extraction.

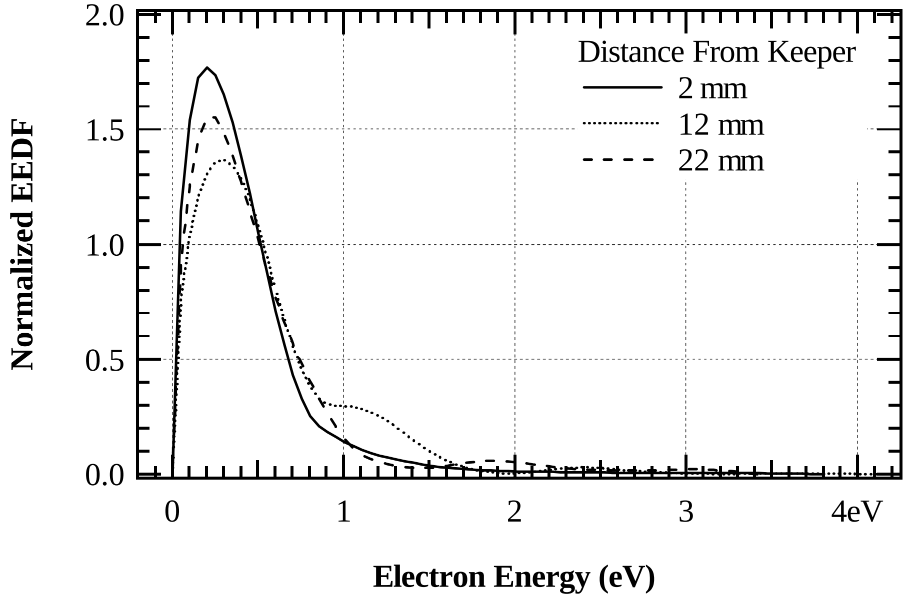

Figure 3.39 - Electron Energy Distribution Function Downstream of the Keeper at 0.75-A and 2.4-sccm.

The plasma potential data also illustrate the processes described above, as shown in Figure 3.40. In the case of zero current to the secondary anode, the plume-mode (0.50-A) plasma potential decayed rapidly downstream of the keeper, indicative of the low-density plasma. In spot-mode, the downstream plasma potential was nearly invariant with keeper current. The higher density spot-mode plasma was able to sustain a greater charge density than the plume-mode plasma. While the plasma potential generally decayed with increasing distance from the keeper, Figure 3.41 shows that during current extraction, the downstream potential leveled out and increased with the extraction current. As the electrons were depleted from the plasma at the secondary anode, the potential was adjusted to facilitate current collection.

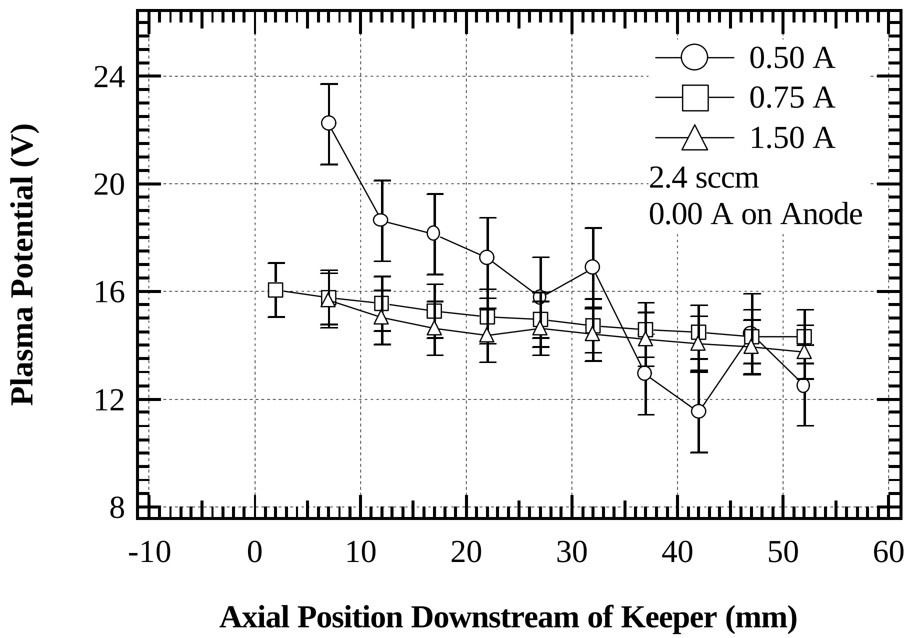

Figure 3.40 - Potential Variation in the Emission Plasma

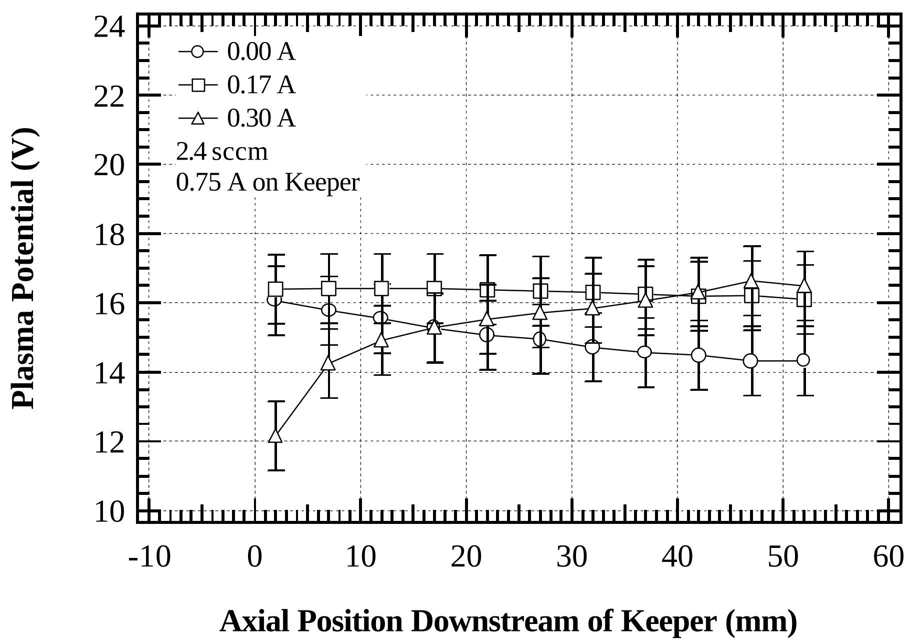

Figure 3.41 - Potential Variation While Extracting Current Downstream.

The electron number densities in the emission plasma are plotted in Figure 3.42. To summarize Figure 3.42, the number density increased with flow-rate, keeper current, and emission current, and the densities approximately followed a cubic expansion with radius as expected. The keeper current appeared to have the strongest effect upon the downstream density. The emission electron number densities were one to two orders of magnitude lower than those observed in the very-near-field of the 1.35 kW D55 anode layer thruster.[65] Ion thruster beam densities are of the same order as those observed emitted from the hollow cathode.[66]

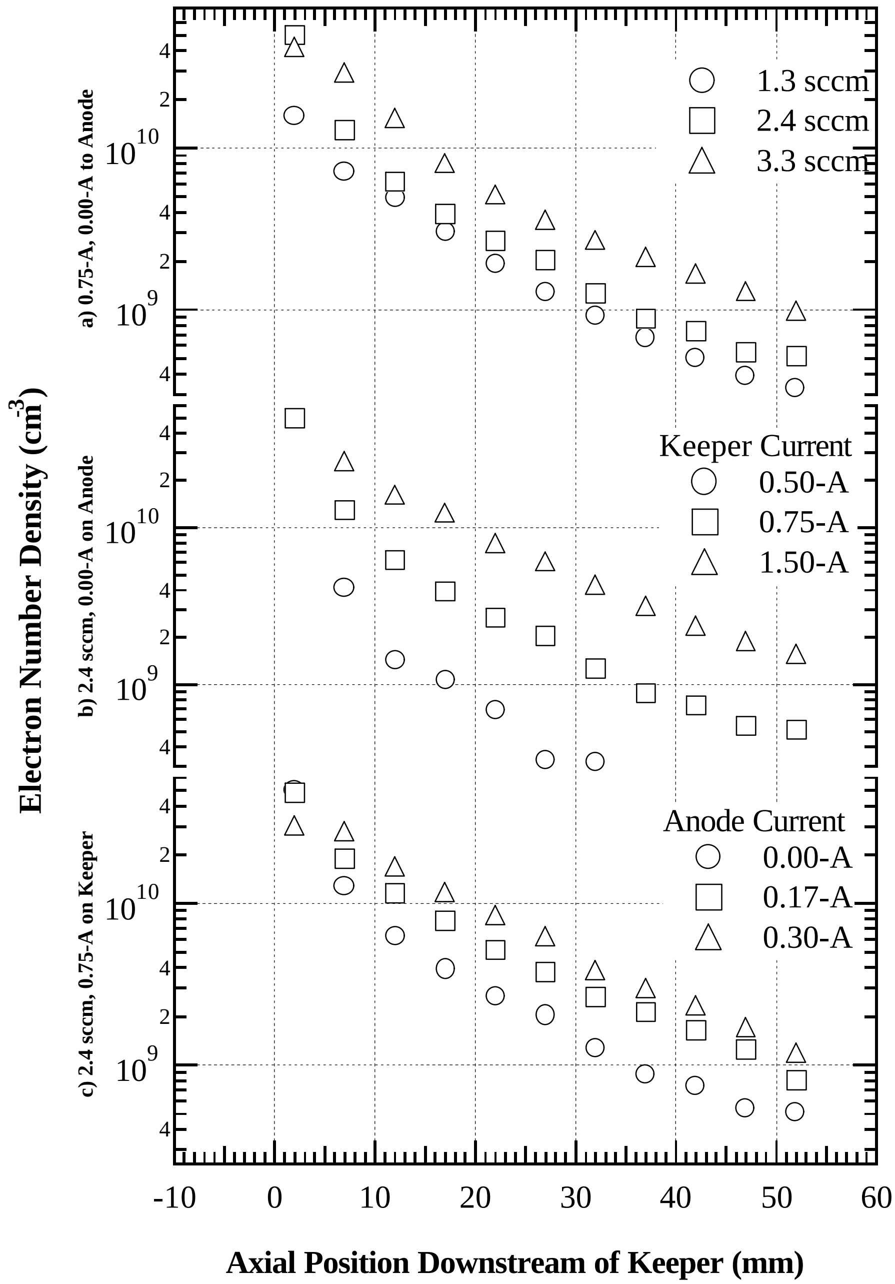

Figure 3.42 - Emission Electron Number Density.

3.3.4 Calculation of Plasma Parameters

Having presented the number density and temperature data, it is useful to calculate the parameters that were assumed to perform the analysis. Appendix B presents a detailed discussion of the validity of the probe theory. The Langmuir probe analysis assumed an isotropic, Maxwellian plasma with cold ions. A collisionless, thin sheath was also assumed which is especially critical for planar probes without a guard ring; at the probe edge, a large sheath creates an effective collection area much greater than the probe diameter used in the analysis. The isotropic and Maxwellian assumptions were discussed in Chapter 2. The assumption of cold ions will be evaluated in Chapter 4. As Table 3.3 shows, the probe diameter was 3 times the Debye length for plume-mode in the insert region, at 1.3-mm upstream of the orifice, and at approximately 6 cm downstream of the keeper. In both instances, the data were of approximate quantitative interest, and large induced error could be tolerated. The electron-electron collision mean free path was used to estimate whether the sheaths were collisionless; the ion-ion mean free path is proportional to that of the electrons by the following ratio.

$$\frac{l_{ii}}{l_{ee}} \approx \frac{T_i^2}{T_e^2}\sqrt{\frac{m_e}{m_i}} \tag{3.2}$$

The ion-ion mean free paths were greater than or equal to the Debye lengths for ion temperatures between 0.1 and 0.5-eV.

Table 3.3 - Summary of Plasma Length Scales and Definition Parameters.

Region	*Mode*	d_{pr} *(cm)*	l_{ch} *(cm)*	T_e *(eV)*	n_e *(cm^{-3})*	l_D *(cm)*	V_{sph} *(cm^3)*	N_{sph}	l_{ee} *(cm)*
Insert	Spot	3×10^{-2}	0.1	0.75	10^{14}	6×10^{-5}	1×10^{-12}	100	3×10^{-2}
	Plume			1.50	10^{10}	9×10^{-3}	3×10^{-6}	30000	6×10^{2}
CK Gap	Spot	1×10^{-2}	0.1	0.50	2×10^{13}	1×10^{-4}	7×10^{-12}	140	6×10^{-2}
	Plume			1.80	3×10^{12}	6×10^{-4}	8×10^{-10}	2400	4
Emission	Spot	0.2	>1	0.2	5×10^{10}	2×10^{-3}	1×10^{-8}	500	3
	Plume			2.5	3×10^{8}	7×10^{-2}	1×10^{-3}	4×10^{5}	5×10^{4}

The most basic assumption contained within the Langmuir probe analysis was the presence of a plasma. The two relevant definitions for a plasma are that the characteristic length scale of the plasma is much larger than the Debye length and that there are a large number of electrons and ions in a Debye sphere. In each case, the characteristic length scale was much larger than the Debye length. The minimum electron count in a Debye sphere was 100 for the insert region in spot-mode. Although this number is considered to be borderline for the definition of a plasma, the ionized gas in this region will be treated as a plasma nevertheless in the model presented in Chapter 4.

CHAPTER 4

HOLLOW CATHODE MODEL AND RESULTS

The primary goal of the theoretical examination of low-current hollow cathodes was to be able to examine the sensitivity of cathode performance to geometry and material choices. The model presented in this chapter is an ensemble of original work by the author and previous work by others, specifically, Mandell and Katz,[24] Salhi,[26] Ferreira and Delcroix,[5] and Capacci, et al.[27] To begin with, the processes in the orifice region were considered to be one of the primary drivers in determining cathode performance, since the current density was greatest in this volume (up to 1.6 x 10^8 A/m^2 for AR1). The presentation of the hollow cathode model begins with the orifice model derived from that of Mandell and Katz.[24] The orifice model contained comparatively few free parameters, and its results were used to bound the free parameters for the insert model. Next, the insert region model is presented followed by the results of both the orifice and insert models. A recently developed thermal model by Van Noord[67] successfully examined the roles of cathode material properties, and in lieu of duplicating that work here, the major findings are discussed. The orifice and insert models, with consideration of the thermal model findings, are sufficient to describe cathode performance. However, the experimentally determined cathode internal pressure was significantly greater than that predicted by the orifice and insert models. Finally, a hydrodynamic pressure model is discussed, and plasma processes are assessed for their contribution to the cathode internal pressure.

4.1 Orifice Model

As the electrons conducting the current enter the orifice, they experience both elastic and inelastic collisions with the neutrals and ions present in the orifice. These collisions produce the ions and a resistance to the electron current. In steady-state operation, the ion production and loss rates must be equal, and the Ohmic heating in the plasma must be balanced by the energy losses. Mandell and Katz[24] developed a simple model of the orifice processes based on these conservation equations, and the present derivation includes current continuity.

4.1.1 Conservation of Ions

The insert region is modeled as a cylindrical control volume bounded by a cathode sheath at the orifice radius, by a double sheath at the entrance to the orifice, and by the exit plane of the orifice. Figure 4.1 illustrates the orifice model approximations. The chamfer is neglected in the analysis of the control volume. In the formulation of the model, the plasma properties are assumed to be uniform within the orifice, and the radial electric field is neglected. The axial electric field, however, is included in the orifice model.

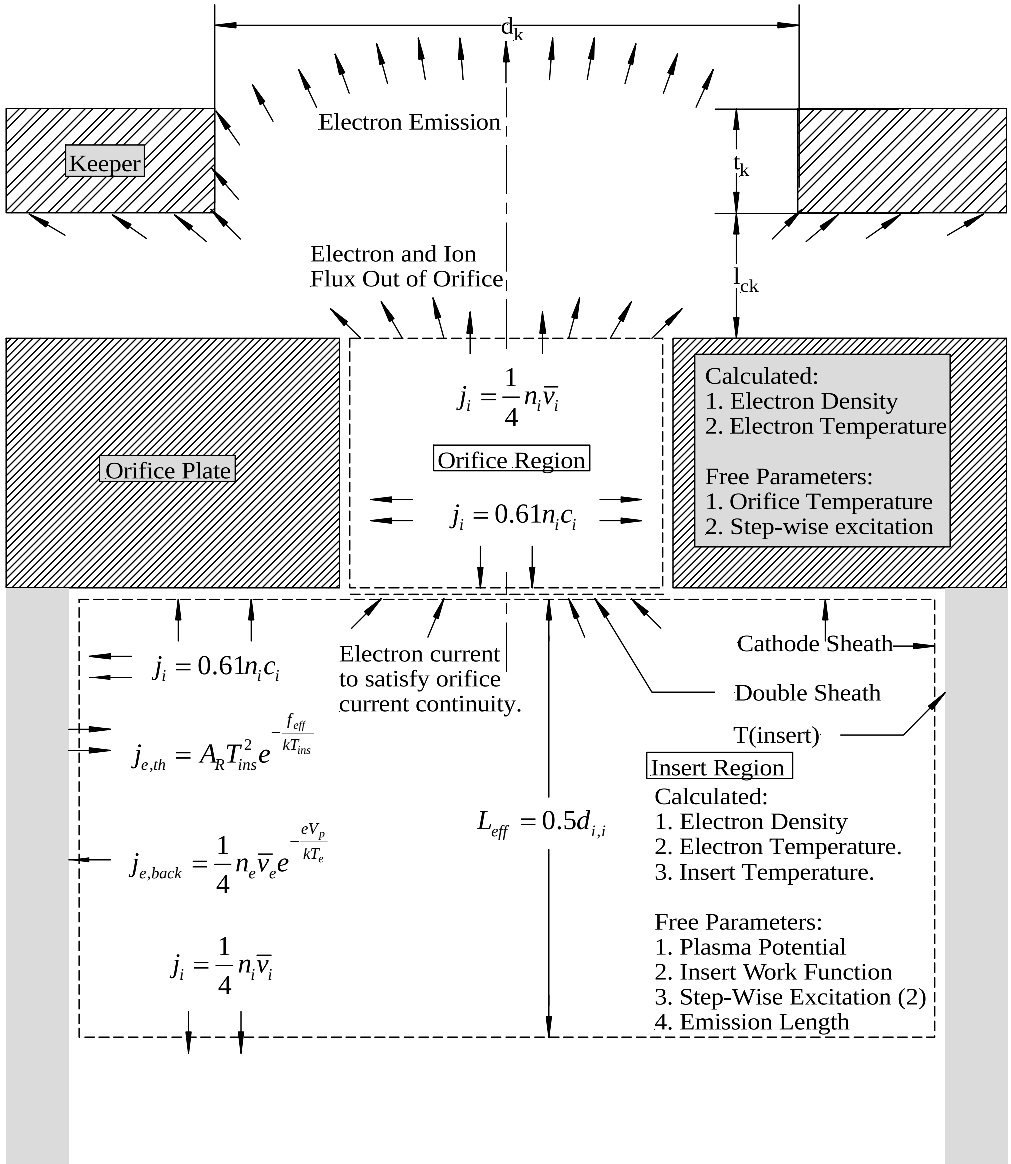

Figure 4.1 - Illustration of the Orifice and Insert Model Approximations.

The steady-state continuity equation applied to the ions states that the creation and in-flux of ions is balanced by the out-flux.

$$\frac{dn_i}{dt} = 0 = \left(\frac{dn_i}{dt}\right)_{ionization} + \left(\frac{dn_i}{dt}\right)_{in-flux} - \left(\frac{dn_i}{dt}\right)_{out-flux} \quad \textbf{(4.1)}$$

The second term is negligible, and a justification follows. The flux of ions from the insert region into the orifice is impeded by the potential structure in this region. Nevertheless, an upper bound was evaluated based on the thermal flux of insert ions to a surface with the same area as the orifice. The thermal flux is used in this estimation since the sheath at the orifice repels ions, and the Bohm sheath criterion is inapplicable. The experimental data from Chapter 3 were used with the electron temperature, and the in-flux was found to be approximately 3.2 x 10^{14} ions/s or about 5 μA. Since this estimate neglects the presence of an ion retarding sheath, the real number is much lower. As will be seen, the other terms were consistently more than 1000 times this number. Ions in the cathode-to-keeper gap tend to fall toward the cathode due to the axial electric field. Given the large density gradient between the orifice plasma and the CK gap, ions backstreaming toward the cathode are more likely to recombine on the downstream side of the orifice plate than to enter the orifice. In order to evaluate the first term in Equation (4.1), a collision analysis was performed, and the derivation appears in Appendix C. For simplicity, electron-impact ionization was assumed to be the only mechanism for creating ions within the orifice. Equation (4.2) describes the ionization rate

$$\left(\frac{dn_i}{dt}\right)_{ionization} = \left(\pi \frac{d_o^2}{4} l_o\right)\left(\frac{m_e}{2\pi k T_e}\right)^{3/2} 4\pi n_e n_o \int_0^{\infty} dv_e v_e^3 \sigma_{ion}(v_e) e^{-\frac{m v_e^2}{2kT_e}} \tag{4.2}$$

where v_e is the electron velocity and $\sigma_{ion}(v_e)$ is the cross section for electron-impact ionization. The neutral number density is calculated by assuming choked flow at the exit of the orifice

$$n_o = \frac{\dot{m}}{M_o A_o \sqrt{\gamma R_{sp} T_o}} \tag{4.3}$$

where M_o is the atomic mass of the propellant, A_o is the orifice cross sectional area, and the neutral temperature is assumed to be equal to the orifice plate temperature. The orifice plate temperature was estimated based on the experimental data. The integral in Equation (4.2) is evaluated numerically using the experimental values for the cross-section by Rapp and Englander-Golden.[68] The ion flux out of the control volume is determined using the Bohm condition at sheath boundaries and the thermal flux at the downstream boundary of the control volume.

$$\begin{aligned}\left(\frac{dn_i}{dt}\right)_{out-flux} &= \frac{I_i}{e} = \frac{J_i}{e}\left(2\pi\left(r_o l_o + r_o^2\right)\right) = 0.61 n_i c_i \left(2\pi r_o l_o + \pi r_o^2\right) + \frac{1}{4} n_i \overline{v}_i \left(\pi r_o^2\right) \\ &= 0.61 n_e \sqrt{\frac{kT_e}{m_i}}\left(2\pi r_o l_o + \pi r_o^2\right) + \frac{1}{4} n_i \sqrt{\frac{8kT_i}{\pi m_i}}\left(\pi r_o^2\right)\end{aligned} \tag{4.4}$$

This equation implicitly includes the effects of the radial electric field with the use of the Bohm criterion. At the exit of the orifice the thermal flux of ions is used. The Debye lengths in the orifice indicate that the bulk of the orifice volume is free of the strong radial electric field near the orifice wall. Consequently the density gradient at the exit of the orifice determines the ion motion. The model by Capacci, et al.[27] included a sheath at the downstream end of the orifice which is neglected in the present derivation. The sudden expansion of the plasma at the orifice exit approximates the conditions of a decaying plasma, and ion transport was hypothesized to occur by ambipolar diffusion. The transport of ions downstream of the orifice in a quasineutral plasma is essential to the theory of spot and plume-mode operation proposed by Mandell and Katz.[24] In the present model, the emitted ion current is also used to estimate the emitted electron current beyond the keeper.

Current continuity is described at the orifice entrance and at the orifice exit. At the entrance, the total discharge current is calculated as the sum of the electron current from the insert region and the ion current to the walls of the orifice less the ion current emitted into the cathode-to-keeper gap.

$$I_D = I_{e,ins} + I_{i,ori} - I_{i,emit} \tag{4.5}$$

The orifice ion current is calculated as part of Equation (4.4), as is the emitted ion current. The insert electron current is determined using Equation (4.5). At the downstream end of the orifice, the discharge current is assumed to be the difference between the emitted electron and ion currents.

$$I_D = I_{e,ori} - I_{i,emit} \tag{4.6}$$

Equation (4.7) combines Equations (4.5) and (4.6).

$$I_D = I_{e,ins} + 0.61 n_e c_i p \left(2 r_o l_o + r_o^2\right) - \frac{1}{4} n_e \bar{v}_i \left(p\, r_o^2\right) = I_{e,ori} - \frac{1}{4} n_e \bar{v}_i \left(p\, r_o^2\right) \tag{4.7}$$

This type of accounting is necessitated by estimation of the ion current in the orifice being on the order of ten percent of the total current. The electron current is assumed to increase linearly between the orifice boundaries. While the rest of the orifice plasma model treats all of the properties as spatially invariant, the axial variation of the electron current influences the Ohmic heating within the orifice.

4.1.2 Conservation of Energy

Conservation of energy within the orifice control volume is approximated by equating the Ohmic heating with the losses from ionization, radiative decay of excited states, and convection.

$$q_{Ohmic} = q_{ion} + q_{ex} + q_{conv} \tag{4.8}$$

The Ohmic heating is calculated using the resistivity based on electron-neutral and electron-ion collisions, as shown in Equation (4.9)[69]

$$h = \frac{n\, m_e}{n_e e^2} \tag{4.9}$$

where ν is the sum of electron-ion and electron-neutral elastic collision frequencies. The electron-ion collision frequency is calculated from the formula in the NRL Plasma Formulary.[70]

$$n_{ei} = 3.9 \ln \Lambda n_e T_e^{-\frac{3}{2}} \tag{4.10}$$

where the dimensions are consistent with those listed in the Nomenclature and the Coulomb logarithm is

$$\ln\Lambda = 23 - \ln\left(\frac{\left(10^{-6} n_e\right)^{1/2}}{T_e^{3/2}}\right) \tag{4.11}$$

An effective value of the electron-neutral elastic collision cross-section is estimated by numerically integrating the velocity dependent elastic collision cross-section data from Brode over the Maxwellian electron population in the same manner as Equation (4.2).[71] The effective cross-section is then used to evaluate the electron-neutral elastic collision frequency as defined in Equation (4.12),

$$\nu_{e,o} = \left(n_o - n_e\right)\left\langle \sigma_{e,o} v_e \right\rangle \tag{4.12}$$

where the neutral number density based on flow, n_o, is reduced by the electron density under the quasineutral assumption, and the velocity of the electrons is defined as

$$v_e = \sqrt{\frac{kT_e}{m_e}} \tag{4.13}$$

The factor of $\sqrt{2}$ typically used to calculate the collision frequency is omitted from Equation (4.12) because the electron velocity is assumed to be much greater than the neutral velocity, thus defining the relative velocity. Since the properties within the orifice are assumed to be constant everywhere, Equation (4.9) defines the plasma resistivity in the orifice. The electron current in the orifice is assumed to increase linearly toward the orifice exit due to the creation of ions and electrons through collisions with neutrals along the length of the orifice. The variation in the electron current implies an axial variation in electron density, however the electron density was treated as uniform in the orifice control volume for simplicity. The formulation of the Ohmic heating term accommodates the axial variation of the electron current. Thus for $x < l_o$

$$I_e\left(x\right) = I_{e,ins} + bx \tag{4.14}$$

where $I_{e,ins}$ and b are determined by the requirement for current continuity, and are defined in Equations (4.15) and (4.16), respectively.

$$I_{e,ins} = I_D - 0.61 n_e c_i \left(2\pi r_o l_o + \pi r_o^2\right) \tag{4.15}$$

$$b = \frac{I_{e,ori} - I_{e,ins}}{l_o} = \frac{1}{l_o}\left[0.61 n_e c_i \left(2\pi r_o l_o + \pi r_o^2\right)\right] \tag{4.16}$$

Calculation of the Ohmic heating of the electrons is modified to account for the variable electron current along the length of the orifice.

$$q_{Ohmic} = I^2 R = \frac{\eta}{A_o}\left[I_{e,ins}^2 l_o + I_{e,ins} b l_o^2 + \frac{1}{3} b^2 l_o^3\right] \tag{4.17}$$

The ionization power loss due to the flow of ions out of the control volume is the product of the ionization rate, the charge, and the ionization potential:

$$q_{ion} = \left(\frac{dn_i}{dt}\right)_{ionization} e\phi_i = N_{eo}\left(\pi r_o^2 l_o\right) e\phi_i \tag{4.18}$$

where N_{eo} is determined from Equation (4.2), and ϕ_i was equal to 12.12 eV for xenon.

The second term on the right-hand side of Equation (4.8) describes the power lost from the free electrons as they excite bound electrons within neutral xenon. The energy lost by free electrons in excitation events is calculated similarly to the ionization energy loss. The excitation collision rate in the orifice is (4.19)

$$\left(\frac{dn_{ex}}{dt}\right) = \left(\pi r_o^2 l_o\right)\left(\frac{m_e}{2\pi k T_e}\right)^{3/2} 4\pi n_e \left(n_o - n_e\right)\int_0^\infty dv_e v_e^3 \sigma_{ex}\left(v_e\right) e^{-\frac{m v_e^2}{2kT_e}} \tag{4.19}$$

where the collision cross-section data were taken from Hayashi.[72] The total energy loss of the free electrons to the excitation of the bound electrons is

$$q_{ex} = \left(\frac{dn_{ex}}{dt}\right) eU_{ex} \tag{4.20}$$

where the average energy lost in an excitation event, U_{ex}, is a constrained parameter. Similarly to Mandell and Katz,[24] the average excitation energy is set to 10 eV. While this value is representative, provided the overwhelming majority of the excitations are from the ground state, the average excitation energy decreases as the fraction of secondary excitations increases. In order to rigorously evaluate the power loss due to neutral excitation, a detailed ionization model is required. Development of such an ionization model was beyond the scope of the present investigation, and reduced accuracy of the results can be tolerated when using the model to assess the relative capabilities of a given cathode design.

The convective power loss considers the temperatures of the electrons entering the control volume from the insert region and those exiting the orifice:

$$q_{conv} = I_{e,ori} T_{e,ori} - I_{e,ins} T_{e,ins} \tag{4.21}$$

Equation (4.21) leaves the insert region electron temperature as a free parameter, however, the data presented in Chapter 3 showed that in spot-mode, the insert region electron temperature was nearly invariant. In general, the total convection term is a small fraction of the energy lost in neutral excitation.

The ion continuity (4.1) and energy equations (4.8) are solved iteratively by using a numerical goal seeking program which varies the electron temperature and number density, respectively. First the electron temperature is varied to satisfy Equation (4.1). Next, the number density is determined, satisfying Equation (4.8). If the solution of Equation (4.1) holds within established limits, the solution is considered to have converged. The solution technique is discussed in more detail in Appendix D.

After the orifice model solution converges, several Knudsen numbers are calculated to verify that the plasma is indeed collisional, and the Debye ratio and particle count in a Debye sphere are evaluated to determine if the ionized gas meets the conditions for a plasma. The results showed that the plasma was collisional with Knudsen numbers generally much less than one for plasma-related collisions. The

Knudsen numbers for neutral and ion self-collisions were as high as a few tenths. This is considered borderline for any continuum theory describing their properties.

The converged solution also permits a relative estimate of the electron emission capabilities of a given cathode design. For a cathode operating in spot-mode, the absence of a luminous plume suggests that few ions are created in the plume. Hence, the requirement of quasineutrality implies that ions are emitted with the electrons. Equation (4.4) states that the ions are emitted based on the thermal efflux. The emitted electron current is calculated based on the ratio of electron-to-ion mobility.

$$I_{e,emit} = f\sqrt{\frac{m_i}{2p\, m_e}}\, I_{i,emit} \tag{4.22}$$

where f is the escape fraction of electrons moving beyond the keeper. The escape fraction is estimated based upon a cosine distribution to be

$$f = \sin^2\left(\frac{p}{2} - q_T\right) \tag{4.23}$$

where q_T is calculated using the cathode and keeper geometries

$$q_T = \arctan\left(\frac{l_{ck} + t_k}{d_k/2}\right). \tag{4.24}$$

Examination of Equation (4.24) shows that the emission current can be increased by decreasing l_{ck} or t_k or by increasing d_k. These modifications also influence spot-to-plume-mode transition and the cathode-to-keeper discharge voltage. Despite their potential for increasing electron emission, keeper geometry changes were ignored for simplicity.

4.2 Insert Model

In the same spirit as the orifice model, the plasma in the insert region is approximated by a control volume with uniform plasma properties throughout. Figure 4.1 illustrates the basis for the insert model. The efficiency of the ionization processes within the insert region is expected to contribute to the overall performance. In addition to the statements of ion continuity and energy conservation, the insert model has an explicit statement of current continuity. These three equations still leave four free parameters, and the choice of those parameters is discussed below.

4.2.1 Current Continuity

In the insert region, the current continuity statement is written by equating the total operating current, I_D, with the current emitted from and collected at the cathode surface. This approach necessitates inclusion of the ion current in the orifice, and the statement is therefore dependent upon the results of the orifice model calculations. The mathematical expression representing current continuity is written in Equation (4.25).

$$I_D = I_{e,emit} + I_{i,coll} - I_{e,coll} - I_{i,emit} \tag{4.25}$$

The first term in Equation (4.25) refers to the thermionic electron emission current from the insert which is determined using the Richardson-Dushman equation.

$$I_{e,emit} = I_{e,th} = \left(2\pi r_i L_{eff}\right) A_R T_{ins}^2 e^{-\frac{\phi_{eff}}{kT_{ins}}} \tag{4.26}$$

The value of the Richardson coefficient was set constant at 60-A/cm^2-K^2 which is consistent with Goodfellow.[73] The work function is considered as a bounded free parameter. Typical values for the work function of the insert range from 2.0 to 2.1-eV, and the variation of the thermionic current density as a function of temperature is plotted in Figure 4.2.[8] An effective work function is used to account for the Schotky effect which acts to reduce the apparent work function of a material in the presence of a strong electric field.

$$\phi_{eff} = \phi_o - \sqrt{\frac{e\left|E_{ds}\right|}{4\pi\varepsilon_o}} \tag{4.27}$$

A double sheath analysis for an electron emitting surface estimates the electric field in Equation (4.27) to be[43]

$$E_{ds} = \sqrt{\frac{n_e kT_e}{\varepsilon_o}}\left[2\sqrt{1+2\frac{eV_p}{kT_e}} - 4\right]^{1/2} \tag{4.28}$$

The plasma potential in Equation (4.28) is a restricted parameter in this investigation. Experimental data showed that the plasma potential varied between 8 and 12-V above the cathode potential depending upon axial position. The effect of the plasma potential on the thermionic current density is depicted in Figure 4.3 for plasma parameters similar to those expected. While the emission current density is relatively insensitive to the plasma potential, the double sheath effect increases the emission current density significantly. The insensitivity of the emission current to the plasma potential argued for its use as a free parameter.

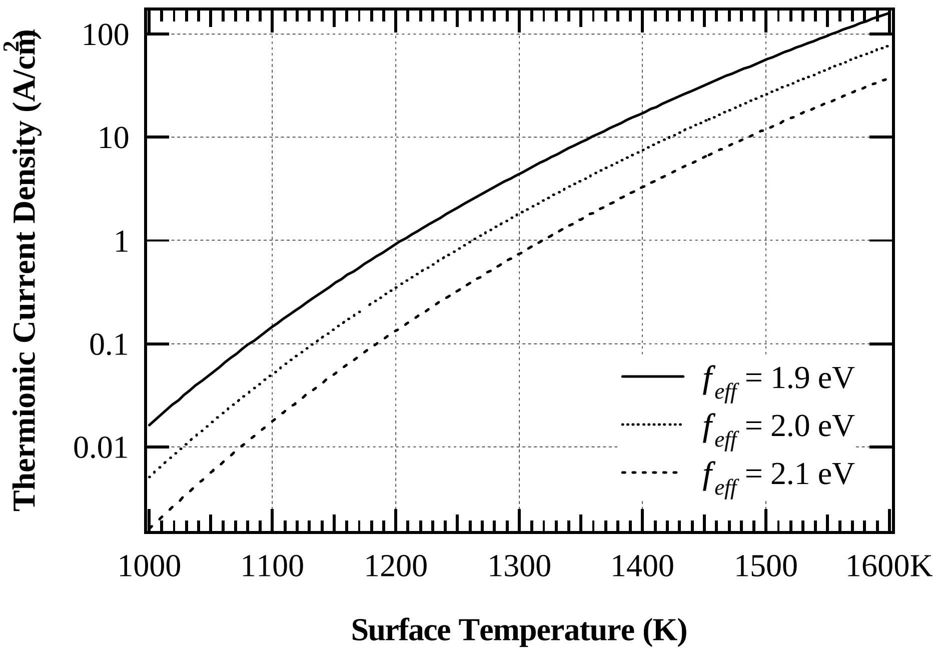

Figure 4.2 - Thermionic Current Density for Various Effective Work Functions.

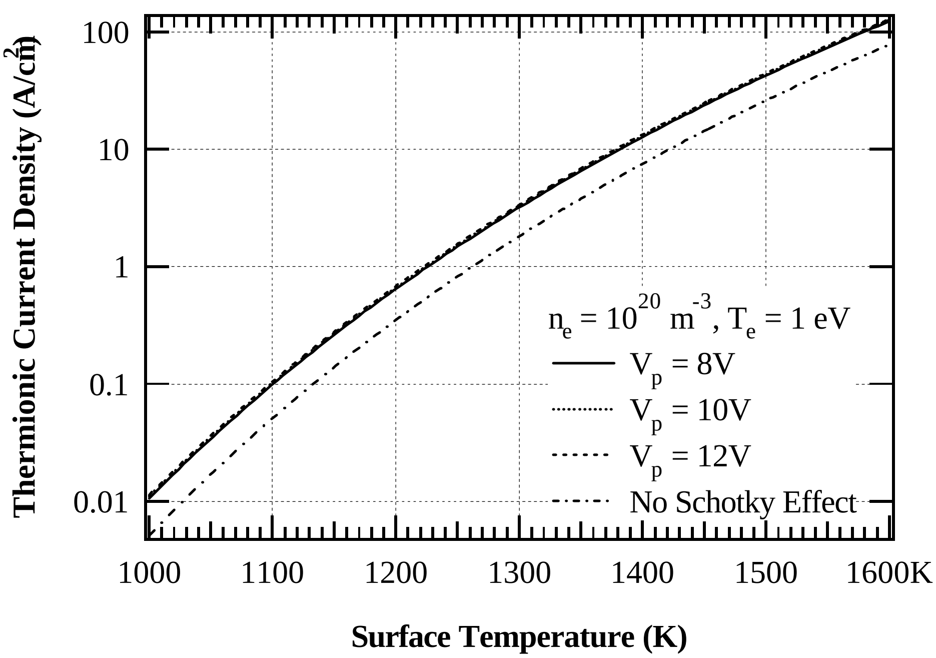

Figure 4.3 - Dependence of the Thermionic Emission Current Density on the Plasma Potential Based on Double Sheath Analysis. Material Work Function = 2.0-eV.

The ion current collected at the cathode surfaces includes the ion flux in the orifice and insert regions. Ion backstreaming to the insert region is also calculated using the Bohm criterion, and these ions are assumed to recombine on the cathode surface in the insert region. Additionally, the plasma ions, generated in the insert region, also contribute to the ion current. In the context of the control volume approximation, ions enter the cathode sheath at the Bohm velocity and diffuse upstream at the thermal velocity. Ions diffusing upstream were also assumed to recombine on the cathode surface. In actuality, some ions are collected on the external cathode surfaces. The ion current to the external cathode surfaces is assumed to be negligible due to the reduced density in this region. Based on the results presented in Chapter 3, the external ion current was on the order of a few 10^{-2} A, or about one percent of the total.

Ion emission and electron backstreaming are both small terms, however they are included for completeness. Electron backstreaming to the insert surface is described using Equation (4.29)

$$I_{e,back} = \frac{1}{4} n_e \overline{v}_e e A_{eff} e^{-\frac{eV_p}{kT_e}} \tag{4.29}$$

which is on the order of a few milliamperes typically. The effective surface area for electron collection, A_{eff}, includes both the effective emission region of the insert and the orifice plate surface. Diffusion of electrons upstream of the insert control volume is neglected based on the assumption that the axial electric field overwhelms the tendency of the electrons to diffuse in that direction.

4.2.2 Ion Conservation

This species specific form of conservation of mass is essentially the same as that used in the orifice mode, Equation (4.1). The primary difference is the consideration of two electron populations: one a low-temperature beam from the thermionic emission through a double sheath, and the other the Maxwellian plasma electrons. The contribution of the plasma electrons to the creation of ions and excited atoms is exactly that prescribed by Equations (4.2) and (4.19) using the insert effective volume.

The electrons emitted from the insert are referred to here as the primary electrons. The primary electron speed distribution function is approximated as

$$f\left(v_e\right) = 4p\left(\frac{m_e}{2p\, kT_{ins}}\right)^{\frac{3}{2}} v_e^2 e^{-\frac{m_e\left(v_e - v_d\right)^2}{2kT_{ins}}} \tag{4.30}$$

where v_d is the electron drift velocity induced by the sheath voltage, and the temperature of the primary electron beam is assumed to be the insert temperature. Since the primary electrons were created at the insert, excitation and ionization collisions deplete the population with increasing distance from the insert. The mean free path for either of these collisions is calculated as shown in Equation (4.31)

$$\begin{aligned} l &= \frac{1}{ns} \\ &= \left[n4p\left(\frac{m_e}{2p\, kT_e}\right)^{\frac{3}{2}} \int_0^\infty dv_e v_e^3 s\left(v_e\right) e^{-\frac{m_e\left(v_e - v_b\right)^2}{2kT_e}} \right]^{-1} \left\langle v_e \right\rangle \end{aligned} \tag{4.31}$$

where the number density is that of the target. Evaluation of Equation (4.31) for the electron-impact excitation cross-section and the electron-impact ionization cross-section indicates that the mean free path for the ionization interaction is at least 10 times greater than for excitation. For simplicity, a planar geometry is used to approximate the primary electron number density at the mean free path for electron-impact ionization.

$$n_{e,pr}\left(r_o - l_{ion}\right) = n_{e,pr}\left(r_o\right)\left[1 - erf\left(\frac{l_{ion}}{l_{ex}}\right)\right] \qquad \textbf{(4.32)}$$

For $l_{ion} \gg l_{ex}$, the contribution of electron-impact ionization by the primary electrons is negligible. Consequently the only mechanisms considered for ion creation are electron-impact ionization by plasma electrons, and step-wise excitation by the primary electrons, leading to ionization. The latter phenomenon is considered without a rigorous derivation of the contribution of this term. To evaluate the contribution, a fixed percentage of the excitation collisions are assumed to create ions. The resulting expression describing the ion production in the insert region is

$$\begin{aligned}\left(\frac{dn_i}{dt}\right)_{ionization} &= \left(p\, r_i^2 L_{eff}\right)\left(\left(\frac{m_e}{2p\, kT_e}\right)^{3/2} 4p\, n_e n_o \int_0^\infty dv_e v_e^3 s_{ion}\left(v_e\right) e^{-\frac{mv_e^2}{2kT_e}}\right) \\ &+ f_{ex}\left[p\left(r_i^2 - \left(r_i - 2\,l_{ex}\right)^2\right) L_{eff}\right]\left(\frac{m_e}{2p\, kT_{ins}}\right)^{3/2} \\ &\times 4p\, n_{e,pr}\left(n_o - n_e\right)\int_0^\infty dv_e v_e^3 s_{ex}\left(v_e\right) e^{-\frac{mv_e^2}{2kT_{ins}}}.\end{aligned} \qquad \textbf{(4.33)}$$

The percentage of excitation collisions which create ions f_{ex} is one of the free parameters in the insert model, and was expected to be a few percent at most. The effective volume for the excitation of neutrals is limited to two mean free paths from the insert. This adjustment accounts for the depletion of primary electrons beyond this distance from the insert. This picture of the ionization processes in the insert is considered simplistic, but the approximations are expected to yield meaningful results.

Ion creation by collisions of electrons with neutrals and ion in-flux from the orifice are balanced by ion convection across the control-volume boundaries. Plasma ions enter the cathode sheaths at the insert radius and at the orifice plate with a flux determined by the Bohm condition. Ion loss from the control volume is also calculated by the thermal flux to the upstream boundary. The various fluxes calculated in this section are also useful in determining the conservation of energy within the orifice.

4.2.3 Conservation of Energy

The conservation of energy in the insert region is written for the plasma as a whole. Energy enters or is released in the control volume by electron convection from the insert, ion convection from the orifice region, and Ohmic heating. The energy convected with the thermionic electrons is

$$q_{thm} = I_{e,thm}\left(V_f + \frac{3kT_{ins}}{2e}\right) \quad \textbf{(4.34)}$$

where the fall voltage, V_f, is approximated by the plasma potential. The energy convected with the orifice ions is

$$q_{i,ori} = \left(0.61 n_e c_i e\pi r_o^2\right)_{ori}\left(V_{ds} + \frac{2kT_i}{e}\right) \quad \textbf{(4.35)}$$

where the average thermal energy of the ion flux to the upstream orifice boundary is $2kT_i$ because the energy transport favors the high-energy particles.[81] The voltage drop across the double sheath at the boundary between the insert and orifice regions, V_{ds}, was estimated by Capacci, et al.[27] to be

$$V_{ds} = \left(\frac{9 I_D kT_e}{7.5 A_o n_e e^2}\sqrt{\frac{m_e}{2e}}\right)^{2/3}. \quad \textbf{(4.36)}$$

Ohmic heating is calculated in a similar manner as described for the orifice. The plasma resistivity is determined assuming uniform density and temperature. The electron current to the orifice calculated from Equation (4.5) is used for the Ohmic heating calculation. Since the current is carried mostly in the radial direction, an average cross-sectional area for current conduction is used. The resulting expression for the Ohmic heating is

$$q_{Ohmic} = I_{e,ins}^2 \eta \frac{r_i}{4/3\, r_i L_{eff}}. \quad \textbf{(4.37)}$$

The energy loss mechanisms from the insert region are ion loss, excitation collisions, electron convection of the current, and electron backstreaming to the insert. The ion loss term is calculated based on the ion flux to the boundaries of the control volume.

$$\begin{aligned} q_{i,loss} = &\left[0.61 n_e c_i e\left(2\pi r_i L_{eff} + \pi\left(r_i^2 - r_o^2\right)\right) + \frac{1}{4} n_e \bar{v}_i e\right] \\ &\times\left(\phi_i + \frac{2kT_i}{e}\right) \end{aligned} \quad \textbf{(4.38)}$$

The energy lost in excitation collisions is calculated as the product of the rate of excited neutral production and the average excitation energy.

$$\begin{aligned} q_{ex} &= \left(\frac{dn_{excited}}{dt}\right) eU_{ex} \\ &= \left[n_e\left(n_o - n_e\right)\left\langle v_e \sigma_{ex}\right\rangle_p \left(2\pi r_o L_{eff}\right) + n_{e,pr}\left(n_o - n_e\right)\left\langle v_e \sigma_{ex}\right\rangle_{pr}\right] eU_{ex} \end{aligned} \quad \textbf{(4.39)}$$

where the average excitation energy U_{ex} is another free parameter. The value of U_{ex} is somewhat lower than in the orifice because the energy lost by electrons in secondary excitation collisions, which play an important role in ionization in the insert region, is less than 4-eV, thereby reducing the average energy compared to the case where only ground-state excitation occurs. For most of the results presented, U_{ex} is set equal to 5-eV, and a sensitivity analysis was conducted. The energy lost by electron conduction of the current is

$$q_{e,con} = \frac{I_{e,ins}}{e} 2kT_e \qquad \textbf{(4.40)}$$

where T_e is the Maxwellian electron temperature in the insert region. The insert electron temperature calculated from this model could be used as an input for the orifice model. Since the orifice model is relatively insensitive to this parameter, an average value of the insert temperature is used to expedite the solution. Finally, the electron backstreaming component of the energy equation is

$$q_{e,back} = \frac{I_{e,back}}{e} 2kT_e \qquad \textbf{(4.41)}$$

The solution method for the insert model is essentially the same as for the orifice model. Ion continuity is satisfied by varying the electron temperature. Conservation of energy is achieved by solving for the electron number density, and the insert temperature is varied to achieve current continuity. Both the orifice and insert models were run with inputs matching those for the experimental set-up, and the results are discussed in the next section.

4.3 Model Predictions

The inputs for the orifice and insert models are the current, flow-rate, cathode material, and cathode geometry. By using the same inputs available to an experimental investigation, the results of the model are directly comparable to the experimental data. In this investigation, the AR6 geometry was input to the orifice and insert models, and the flow-rate and current were varied over the range tested experimentally. Additionally, the models were also used to evaluate the effects of geometry and material changes for low-current cathodes. While the standard operating procedure for the models was to vary only the parameters controllable in an experimental situation, several free parameters remained. The model was evaluated to test the sensitivity of the various solutions to the free parameters.

4.3.1 Sensitivity of the Orifice Results to the Free Parameters

The orifice model neglects the creation of ions by step-wise excitation, and the calculated Knudsen numbers for this type of collision indicate that this phenomenon occurs infrequently. Nevertheless, the effects of a fixed percentage of the excitation collisions creating ions were evaluated, and the results are plotted in Figure 4.4. The number density shows the largest change, monotonically increasing with f_{ex}. In terms of a figure of merit for cathode optimization, the Ohmic heating and excitation energy loss both scaled with nearly a ten percent reduction for every five percent increase in f_{ex}. Since the Knudsen numbers suggested that step-wise ionization was the exception in the orifice, f_{ex} was set to zero for subsequent calculations.

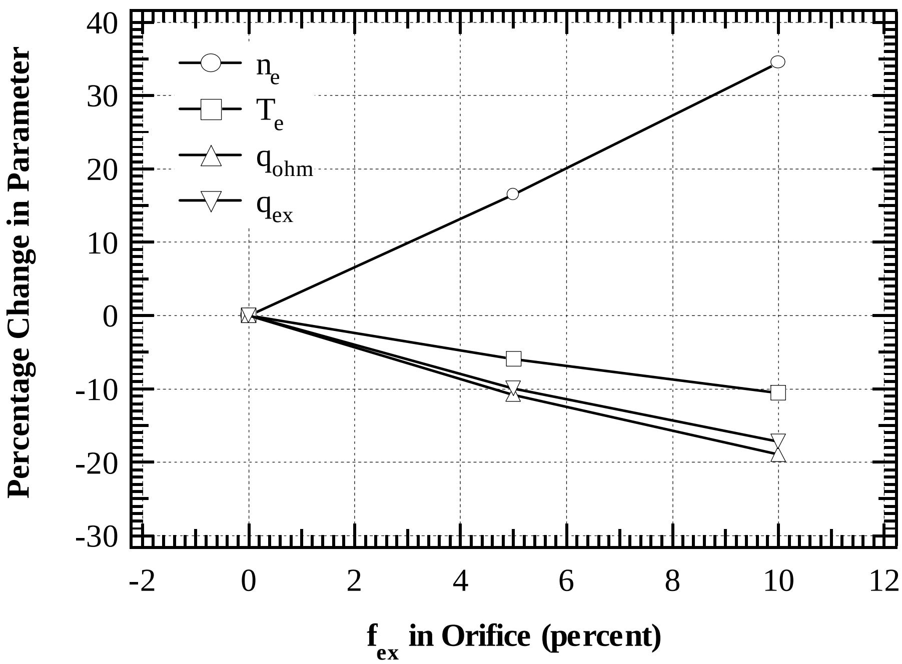

Figure 4.4 - Relative Dependency of Orifice Plasma Properties on the Fraction of Excitation Collisions Contributing to Ionization. AR6 Geometry at 0.50-A and 0.9-sccm.

The average excitation energy is also considered a free parameter since the distribution of the excitation transitions was unknown. Excitation from the ground state in xenon costs between 8.44 and 10.40-eV.[74] If this event dominates the excitation collisions, then the average excitation energy is on the order of 10-eV. While the preceding paragraph discounted the contribution of step-wise excitation in the orifice, the effect of reducing the average excitation energy was evaluated to examine the potential consequences of this simplification, and the results are shown in Figure 4.5. The most sensitive parameters are the number density and the power consumption. The power consumption was expected to scale with the excitation energy. The number density increases as the excitation energy decreased, ensuring that the convective power terms account for the difference between the Ohmic heating and the excitation loss. The previous discussion concerning the orifice Knudsen number for excitation supports the conclusion that ground state excitations dominate, and the average excitation energy was set to 10-eV for all subsequent calculations.

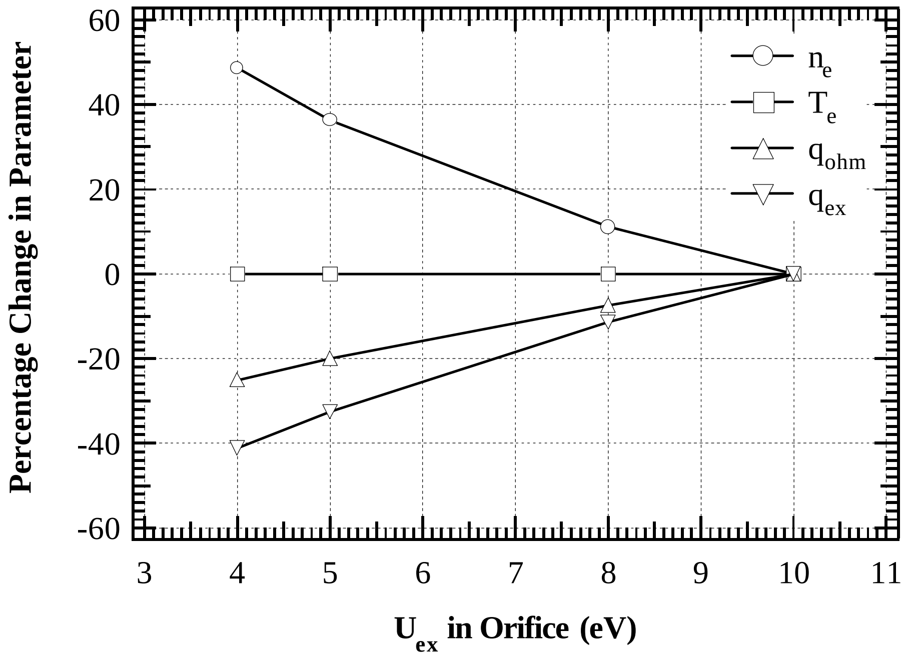

Figure 4.5 - Relative Dependency of the Orifice Region Plasma Properties on the Average Excitation Energy. AR6 Geometry at 0.5-A and 0.9-sccm.

4.3.2 Sensitivity of the Insert Results to the Free Parameters

By contrast, the excitation processes in the insert region are essential to plasma generation. The primary electrons undergo excitation collisions almost exclusively. Figure 4.6 depicts the sensitivity of insert region plasma parameters and power consumption to the value of f_{ex} in the insert region. Electron convective power consumption decreases by ten percent for an increase of two percent to f_{ex}, while the number density increases by twenty percent over the same interval. Although the number of excitation events possible in xenon argue that only a small fraction create ions, an ionization model is needed to rigorously determine the value of f_{ex}. The fraction of excitations creating ions was set to 0.05 for all subsequent calculations, since the results agreed well with the experimental data.

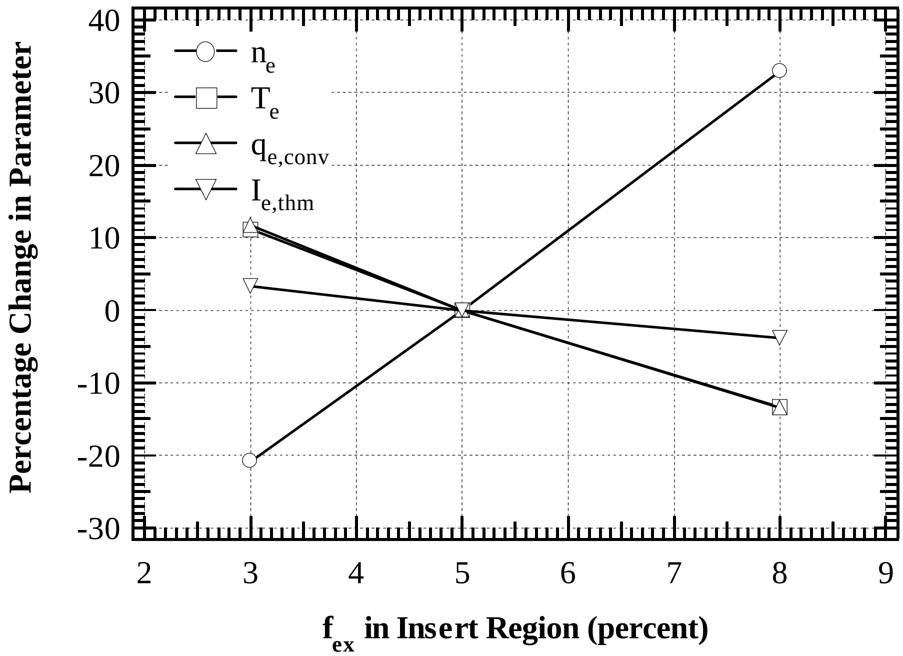

Figure 4.6 - Dependency of the Insert Region Plasma Properties on the Fraction of Excitation Collisions Contributing to Ionization. AR6 Geometry at 0.50-A and 0.9-sccm.

As important as the value of f_{ex} is to the solution of the insert region parameters, the average excitation energy in the insert region influences the solution to a greater degree. Figure 4.7 depicts the sensitivity of the plasma properties and energy terms in the insert region to changes in the average excitation energy. While the plasma properties and energy terms are highly sensitive to U_{ex}, the preponderance of the secondary excitations in the insert region is expected to reduce the average excitation energy compared with the ground-state value used in the orifice calculations. Over the range from 3 to 8-eV, the change in power consumption by excitations scales with U_{ex}. The number density is highly sensitive to the average excitation energy in the insert region, changing by about ten percent per electron-Volt. Since many of the possible transitions between excited states in neutral xenon involve less than 1-eV,[74] the lack of detailed accounting of the population of the excited states makes the value chosen for U_{ex} somewhat arbitrary, although it should be weighted for the ground-state transitions which enable secondary excitations. The average excitation energy was set to 5-eV in lieu of a more rigorous evaluation. This number accounts for electron collisions with excited states while a lower number requires that the plasma approach optically thick conditions. The experimental data indicated that the insert region plasma was far from optically thick conditions.

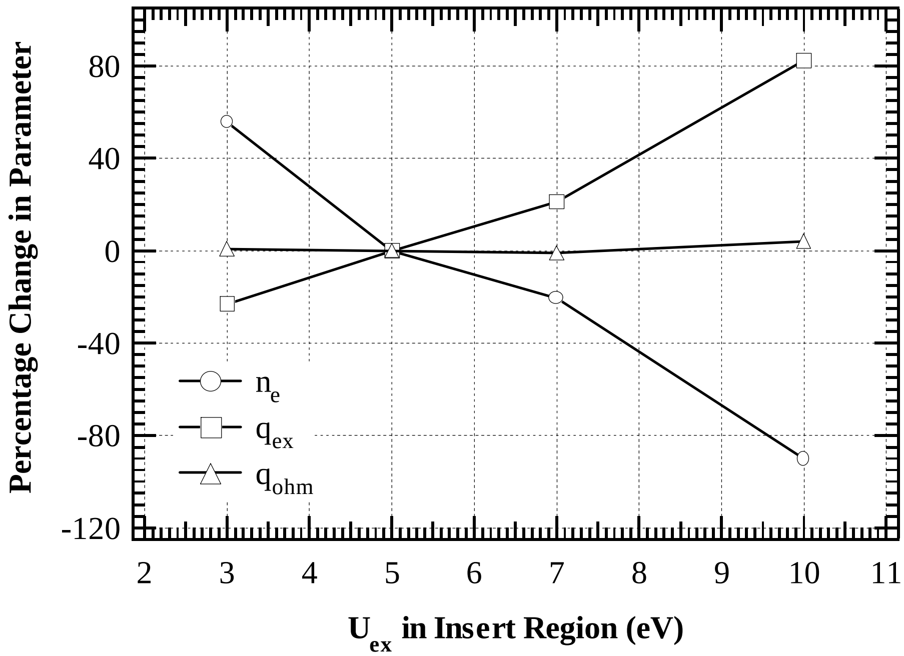

Figure 4.7 - Dependency of the Insert Region Plasma Properties on the Average Excitation Energy. AR6 Geometry at 0.50-A and 0.9-sccm.

The plasma potential is a free parameter in the insert model, although experimental data put bounds on the value chosen. Furthermore, the sharp axial gradient in the plasma potential made the choice of a volume-averaged value perilous. The plasma potential was varied from 7 to 12-eV to obtain the data in Figure 4.8. Again the number density is highly sensitive to this parameter as is the convected energy from the thermionic emission current. The latter finding is expected since the reduction in the work function by the Schotky effect scales with number density. While the insert region plasma potential near the insert was as high as 12-V, a value of 8-V was used for subsequent calculations both in consideration of the volume averaged value and because large values for V_p degraded the stability of the model.

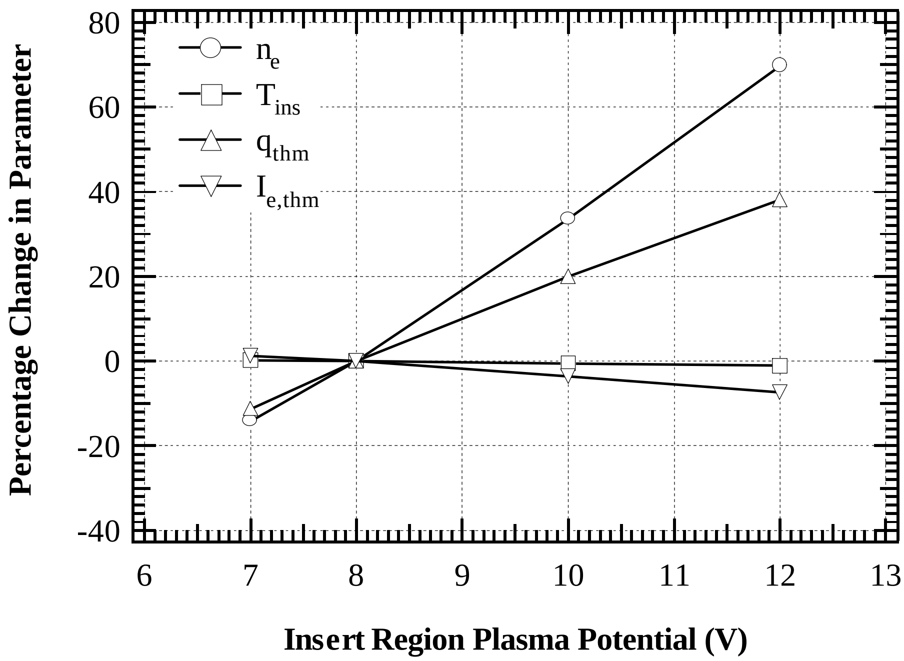

Figure 4.8 - Dependency of the Insert Region Plasma Parameters on the Plasma Potential. AR6 Geometry at 0.50-A and 0.9-sccm.

The final free parameter considered here is the material work function of the insert. While the available data confine the work function to between 2.0 and 2.1-eV, this range strongly affects the requisite cathode operating temperature as shown in Figure 4.9. A change of 0.1-eV in the work function leads to more than a 50-K increase in the insert temperature. It should be noted that in a real system, the plasma potential depends upon the material work function, and the variation of either of these parameters independently is artificial. A value of 2.00-eV was chosen for subsequent calculations primarily due to an apparent over-prediction of power consumption; a low-work function reduces the power consumption gap at high flow-rates.

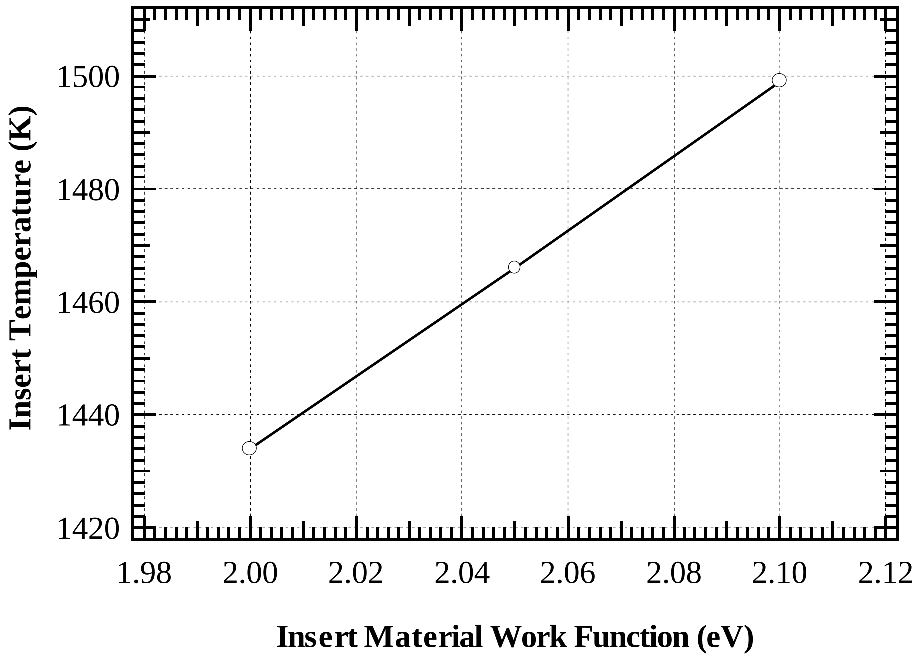

Figure 4.9 - The Effect of the Material Work Function on the Predicted Insert Temperature for AR6 at 0.50-A, and 0.9 sccm.

4.3.3 Low-Current Predictions for Various Conditions and Geometries

The values of the free parameters are listed in Table 4.1, as is the matrix of operating conditions and geometries evaluated using the orifice and insert models. The AR6 geometry is used as the baseline condition. In each test, the flow-rate is varied over its full range. The effect of the discharge current on the predicted cathode operating conditions was examined for consistency with the experiments. The orifice diameter is varied for two different orifice lengths. The shorter orifice accommodates the AR3´ geometry. The orifice length is altered to provide data on aspect-ratios from 1 to 6. Finally the sensitivity of the insert plasma properties to the inner diameter of the insert was examined. The results of these numerical experiments are presented below.

Table 4.1 - Test Matrix for the Orifice and Insert Models

Test	$\dot{m}$ *(sccm)*	I_D *(A)*	d_o *(mm)*	l_o *(mm)*	$d_{i,i}$ *(mm)*
Current	0.6 to 2.4	0.50 to 1.25	0.127	0.71	1.2
d_o Test 1	0.6 to 2.4	0.50	0.08 to 0.25	0.25	1.2
d_o Test 2	0.6 to 2.4	0.50	0.13 to 0.25	0.71	1.2
l_o	0.6 to 2.4	0.50	0.13	0.13 to 0.71	1.2
$d_{i,i}$	0.6 to 2.4	0.50	0.13	0.71	0.8 to 2.0

Free Parameters	f_{ex} *(orifice)*	U_{ex} *(orifice)*	f_{ex} *(insert)*	U_{ex} *(insert)*	V_p *(insert)*	ϕ *(insert)*
Value	0.0	10.0-eV	0.05	5.0-eV	8.0-V	2.00-eV

4.3.2.1 Results of the Orifice Model

Figure 4.10 depicts the results of the calculations varying the discharge current. The lack of experimental data in the orifice region dictates that the results are compared only with the overall experimentally observed performance trends. The electron number densities are greater than those determined experimentally both upstream and downstream of the orifice plate. This result is consistent with the expectation of a maximum current density in the orifice. Further, the number density increases with both current and flow-rate. The dependency of number density on both of these parameters is consistent with experimental data downstream of the orifice plate. The electron temperature by contrast is insensitive to current and only varies with flow-rate. For spot-mode operation, the experimentally determined electron temperature downstream of the orifice was also found to be insensitive to current. The magnitude of the electron temperature is larger than expected based on the experimental data. The requirement that the tail of a Maxwellian electron population create the ions in the orifice drives the solution toward high electron temperature. The Druyvesteyn distributions observed both upstream and downstream of the orifice contained a larger fraction of the electrons at the energies of interest for ionization than a Maxwellian with the same average energy. Consideration of a Druyvesteyn distribution function may bridge the gap between the theory and the experiment. Also of note in Figure 4.10 are the power generated by Ohmic heating and the power lost through excitation. Excitation power losses represent the largest fraction of the loss terms in all cases. In some cases, the predictions of power consumption exceed the experimentally determined discharge power of the cathode. This non-physical solution had several possible contributing factors, including the use of a Maxwellian electron population, the neglect of excitation-based ionization, and the value assumed for the average excitation energy. Both the ionization and excitation rates were dependent upon the electron temperature, and an over-prediction of the electron temperature leads to excessive power consumption. Finally, the electron emission current is predicted to scale with current and flow-rate in nearly the same manner as the electron number density. This finding is a result of the proportionality of the emitted ion current to the orifice electron number density. The emitted electron current also scales more strongly with the discharge current, in agreement with the findings shown in Figure 3.18 (page 55). These results show that the orifice model accurately predicts the trends expected with flow-rate and current, while the electron temperature and the power consumption are slightly higher than expected.

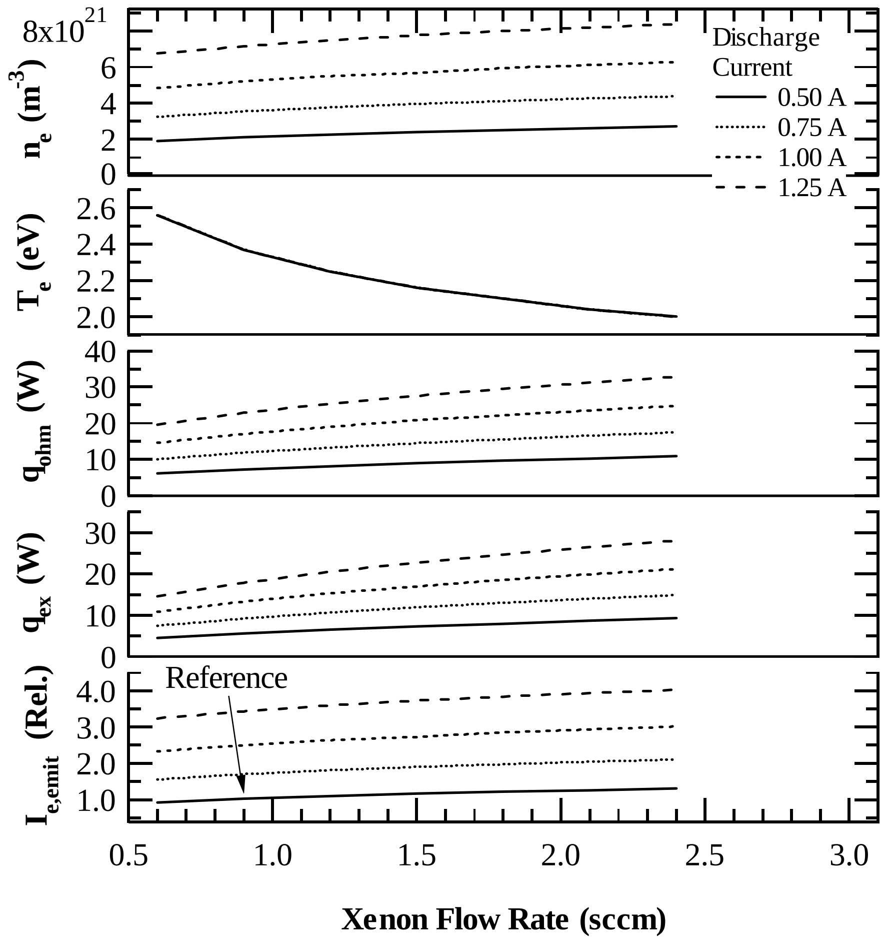

Figure 4.10 - Variation of Plasma and Control Volume Properties within the Orifice as Functions Discharge Current And Flow-rate. AR6 Geometry.

The dependency of the orifice plasma properties on the orifice diameter is depicted in Figure 4.11. The density scales inversely with the orifice diameter, while the electron temperature increases with the diameter. The neutral number density decreases with increasing orifice diameter, according to Equation (4.3). The ionization rate is directly proportional to the neutral number density, while the ion loss rate is dependent only on the electron temperature and number density. The reduction in neutral number density with increasing orifice diameter is responsible for both the decrease in the electron number density and the increase in the electron temperature, through the ion continuity condition. The power consumption terms are equally sensitive to orifice length and diameter. Both the Ohmic heating and excitation terms are strongly dependent upon both electron and neutral number densities, and the relation is seen in Figure 4.11. The power consumption in the orifice increases with orifice length as expected. The plasma resistivity is relatively insensitive to the orifice length, and the Ohmic heating term scales strongly with orifice length. Similarly, the excitation energy loss term also increases; the addition of orifice length enabled more ionization collisions to occur. The emission current again follows the electron number density, with electron emission increasing with diminishing orifice diameter.

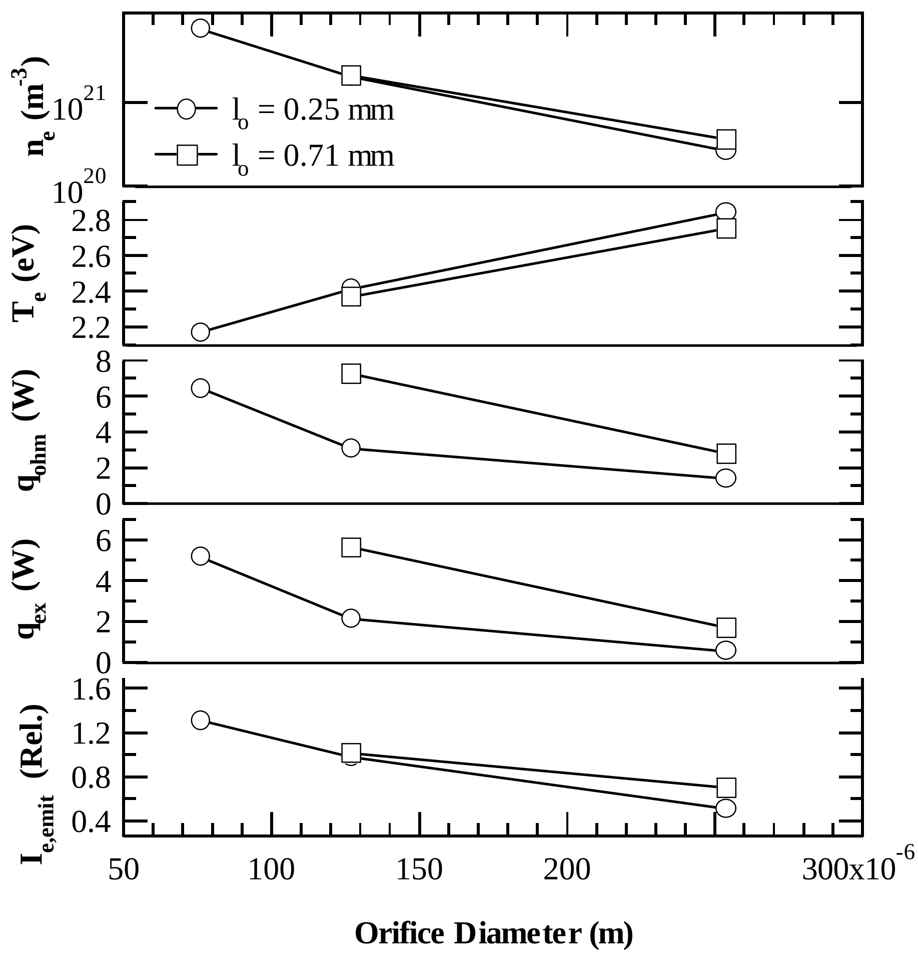

Figure 4.11 - Variation of Orifice Model Calculated Properties as a Function of Orifice Diameter and Length. I_D = 0.50-A at 0.9 sccm with $d_{i,i}$ = 1.2-mm.

The results of varying the orifice length are plotted in Figure 4.12. The number density becomes nearly invariant with increasing orifice length at three times the orifice diameter, while the electron temperature still exhibits a modest decline. Increases in orifice length are met with corresponding rises in ionization and excitation collisions. As the orifice length is increased beyond three times the diameter, the loss of ions to the walls of the orifice scale with orifice length in nearly the same proportion as the ionization rate, resulting in little change in either electron temperature or number density. Conversely, the additional collisions predicted by the increasing orifice length meant that power consumption scaled linearly with orifice length. The design tolerance for the orifice diameter was 1 x 10^{-5} m, which according to Figure 4.11 results in a variance in the Ohmic power term on the order of 1-W. The experimental findings showed little difference in the power consumption between AR6 and AR3 (Figure 3.16, page 53), which was partially explained by the design tolerance in the orifice. Nevertheless, Figure 4.12 also argues for limitation of the orifice aspect-ratio to three; increasing values for the orifice aspect-ratio yield no additional emitted electron current while power consumption is increased.

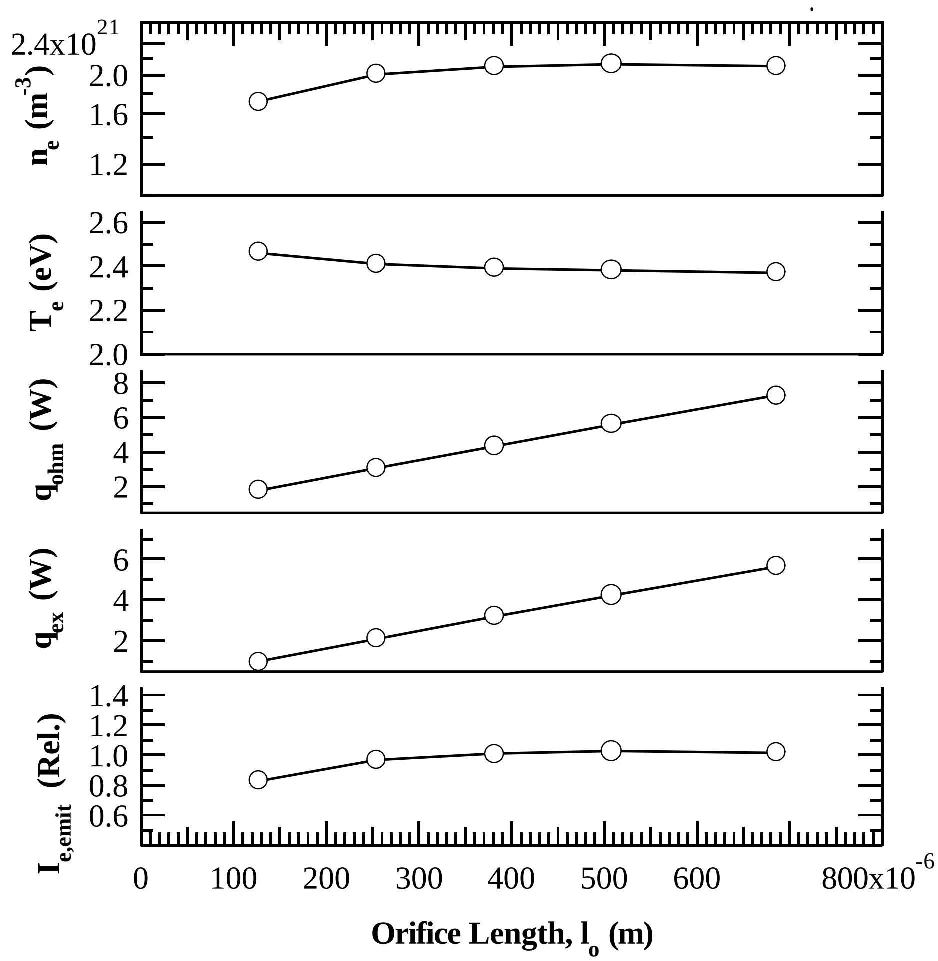

Figure 4.12 - Variation of Orifice Model Calculated Properties as a Function of the Orifice Length. AR6 Geometry at 0.50-A and 0.9 sccm.

4.3.2.2 Results of the Insert Model

The results of the insert model are plotted in Figure 4.13 for several discharge currents and flow-rates. The density and temperature follow trends similar to those in the orifice, with reduced sensitivity. Both the electron temperature and number density agree with the experimental data. The electron temperature results also display a degree of instability in the numerical solution. The predicted insert temperature and emitted thermionic current are more dependent upon current than flow-rate.

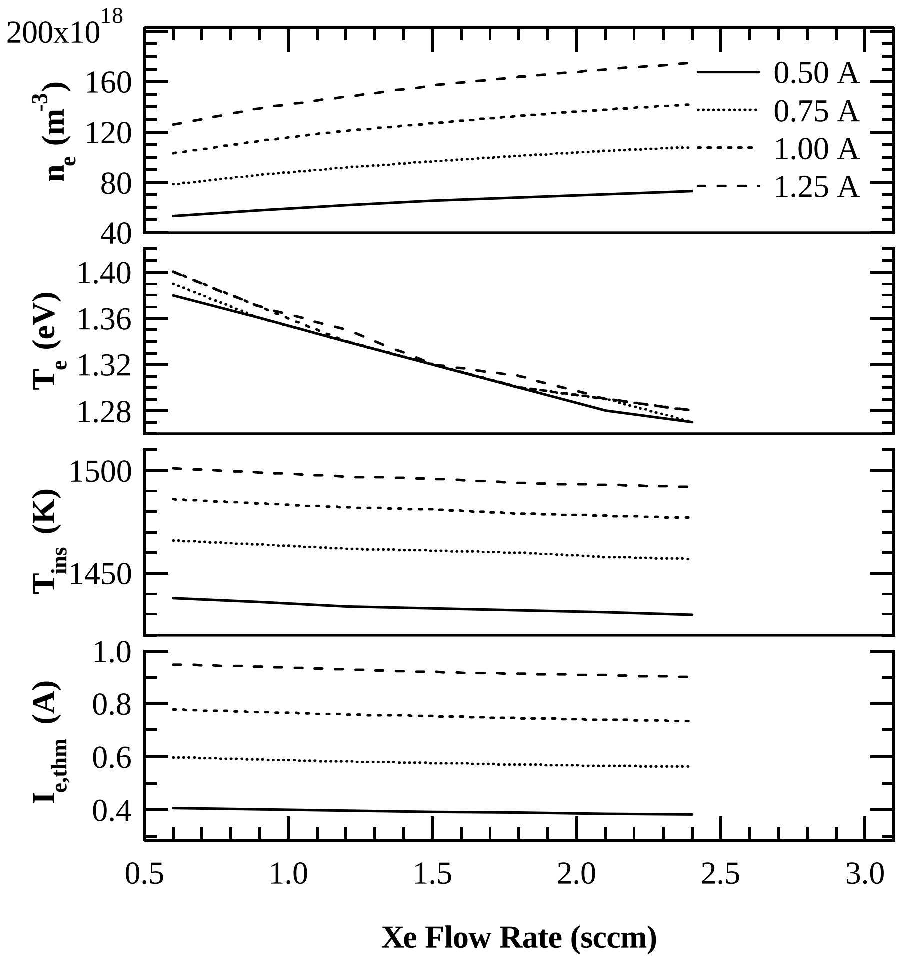

Figure 4.13 - Insert Model Calculated Plasma and Control Volume Properties as Functions of Both Current and Flow-rate. AR6 Geometry.

The insert power consumption and thermionic current are dependent upon the orifice diameter through the current continuity requirement. Figure 4.14 depicts the variation of insert plasma conditions with orifice diameter. For the large orifice diameter, the insert electron temperature decreases significantly with diminishing orifice length. The convected thermionic electron power term is highly dependent not only on orifice diameter, but also the length. The thermionic current is expected to decrease as the length of the orifice increased due to the collected ion current. Recalling Figure 4.11, the electron number density in the orifice decreases sharply as the diameter is increased. The ion current to the orifice walls is proportional to the number density. Consequently the increased orifice diameter reduces the ion current, and the thermionic current is required to maintain current continuity. This finding also implies that to minimize power consumption in the insert region, the orifice diameter should be as small as possible for a given application.

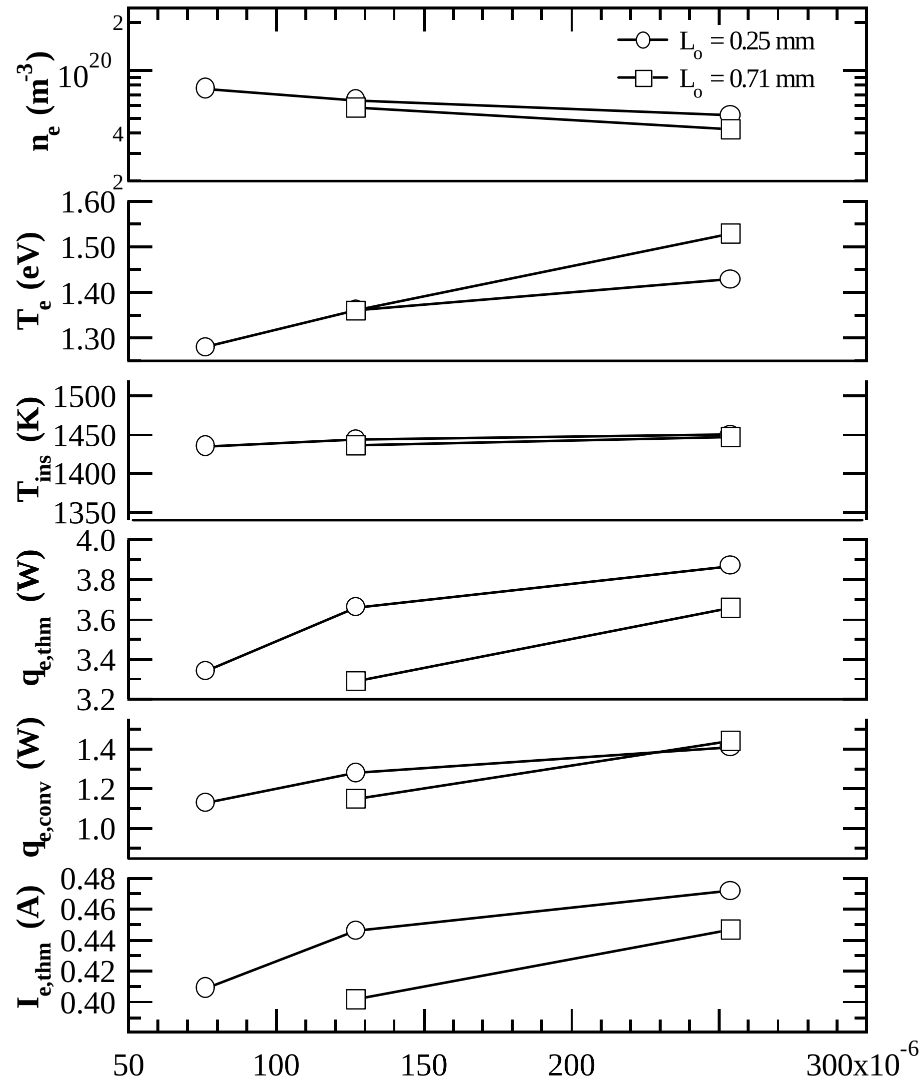

Figure 4.14 - Variation of Insert Region Properties with Orifice Diameter. I_D = 0.50-A at 0.9 sccm and $d_{i,i}$ = 1.2-mm.

The formulation of the orifice and insert models is such that variation of the insert inner diameter did not alter the results from the orifice model, and the influence of the insert inner diameter on the plasma properties is presented in Figure 4.15. The most significant dependencies are that of the number density and the insert temperature. The number density is expected to rise as the insert inner diameter decreased out of necessity to provide a sufficient plasma for current conduction. The electron convection term, proportional to the electron temperature, is only slightly higher for the small diameter insert than the large insert diameter. The effective emission length is set to half of the insert diameter. Consequently, the power density increased greatly for the small insert diameter. While the power convected into the control volume by the thermionic electrons is a weak function of the insert diameter, the reduced power density enables electron emission at decreasing insert temperatures. The result is that the heat conducted and radiated away from the insert is reduced with increasing insert diameter, and efficiency is increased.

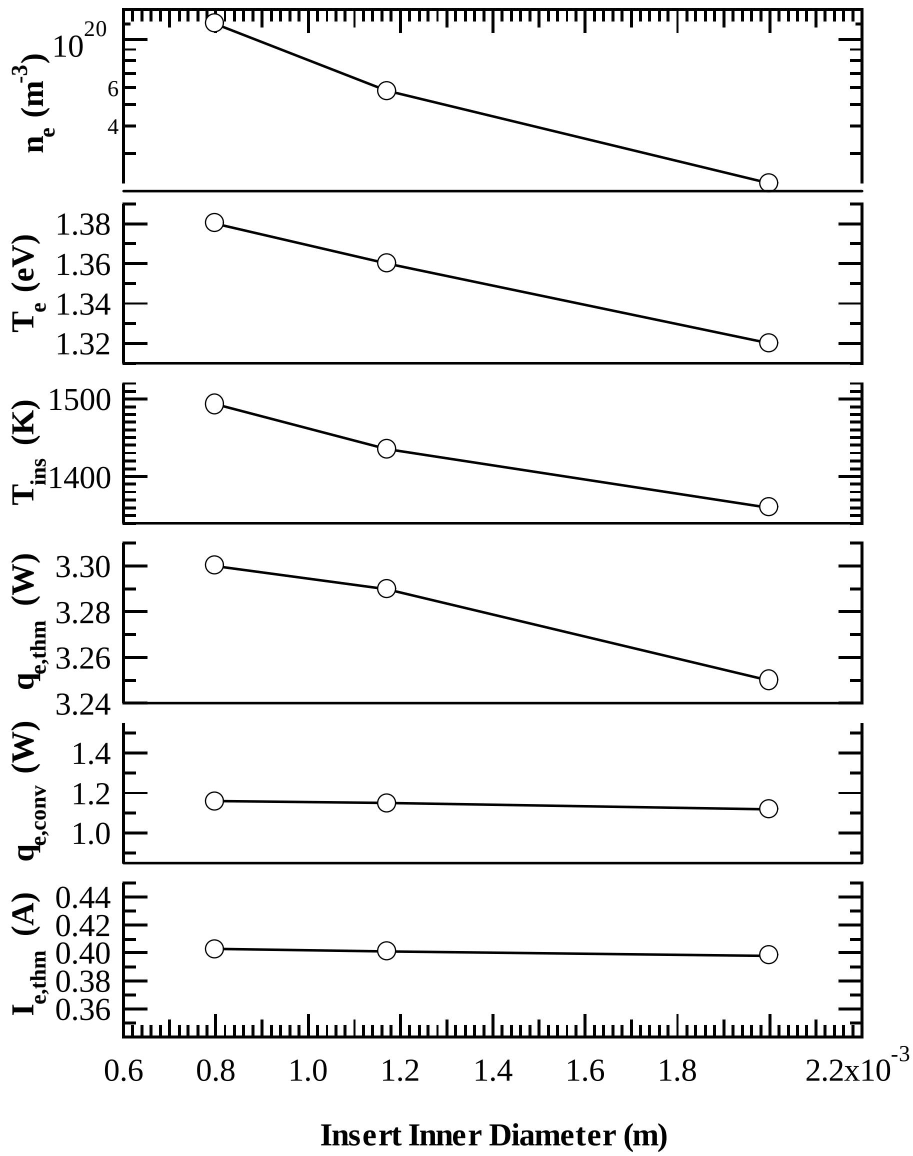

Figure 4.15 - Dependency of Insert Region Properties on the Insert Inner Diameter.

4.3.4 Discussion of Implications for Low-Current Hollow Cathode Performance

The findings from the orifice and insert models indicate some trends and limitations to consider in the design of low-current hollow cathodes. In terms of the orifice, the diameter should be as small as necessary to carry the current based on the Kaufman criterion. The orifice aspect-ratio should be kept less than three as further increases yield no additional electron emission, and power consumption increases with length. The efficiency of the insert region also favored a minimized orifice diameter. It should be noted that this finding was in agreement with Salhi and Turchi.[45] The insert model also showed that ion collection in the orifice reduced the thermionic electron emission requirements for the insert, thereby reducing the power consumption. A trade-off must be struck between ion current collected in the orifice and thermionic electron current to determine the most efficient combination, and the orifice length can then be determined. Finally, maximizing the insert inner diameter was found to improve performance. This last suggestion cannot be taken to extremes in the absence of a thermal model. Cathode thermal mass and heat transfer from the cathode tip must also be considered when significant modifications to the design are proposed.

4.4 Discussion of a Recently Developed Cathode Thermal Model

Considering the axial temperature distributions presented in Chapter 3, calculation of the heat transfer in the cathode tube was considered to be advantageous. However, Van Noord[67] has developed a thermal model of the hollow cathode which considers more of the processes determining the cathode operating temperature than previous models.[27,38] The model was largely derived from the works by Siegel and Perlmutter,[75] and Siegel and Keshock.[76] The plasma parameters were estimated based on the data by Salhi.[26] Only classical gray body radiation was considered. The plasma radiation, both blackbody and Bremsstrahlung, were estimated and determined to be negligible. The heating terms for the orifice by the plasma were largely the reciprocal of the insert model conservation of energy terms. The model solved for a solution which ensured current continuity. The resulting model contained second order differential terms, fourth order temperature terms, and two integrations. Van Noord[67] solved the heat transfer equation by linearizing the radiation terms and using a finite difference method similar to that employed by Siegel and Keshock.[76] With the model, Van Noord was able to examine the roles of thermal conductivity, convection with the propellant, the emissivity, and the plasma heat deposition in determining the cathode temperature distribution. The findings of the work by Van Noord[67] provided sufficient closure to the question of designing thermally efficient cathodes.

Several of Van Noord's[67] conclusions directly concerned this investigation. In agreement with the findings of the experimental investigation, the heat transfer along the cathode length was conduction limited. This finding suggested that alternate materials should be considered, particularly for low-current hollow cathodes. As expected, the material work function strongly influenced cathode operating temperature. This finding was similar to that from Figure 4.9. Van Noord[67] also showed that the external emissivity dominates the radiative portion of the heat transfer. These findings were the most pertinent to the design of low current hollow cathodes.

4.5 Theoretical Treatment of Cathode Internal Pressure

The cathode pressures reported in Chapter 3, though high, were consistent with the values reported by Salhi[26] scaled by the ratio of the orifice areas. Under the assumptions made previously that the ions and neutrals were at the same temperature as the cathode, the predicted internal cathode pressure fell well short of the measured values. The cathode internal pressure was written as

$$p = n_o k T_o + n_i k T_i + n_e k T_e \qquad \textbf{(4.42)}$$

Based on typical values calculated for the orifice, the neutral, ion, and electron partial pressures were 2.57 kPa, 0.10 kPa, and 1.96 kPa, respectively. By contrast, the experimental total pressure for similar operating conditions was more than 40 kPa. The works by Siegfried[25] and by Capacci, et al.[27] avoided this issue by using an empirically derived pressure relation. A predictive model requires an expression for the pressure which limits the use of empirical relations. Salhi[26] introduced an expression based on isothermal flow in the cathode with a sonic condition at the exit of the orifice. In the present derivation, an effort was made to account for the pressure drop between the cathode interior and the sonic point at the orifice exit. The Reynolds numbers were below five for the cases expected in the 3.2-mm diameter cathodes, indicating laminar flow. Borderline Knudsen numbers were calculated for a flow-rate of 0.6 sccm, and the flow was more accurately described by continuum theory at higher flow-rates. Ferreira and Delcroix[5] derived a Poiseuille flow expression which used an empirically determined weight factor to address the degree of continuum flow. This approach was discarded due to both the empirical constant and the fact that the viscous solution supported a larger pressure gradient than the free-molecular result. The flow was modeled as continuum Poiseuille flow. The resulting equation for the pressure in insert region was

$$p_{in} = \left[\dot{m} \frac{128\mu}{\pi d_o^4} R_{sp} T \left(2x \right) + p_c^2 \right]^{0.5} + \frac{1}{2} \rho_o \bar{u}_o^2 \left(1 + K_L \right) \qquad \textbf{(4.43)}$$

where μ is the dynamic viscosity, x is the distance upstream, $\bar{u}_o$ is the bulk average gas velocity, K_L is a loss coefficient associated with the orifice entrance, and

$$p_c = \dot{m} R_{sp} T \frac{4}{\pi d_o^2} \sqrt{\frac{1}{\gamma R_{sp} T}} \qquad \textbf{(4.44)}$$

is the sonic condition at the orifice.

Equations (4.43) and (4.44) were used to model the pressure measured in the hollow cathode with a neutral flow, and the comparison is depicted in Figure 4.16 and Figure 4.17. Initially, the xenon temperature was equated with the observed orifice plate temperature at 298 and 1228-K. The agreement between the theory and the experiment was poor at 298-K, although the accuracy of the theory improved at 1228-K. The prediction for the latter case suggested that the gas temperature was greater than the orifice plate temperature. Physically this was reasonable considering that the interior of the hollow cathode acted like a blackbody enclosure, and the temperature interrogation point was external to the cathode, where radiative losses were important.

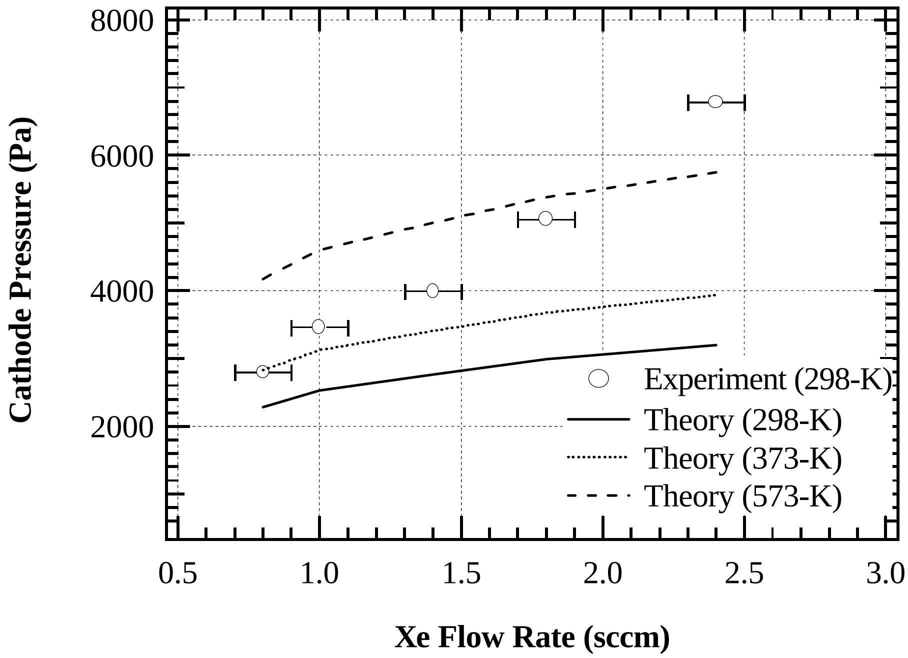

Figure 4.16 - Comparison of the Flow-rate Calculations With Experiments for Room Temperature Neutral Xe Flow for AR6.

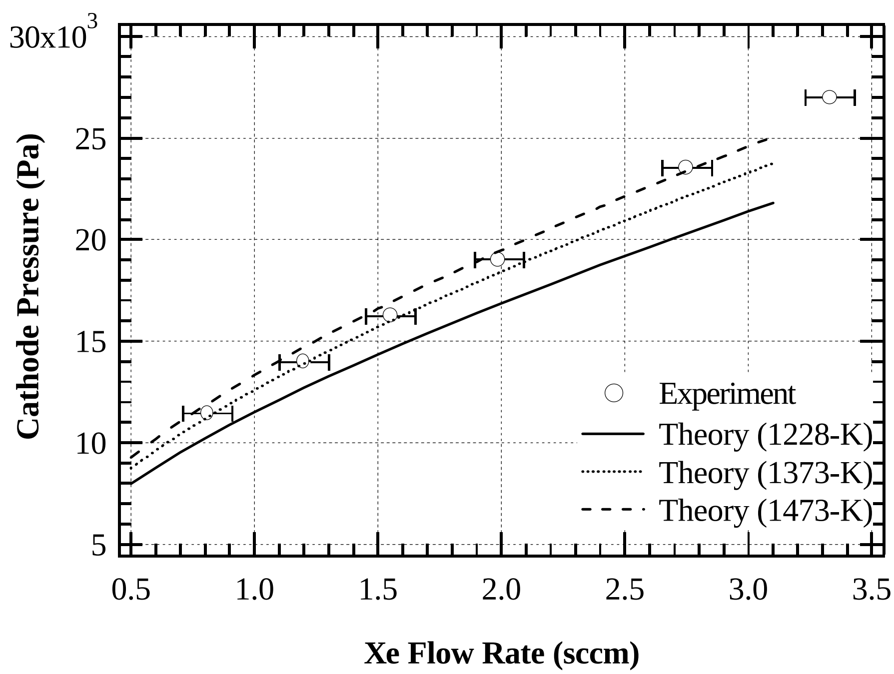

Figure 4.17 - Comparison of the Flow-rate Calculations With Experiments for 1228-K Neutral Xe Flow in AR6.

Examination of Figure 3.20 (page 57) and Figure 4.17 indicates that the theory developed here would require very-high heavy particle temperatures to match the pressures observed during the cathode discharge. By varying only the temperature in Equations (4.43) and (4.44), the data between 0.50 and 1.50-A were modeled adequately for gas temperatures ranging from 3300 to 6500-K, as listed in Table 4.2. While Williams, et al.[60] presented data indicating ion and neutral temperatures of several thousand Kelvin, the existence of high-temperature heavy particles has so far defied explanation.

Table 4.2 – Calculated Heavy Particle Temperature to Match Cathode Internal Pressure Data

Current (A)	*Heavy Particle Temperature (K)*
0.50	3300 ± 100
0.75	4800 ± 100
1.00	5700 ± 100
1.25	6200 ± 100
1.50	6500 ± 150

Several plasma related phenomena were evaluated to determine if they were responsible for either the elevated cathode internal pressure or the observed high-temperature heavy particles. Given the current density within the orifice, the pinch-effect was examined. Finally, a radial distribution of the heavy particle temperatures was calculated based on heat transfer with the electrons.

4.5.1 Current Density Induced Pinch Effect Pressure

The pinch effect in the orifice was estimated in order to determine whether it contributed significantly to the cathode internal pressure. The pressure generated by the pinch effect in the hollow cathode was approximated by Equation (4.45).[77]

$$p(r) = \frac{m j^2}{4}\left(r_o^2 - r^2\right) + p_o \qquad \textbf{(4.45)}$$

where p_o is the ambient pressure outside of the arc. The permeability of the plasma was approximated by that of free space, μ_o.[78] Using this substitution and calculating the maximum pressure, r = 0, the pinch effect was estimated to contribute on the order of 10-Pa for the operating conditions of the hollow cathode. Equation (4.45) was evaluated for a range of radii and currents to explore what radius was required for the pinch effect to account for the experimentally determined pressures. The results are shown in Figure 4.18, and they indicate that the pinch effect could account for the internal cathode pressure only if the arc were constricted to a few micrometers. The veracity of this hypothesis has yet to be proven experimentally. However, the gas temperature in the arc is related to the pressure by an equation of state, and this mechanism would explain the temperature measurements by Williams, et al.[60] Indeed, the ion and neutral temperatures were measured in the expansion downstream of the orifice, where one would expect the temperature to be less than in the orifice according to the equation of state.

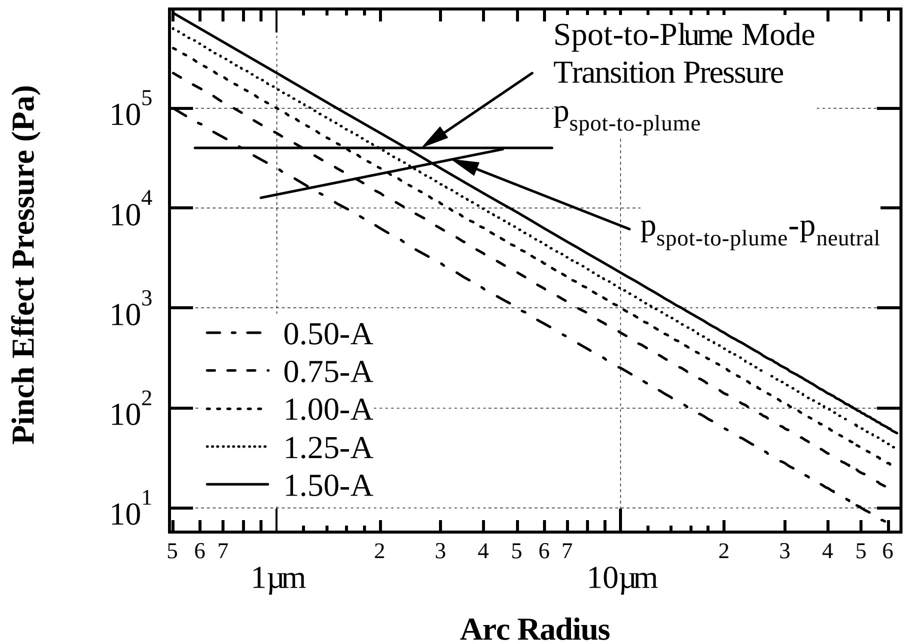

Figure 4.18 - Predicted Peak Pinch Effect Pressures as a Function of Arc Radius.

4.5.2 Radial Distribution of the Heavy Particle Temperatures

A model was developed to examine the radial distribution of heavy particle temperatures in the orifice of low-current hollow cathodes. The model considered the heat transfer between the electrons, ions, and neutrals in the orifice. While the energy equation was based on continuum assumptions, the conductivity used was derived from the mean free path method. Spitzer[79] reported a model for the equipartition in a two-temperature plasma, which Salhi[26] modified to predict the radial distribution of the ion temperature in the insert region. Salhi assumed that the neutrals equilibrated with the ions over length scales much shorter than the dimensions of the cathode. Rather than assuming that the neutrals equilibrated with the ions, the present derivation included ion-neutral energy transport in Equation (4.46).

$$\frac{1}{r}\frac{d}{dr}rk\,\frac{dT_i}{dr} = r\,c_p\,\frac{dT_i}{dt} \qquad \textbf{(4.46)}$$

The time derivative was defined according to Spitzer:[79]

$$\frac{dT_i}{dt} \approx \frac{T_i - T_e}{t_{eq}} \qquad \textbf{(4.47)}$$

where t_{eq} was the equipartition time. Spitzer[79] reported the convenient form of the equipartition time show below:

$$t_{eq} = 5.87 \frac{M_e M_i}{n_e Z_e^2 Z_i^2 \ln \Lambda} \left(\frac{T_e}{M_e} + \frac{T_i}{M_i} \right)^{3/2} \tag{4.48}$$

An approximately equivalent statement to Equations (4.47) and (4.48) was used to describe the transport of energy from the electrons to the neutrals, and is shown in Equation (4.49).[80]

$$r c_p \left. \frac{dT_n}{dt} \right|_{n-e} = \frac{2m_e}{m_n} \frac{3}{2} k \left(T_n - T_e \right) n_{n,e} n_n \tag{4.49}$$

where $\nu_{n,e}$ is an energy weighted momentum transfer collision frequency. Equation (4.49) was modified to describe the transport of energy from the ions to the neutrals.

$$r c_p \left. \frac{dT_n}{dt} \right|_{n-i} = 3k \left(T_n - T_i \right) n_{n,i} n_n \tag{4.50}$$

The collision frequencies were calculated from the generalized formula[81]

$$n_{a,b} = s_{ab} n_b \sqrt{\frac{8kT_a}{p\, m_a} + \frac{8kT_b}{p\, m_b}} \tag{4.51}$$

The energy balance for the ions contained a reciprocal statement to Equation (4.50). Finally, Equation (4.46) was rewritten in terms of both the ion and neutral temperatures, as shown in Equations (4.52)

$$\begin{aligned} \frac{1}{r} \frac{d}{dr} rk \frac{dT_i}{dr} &= r c_p \left[\frac{T_i - T_e}{t_{eq}} + 2 \left(T_i - T_n \right) n_{i,n} \right] \\ \frac{1}{r} \frac{d}{dr} rk \frac{dT_n}{dr} &= r c_p \left[\frac{2m_e}{m_n} \left(T_n - T_e \right) n_{n,e} + 2 \left(T_n - T_i \right) n_{n,i} \right] \end{aligned} \tag{4.52}$$

The thermal conductivity was calculated using the mean free path method,[81]

$$k = \frac{2k}{s} \sqrt{\frac{kT_{i,n}}{p\, m_{i,n}}} \tag{4.53}$$

and the density and specific heat were rewritten using the kinetic description[81]

$$r c_p = n_{e,n} m_i \left(\frac{3}{2} \frac{k}{m_i} \right) = \frac{3}{2} n_{e,n} k \tag{4.54}$$

Note that the conductivity is independent of density and depends only on the temperature, mass, and collision cross-section. The collision cross section used was that defined based on the hard sphere molecule assumption.[81]

$$s = \frac{2}{3} p d_m^2 \tag{4.55}$$

Equation (4.55) yielded a cross-section of 9.3 x 10^{-20} m^2.[82] The boundary conditions for Equations (4.52) were that the temperature at the orifice surface was equivalent to the wall temperature and that the radial temperature gradient was zero on the axis. These boundary conditions are expressed mathematically in Equations (4.56):

$$\begin{gathered} T\left(r = r_o\right) = T_{wall} \\ \left[\frac{dT_{i,n}}{dr}\right]_{r=0} = 0 \end{gathered} \tag{4.56}$$

Equations (4.52) were solved using a 4th order Runge-Kutta technique, and iteration toward a solution was necessary since the temperature distributions were interdependent. Note that Salhi[26] calculated the heavy particle distribution in the insert region, whereas the present discussion focuses on the orifice region.

The orifice mode was used to obtain estimates of the electron temperature and number density within the orifice. The predicted number densities varied from 3 x 10^{20} to 1 x 10^{22} m^{-3}, and the electron temperatures ranged between 1.8 and 3.0 eV for the geometries of AR6, AR3, and AR1. Figure 4.19 presents the radial temperature distribution of the ions and neutrals for AR6 at 1.25-A and 2.4-sccm. Under the assumption of uniform particle density, the results from the orifice model yielded only modest increases in the heavy particle temperature based on the orifice model results. At slightly higher densities and lower electron temperatures, the results indicated that the ions and neutral temperatures on centerline were several hundred to around 1000 K higher than the wall temperature. The remainder of this section discusses the solutions obtained from Equations (4.52) in the range where the ion and neutral temperatures deviate significantly from the wall temperature.

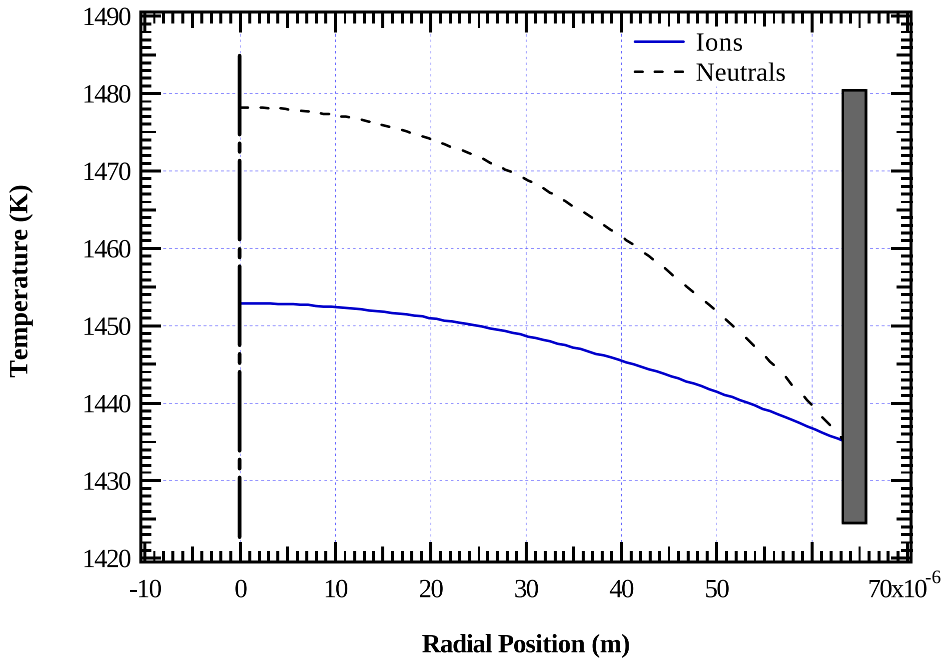

Figure 4.19 - Radial Heavy Particle Temperature Profile for AR6 at 1.25-A and 2.4-sccm (T_e = 2.00-eV, n_e = 8.5 x 10^{21} m^{-3}, n_o = 2.3 x 10^{23} m^{-3}).

Under the conditions depicted in Figure 4.19, the electron-neutral momentum transfer frequency was so much greater than the electron-ion collision frequency that the neutrals were better heated by the electrons. This situation occurred due to the high electron temperature. As the electron temperature was reduced from the values in Figure 4.19, the ions were better able to accommodate towards the electron temperature, as shown in Figure 4.20. Nevertheless, the maximum centerline temperature in this example was still considerably below that predicted by the gasdynamic model. Figure 4.21 illustrates the radial distribution of the heavy particle temperatures for electron number densities in excess of 8.5 x 10^{21} m^{-3}. While the results indicated that the heavy particle could deviate by several thousand K from the wall temperature, the number densities required to yield this result also violated the current continuity expression for the orifice and insert models.

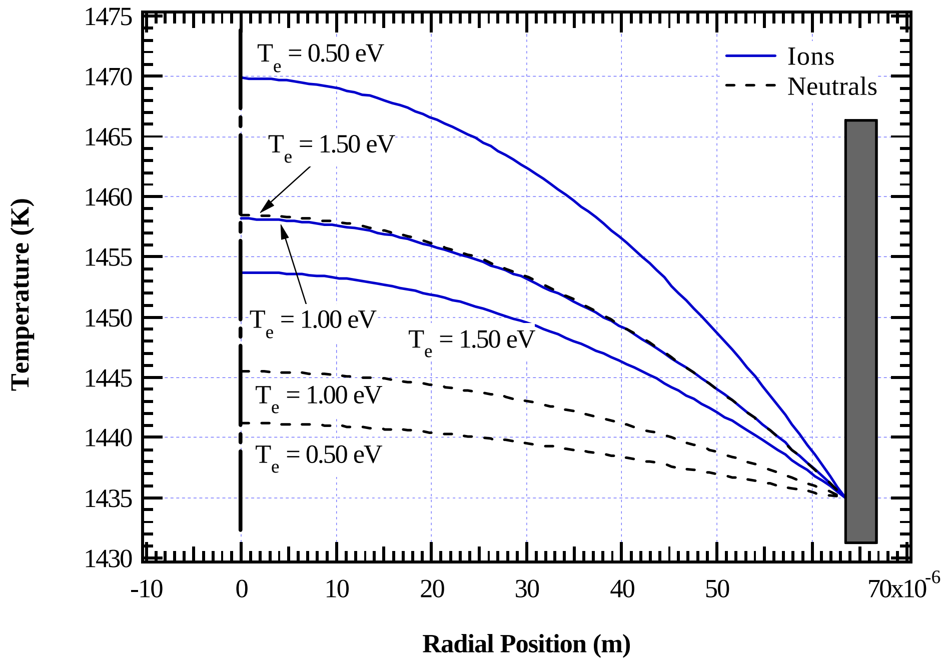

Figure 4.20 - Radial Variation of the Ion and Neutral Temperatures in the Orifice as a Function of Electron Temperature. ($n_e = 8.5 \times 10^{21}$ m^{-3}, $n_o = 2.3 \times 10^{23}$ m^{-3}).

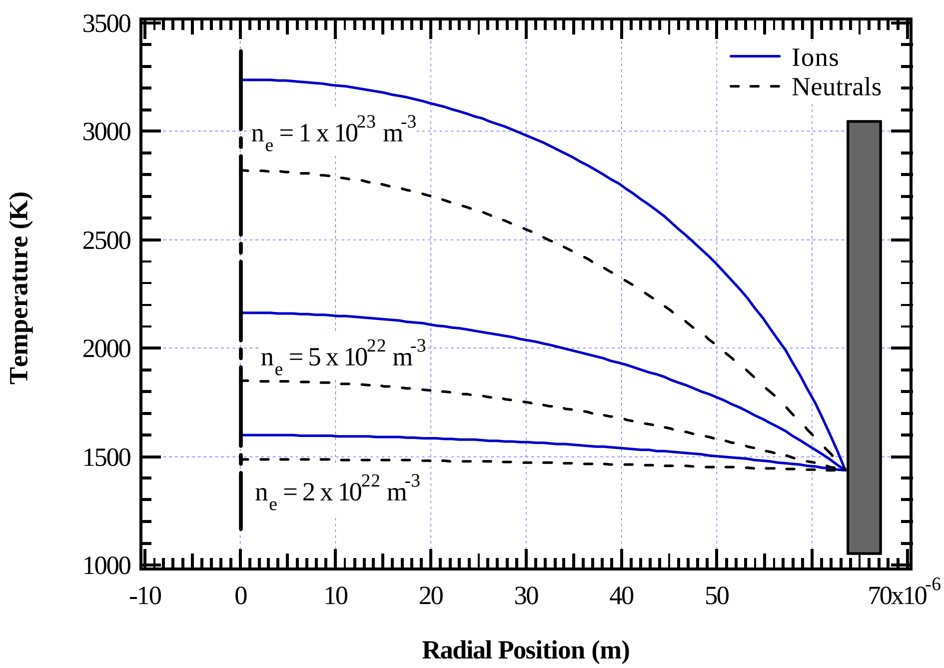

Figure 4.21 - Radial Variation of the Ion Temperature within the Orifice as a Function of Electron Number Density. T_e = 0.50 eV and $n_o = 2.3 \times 10^{23}$ m^{-3}.

The orifice model was run with several test cases to evaluate whether the properties within a constricted arc could satisfy the current continuity condition and yield elevated ion and neutral temperatures. The neutral number density was initially calculated for the orifice model given the standard orifice radius. This value was fixed for the orifice model, and the "radius" of the orifice was reduced to the limits of the models' ability to converge. The result was a nearly fully ionized plasma within the arc, and the electron density was then artificially forced to decay smoothly for positions beyond the arc radius. The electron and neutral densities in the orifice are illustrated in Figure 4.22. The results of the of the heavy particle temperature distribution, also shown in Figure 4.22, indicated that the ion temperature could exceed the wall temperature by about 1000-K for an arc of about twenty percent of the orifice radius.

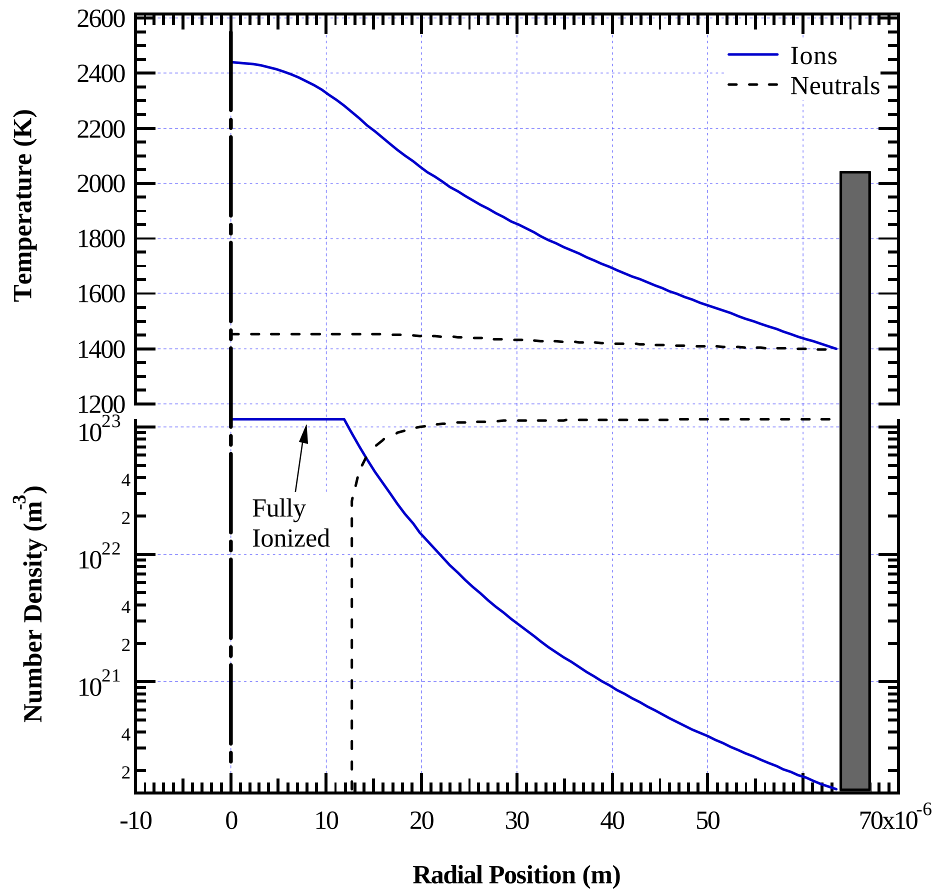

Figure 4.22 - Radial Distribution of Heavy Particle Temperatures Based on the Arc Column Hypothesis (T_e = 2-eV).

Although the evidence to suggest that current conduction in the orifice occurred by means of a constricted arc was indirect, this theory was suggested for the operation of orificed hollow cathodes. Optical methods offer the best opportunity for experimental verification of this theory. The important processes should be preserved if scaling of the cathode is necessary to facilitate optical access. Experimental measurement of this phenomenon was left to future work.

CHAPTER 5

DESIGN AND TESTING OF NEXT-GENERATION LABORATORY MODEL CATHODE

The best test of a theory or empirically drawn conclusions is to use that knowledge to predict the outcome of a new experiment. In the case of the present investigation, the goal was to use the knowledge and insights gained from the experimental investigation to develop a theoretical model which can be used to design more efficient cathodes. This chapter presents the design and performance of a second-generation, laboratory-model hollow cathode.

5.1 Cathode Design

The design of the second-generation, low-current hollow cathode SC.012 incorporated improvements based on several findings of the experimental and theoretical investigations combined with the practical considerations of available material. While comprehensive testing of the model predictions requires comparison between theory and experiment of the effects of individual design changes, several design modifications were implemented simultaneously at the risk of introducing an unexpected outcome. This was done in order to achieve the goal of a low-consumption, low-current hollow cathode more directly. Heat conduction was reduced in order to better thermally isolate the thermionic emitter. The insert electrical connection was modified to improve insert position accuracy. The insert geometry was modified to facilitate ionization. The orifice plate was designed for low-flow-rate operation with minimal power. The keeper was designed to enhance ion and electron transport to a secondary anode or plasma. The design of SC.012 is discussed in detail below.

5.1.1 Thermal Design

Minimization of the heat conduction from the high temperature region of SC.012 was accomplished geometrically and by using materials with lower thermal conductivity. Figure 5.1 depicts SC.012 schematically. Although the insert used in SC.012 had a larger diameter than any of the cathodes examined in Chapter 3, conduction and thermal mass were reduced by shortening the insert, 9.5-mm as opposed to 12.7-mm. The use of two tube diameters required that the insert be electron beam welded in place (see Figure 5.2). Electron beam welding the insert to the cathode tube eliminated the cathode legs and leg holder, and the thermal conduction path was reduced to the thin wall of the cathode tube upstream of the insert. The interface between the cathode tube and the insert was isolated to the upstream edge of the insert. Any contact between the insert and the cathode tube or orifice plate was incidental and would have a high contact resistance. The cathode tube and orifice plate of SC.012 were made of tantalum. Tantalum has a conductivity of approximately 61 W/m-K at 1300 K which is only slightly better than Mo-50%Re alloy (64 W/m-K).[83,84] The conductivity of the tungsten is 113 W/m-K at 1300 K, and the use of tantalum for the orifice plate significantly reduced the heat lost from this high-temperature region.[83] While the conductivity of titanium at 1300 K is 23 W/m-K, tantalum was chosen both for its availability and heritage as a material used for hollow cathodes.[83] The sputter-yield of the orifice plate material must also be considered, and both niobium and titanium have superior sputter resistance compared to tantalum.[85] Titanium and niobium are mentioned to illustrate that other materials may be more optimal for low-current hollow cathodes, and although the design of SC.012 was intended to improve the state-of-the-art, the results were more important as a gage of the effectiveness of the model..

The radiation shield on the cathode heater, typically comprised of 12 tight wraps of smooth 0.13-mm thick tantalum foil securely spot welded in place, was modified to increase the effectiveness of the shield. Spot welding was necessary to attach the foil securely. Crumpling the foil so that the conduction path between layers was poor would produce the most effective radiation shield. Precise replication of this type of radiation shield would be difficult. Since reproducible cathode performance is preferred, a crinkled radiation shield was left as the subject of a future investigation. Out of consideration for the ability to reproduce its fabrication, the radiation shield for SC.012 was made of loosely-wrapped, smooth tantalum foil. By avoiding the use of tight wraps, the contact resistance for thermal conduction was increased.

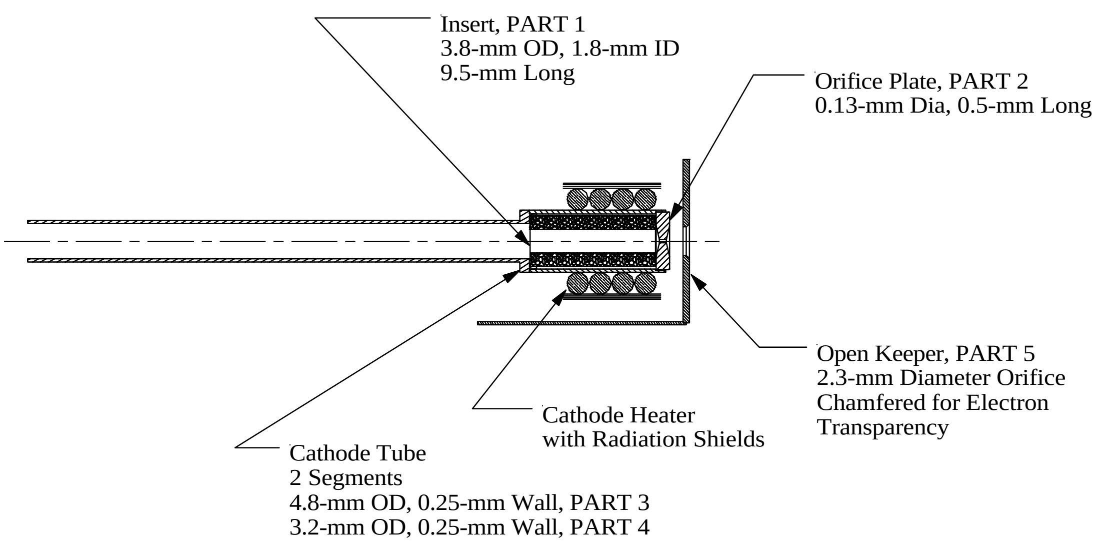

Figure 5.1 - Schematic of the Next-Generation Laboratory Model Low-Current Hollow Cathode (SC.012).

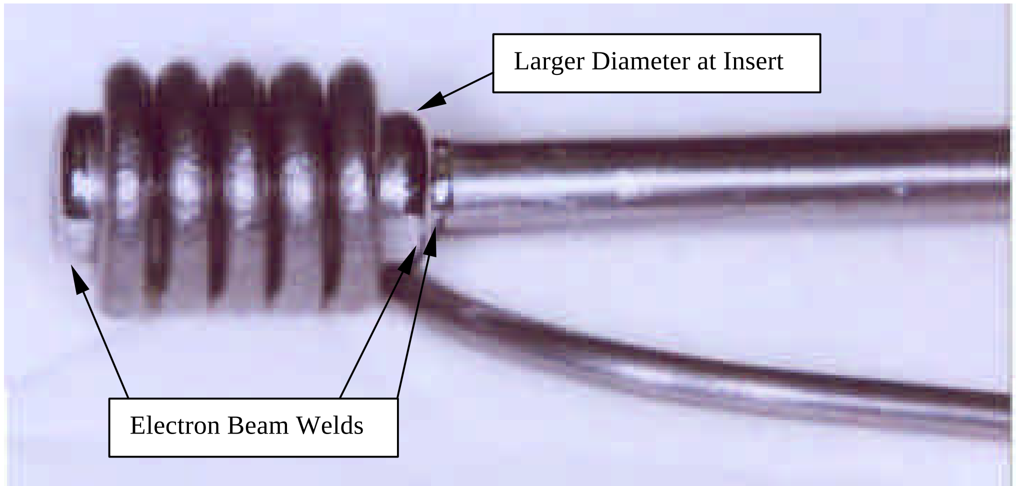

Figure 5.2 - Photograph of SC.012 Showing The Electron Beam Welds and Two Tube Diameters

5.1.2 Insert Design

The insert inner diameter for SC.012 was 0.6-mm (50 percent) larger than that of any other cathode tested in this investigation. The findings of both the experimental and theoretical investigations indicated that the insert diameter should be large for increased efficiency. The experiments showed reduced power and propellant consumption with increasing insert inner diameter. The insert temperature required to emit the electrons decreased as the emission surface area increased. Consequently, heat loss was reduced by increasing the insert inner diameter. Further, Salhi and Turchi[45] developed some scaling relations for hollow cathodes including a relation between cathode performance and insert-to-orifice diameter ratio. As the insert diameter increases relative to the orifice diameter, spot-mode cathode propellant consumption is reduced. The physical path length for the primary electrons from the insert increases with insert diameter, facilitating ionization. While the choice of the insert used in SC.012 was driven by hardware availability, the resulting geometry was serendipitous; the larger insert inner diameter would enhance ionization. The larger outer diameter and the need to minimize conduction were the reasons for the use of two diameters of cathode tube. The electron beam weld fixed the insert position, mitigating the issue raised by mismatch of the insert outer diameter with the cathode tube inner diameter.

5.1.3 Orifice Plate Design

As with the cathodes evaluated in Chapter 3, the diameter of SC.012 was chosen based upon the Kaufman[50] criterion for the maximum current. To safely maintain an emission of 1.5-A, the orifice diameter was 0.125-mm. The orifice length was chosen based on both the experimental and theoretical results. The experimental results showed that transition flow-rate scaled inversely with orifice length, and power consumption increased with orifice length. These trends were mirrored in the theoretical predictions.

An orifice length of 0.38-mm was chosen as a compromise slightly favoring low-flow-rate over low-power consumption. Figure 5.3 is an engineering drawing of the orifice plate.

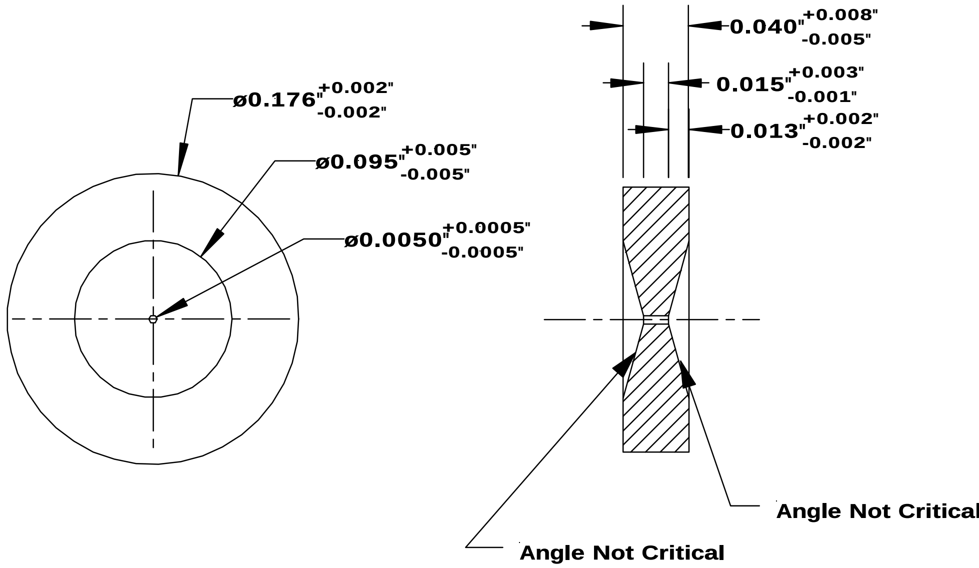

Figure 5.3 - Engineering Drawing of SC.012 Orifice Plate (Dimensions in inches).

In addition the orifice dimensions, the plate thickness and chamfer were also considered in the design. As with previous designs, the thickness was driven largely by the requirements of the spot welding process. If the orifice plate were too thin, welding it would cause melting or softening of the entire plate, and the orifice could become distorted or closed. The orifice plate thickness was 1.0-mm, which was 2.67 times larger than the designed orifice length.

The orifice of SC.012 was chamfered to accommodate the difference between the desired orifice length and required plate thickness. The shape of the chamfer was derived from a concept proposed by Katz and Patterson.[86] According to the orifice model, ions were lost from the orifice control volume with a uniform flux equal to the product of the electron number density and ion acoustic speed. The flux to the downstream surface provided an estimate of the ion emission from the hollow cathode. Regardless of whether the emitted ion flux was hemispherical or cosine in distribution as shown in Figure 5.4, the fraction of ions lost to downstream cathode surfaces decreases as the chamfer angle and depth are decreased. Consequently, a shorter chamfer with a shallower angle enables increased ion emission for charge neutralization in the cathode-keeper gap and spot-mode emission at reduce flow-rates. The orifice plate was made symmetrically with internal and external chamfers of 0.32-mm depth and 15 degree half-angle; most hollow cathodes employ a 45 degree half-angle. The internal chamfer facilitated a shallower external chamfer without greatly increasing the distance from the insert to the orifice. The downstream angle was limited to avoid interference with the welding process, and Figure 5.5 illustrates this point.

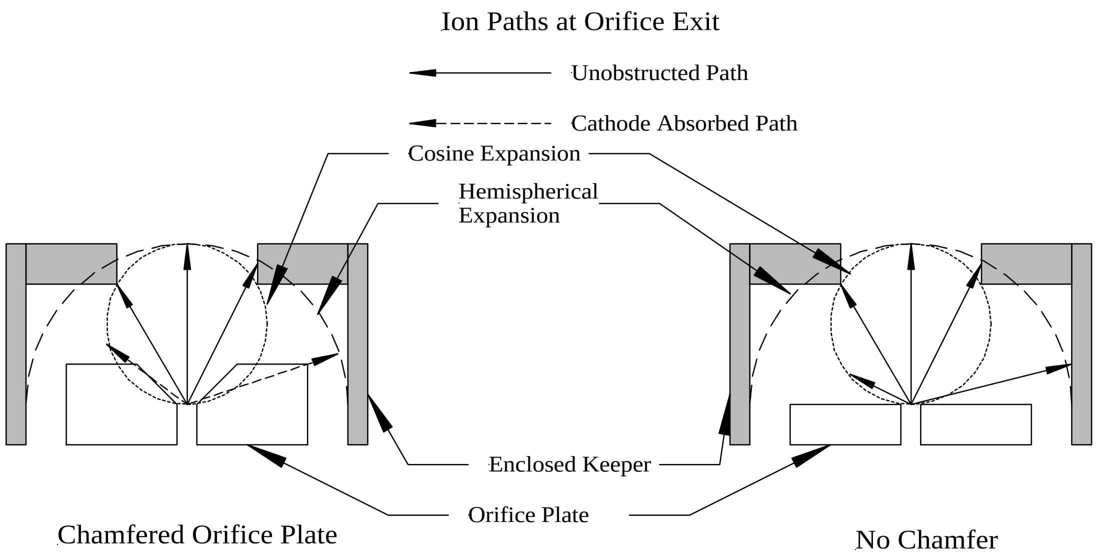

Figure 5.4 - Illustration of the Tendency of Chamfered Orifice Plate to Collect Ions Emitted from the Orifice.

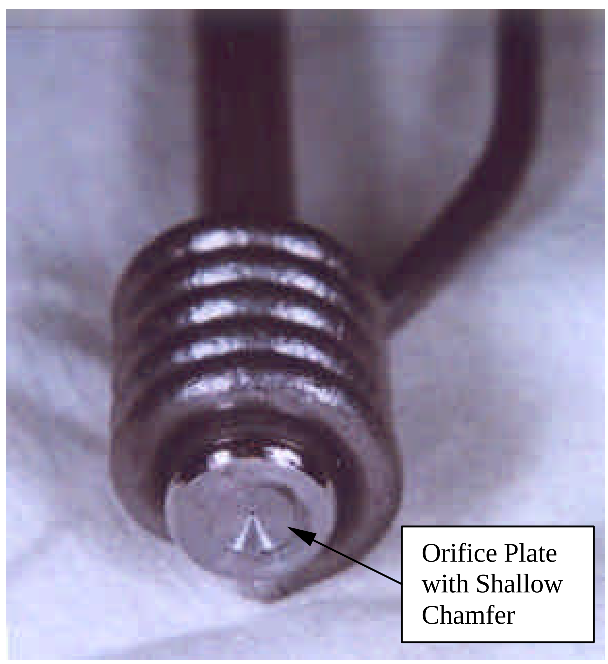

Figure 5.5 - Photograph of SC.012 with Shallow Orifice Plate Chamfer.

5.1.4 Keeper Design

An engineering drawing of the keeper is shown in Figure 5.6. While an enclosed keeper is more thermally efficient than an open keeper, the open geometry was considerably simpler to fabricate and enabled optical and thermocouple access to the entire cathode tube. The keeper orifice diameter was identical to the cathodes reported in Chapters 2 and 3. A chamfer was added to the downstream end to facilitate electron transport downstream of the keeper. In this case, electrons entering the keeper sheath are lost for carrying current to a downstream electrode. The chamfer minimizes the keeper surface area presented to the emitted plasma without increasing the aperture diameter. The purpose was to increase electron emission capacity at a given flow-rate.

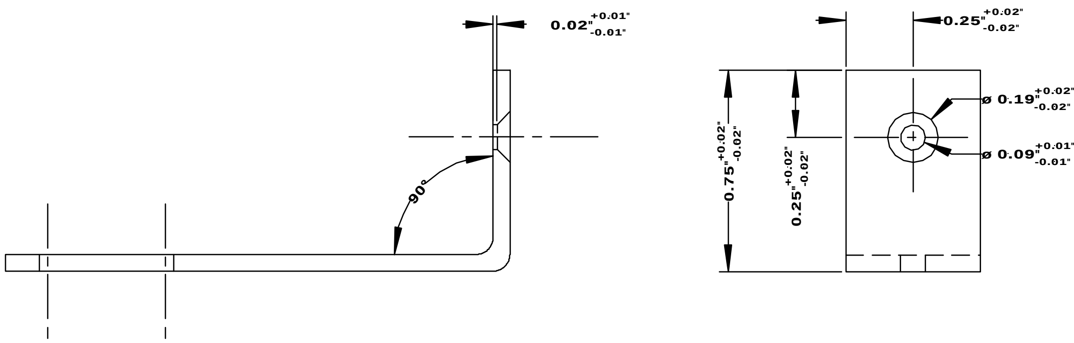

Figure 5.6 - Diagram of the Open Keeper Used with SC.012.

5.1.5 Design Summary

In order to summarize the design process for low-current hollow cathodes, the various considerations are listed in Table 5.1. The reader should keep in mind that although the model presented in Chapter 4 is a useful design tool, the number of factors influencing cathode operation make a comprehensive optimization routine beyond the scope of this work.

Table 5.1 Low-Current Hollow Cathode Design Considerations

Design Aspect	*Specific Considerations*
Material Choice	• Low-thermal conductivity • Low-sputter yield/high-sputter threshold • Strength at elevated temperature
Insert Design	• Low-work function • Maximize inner diameter • Maximize insert position accuracy • Maximize thermal isolation
Orifice Design	• Diameter determined by total current requirement • Length a trade-off between power and flow consumption • Minimize chamfer dimensions • Orifice plate thickness determined by fabrication technique
Keeper Design	• Aperture diameter determines power consumption and spot-to-plume transition • Downstream chamfer to facilitate electron transport

	• Enclosed keeper to limit radiative heat loss

5.2 Performance Evaluation

The most meaningful test of any cathode determines the cost in terms of flow-rate and power consumption for a given current. Consequently the test of SC.012 focused on cathode performance throughout its operating regime. Cathode current, voltage, flow-rate, and internal pressure were measured according to the techniques outlined in Chapter 2. Cathode flow-rate was initially set to approximately 2.4 sccm at a constant current. The flow-rate was then decreased until the onset of plume-mode or an unstable condition was reached. In this respect, the evaluation was very similar to those performed previously.

Evaluation of the keeper voltage as a function of flow-rate and current is depicted in Figure 5.7. The trends observed with SC.012 were very similar to those of the other cathodes. While the lowest flow-rate condition of each of the characteristics in Figure 5.7 appears to indicate plume-mode operation, the high-frequency, large-amplitude AC component of the keeper voltage was absent at each of the data points in Figure 5.7. The previously defined plume-mode condition was observed with SC.012 at flow-rates lower than reported in Figure 5.7. However, the plume-mode operation was comparatively unstable, and the arc extinguished itself within a few seconds of the onset of the mode. Due to the nature of this phenomenon, it was difficult to define precisely the transition flow-rate. Consequently, the reader is left to observe from Figure 5.7 that stable, spot-mode operation of SC.012 was achieved at lower flow-rates for a given current than all of the cathodes tested previously in this investigation.

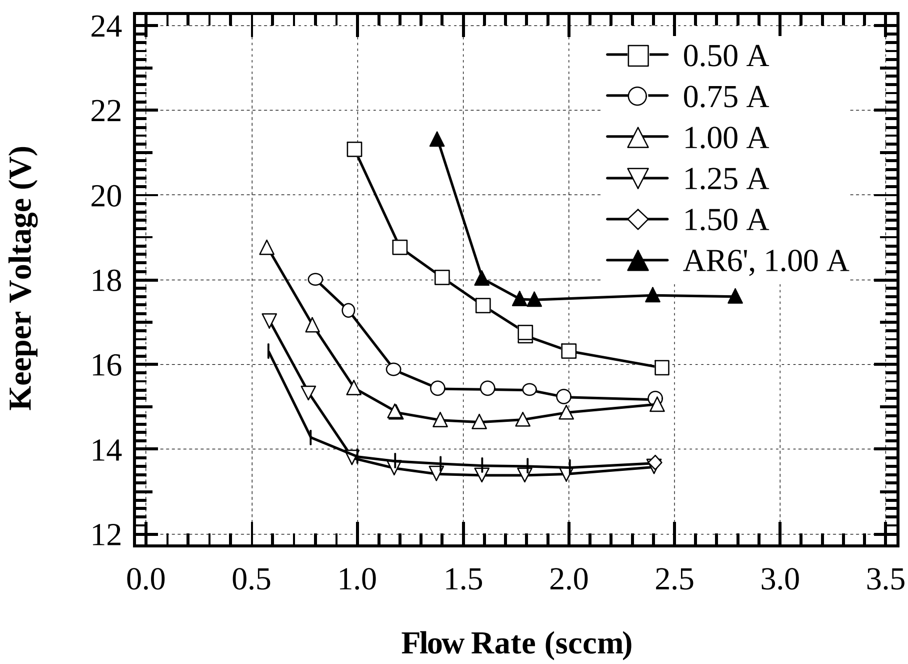

Figure 5.7 - Voltage-Flow-rate Characterization of SC.012.

Both the increased insert inner diameter and the orifice geometry contributed to the reduced spot-mode flow-rates. Figure 5.8 shows that SC.012 could operate in spot-mode with internal pressures significantly below those of the first-generation cathodes. The internal pressure of SC.012 was intermediate between that of AR3 and EK6 for the same operating conditions. Geometrically the orifices of SC.012 and AR3 were nearly identical, and the difference in internal pressure for SC.012 was attributed to more efficient arc-heating of the ions. In some cases, spot-mode emission was maintained with SC.012 at slightly more than half the flow necessary for EK6.

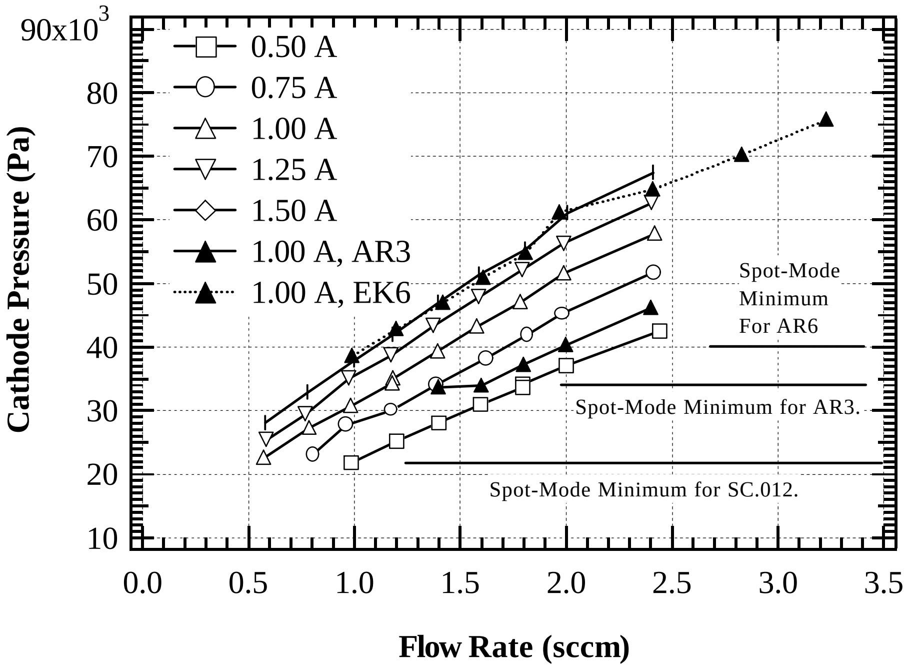

Figure 5.8 - Reduction of Cathode Internal Pressure for Spot-Mode Operation.

To directly compare the performance of SC.012 with the other cathodes, Figure 3.16 (page 53) was replicated in Figure 5.9, and the data from SC.012 were added. Since plume-mode operation was absent from SC.012, the transition flow-rates for AR6´ were used in Figure 5.9. At each keeper current, SC.012 consumed approximately 20 percent less power than AR6´. Thus cathode operation was improved in SC.012 in both power and flow consumption. The power consumption of SC.012 was also less than that of AR1, illustrating that although the orifice length of SC.012 results in a larger amount of Ohmic heating in the orifice, the rest of the thermal design makes up the difference.

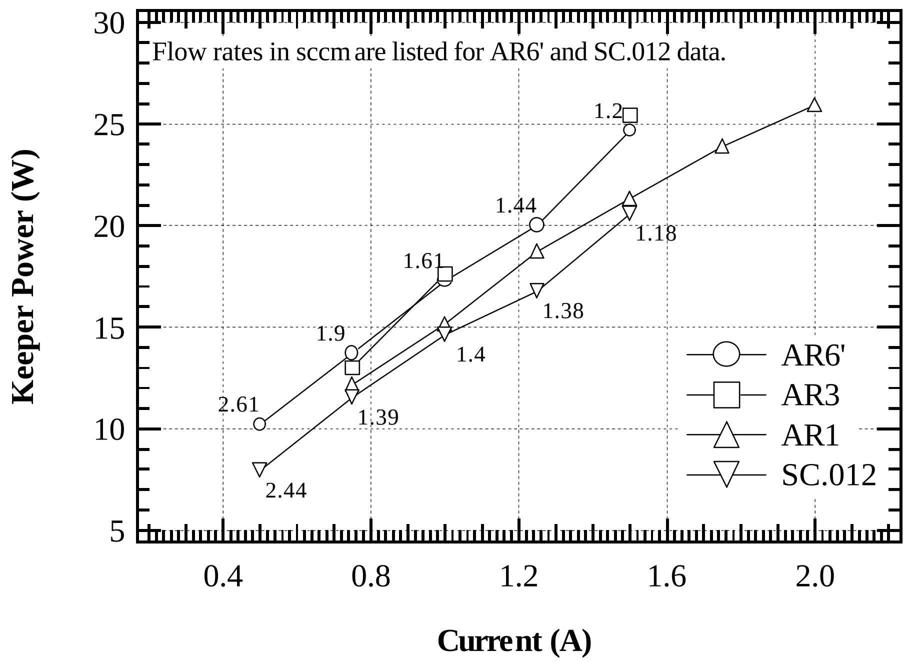

Figure 5.9 - Comparison of the Minimum Power Consumption at Transition.

Finally, SC.012 was also operated in the triode configuration used previously to gage its emission capabilities. The only test was performed with a keeper current of 0.5-A under the premise that in most applications, the keeper would be operated at the minimum current necessary for stable operation. The resulting emission current is compared with EK6 in Figure 5.10. The scale in Figure 5.10 is expanded to show the capability of SC.012. Although SC.012 was operated over a more limited range of anode voltage than EK6, the emission current capabilities of SC.012 were clearly superior to EK6. This result is a product of both the improved efficiency of the cathode design and the chamfered keeper.

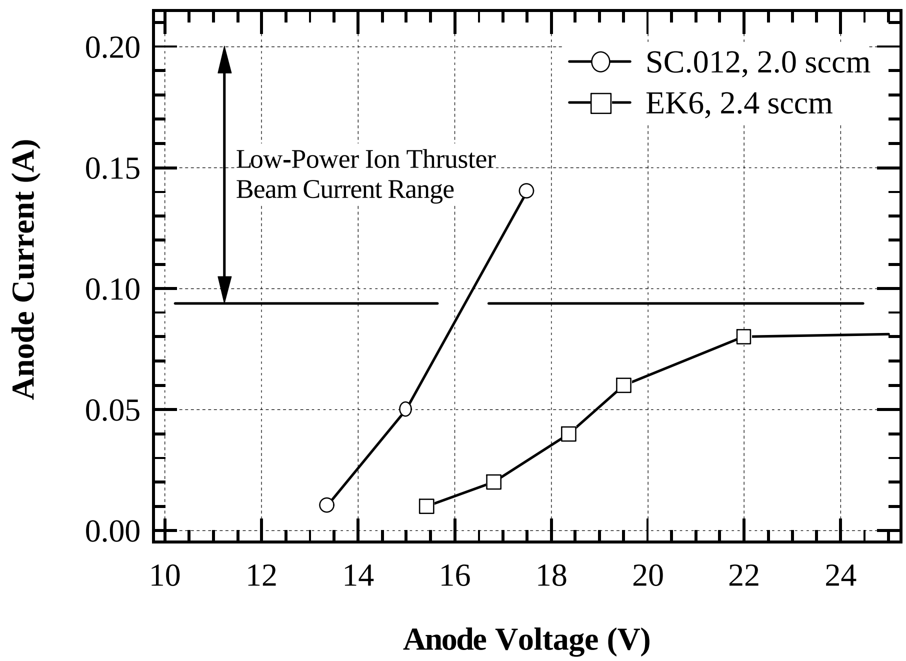

Figure 5.10 - Emission Current at 0.50-A to the Keeper.

5.3 Summary

A second-generation laboratory model hollow cathode was designed to operate at reduced flow-rate and power requirements compared with those tested initially. The initial experimental and theoretical investigations were used to determine the most effective modifications to be employed in the second-generation cathode. The resulting design balanced the considerations of performance optimization, available materials, and fabrication techniques. While other materials and geometries were presented which would be more optimal for very-low-current hollow cathodes, the cathode SC.012 demonstrated superior performance to all of the cathodes tested initially. The power consumption was reduced by 20 percent compared with the best first-generation cathode at comparable flow-rates. The spot-mode requisite flow was less at each keeper current than all of the previously tested cathodes. Finally, SC.012 demonstrated superior electron emission capabilities when operated as part of a triode configuration. The successful design of SC.012 is testament to the lessons learned in the experimental and theoretical investigations.

CHAPTER 6

CONCLUSIONS AND FUTURE WORK

This work focused on reduction of the power and propellant consumption of low-current orificed hollow cathodes. Hollow cathodes which operate with minimal power and flow consumption are of interest for electric propulsion devices and as plasma contactors. Recent efforts to develop 100 to 300-W class electric propulsion systems heightened the need for efficient hollow cathodes.[11,12,16] As the scale of the electric thrusters decreases, plasma generation is hampered by the reduction in the available volume to surface area ratio of the ionization region; ions are more easily lost to the walls and the close proximity of the walls tends to cool the plasma. These phenomena occur in hollow cathodes as well, and the research presented here examined the factors driving low-current hollow cathode efficiency.

The approach taken in this investigation had four components. Initially a number of hollow cathodes were designed using a mixture of existing scaling relationships and design heritage. Next, the performance of these cathodes was evaluated, the cathode temperature distributions were measured, and the plasma environment was mapped extensively. The results of the experimental investigation were used to validate a model of the orifice and insert regions of low-current hollow cathodes. Finally the results of both the experimental investigation and the model were used to design a second-generation low-current hollow cathode.

6.1 Performance of Low-Current Hollow Cathodes

Five separate 3.2 mm diameter orificed hollow cathodes were designed and tested in a number of different configurations. Power consumption increased with orifice length, while the minimum flow-rate decreased. The use of an enclosed keeper reduced the power consumption, however the minimum flow-rate was observed to increase. The latter finding was unexpected because the use of an enclosure increases the local pressure in the cathode-keeper gap, which should lead to increased ion creation and transport with the electrons downstream. The cathode internal pressure was found to vary from 39.2 to 66.5 kPa in spot-mode, and the transition to plume-mode occurred at a nearly fixed internal pressure regardless of the current or flow-rate. Subsequent analysis of the insert plasma with Langmuir probes and the cathode-to-keeper plasma suggested that several tens of kPa were possible only if the heavy particle temperature was on the order of several thousand Kelvin. LIF measurements by Williams, et al.[60] indicated that the neutral temperatures were several thousand Kelvin.

The behavior of the cathode external temperatures was also studied to determine the important heat transfer modes. Conduction dominated the heat transfer from the cathode surface. The condition was more pronounced when an enclosed keeper was used. This conclusion means that cathode performance at low-power can be readily improved by choosing materials with a low-thermal conductivity. In the limit of low-power density, the issue of thermal stability only arises when attempting to maintain sufficient temperature for electron emission.

Finally, plasma parameters were measured in the insert region, in the cathode-to-keeper gap, and downstream of the keeper. These data were intended to provide validation for a cathode model. While the dimensions in the insert region precluded detailed mapping similar to Salhi,[26] the resolution was sufficient to compare the plasma properties in the 3.2-mm orificed hollow cathodes with those measured by others.[25,26] The electron number density in the insert was of the same order, and exhibited a sharper gradient near the orifice than the data by Siegfried.[25] The electron temperature in spot-mode was consistently less than 1-eV, while the onset of plume-mode led to electron temperatures above 1-eV. The number density in all regions scaled with the flow-rate and the current. The anisotropy of the plasma downstream of the keeper was found to increase with beam extraction. The electron energy distribution function was also measured to validate the parameters determined using the standard Langmuir probe analysis. While the distribution functions all appeared to be Druyvesteyn, the calculated average electron energies agreed well with the previously determined electron temperatures.

6.2 Orifice and Insert Models

A model describing the processes occurring in the orifice was derived from the one by Mandell and Katz.[24] The model evaluated ion continuity and conservation of energy within the orifice assuming uniform properties. A current continuity statement was added for use with the insert model. The orifice model, like its predecessor, was used to evaluate the effects of orifice geometry on the performance of the cathode. The orifice model was used in conjunction with an insert model based along similar simplifying assumptions. This model was used to examine which factors influenced power consumption in the insert region. The prediction of the plasma properties were in good agreement with the experimentally determined values. The prediction of the electron temperature in the orifice was significantly higher than was observed either upstream or downstream of the orifice. Since the electron temperature was obtained by solving for ion continuity, the use of a Maxwellian versus a Druyvesteyn electron population resulted in an overestimation of electron energy due to the need for ionization. For a given electron temperature, the Druyvesteyn distribution has a greater number of high-energy electrons which facilitate ionization. An overestimation of the electron temperature was also responsible for the predicted power consumption exceeding the discharge power in some cases.

The combined orifice/insert model was used to determine an approach to optimal cathode design. The results showed that the orifice diameter should be as small as possible to facilitate electron emission. As the orifice aspect-ratio increased beyond three, the cathode simply consumed additional power in the orifice without additional electron emission. Power consumption decreased as the insert diameter was increased.

The findings of the orifice and insert models were combined with a gasdynamic expression for the pressure in the cathode as a function of temperature and flow-rate. The model indicated that for heavy particle temperatures of several thousand Kelvin, the calculated cathode pressure agreed with the experimental results. A constricted arc column in the orifice was proposed as the mechanism responsible for the elevated neutral and ion temperatures.

6.3 Test of Improved Design

A second-generation laboratory model hollow cathode was designed, fabricated, and tested based on the findings of both the experimental and theoretical investigations. In addition to the design features inspired by the previous results, the cathode incorporated several new fabrication techniques which were expected to further reduce the heat loss from the insert region. The orifice plate was modified so that the fraction of the emitted ions which became lost to the cathode sheath was reduced. Tests of the cathode showed that at the same current and flow-rate, it consumed twenty percent less power than the best of the first-generation cathodes. This result was especially remarkable considering the increased thermal mass of the cathode imposed by material availability. The cathode also demonstrated spot-mode operation to significantly lower flow-rates than previously achieved.

6.4 Suggested Future Work

While the design changes incorporated in SC.012 resulted in significantly improved low-current performance, examination of Table 1.1 (page 3) shows that the design goals for the neutralizer on a 100 to 300 W ion thruster remain out of reach. For the 100-W case, the total current (keeper and emission/beam neutralization) is only 0.2-A. In the course of this investigation, none of the cathodes demonstrated even short term (tens of hours) stability below 0.5-A. Further, spot-mode operation at 0.5 sccm, the flow-rate requirement, was achieved only for relatively high current conditions. The design of a neutralizer for the low-power ion engine must incorporate as many of the modifications suggested in Chapter 5 as is feasible. Below are discussions of several possibilities for future development of low-current hollow cathodes.

To begin with, the extremely low current requirement means that the materials will be exposed to a relatively low-density plasma and experience a low-thermal load. Consequently the sputter yield and melting point requirements become relaxed compared with high-current cathodes. The extremely low thermal conductivity of titanium compared with the other materials used in this investigation is ideal for this application. The sputter yield is also acceptable despite the lower melting temperature of titanium. In addition to reducing the thermal conductivity, the design must also include an enclosed keeper. In a further effort to minimize the conduction away from the high temperature components, the insert could be brazed directly to the orifice plate prior to impregnation of the insert. This process would be similar to the method currently used to braze the collar to the insert. The issue of whether the braze material could withstand the cathode operating temperature must be addressed. The power deposited in the orifice would be easily conducted to the insert, where it is needed, and conduction to the low temperature end of the tube would be more torturous. This configuration also lends itself to the use of a short insert, where the thermal mass is reduced. In the spirit of reducing the thermal mass, a trade study should be implemented comparing the benefits of increased insert inner diameter with the need to keep the overall dimensions small to minimize both conductive and radiative losses.

The low emission current specified for a 100-W class ion thruster raises the possibility of significantly altering the keeper geometry. If the electron emission from the hollow cathode tends toward a cosine distribution, then placing the keeper immediately downstream of the orifice would reduce the cathode-to-keeper voltage and enable reduced flow-rate. The low emission current would be accommodated by the emission at high angles of the cosine distribution. This configuration would have to be tested since the emission current generally decreases with flow-rate.

For applications where low-power is important and a flow-rate of several sccm can be tolerated, the multichannel hollow cathode may be an option. The design of these cathodes must be modified so that the low work function surface is long lived. The results of the current investigation showed that these cathodes scale poorly to low current applications since the physical path lengths for ionization to occur are too short for low flow-rates. The multichannel hollow cathodes lend themselves to higher current applications.

In order to meet the specifications set out in Table 1.1 (page 3) or more restrictive design goals, alternate cathode schemes must be considered. One of the most promising technologies for low current electric propulsion is the field emitter array cathode. These cathodes operate without propellant. The field emitter array cathodes consist of millions of field emission cones with a gate electrode which functions similarly to the keeper on a hollow cathode. The small scale of the cones (typically a few atoms wide at the tip) enables a very strong electric field to be generated with relatively low voltage (<100-V on the gate). The technology, primarily developed for flat-panel displays, typically requires ultra-high vacuum to ensure life, and long-term operation in millitorr environments must be established.

APPENDICES

APPENDIX A

SAMPLE ANALYSIS OF LANGMUIR PROBE DATA AND ELECTRON ENERGY DISTRIBUTION FUNCTION CALCULATION

The raw current-voltage data from the Langmuir probes was sufficiently free of noise to perform the standard analysis. However, small fluctuations were amplified by taking two numerical derivatives of the data, and a cubic spline interpolation of the raw data was necessary to calculate the derivatives. Consequently, the cubic spline interpolation was used in the standard analysis out of convenience. The ion saturation current was subtracted from the total probe current to calculate the electron current as shown in equation (A.1).

$$I_e\left(V_{pr}\right) = I_{pr}\left(V_{pr}\right) - I_{i,sat} \tag{A.1}$$

Next, the natural logarithm of the electron current was evaluated. As shown in Figure A.1, a linear curve fit was performed, and the electron temperature was set equal to the inverse slope of the line. This statement is equivalent to equation (2.3). The plasma potential was determined by the probe voltage at the peak of the first derivative of the probe current as defined in equation (2.4). The derivatives were evaluated according to the following formulas:

$$\begin{aligned} \frac{d}{dx} f\left(x_0\right) &= \frac{f\left(x_1\right) - f\left(x_0\right)}{\Delta x} \\ \frac{d}{dx} f\left(x_i\right) &= \frac{f\left(x_{i+1}\right) - f\left(x_{i-1}\right)}{2\Delta x} \\ \frac{d}{dx} f\left(x_{N-1}\right) &= \frac{f\left(x_{N-2}\right) - f\left(x_{N-1}\right)}{\Delta x} \end{aligned} \tag{A.2}$$

The nature of the current-voltage characteristic in Figure A.1 made determination of the electron saturation current problematic. All of the data collected in this investigation exhibited the gentle positive slope seen in Figure A.1. In order to establish a consistent means of determining the electron number density based on this portion of the curve, the current at the plasma potential was used in equation (2.5). While the ion saturation region of the current-voltage characteristic in Figure A.1 appears to mitigate the issues raised in the electron saturation region, sufficiently accurate measurement of the ion saturation current was accomplished only in the cathode-to-keeper gap. In fact, the data in Figure A.1 were taken in the insert region, and the ion saturation current was measured as 1.9×10^{-8} A; a negative current is needed for equation (2.6) to calculate a real number density.

Figure A.2 summarizes the procedure involved in evaluating the two derivatives of the probe current to calculate the EEDF. The first derivative must be interpolated by another cubic spline so that the second derivative is piecewise smooth. Equations (A.2) are then used to compute the second derivative of the probe current. Next the electron energy must be defined according to Equation (2.8). Examination of Figure A.2 shows that the probe voltage at the peaks of the first and second derivatives are different. With a Maxwellian EEDF, these peaks occur at the same voltage, the plasma potential. This represents the first indication that the population is non-Maxwellian. As stated in Chapter 2, the peak of the second derivative was used in Equation (2.8) so that the distribution more closely resembled either a Maxwellian or Druyvesteyn. This assumption is justified by considering that for a Maxwellian distribution, the probe voltage at the peak of the second derivative is the plasma potential which is used in Equation (2.8). Figure A.3 shows the results of multiplying the second derivative by the square root of the electron energy. The EEDF calculated based on the peak of the first derivative is included for reference. Figure A.3 also shows the effect of small signal perturbations at electron energies significantly higher than the bulk of the population; the factor of $E^{1/2}$ amplifies the noise at large values of E.

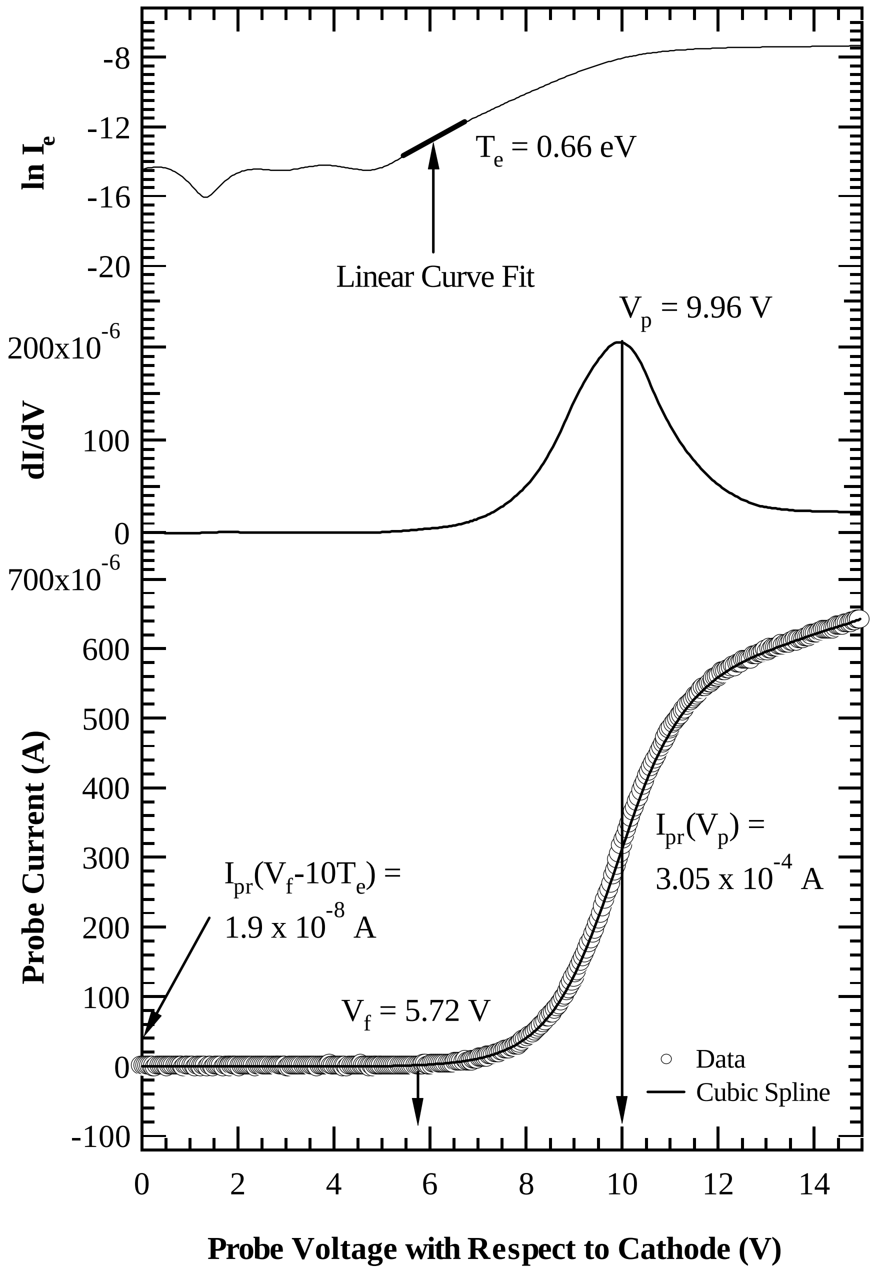

Figure A.1 Illustration of the Standard Langmuir Probe Analysis.

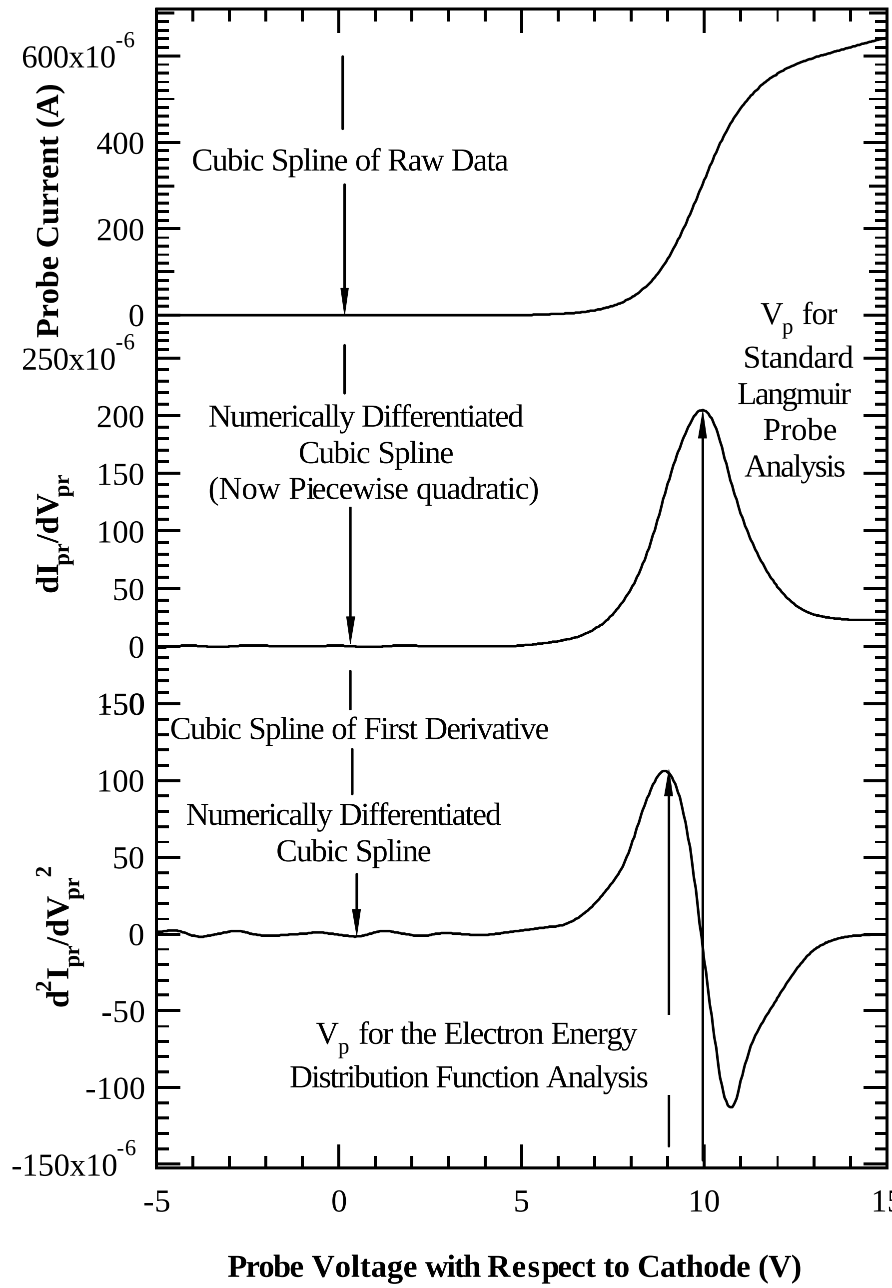

Figure A.2 - Sequence of Derivatives Calculated for the EEDF Analysis.

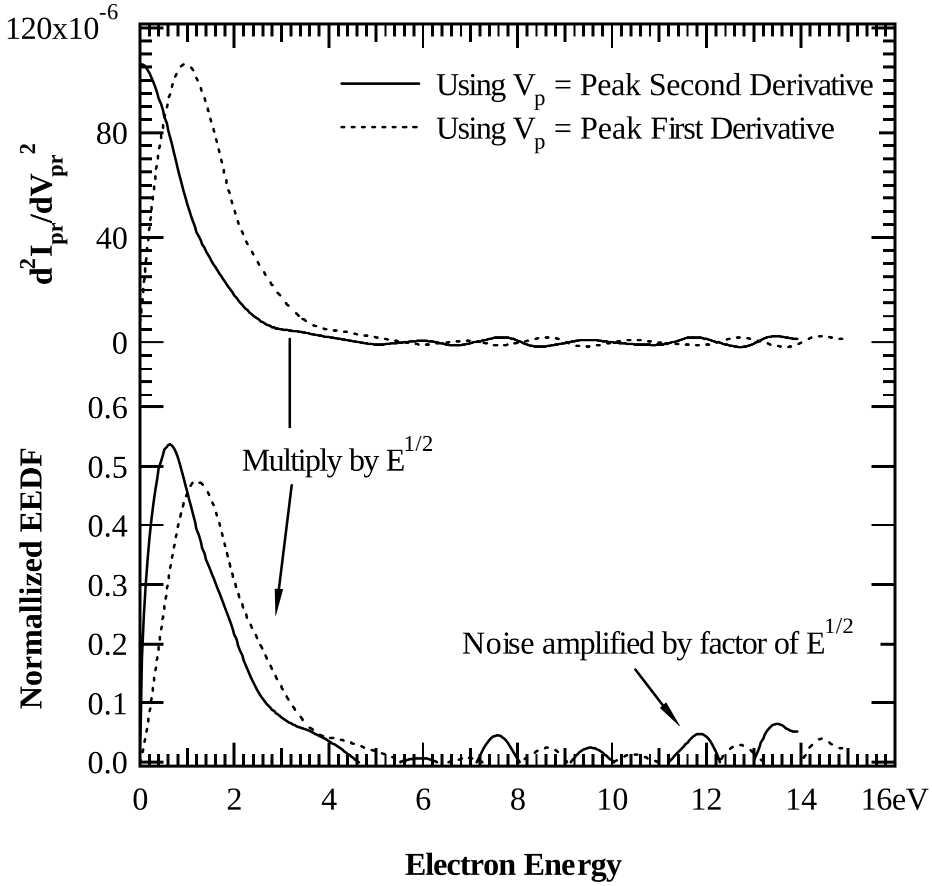

Figure A.3 - Final Processing of the EEDF Data and Comparison of Results Based on Two Values for the Plasma Potential.

APPENDIX B

EVALUATION OF THE VALIDITY OF THE STANDARD LANGMUIR PROBE ANALYSIS

The Langmuir probe analysis used in this dissertation assumed that the sheath was thin and collisionless. A sheath is considered thin when it is much smaller than the characteristic dimensions of the Langmuir probe, in this case the diameter. If the sheath is large compared to the probe diameter, the effective collection area is larger than expected and the measured density is greater than the true density. Since sheath size is typically several Debye lengths, the thin sheath assumption requires that the probe diameter be much larger than the Debye length. The collisionless sheath assumption is necessary to insure that the electrons and ions entering the sheath have the same identity as when they entered the sheath; collisional exchange phenomena within the sheath alter the character of the ions or electrons collected by the probe. The collisionless sheath assumption is satisfied if the collision mean free paths are much greater than the Debye length.

The length scales 1.3-mm upstream of the orifice plate are depicted in Figure B.1. In this case, the collisionless sheath assumption holds while the thin sheath approximation was considered to be marginally valid. The closeness of the Debye length to the probe diameter results in increased error in the electron number density measurements. The data presented in Figure B.1 represent the worst-case conditions for the insert plasma, as do those in Figure B.2 for the CK gap plasma. In the cathode-to-keeper gap, probe diameter and mean free paths were both 10 to 100 times larger than the Debye length, and the standard Langmuir probe analysis was considered valid.

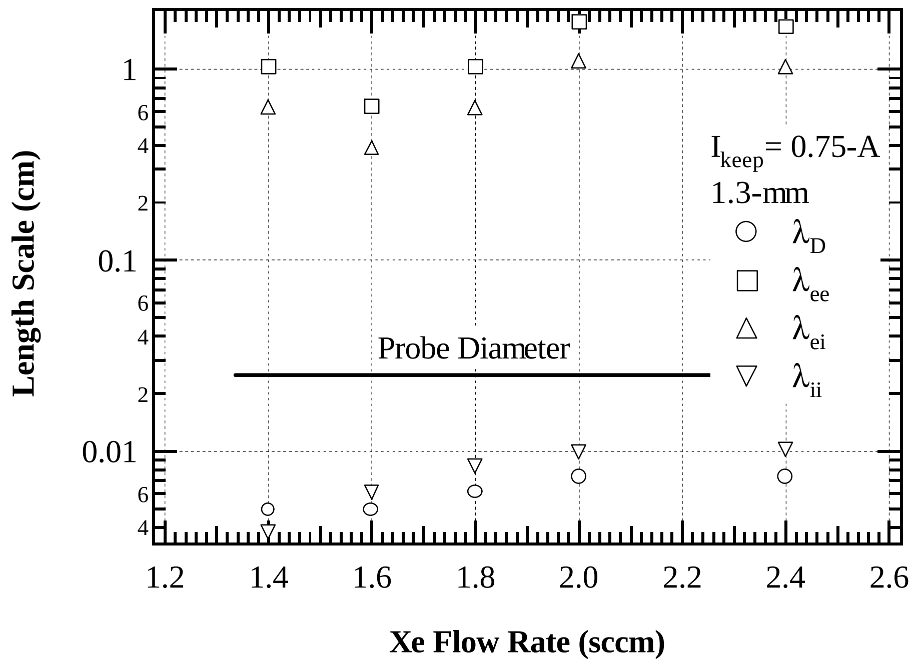

Figure B.1 - Length Scales 1.3-mm Upstream of the Orifice Plate.

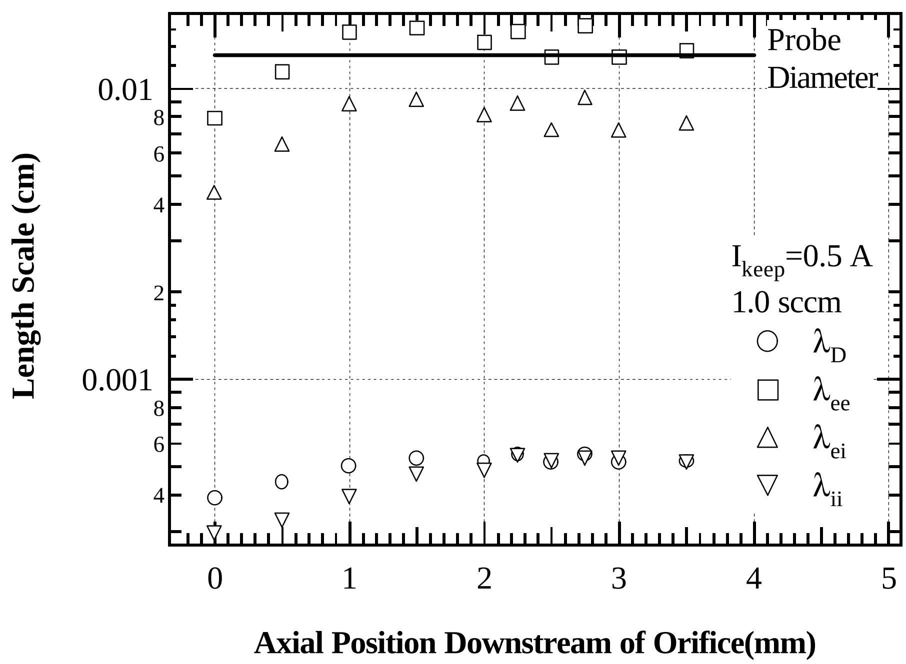

Figure B.2 - Length Scales in the CK Gap at 0.5-A and 1.0-sccm.

The length scales downstream of the keeper are depicted in Figure B.3 and Figure B.4 for two different operating conditions. The operating conditions were taken to represent the range of length scales. With a keeper current of 0.5-A, both assumptions become marginal. Far from the keeper, the Debye length is on the order of the probe diameter, and the ion-ion mean free path is everywhere of the same order as the Debye length. The former condition decreases the accuracy of the density measurement, while the latter condition adversely affects the ion saturation portion of the probe characteristic.

As noted in Chapter 2, the electron saturation portion of the probe characteristic was used because of the poor resolution in the ion saturation region. The poor resolution was due in part to the collisional ion sheath. Even at higher current, Figure B.4, the ion mean free path is still on the order of the Debye length suggesting a collisional sheath for the ions. The thin sheath approximation holds for the 1.50-A case indicating that for all but the 0.50-A case, the error induced by this assumption was negligible.

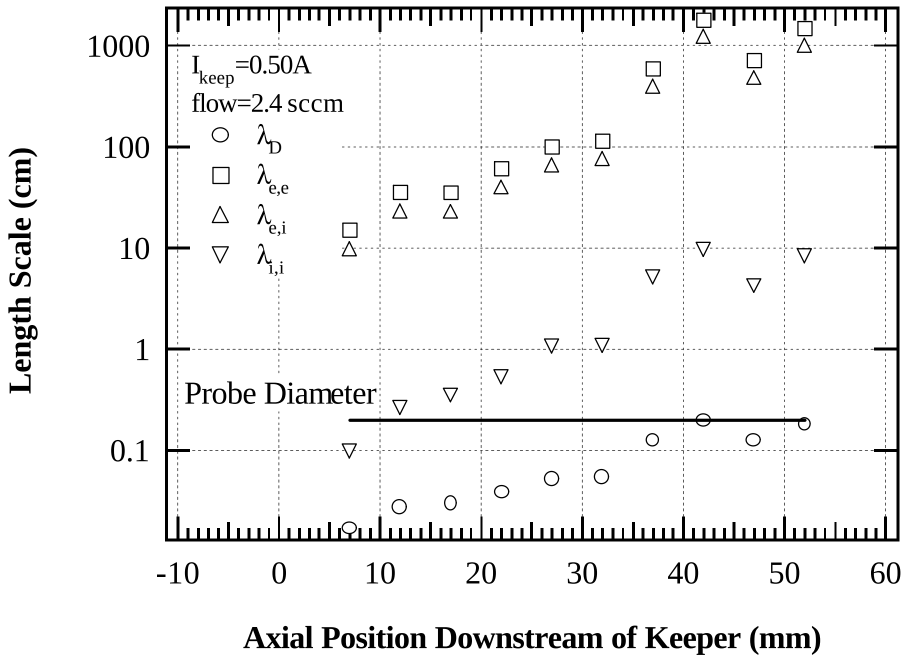

Figure B.3 - Length Scales Downstream of the Keeper at 0.5-A and 2.4-sccm.

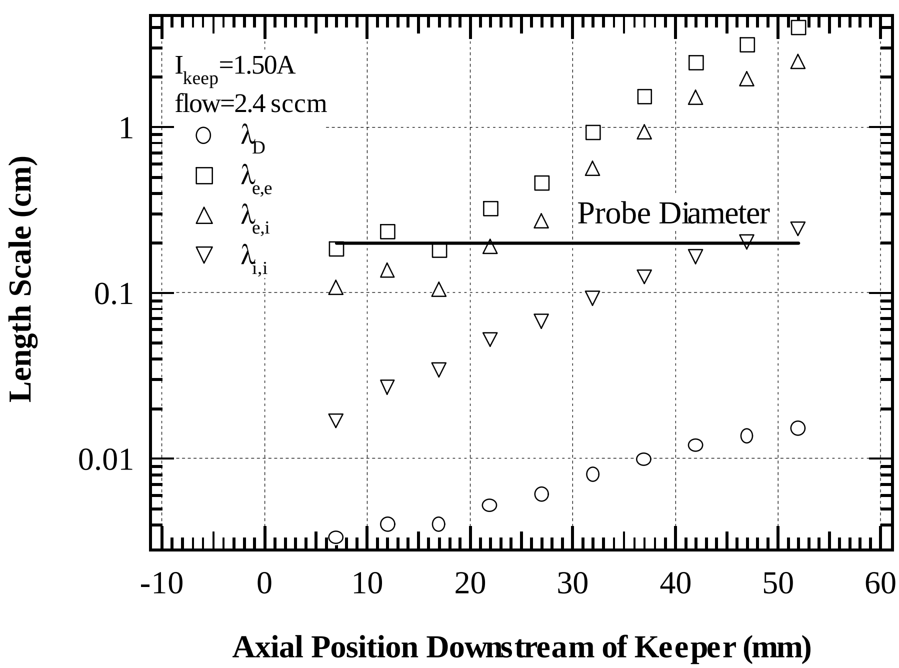

Figure B.4 - Length Scales Downstream of the Keeper at 1.50-A and 2.4 sccm.

APPENDIX C

DERIVATION OF THE EQUATIONS USED IN THE HOLLOW CATHODE MODEL

C.1 Orifice Plasma Model Collision Operators Derivation

Since the ionization fraction of the hollow cathode plasma is expected to be much less than one, the primary energy exchange mechanisms for the electrons are Coulomb collisions with other electrons, and elastic and inelastic collisions with neutrals. The collisional processes between the electrons and neutrals are derived from the collision rate equation:[81]

$$N_{12} = \kappa_{12} n_1 n_2 \iiint_{\infty} d^3 v_1 \iiint_{\infty} d^3 v_2 \sigma\left(g\right) g f_1\left(v_1\right) f_2\left(v_2\right) \qquad \textbf{(C.1)}$$

Since we are considering neutrals and electrons, κ_{12} is set equal to one. The neutrals are taken to be essentially motionless with respect to the electrons, and we can write

$$f_o\left(v_o\right) = \delta\left(0\right) \qquad \textbf{(C.2)}$$

$$g = v_e \qquad \textbf{(C.3)}$$

which enables the following simplification of equation (C.1),

$$N_{eo} = n_e n_o \iiint_{\infty} d^3 v_e \sigma\left(v_e\right) v_e f_e\left(v_e\right) \qquad \textbf{(C.4)}$$

The neutral number density, n_o, is calculated based on the mass flow-rate. Next, the triple integral is split up using spherical coordinates.

$$N_{eo} = n_e n_o \int_0^{2\pi} d\varphi \int_0^{\pi} d\theta \sin\theta \int_0^{\infty} dv_e v_e^2 \sigma\left(v_e\right) v_e f\left(v_e\right) \qquad \textbf{(C.5)}$$

This simplifies to

$$N_{eo} = 4\pi n_e n_o \int_0^{\infty} dv_e \sigma\left(v_e\right) v_e^3 f\left(v_e\right) \qquad \textbf{(C.6)}$$

Equation (C.6) was numerically integrated with experimental data for the appropriate collision cross-section for ionization, excitation, and elastic collisions with neutrals. Figure C.1 summarizes the experimental cross-sections used for xenon.[68,71,72] The neutral number density used in Equation (C.6) when calculating the rate of ionization was based on the flow-rate. In equilibrium, the rate of ionization must equal the rate of ion loss from the control volume, and ions leaving the control volume are replaced by soon-to-be-ionized neutrals. In the case of excitation and elastic collisions, the number density of neutrals is the difference between the density predicted by the flow-rate requirement and the electron number density. The ionization collisions de-populate the neutral population by an amount equal to the electron number density, and excitation and elastic collisions occur with the remaining neutral population.

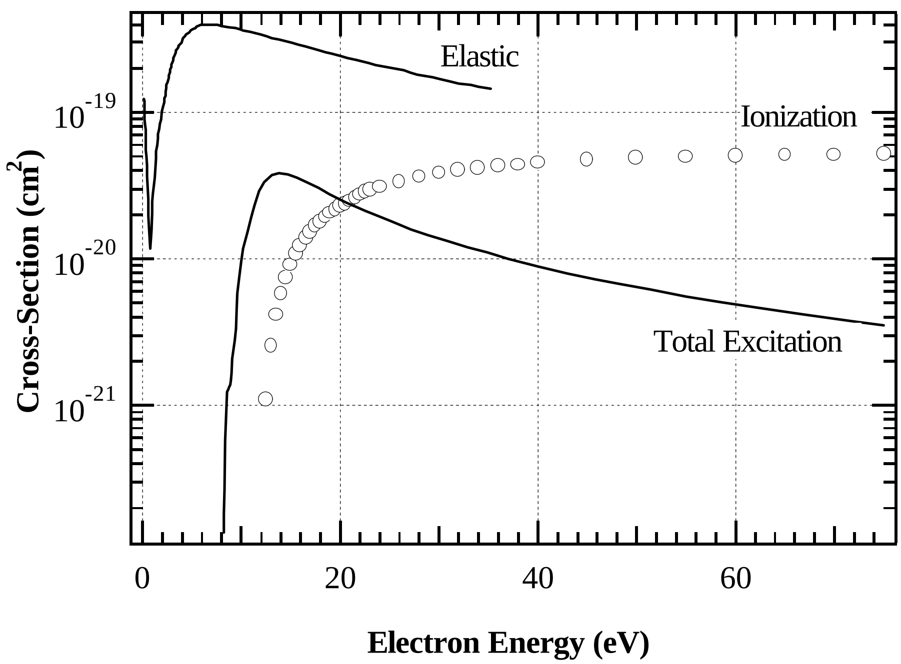

Figure C.1 - Electron Impact Cross-Sections in Xenon.[68,71,72]

The ionization rate calculated using Equation (C.6) was multiplied by the orifice volume to determine the rate at which ions were created in the orifice, and this rate was equated to the rate of ions lost from the volume. The ionization rate was also used to determine the power consumed by electron impact ionization. Equation defines the power consumed by ion production.

$$q_{ionize} = e\phi_i N_{eo}^{ionize} \left(\pi r_o^2 l_o\right) \tag{C.7}$$

where the ionization potential, ϕ_i, for xenon is 12.12 eV. A similar expression was used to evaluate the power consumed in neutral excitation.

$$q_{excite} = e\phi_e N_{eo}^{excite} \left(\pi r_o^2 l_o\right) \tag{C.8}$$

where ϕ_e is an average number for the energy consumed in an excitation event, and was set equal to 10-eV, unless stated otherwise. The elastic collisions with neutrals enter the energy equation in the calculation of the Ohmic heating. From the results of Equation (C.6), the collision frequency is calculated

$$\nu_{eo} = \frac{N_{eo}}{n_e} \tag{C.9}$$

which is used to determine the resistivity in a partially ionized gas.

C.2 Orifice Pressure Model Derivation

Here, an expression is derived which includes elements from Salhi[26] with consideration of the effects of a finite length orifice. It should be noted that the mass flow equations reported by Salhi[26] contains errors which have been corrected in the present derivation. In order to determine the appropriate set of equations to use, the Reynolds number is calculated:

$$\mathrm{Re}_D = \frac{r uD}{m} \tag{C.10}$$

In order to determine the flow velocity, mass continuity in steady state, 1-D, incompressible flow is assumed,

$$\frac{Dm}{Dt} = 0 = div\vec{u} \tag{C.11}$$

hence

$$\dot{m} = r Au \tag{C.12}$$

where $\dot{m}$ is the Xe flow-rate in kg/s, μ is the dynamic viscosity of Xe in kg/m-s, and D is the insert diameter in m. For Xe in the temperature range expected in the hollow cathode, the viscosity ranges from 23.3 x 10^{-6} to 83.3 x 10^{-6} kg/m-s.[87] This results in Reynolds numbers below 5 for all of the cases expected in the 3.2-mm diameter cathodes.

Ferreira and Delcroix[5] derived a Poiseuille flow expression which uses a weight factor to address the degree to which they were in continuum flow. The 3.2-mm hollow cathodes are fully in continuum flow internally (>100 Torr, 1.2-mm inner diameter), consequently, this region was modeled using continuum Poiseuille flow. The average velocity expression for Poiseuille flow is,

$$\bar{u} = \frac{D^2}{32m}\left(-\frac{dp}{dx}\right) \tag{C.13}$$

The pressure gradient was linearized

$$-\frac{dp}{dx} = \frac{p(x) - p_o}{x} \tag{C.14}$$

where p_o is a reference pressure in the cathode, and x indicates an upstream location. At the low flow velocity in the cathode, the pressure drop along the cathode tube is negligible compared with the drop across the orifice. Consequently, the reference pressure must be in the orifice. The result when put back into continuity is an expression for the mass flow-rate as a function of the pressure p(x):

$$\dot{m} = \frac{p D^4}{128m} \frac{M}{\tilde{R}T} \frac{p_o + p(x)}{2} \frac{p(x) - p_o}{x} \tag{C.15}$$

from which we can solve for p(x):

$$p\left(x\right)=\left[\dot{m}\frac{128m}{p\,D^{4}}\frac{\tilde{R}T}{M}\left(2x\right)+p_{o}^{2}\right]^{0.5} \tag{C.16}$$

This leaves p_o and the temperature unknown. The continuity equation and a choked flow condition at the exit of the orifice lead to the following relation:

$$p_{c}=p_{o}=\dot{m}\frac{\tilde{R}T}{M}\frac{4}{p\,D^{2}}\sqrt{\frac{M}{g\,\tilde{R}T}} \tag{C.17}$$

By equating p_c with p_o, the pressure at the entrance of the orifice is determined for a given gas temperature. To account for the pressure drop across the orifice entrance, an isothermal energy equation is used

$$p_{in}=p_{x}+\frac{1}{2}\,r_{o}\overline{u}_{o}^{2}\left(1+K_{L}\right) \tag{C.18}$$

where p_{in} is the pressure in the insert region, and K_L=0.5 is the coefficient of loss at the orifice entrance.

APPENDIX D

HOLLOW CATHODE DESIGN CODE OPERATING MANUAL AND DESCRIPTION

The hollow cathode model described in Chapter 4 and Appendix B was implemented in an Excel™ spreadsheet utilizing Visual Basic™ developed macros. The code presumes a working knowledge of Excel™ and macros. In addition, the model should be used primarily to evaluate how a given design will perform. The code is titled hollcat.xls, and can be found at the following website:

http://www.engin.umich.edu/dept/aero/spacelab/research/cathode/

This appendix is intended to be a guide to the specific worksheets in the model and to provide a basic description of the functions of the macros in the spreadsheet.

Inputs Worksheet

This worksheet, shown in Figure D.1, contains the cathode dimensions and material properties which are used in the various sub-models. A drawing is included in this worksheet to define the geometry. The worksheet also contains parameters used specifically in the axial heat transfer calculations. Physical constants are listed on this worksheet. Finally the cathode flow-rate and current are entered in this worksheet.

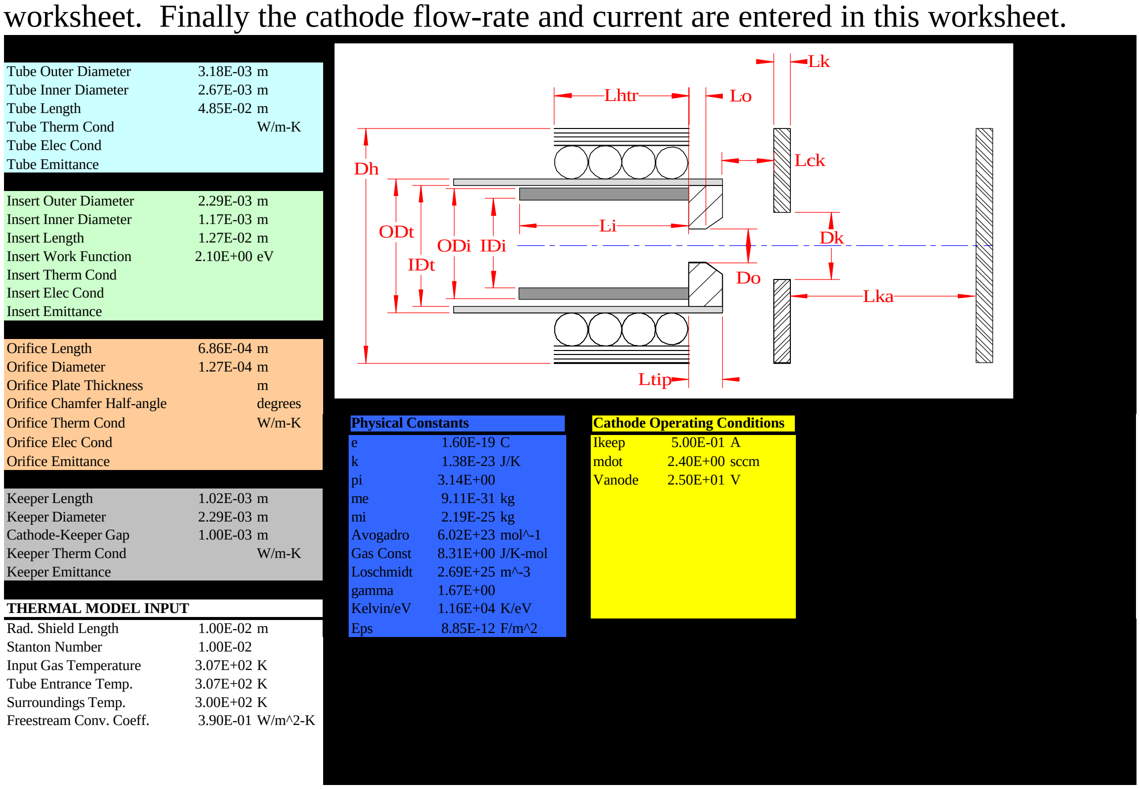

Figure D.1 – The *Inputs* Worksheet

Orifice Worksheet

This worksheet, shown in Figure D.2, contains the equations used to solve for the plasma properties and power consumption in the orifice. This worksheet may be used in either of two ways, as a stand-alone model or as part of the overall hollow cathode model. In the first case, the **OrificeNeTe** macro is used after the geometry and operating conditions have been set-up in the *Inputs* worksheet. This macro uses Excel's Goalseek function to solve for the electron temperature and number density for a consistent solution. This solution technique has limited stability, and the initial values for electron temperature and number density must be close to the final solution. Abrupt changes in geometry, flow-rate, or current can cause the solution to diverge when there is in fact a stable solution. A number of orifice geometries and cathode operating conditions can be evaluated automatically using the *Results* worksheet as will be described below. The *Orifice* worksheet is also used to determine plasma properties in the orifice for use in the other parts of the hollow cathode model. The *Orifice* worksheet also calculates several Knudsen numbers, the Debye ratio, and the number of ions in a Debye sphere to examine the validity of the theory used.

Preliminary Calculations	**Value**	**Units**	Devel
Equivalent Current	1.72E-01	A	
Electron Current Density	3.95E+07	A/m^2	Avera
Orifice Temperature	1.12E-01	eV	May n
Orifice Temperature	1.30E+03	K	
Input Elec. Temp.	2.00E-01	eV	Not ne
Neutral Average Velocity	4.57E+02	m/s	Ira use
Neutral Sonic Velocity	3.70E+02	m/s	This v
Ion Acoustic Velocity	1.21E+03	m/s	Used f
Ion Average Velocity	4.57E+02	m/s	
Ion Thermal Velocity	2.86E+02	m/s	
Electron Thermal Velocity	5.93E+05	m/s	SQRT(kT/m)
Neutral Density	2.30E+23	m^-3	Based
	2.30E+23		Dumm
Coulomb Logarithm i-e	1.30E+01		NRL.
Electron Debye Length	1.54E-07	m	NRL.
Coulomb Logarithm i-i	4.97E+00		NRL.
Double Sheath Voltage	3.62E-01	V	
Orifice Viscosity	7.57E-05	kg/m-s	Curve
Bulk Neutral Velocity	1.36E+02	m/s	Avera
Orifice Volume	8.69E-12	m^3	
Orifice Area	1.27E-08	m^2	
Fraction of Ionize from Excite	0.00E+00		Used t
Average Excitation Energy	5.00E+00	eV	
Hemispherical Emission Frac.	1.13E-01		
Cosine Emission Fraction	2.13E-01		

Collisional Analysis	**Value**	**Units**
Elastic XS at Te	2.21E-13	m^2
Electron Elastic mfp	1.39E-11	m
Electron Elastic freq	4.98E+10	Hz
Electron-Ion Scat freq	8.24E+10	Hz
Scattering Events	6.94E+03	#
Elastic n Scattering	2.61E+03	#
Coulomb Scattering	4.32E+03	#
.		
.		
Ionization Fraction	2.00%	
Elec. Current In	3.73E-01	A
Elec. Current Slope	1.87E+02	A/m
.		
Ionization mfp	2.89E-08	m
Excitation mfp	2.88E-09	m
n-n mfp	2.26E-05	m
i-i mfp	2.06E-07	m
h-h mfp	2.22E-05	m
Kn electron-elast	1.10E-07	
Kn electron-ionize	2.27E-04	
Kn electron-excite	2.27E-05	
Kn n-n	1.78E-01	
Kn i-i	1.62E-03	
Kn h-h	1.74E-01	
.		

	Orifice Outputs	**Value**	**Units**	
	Electron Temperature	**2.00E+00**	**eV**	
	Electron Number Density	**4.60E+21**	**m^-3**	
NRL	Plasma Conductivity	9.77E+02	mho/m	Chen
	Plasma Resistivity	1.02E-03	ohm-m	
	Voltage (IR)	2.42E+01	V	Calc
	Ions Out	**1.06E-03**	**A**	Ther
	Ion Loss	9.78E+17	#/s	Bohr
	Ionization	9.78E+17	#/s	Form
	Ion Cathode Current	2.55E-01	A	
	Ohmic Heating	**1.07E+01**	**W**	
Tota	Ionization Power Loss	1.91E+00	W	
(Tot	Radiative Losses	7.84E+00	W	
	Convective Losses	9.00E-01	W	
	Power OUT	**1.06E+01**	**W**	
	Continuity	-2.61E+14		
	Energy	9.27E-03		
	Max e- Emission Current	4.42E-02	A	
	Orifice Pressure	5.67E+03	Pa	sum
	Critical Pressure (sonic)	4.13E+03	Pa	
	Reynolds Number	1.15E+01		
	e- orifice pressure	1.47E+03	Pa	
	e- insert pressure	1.47E+01	Pa	
	Debye Ratio	1.22E-03	<< 1?	
	Debye Sphere	7.08E+01	>> 1?	

Figure D.2 - The *Orifice* Worksheet.

Insert Worksheet

The *Insert* worksheet, shown in Figure D.3, contains the equations for the insert model. The inputs are linked to the *Inputs* worksheet. The worksheet solves for the ion continuity, energy conservation, and current continuity by varying the electron temperature, the electron number density, and the insert temperature, respectively. The worksheet can be used either as a stand alone model, or as part of the combined orifice-insert model. In the stand alone case, the macro **Insert** is run after the inputs have been configured. The model can also be solved in conjunction with the orifice model, and a large number of solutions can be generated using the *Results* worksheet. The latter technique is recommended since the insert model relies on inputs from the orifice model.

Preliminary Calculations	Value	Units
Equivalent Current	0.107	A
Insert Work Function	2.00	eV
Insert Temperature	0.128	eV
Plasma Potential	8.00	V
Neutral Average Velocity	457	m/s
Neutral Sonic Velocity	370	m/s
Ion Acoustic Velocity	1258	m/s
Ion Average Velocity	457	m/s
Ion Thermal Velocity	286	m/s
Electron Thermal Velocity	4.82E+05	m/s
Electron Beam Velocity	1.19E+06	m/s
Neutral Density	1.43E+23	m^-3
Coulomb Logarithm i-e	7.18	
Electron Debye Length	7.54E-07	m
Coulomb Logarithm i-i	6.14	
Double Sheath Voltage	0.526	V
Orifice Viscosity	8.26E-05	kg/m-s
Effective Insert Volume	6.26E-10	m^3
Effective Emission Area	2.14E-06	m^2
Insert Ion Collection Area	4.28E-06	m^2
Eff. Primary Ionization Volume	6.01E-10	m^3
Eff. Primary Excitation Volume	1.58E-11	m^2
Fraction of Ionize from Excite	5.00%	
Average Excitation Energy	5.00	eV

Collisional Analysis	Value	Units
Elastic XS for Te	1.26E-13	m^3/s
Elastic XS for Beam	1.65E-10	m^3/s
Ionize XS for Te	3.50E-18	m^3/s
Ionize XS for Beam	6.26E-15	m^3/s
Excite XS for Te	9.49E-17	m^3/s
Excite XS for Beam	1.58E-12	m^3/s
Elastic freq for Te	1.80E+10	Hz
Ionize freq for Te	5.02E+05	Hz
Ionize freq for Beam	8.99E+08	Hz
Excite freq for Te	1.36E+07	Hz
Excite freq for Beam	2.26E+11	Hz
Electron-Ion Scat freq	2.35E+09	Hz
Scattering Events	9.46E+03	#
Elastic n Scattering	8.37E+03	#
Coulomb Scattering	1.09E+03	#
Elastic mfp for Te	1.89E-05	m
Elastic mfp for Beam	3.55E-08	m
Ionize mfp for Te	6.79E-01	m
Ionize mfp for Beam	9.33E-04	m
Excite mfp for Te	2.50E-02	m
Excite mfp for Beam	3.71E-06	m
n-n mfp	3.55E-05	m
i-i mfp	7.30E-06	m
h-h mfp	3.55E-05	m
Kn electron-elast	1.62E-02	
Kn electron-ionize	7.98E-01	
Kn electron-excite	3.17E-03	
Kn n-n	3.04E-02	
Kn i-i	6.25E-03	
Kn h-h	3.03E-02	

Insert Outputs	Value	Units
Electron Temperature	**1.32**	**eV**
Electron Number Density	**1.27E+20**	**m^-3**
Insert Temperature	**1481**	**K**
.		
Thermionic Efield Assist	3.14E+06	V/m
Effective Work Function	1.933	eV
Thermionic Current Density	3.52E+05	A/m^2
Thermionic Electron Density	1.31E+18	m^-3
Thermionic Current	0.7541	A
Collected Ion Current	0.2664	A
Emitted Ion Current	0.0013	A
Electron Backstreaming	1.98E-02	A
Ion Loss	3.29E+17	#/s
Ionization	3.29E+17	#/s
Plasma Conductivity	1.76E+02	mho/m
Plasma Resistivity	5.70E-03	ohm-m
Voltage (IR)	1.87E+00	V
Ohmic Heating	1.26E+00	W
Thermionic Electrons	6.18E+00	W
Ion Backstreaming	6.62E-03	W
Power IN	**7.44E+00**	**W**
Radiative Losses	4.62E+00	W
Backstreaming Electrons	5.23E-02	W
Current Carrying Electrons	2.12E+00	W
Ion Flux to Walls	6.51E-01	W
Power OUT	**7.44E+00**	**W**
Ion Continuity	**-2.75E+14**	**#**
Energy	**1.88E-03**	**W**
Current Continuity	**6.42E-04**	**A**
Ionization Fraction	0.09%	
Debye Sphere	2.28E+02	<< 1?
Debye Ratio	1.55E+03	>> 1?

Figure D.3 - The *Insert* Worksheet

Results Worksheet

The *Results* worksheet, shown in Figure D.4, was created to facilitate the performance evaluation of a number of different orifice geometries and operating conditions. The first five columns contain geometry and operating condition inputs. Next, the fraction of excitation events which create ions and the average excitation energy are included as free parameters. The insert region plasma potential and the insert work function are also considered free parameters. These are color-coded gray to emphasize that variation of these numbers is a "gray" area. The defaults for the fraction of excitation events which create ions and the average excitation energy are zero percent and 10-eV, respectively. Next, are the various results from the orifice model. The **IterCatSets** macro is used with this worksheet to run the orifice model over a number of data sets. When run, the macro asks the user the number of data sets to be iterated. The *Results* worksheet must be active, and the orifice diameter cell of the first data set must be selected before running the **IterCatSets** macro. The macro runs **OrificeNeTe** and **Insert** after transferring the inputs to the appropriate cell, and the outputs are transferred to the *Results* worksheet. When the solution fails to converge, the results are highlighted in bright, light-blue. The **IterCatSets** macro then goes to the next line where there is a positive number for the orifice diameter and repeats the process. The first row of the *Results* worksheet is frozen so that the data columns can be easily referred to regardless of the position within the sheet.

Do (m)	*lo (m)*	*Idis (A)*	*mdot (sccm)*	*Excitaion Contribution (%)*	*Uexcite (eV)*	*ne (m^-3)*	*Te (eV)*	*dni/dt (#/s)*	*ions out (A)*	*Ohmic (W)*	*Ionize (W)*	*Convect (W)*	*Radiate (W)*	*IR (V)*	*Max Ie (A)*
AR6, 5 percent from excitation, my model, diffuse orifice plasma															
1.27E-04	6.86E-04	0.50	0.60	5%	1.00E+01	2.18E+21	2.42	5.09E+17	5.05E-04	5.94	0.74	1.11	4.14	12.70	0.0210
1.27E-04	6.86E-04	0.50	0.90	5%	1.00E+01	2.47E+21	2.23	5.54E+17	5.71E-04	6.88	0.77	1.01	5.08	14.80	0.0237
1.27E-04	6.86E-04	0.50	1.20	5%	1.00E+01	2.70E+21	2.11	5.90E+17	6.25E-04	7.61	0.79	0.95	5.85	16.44	0.0260
1.27E-04	6.86E-04	0.50	1.50	5%	1.00E+01	2.89E+21	2.02	6.18E+17	6.69E-04	8.23	0.81	0.91	6.50	17.85	0.0278
1.27E-04	6.86E-04	0.50	1.80	5%	1.00E+01	3.05E+21	1.96	6.42E+17	7.06E-04	8.78	0.82	0.88	7.07	19.09	0.0293
1.27E-04	6.86E-04	0.50	2.10	5%	1.00E+01	3.19E+21	1.91	6.63E+17	7.39E-04	9.27	0.83	0.85	7.57	20.22	0.0307
1.27E-04	6.86E-04	0.50	2.40	5%	1.00E+01	3.32E+21	1.86	6.82E+17	7.68E-04	9.72	0.84	0.83	8.04	21.24	0.0319
1.27E-04	6.86E-04	0.75	0.60	5%	1.00E+01										
1.27E-04	6.86E-04	0.75	0.90	5%	1.00E+01										
1.27E-04	6.86E-04	0.75	1.20	5%	1.00E+01										
1.27E-04	6.86E-04	0.75	1.50	5%	1.00E+01										
1.27E-04	6.86E-04	0.75	1.80	5%	1.00E+01										
1.27E-04	6.86E-04	0.75	2.10	5%	1.00E+01										
1.27E-04	6.86E-04	0.75	2.40	5%	1.00E+01										

Figure D.4 - The *Results* Worksheet with Completed and Uncompleted Data Sets.

Orifice X-Sec Dat and *Insert X-sec Dat* Worksheets

These worksheets contain the experimental collision cross section which are integrated to provide the collision terms for the orifice and insert models. The references are listed on this worksheet, and the data have been converted to a function of speed for use in the equations presented in Chapter 4. This worksheet supports the orifice and insert models, and users need modify the data only when considering hollow cathode operation on gases other than xenon. In such a case, the electron-impact ionization, electron-impact total excitation, and the elastic electron-neutral collision cross-sections must replace those for xenon on this sheet.

Pressure Worksheet

The *Pressure* worksheet, shown in Figure D.5, calculates the pressure in the insert region of the hollow cathode based on some of the results of other sections of the model. The theory behind this mode is presented in Chapter. 4. Since the model consists of straightforward algebraic equations, the worksheet is stand-alone, independent of any macros.

Preliminary Calculations		**Pressures**	
Mass Flow Rate	2.33E-07 kg/s	Critical Sonic Pressure	4.08E+03 Pa
Specific Gas Constant	6.31E+01 J/kg-K	Orifice Entrance Pressure	1.81E+04 Pa
Orifice Viscosity	7.57E-05 kg-m/s	Insert Region Pressure	1.92E+04 Pa
		Insert Region Pressure (Torr)	1.45E+02 Torr

Figure D.5 - The Pressure Worksheet.

Ion, Neutral Temps Worksheet

The *Ion, Neutral Temps* worksheet, shown in Figure D.6, is used to calculate the radial temperature profiles of the ions and neutrals in the orifice. The differential equations describing radial temperature variation are solved using a fourth order Runge-Kutta method. The centerline boundary condition of zero temperature gradient is specified in the problem formulation. The Excel™ Solver analysis tool was used to determine the centerline temperature which satisfied the boundary condition that the ions and neutrals must equal the wall temperature at the wall. Typically this technique was iterated upon until both the ions and neutrals matched the boundary conditions, and the constraints for the solver were restrictive in order to maintain stability. A major drawback of this method was that once the solver solution went unstable, a stable solution was no longer possible. The results of this model could be used with the orifice model to provide a more accurate estimate of the neutral density in the orifice.

CONSTANTS:			**INPUTS:**			**CALCULATED:**			**Results:**		
k =	1.38E-23	J/K	Mi =	1.31E+02	amu	Coul.Log =	2.27E+00		Ti (axis) =	1442	K
pi =	3.14E+00		ne avg =	1.00E+23	m^-3	Step Size =	7.94E-07	m	Tn (axis) =	1457	K
me =	5.46E-04	amu	Te =	2.16E+00	eV	Coll. XS (i,n) =	1.39E-19	m^2			
h =	6.63E-34	J-s	Ze =	-1.00E+00	Charge	Cond. Coeff.	8.90E-04	(J/K-m^2)*(J/K-kg)^0.5			
			Zi =	1.00E+00	Charge	Coll. XS (e,n) =	6.16E-22		**Ti, Tn Guesses**		
ne radial function	Step		nn =	1.15E+23	m^-3				Ti (axis) =	1442	K
A =	1.61E-10		Ro =	6.35E-05	m		1.71E-02		Tn (axis) =	1457	K
C2 =	8.28E-05		Steps =	8.00E+01	#	dTwall_Neu =	1.00E-02	K (should be zero)			
C3 =	-8.86E-10		Twall in =	1.44E+03	K	dTwall =	-7.07E-03	K (should be zero)			

			IONS		Electron	Neutral					
Radius (m)	*ne(r)*	*nn(r)*	*teq (s)*	*nu,in (Hz)*	Heat	Heat	*k1z*	*k2z*	*k3z*	*k4z*	*z*
0.00E+00	5.67E+21	1.43E+23	1.02E-05	1.36E+07	-5.39E+09	-1.50E+09	-6.89E+09	-1.69E+08	-6.72E+09	-2.49E+08	0.00E+00
7.94E-07	5.67E+21	1.43E+23	1.02E-05	1.36E+07						09	-2.77E+03
1.59E-06	5.67E+21	1.43E+23	1.02E-05	1.36E+07						09	-5.49E+03
2.38E-06	5.67E+21	1.43E+23	1.02E-05	1.36E+07						09	-8.21E+03
3.18E-06	5.67E+21	1.43E+23	1.02E-05	1.36E+07						09	-1.09E+04
3.97E-06	5.67E+21	1.43E+23	1.02E-05	1.36E+07						09	-1.37E+04
4.76E-06	5.67E+21	1.43E+23	1.02E-05	1.36E+07						09	-1.64E+04
5.56E-06	5.67E+21	1.43E+23	1.02E-05	1.36E+07						09	-1.91E+04
6.35E-06	5.67E+21	1.43E+23	1.02E-05	1.36E+07						09	-2.19E+04
7.14E-06	5.67E+21	1.43E+23	1.02E-05	1.36E+07						09	-2.46E+04
7.94E-06	5.67E+21	1.43E+23	1.02E-05	1.36E+07						09	-2.73E+04
8.73E-06	5.67E+21	1.43E+23	1.02E-05	1.36E+07						09	-3.00E+04
9.53E-06	5.67E+21	1.43E+23	1.02E-05	1.36E+07						09	-3.27E+04
1.03E-05	5.67E+21	1.43E+23	1.02E-05	1.36E+07						09	-3.55E+04
1.11E-05	5.67E+21	1.43E+23	1.02E-05	1.36E+07						09	-3.82E+04
1.19E-05	5.67E+21	1.43E+23	1.02E-05	1.36E+07						09	-4.09E+04
1.27E-05	5.67E+21	1.43E+23	1.02E-05	1.36E+07	-5.39E+09	-1.44E+09	-3.40E+09	-3.40E+09	-3.40E+09	-3.40E+09	-4.36E+04
1.35E-05	5.67E+21	1.43E+23	1.02E-05	1.36E+07	-5.39E+09	-1.43E+09	-3.40E+09	-3.40E+09	-3.40E+09	-3.40E+09	-4.63E+04
1.43E-05	5.67E+21	1.43E+23	1.02E-05	1.36E+07	-5.39E+09	-1.43E+09	-3.39E+09	-3.39E+09	-3.39E+09	-3.39E+09	-4.90E+04
1.51E-05	5.67E+21	1.43E+23	1.02E-05	1.36E+07	-5.39E+09	-1.42E+09	-3.38E+09	-3.39E+09	-3.39E+09	-3.39E+09	-5.17E+04
1.59E-05	5.67E+21	1.43E+23	1.02E-05	1.36E+07	-5.39E+09	-1.41E+09	-3.38E+09	-3.38E+09	-3.38E+09	-3.38E+09	-5.44E+04
1.67E-05	5.67E+21	1.43E+23	1.02E-05	1.36E+07	-5.39E+09	-1.40E+09	-3.37E+09	-3.37E+09	-3.37E+09	-3.37E+09	-5.70E+04
1.75E-05	5.67E+21	1.43E+23	1.02E-05	1.36E+07	-5.39E+09	-1.39E+09	-3.36E+09	-3.37E+09	-3.37E+09	-3.37E+09	-5.97E+04

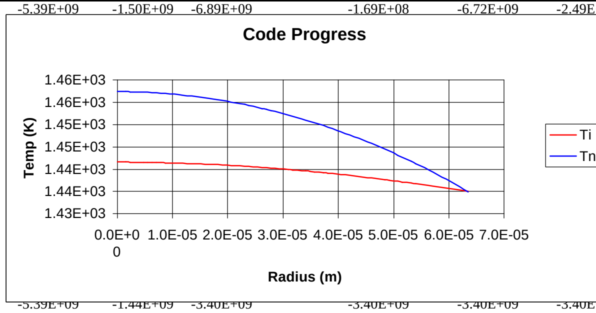

Figure D.6 - Partial Illustration of the *Ion, Neutral Temps* Worksheet.

BIBLIOGRAPHY

[1] Rawlin, V. K. and Pawlik, E. V., "A Mercury Plasma-Bridge Neutralizer," Journal of Spacecraft and Rockets, Vol. 5, No. 7, July 1968, pp. 814-820.

[2] Kerkow, H., Boubetra, D., and Holldack, K., "A Cold Cathode Ion Source with a Magnetic Hollow Cathode," Nuclear Instruments and Methods in Physics Research, B68, 1992, pp. 41-44.

[3] Kirkici, H. and Bruno, D., "Operating Characteristics of a Segmented Hollow Cathode Over a Wide Pressure Range," IEEE Transactions on Plasma Science, Vol. 23, No. 3, June 1995, pp. 229-234.

[4] Fradkin, D. B., et al., "Experiments Using a 25-kW Hollow Cathode Lithium Vapor MPD Arcjet," AIAA Journal, Vol. 8, No. 5, May 1970, pp. 886-894.

[5] Ferreira, C. M. and Delcroix, J. L., "Theory of the Hollow Cathode Arc," Journal of Applied Physics, Vol. 49, No. 4, April 1978, pp. 2380-2395.

[6] Sarver-Verhey, T. R., "Destructive Evaluation of a Xenon Hollow Cathode After a 28,000 Hour Life Test," NASA/CR—1998-208678.

[7] Forman, R. and Elmer, P., "Life Test Studies on Tungsten Impregnated Cathodes," IEEE Transactions on Electron Devices, Vol. ED-27, No. 7, July 1980, pp. 1309-1310.

[8] Shroff, A. M., Palluel, P., and Tonnerre, J. C., "Performance and Life Tests of Various Types of Impregnated Cathodes," Applications of Surface Science, Vol. 8, 1981, pp. 36-49.

[9] Patterson, M. J. and Rawlin, V. K., "Derated Ion Thruster Design Issues," IEPC Paper No. 91-150, AIDAA / AIAA / DGLR / JSASS 22nd International Electric Propulsion Conference, Viareggio, Italy, Oct. 1991.

[10] Polk, J. E., et al., "The Effect of Engine Wear on Performance in the NSTAR 8000 Hour Ion Engine Endurance Test," AIAA Paper No. 97-3387, 33rd AIAA / ASME / SAE / ASEE Joint Propulsion Conference and Exhibit, Seattle, WA, July 1997.

[11] Patterson, M. J., Grisnik, S. P., and Soulas, G. C., "Scaling of Ion thrusters to Low-power," IEPC Paper No. 97-098, 25th International Electric Propulsion Conference, Cleveland, OH, Aug. 1997.

[12] Patterson, M. J. and Oleson, S. R., "Low-Power Ion Propulsion for Small Spacecraft," AIAA Paper No. 97-3060, 33rd AIAA / ASME/ SAE / ASEE Joint Propulsion Conference and Exhibit, Seattle, WA, July 1997.

[13] Domonkos, M. T., et al, “Very Near-Field Plume Investigation of the D55,” AIAA Paper No. 97-3062, 33rd AIAA / ASME / SAE / ASEE Joint Propulsion Conference and Exhibit, Seattle, WA, July 1997.

[14] Garner, C. E., et al, “Experimental Evaluation of the Russian Anode Layer Thruster,” 3rd Russian-German Conference on Electric Propulsion Engines and Their Technical Applications, Stuttgart, Germany, July 1994.

[15] Garkusha, V. I., Lyapin, E. A., Semyenkin, A. V., and Tverdokhlebov, S. O., “Anode Layer Thrusters, State-of-the-Art and Perspectives,” Proceedings of the 23rd International Electric Propulsion Conference, Vol. 3, 1993, pp. 2120-2124.

[16] Jacobson, D. T. and Jankovsky, R. S., “Test Results of a 200-W Class Hall Thruster,” AIAA Paper No. 98-3792, 34th AIAA / ASME / SAE / ASEE Joint Propulsion Conference, Cleveland, OH, July 1998.

[17] Patterson, M. J., et al, “Space Station Cathode Design, Performance, and Operating Specifications,” IEPC Paper No. 97-170, 25th International Electric Propulsion Conference, Cleveland, OH, Aug. 1997.

[18] Sarver-Verhey, T. R., “Continuing Life Test of a Xenon Hollow Cathode for a Space Plasma Contactor,” NASA Contractor Report 195401, Nov. 1994.

[19] Robson, R. R., et al, “Plasma Contactor for the ISTP/Polar Spacecraft,” IEPC Paper No. 91-064, AIDAA / AIAA / DGLR / JSASS 22nd International Electric Propulsion Conference, Viareggio, Italy, Oct. 1991.

[20] Soulas, G. C., “Multiple Hollow Cathode Wear Testing,” NASA Contractor Report 195335, June 1994.

[21] Ohlinger, W. and Rebestock, K.M., “Barium Calcium Aluminate Impregnant Materials: Interaction with Sea-Level Ambient Atmospheres and Decomposition Behaviors of Reaction Products,” AIAA Paper No. 94-3135, 30th AIAA / ASME / SAE / ASEE Joint Propulsion Conference, Indianapolis, IN, June 1994.

[22] Mirtich, M. J. and Kerslake, W. R., “Long Lifetime Hollow Cathodes for 30-cm Mercury Ion Thrusters,” AIAA Paper 76-985, AIAA International Electric Propulsion Conference, Key Biscayne, FL, Nov. 1976.

[23] Rawlin, V. K., “A 13,000-Hour Test of a Mercury Hollow Cathode,” NASA Technical Memorandum X-2785, June 1973.

[24] Mandell, M. J. and Katz I., “Theory of Hollow Cathode Operation in Spot and Plume-modes,” AIAA Paper No. 94-3134, 30th AIAA / ASME / SAE / ASEE Joint Propulsion Conference, Indianapolis, IN, June 1994.

[25] Siegfried, D. E., A Phenomenological Model for Orificed Hollow Cathodes, Ph. D. Dissertation, Colorado State University, 1983.

[26] Salhi, A., Theoretical and Experimental Studies of Orificed, Hollow Cathode Operation, Ph. D. Dissertation, Ohio State University, 1993.

[27] Capacci, M., Minucci, M., Severi, A., "Simple Numerical Model Describing Discharge Parameters in Orificed Hollow Cathode Devices," AIAA Paper No. 97-2791, 33rd AIAA / ASME / SAE / ASEE Joint Propulsion Conference and Exhibit, Seattle, WA, July 1997.

[28] Rittner, E. S., Rutledge, W. C., and Ahlert, R. H., "On the Mechanism of Operation of the Barium Aluminate Impregnated Cathode," Journal of Applied Physics, Vol. 28, No. 12, Dec. 1957, pp. 1468-1473.

[29] Suitch, P. R., Thermochemical Reactions in Tungsten-Matrix Dispenser Cathodes Impregnated with Various Barium-Calcium-Aluminates, Ph. D. Thesis, Georgia Institute of Technology, 1987.

[30] Crawford, F. W. and Cannara, A. B., "Structure of the Double Sheath in a Hot-Cathode Plasma," Journal of Applied Physics, Vol. 36, No. 10, Oct. 1965, pp. 3135-3141.

[31] Prewitt, P. D. and Allen, J. E., "The Double Sheath Associated with a Hot Cathode," Proceedings of the Royal Society of London A, Vol. 348, 1976, pp. 435-446.

[32] Bohm, D., The Characteristics of Electrical Discharges in Magnetic Fields (Editors Guthrie, A. and Wakerling, R. K.), Ch. 3, McGraw-Hill, New York, 1949.

[33] Anders, A. and Kühn, M., "Characterization of a Low-Energy Constricted-Plasma Source," Review of Scientific Instruments, Vol. 69, No. 3, Mar. 1998, pp. 1340-1343.

[34] Williams, J. D. and Wilbur, P. J., "Electron Emission from a Hollow Cathode-Based Plasma Contactor," Journal of Spacecraft and Rockets, Vol. 29, No. 6, Nov.-Dec. 1992, pp. 820-829.

[35] Byers, D. C. and Snyder, A., "Parametric Investigation of Mercury Hollow-Cathode Neutralizers," Journal of Spacecraft and Rockets, Vol. 8, No. 2, Feb. 1971, pp. 133-139.

[36] Rawlin, V. K. and Kerslake, W. R., "Durability of the SERT II Hollow Cathodes and Future Applications of Hollow Cathodes," AIAA Paper No. 69-304, AIAA 7th Electric Propulsion Conference, Williamsburg, VA, Mar. 1969.

[37] Mirtich, M. J., "Investigation of Hollow Cathode Performance for 30-cm Thrusters," NASA TM X-68298, 1973.

[38] Goldstein, R., Pawlik, E. V., and Wen, L.-C., "Preliminary Investigations of Ion Thruster Cathodes," JPL Technical Report 32-1536, 1971.

[39] Hudson, W. R. and Weigand, A. J., "Hollow Cathodes with BaO Impregnated Porous Tungsten Inserts and Tips," NASA TM X-71417, 1973.

[40] Fearn, D. G. and Philip, C. M., "An Investigation of Physical Processes in a Hollow Cathode Discharge," AIAA Paper No. 72-416, AIAA 9th Electric Propulsion Conference, Bethesda, MD, April 1972.

[41] Rehn, L. A., "Argon Hollow Cathode," NASA CR-135102, Nov. 1976.

[42] Rehn, L. and Kaufman, H. R., "Correlation of Inert Gas Hollow Cathode Performance," AIAA / DGLR 13th International Electric Propulsion Conference, San Diego, CA, April 1978.

[43] Siegfried, D. E. and Wilbur, P. J., "A Model for Mercury Orificed Hollow Cathodes: Theory and Experiment," AIAA Journal, Vol. 22, No. 10, Oct. 1984, pp. 1405-1412.

[44] Rawlin, V. K., "Operation of the J-Series Thruster Using Inert Gas," NASA TM-82977, Nov. 1982.

[45] Salhi, A. and Turchi, P.J., "Scaling Relations for Design and Operation of Orificed Hollow Cathodes," AIAA Paper No. 94-3133, 30th AIAA Joint Propulsion Conference, Indianapolis, IN, June 27-29, 1994.

[46] Salhi, A. and Turchi, P.J., "Theoretical Modeling of Orificed, Hollow Cathode Discharges," Proceedings of the 23rd International Electric Propulsion Conference, Vol. 1, 1993, pp. 253-260.

[47] Groh, K. H., Walther, S. E., and Loeb, H. W., "Recent Neutralizer Investigations at Giessen University," AIAA Paper No. 76-989, AIAA International Electric Propulsion Conference, Key Biscayne, FL, Nov. 1976.

[48] Bianconi, M., Cirri, G. F., Matticari, G., and Severi, A., "Design Consolidation and Space (Pre)Qualification of a Plasma Bridge Neutralizer for the RITA 10 Ion Thruster," IEPC Paper 91-024, AIDAA / AIAA / DGLR / JSASS 22nd International Electric Propulsion Conference, Viareggio, Italy, Oct. 1991.

[49] Cirri, G. F., Matticari, G., Minucci, M., Noci, G., Severi, A., and Svelto, F., "Plasma Contactor Device Based on Hollow Cathode Technology for Spacecrafts

Charging Neutralization and Tethered System Applications: Review of Italian National Program," IEPC Paper No. 93-041, AIAA / AIDAA / DGLR / JSASS 23rd International Electric Propulsion Conference, Seattle, WA, Sept. 1993.

[50] Kaufman, H. R., "Technology of Electron-Bombardment Ion Thrusters," Advances in Electronics and Electron Physics, Vol. 36, 1974, pp. 265-373.

[51] Babkin, G. V., et al, "Experimental Investigation of the Plasma in a Multichannel Cathode", Journal-of-Applied-Mechanics-and-Technical-Physics, Vol.17, No.6, Nov.-Dec. 1976, pp.767-770.

[52] Delcroix, J. L., Minoo, H., and Trindade, A. R., "Gas Fed Multichannel Hollow Cathode Arcs," The Review of Scientific Instruments, Vol. 40, No. 12, Dec. 1969.

[53] DePauw, J. F., "30 cm Thruster Cathode Activation," NASA Tech Ready Information Memo No. 13, NASA Lewis Research Center, Dec. 1977.

[54] McGee, T. D., Principles and Methods of Temperature Measurement, John Wiley & Sons, Inc., New York, 1988.

[55] Yaws, S. L., Handbook of Thermal Conductivity, Volume 4: Inorganic Compounds and Elements, Gulf Publishing Company, Houston, 1997.

[56] Polk, J. E. and Goodfellow, K. D., "High Current Cathode Thermal Behavior, Part II: Experiments," IEPC Paper No. 93-029, Proceedings of the 23rd International Electric Propulsion Conference, Seattle, WA, Sept. 1993, pp. 293-303.

[57] Sarver-Verhey, T. R., "Extended Test of a Xenon Hollow Cathode for a Space Plasma Contactor," NASA Contractor Report 195402, Nov. 1994.

[58] Ramalingam, M. L. and Jacobson, D. L., "An Accurate Method for the Determination of Normal Spectral Emissivities of Refractory Alloys," AIAA Paper No. 87-0321, AIAA 25th Aerospace Sciences Meeting, Reno, NV, Jan. 1987.

[59] Schott, L. "Electric Probes," in Plasma Diagnostics, Lochte-Holtgreven, W., Editor, American Institute of Physics, New York, 1995.

[60] Williams, G., Smith, T., Domonkos, M., Shand, K., and Gallimore, A., "Laser Induced Fluorescence Characterization of Ions Emitted from a Hollow Cathode," AIAA Paper 99-2862, *35th AIAA / ASME / SAE / ASEE Joint Propulsion Conference*, Los Angeles, CA, June 1999.

[61] Druyvesteyn, M. J., Z. Physik, Vol. 64, pp. 781, 1930.

[62] Swift, J. D. and Schwar, M. J. R., Electrical Probes for Plasma Diagnostics, American Elsevier Publishing Company, Inc., New York, 1970.

[63] Rundle, H. W., Clark, D. R., and Deckers, J. M., "Electron Energy Distribution Functions in an O_2 Glow Discharge," Canadian Journal of Physics, Vol. 51, pp. 144-148, 1973.

[64] Sarver-Verhey, T. R., "28,000 Hour Xenon Hollow Cathode Life Test Results," IEPC Paper No. 97-168, 25th International Electric Propulsion Conference, Cleveland, OH, Aug. 1997.

[65] Domonkos, M. T., Marrese, C. M., Haas, J. M., and Gallimore, A. D., "Very Near-Field Plume Investigation of the D55," AIAA Paper No. 97-306, 33rd AIAA / ASME / SAE / ASEE Joint Propulsion Conference, Seattle, WA, July 1997.

[66] Jansen, S. W., "Microwave Diagnostics for Ion Thrusters," IEPC Paper No. 93-237, 23rd International Electric Propulsion Conference, Seattle, WA, Sept. 1993.

[67] Van Noord, Thermal Modeling of an Ion Thruster, Ph. D. Dissertation, The University of Michigan, 1999.

[68] Rapp, D. and Englander-Golden, P., "Total Cross Sections for Ionization and Attachment in Gases by Electron Impact. I. Positive Ionization," The Journal of Chemical Physics, Vol. 43, No. 5, Sept. 1, 1965, pp. 1464-1479.

[69] Chen, F. F., Introduction to Plasma Physics and Controlled Fusion, Volume 1: Plasma Physics, Plenum Press, New York, 1984.

[70] Huba, J. D., editor, Naval Research Laboratory: Plasma Formulary, NRL/PU/6790-94-265, 1994.

[71] Brode, R. R., "The Quantitative Study of the Collisions of Electrons with Atoms," Reviews of Modern Physics, Vol. 5, Oct. 1933, pp. 257-279.

[72] Hayashi, M., "Determination of Electron-Xenon Total Excitation Cross-Sections, from Threshold to 100 eV, from Experimental Values of Townsend's α," Journal of Physics D: Applied Physics, Vol. 16, 1983, pp. 581-589.

[73] Goodfellow, K. D., A Theoretical and Experimental Investigation of Cathode Processes in Electric Thrusters, Ph. D. Dissertation, The University of Southern California, 1996.

[74] Striganov, A. R. and Sventitskii, N. S., Tables of Spectral Lines of Neutral and Ionized Atoms, IFI/Plenum Data Corporation, New York, 1968.

[75] Siegel, R. and Perlmutter, M., "Convective and Radiant Heat Transfer for Flow of a Transparent Gas in a Tube with a Gray Wall," International Journal of Heat Mass Transfer, Vol. 5, 1962, pp. 639-660.

[76] Siegel, R. and Keshock, G., "Wall Temperatures in a Tube with Forced Convection, Internal Radiation Exchange, and Axial Wall Heat Conduction," NASA Technical Note D-2116, March 1964.

[77] Jahn, R. G., Physics of Electric Propulsion, McGraw-Hill Book Company, New York, 1968.

[78] Griffiths, D. J., Introduction to Electrodynamics, Second Edition, Prentice-Hall, Inc., New Jersey, 1989.

[79] Spitzer, L., Physics of Fully Ionized Gases, John Wiley & Sons Interscience Publishers, New York, 1962.

[80] Mitchner, M. and Kruger, C. H., Partially Ionized Gases, John Wiley and Sons, New York, New York, 1973.

[81] Gombosi, T., Gaskinetic Theory, Cambridge University Press, Cambridge, Great Britain, 1994.

[82] Lide, D. R., Editor-in-Chief, CRC Handbook of Physics and Chemistry: 73rd Edition, CRC Press, Boca Raton, 1992.

[83] Touloukian, Y. S., Powell, R. W., Ho, C. Y., and Klemens, P. G., Thermophysical Properties of Matter: Volume 1, Thermal Conductivity, Metallic Elements and Alloys, IFI / Plenum Publishers, New York, 1970.

[84] "Rhenium Alloys, Technical Properties Data," Rhenium Alloys, Inc. Document RA-1001, 1996.

[85] Matsunami, N., et al., "Energy Dependence of the Ion-Induced Sputtering Yields of Monatomic Solids," Atomic Data and Nuclear Data Tables, Vol. 31, 1984, pp. 1-80.

[86] Katz, Ira and Patterson, M. J., "Optimizing Plasma Contactors for Electrodynamic Tether Missions," presented at Tether Technology Interchange, Sept. 9, 1997, Huntsville, AL.

[87] Thermophysical Properties of Matter: Volume 11, Viscosity, IFI/Plenum Publishers, New York, 1970.